

**POROUS GLASS FROM COAL FLY ASH:  
PREPARATION, CHARACTERIZATION AND  
ITS ADSORPTION STUDY**



**Chaturaporn Nimjaroen**

**A Thesis Submitted in Partial Fulfillment of the Requirements for the  
Degree of Doctor of Philosophy in Chemical Engineering  
Suranaree University of Technology  
Academic Year 2013**

วัสดุแก้วพรุนจากเถ้าลอยถ่านหิน: การเตรียม การวัดคุณสมบัติและการศึกษา  
กระบวนการดูดซับ



นายจตุรพร นิมเจริญ

วิทยานิพนธ์นี้เป็นส่วนหนึ่งของการศึกษาตามหลักสูตรปริญญาวิศวกรรมศาสตรดุษฎีบัณฑิต

สาขาวิชาวิศวกรรมเคมี

มหาวิทยาลัยเทคโนโลยีสุรนารี

ปีการศึกษา 2556

**POROUS GLASS FROM COAL FLY ASH: PREPARATION,  
CHARACTERIZATION AND ITS ADSORPTION STUDY**

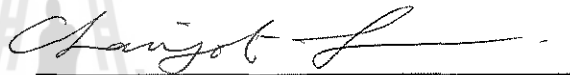
Suranaree University of Technology has approved this thesis submitted in partial fulfillment of the requirements for the Degree of Doctor of Philosophy.

Thesis Examining Committee



(Dr. Terasut Sookkumnerd)

Chairperson



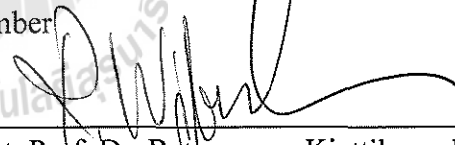
(Prof. Dr. Chaiyot Tangsathitkulchai)

Thesis advisor



(Asst. Prof. Dr. Atichat Wongkoblap)

Member



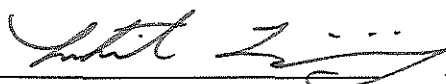
(Asst. Prof. Dr. Ratanawan Kiattikomol)

Member

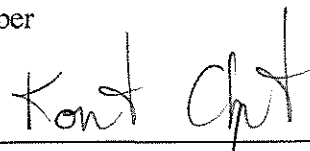
SUPUNNEE J.

(Dr. Supunnee Junpirom)

Member



(Prof. Dr. Sukit Limpijumnong)



(Assoc. Prof. Ft. Lt. Dr. Kontorn Chamniprasart)

Vice Rector for Academic Affairs

Dean of Institute Engineering

and Innovation

จตุพร นิมะเจริญ : วัสดุแก้วพรุนจากเถ้าลอยถ่านหิน: การเตรียม การวัดคุณสมบัติและ  
การศึกษากระบวนการดูดซับ (POROUS GLASS FROM COAL FLY ASH:  
PREPARATION, CHARACTERIZATION AND ITS ADSORPTION STUDY) อาจารย์  
ที่ปรึกษา : ศาสตราจารย์ ดร.ชัยยศ ตั้งสถิตย์กุลชัย, 297 หน้า.

วิทยานิพนธ์นี้มุ่งศึกษากระบวนการเตรียมแก้วพรุนจากเถ้าลอยถ่านหินและประสิทธิภาพ  
ในการดูดซับของแก้วพรุนทั้งในระบบของเหลวและแก๊ส แก้วพรุนที่สังเคราะห์อาศัยหลักการ  
แบ่งวัฏภาคขององค์ประกอบของแก้วพรุน โดยมีกระบวนการเตรียม ดังนี้ ขั้นแรก เริ่มจากการนำ  
เถ้าลอยผสมกับสารประกอบออกไซด์ต่างๆหลอมกลายเป็นน้ำแก้วและขึ้นรูปเป็นแก้วบอโรซิลิเกต  
หลังจากนั้นทำการอบด้วยความร้อนเพื่อให้เกิดกระบวนการแบ่งวัฏภาคที่สภาวะอุณหภูมิและเวลา  
ต่างๆ และขั้นสุดท้ายนำสารละลายกรดร้อนเจือจางละลายในส่วนวัฏภาคบอโรออกไซด์ เพราะวัฏภาค  
บอโรสามารถละลายได้ดีในกรดร้อนเจือจาง สำหรับวัฏภาคซิลิกาไม่สามารถละลายในสารละลาย  
กรดจึงยังคงเป็นโครงสร้างของแก้วพรุนได้ ขนาดรูพรุนเฉลี่ยของแก้วพรุนที่เตรียมได้อยู่ในช่วง 10  
– 2000 นาโนเมตรและพบว่ารูพรุนมีขนาดเพิ่มขึ้นตามระยะเวลาและอุณหภูมิที่ใช้ในการอบด้วย  
ความร้อน และแก้วพรุนที่เตรียมได้มีองค์ประกอบใกล้เคียงกับแก้วพรุนซิราลู ลักษณะรูพรุนของ  
แก้วพรุนเป็นแบบรูพรุนเชื่อมต่อกันและกลไกการเกิดเป็นแบบการเกิดนิวเคลียสและการโต

ในการทดสอบความสามารถของการประยุกต์ใช้แก้วพรุนในกระบวนการดูดซับ โดยการ  
นำแก้วพรุนมาดูดซับในระบบของเหลว โดยทำการดูดซับประจุทองแดง ประจุเงินและประจุทองคำ  
ในสารละลายแบบองค์ประกอบเดี่ยวและแบบองค์ประกอบผสมของประจุทองแดงและเงิน โดย  
ศึกษาการดูดซับบนแก้วพรุนที่เตรียมได้และแก้วพรุนที่เพิ่มหมู่ฟังก์ชันบนพื้นผิว พบว่า แก้วพรุนที่  
ปรับปรุงหมู่ฟังก์ชันด้วยหมู่อะมิโน มีความสามารถในการดูดซับประจุทองแดงได้ดีกว่าประจุเงิน  
และ แก้วพรุนที่ปรับปรุงหมู่ฟังก์ชันด้วยหมู่ไทออล มีความสามารถในการดูดซับประจุเงินได้ดีกว่า  
ประจุทองแดง ผลการดูดซับนี้สอดคล้องทั้งการดูดซับแบบองค์ประกอบเดี่ยวและองค์ประกอบ  
ผสม นอกจากนี้ยังได้นำเสนอผลการวิเคราะห์สมดุลและจลนพลศาสตร์ของระบบดูดซับโดยใช้  
แบบจำลองที่นิยมใช้กันอีกด้วย สำหรับกระบวนการดูดซับในระบบแก๊ส ได้ศึกษาถึงสมบัติความ  
เป็นขั้วของสารดูดซับที่แตกต่างกัน เช่น แก๊สคาร์บอนไดออกไซด์ ไอเอทานอล และไอน้ำ  
ทำการศึกษการดูดซับบนแก้วพรุนที่เตรียมได้ พบว่า การดูดซับของแก๊สคาร์บอนไดออกไซด์บน  
แก้วพรุนเป็นการดูดซับแบบแรงการกระจายและสามารถอธิบายได้ด้วยแบบจำลองแลงมัวร์และ  
ฟรุนดลิชในทางตรงกันข้ามกระบวนการดูดซับของไอเอทานอลและไอน้ำเป็นการดูดซับแบบหลาย  
ชั้น เนื่องจาก การดูดซับของ ไอเอทานอลและไอน้ำเป็นการดูดซับด้วยพันธะไฮโดรเจน จึงมีการดูด

ชั้นบนพื้นผิวระหว่างซิลานอลกับตัวดูดซับและตัวดูดซับกับตัวดูดซับ แบบจำลองไอโซเทิร์มการดูดซับของระบบนี้เหมาะสมกับแบบจำลองบีอีทีแบบหลายชั้น สำหรับการศึกษากระบวนการดูดซับทางจลนพลศาสตร์ ทำการศึกษาที่อุณหภูมิการดูดซับต่างๆ โดยแบบจำลองอันดับสองเสมือนมีความเหมาะสมและสอดคล้องกับผลการทดลองได้ดีที่สุด

สำหรับกระบวนการกำจัดสีสังเคราะห์ ในงานวิจัยนี้ แก้วพรุนถูกประยุกต์ใช้ในคอลัมน์เบดนิ่ง โดยศึกษาการดูดซับของเมทิลินบลูจากสารละลาย โดยศึกษาผลของตัวแปร ได้แก่ ความสูงของเบด อัตราการไหลแรกเข้า ความเข้มข้นของสารละลายแรกเข้า ขนาดของอนุภาคและขนาดของรูพรุนของแก้วพรุน โดยศึกษาและอธิบายผลการทดลองโดยใช้แบบจำลองทั้งหมดสามแบบ ได้แก่ แบบจำลองคลินเคนเบิร์ก แบบจำลองโบฮาร์ทและอดัม และแบบจำลองโทมัส พบว่า แบบจำลองโทมัส สามารถอธิบายและทำนายผลการทดลองได้ดีกว่าแบบจำลองคลินเคนเบิร์กและแบบจำลองโบฮาร์ทและอดัม



สาขาวิชา วิศวกรรมเคมี

ปีการศึกษา 2556

ลายมือชื่อนักศึกษา ๑๗๖๗๑ สันติธร.

ลายมือชื่ออาจารย์ที่ปรึกษา สมศักดิ์

CHATURAPORN NIMJAROEN : POROUS GLASS FROM COAL FLY  
ASH: PREPARATION, CHARACTERIZATION AND ITS ADSORPTION  
STUDY. THESIS ADVISOR : PROF. CHAIYOT TANGSATHITKULCHAI,  
Ph.D., 297 PP.

#### POROUS GLASS/PHASE SEPARATION/ADSORPTION

This thesis work is focused on the preparation of porous glass from coal fly ash and studying its adsorption performance in both the liquid and gas systems. Porous glass was prepared using the phase separation method which consists of the following steps of adjusting the ash composition by oxide addition to meet the required base glass system, melting the raw mix to form the borosilicate base glass product, separating the binary glass phase by heat treating as a function of temperature and time, and finally leaching out the borate rich phase by a dilute mineral acid to obtain the porous framework of silica adsorbent. The median pore diameter of prepared porous glass lies in the mesopore size range from 10-2000 nm and was found to increase with increasing treatment time and temperature. The obtained porous glass shows similar chemical composition to that of commercial Shirasu porous glass. The forming of pore connectivity could take place by the mechanism of nucleation and growth and the rate controlling step could be the diffusion of structural units involving oxygen ions.

To test its potential use as an adsorbent, the adsorption by the prepared porous glass was carried out both in the liquid and gas systems. The single adsorption of  $\text{Cu}^{2+}$ ,  $\text{Ag}^+$  and  $\text{Au}^{3+}$  and the binary adsorption of  $\text{Cu}^{2+}$  and  $\text{Ag}^+$  from aqueous solution were performed with both the virgin and chemically grafted porous glass adsorbents.

It was found that the selective adsorption of copper and silver ions could be achieved with porous glass samples grafted with amino (-NH<sub>2</sub>) and thiol (-SH) groups, respectively, and the amounts adsorbed are the same whether the adsorption takes place in pure or mixture systems. The analysis of adsorption equilibrium and kinetics by the well-known models were also presented. Adsorption in gas phase of adsorbates with different polarity, including carbon dioxide, ethanol and water, was carried out using virgin unmodified porous glass. It was discovered that the adsorption of carbon dioxide involves the dispersive interaction forces and its adsorption isotherm is well described by the Langmuir and Freundlich equations. On the other hand, the adsorption of ethanol and water results from hydrogen bonding through the silanol groups on the porous glass surface and the isotherms can be well fitted with the n-layer BET equation. The kinetics of water adsorption was also studied as a function of temperature and the pseudo second-order model was found to excellently describe the experimental data.

The removal of a model synthetic dye, methylene blue, by porous glass was conducted in a fixed-bed adsorption column. The column dynamics presented as the breakthrough curves was studied as a function of adsorbent bed height, feed flow rate, feed concentration of solute, and particle size and mean pore size of the adsorbent particles. Three breakthrough models, based on different isotherm curvature, were applied to validate the breakthrough data. Thomas model for curved isotherm gave the best predictive capability, as compared to Klinkenberg model for linear isotherm and Bohart and Adams model for square isotherm.

School of Chemical Engineering

Academic Year 2013

Student's Signature Chaturaporn

Advisor's Signature Chaiyot J.

## **ACKNOWLEDGEMENTS**

With the achievement of this research thesis, I am grateful to all the people that have contributed to this dissertation. First and foremost, I would like to express my special thanks to Professor Dr. ChaiyotTangsathitkulchai, my thesis advisor, for his invaluable help and providing me with opportunity to undertake a Ph.D study. My special thanks are also extended to Professor Dr. Tetsuo Yazawa who acts as my thesis co-advisor during my research time at the Hyogo University, Japan and Assistant Prof. Dr. Shigeki Morimoto, co-advisor in the School of Ceramic Engineering for insightful suggestion.

In addition, I am grateful to all of the academic members in the School of Chemical Engineering for their teaching and support and encouragement. Thanks to all graduate students for making good atmosphere in our research rooms. Financial support from Thailand Research Fund (TRF) through the Royal Golden Jubilee Ph.D. Program (RGJ-Ph.D.) is gratefully acknowledged.

Finally, I would like to dedicate this accomplishment to my parents. Many thanks is also due to my brother and sister for their love and support.

ChaturapornNimjaroen



# TABLE OF CONTENTS

	<b>Page</b>
ABSTRACT (THAI).....	I
ABSTRACT (ENGLISH).....	III
ACKNOWLEDGMENTS .....	V
TABLE OF CONTENTS .....	VI
LIST OF TABLES .....	X
LIST OF FIGURES .....	XV
<b>CHAPTER</b>	
<b>I</b> INTRODUCTION .....	1
1.1 Background and significance of the study .....	1
1.2 Research objectives.....	5
1.3 Scope and limitation of the research.....	5
1.4 References .....	7
<b>II</b> PREPARATION AND CHARACTERIZATION OF POROUS	
<b>GLASS</b> .....	9
2.1 Abstract .....	9
2.2 Introduction .....	10
2.3 Theory and general background of porous glass .....	11
2.3.1 Fly ash .....	11
2.3.2 Porous glass .....	14

## TABLE OF CONTENTS (Continued)

	<b>Page</b>
2.3.3 Mechanism of phase separation in porous glass .....	26
2.3.4 Applications of porous glass .....	27
2.4 Experimental .....	29
2.5 Results and discussion .....	35
2.5.1 Compositions and properties of porous glass .....	35
2.5.2 Pore structure of porous glass .....	41
2.5.3 Pore diameter equation .....	51
2.6 Conclusion .....	56
2.7 References .....	57
<b>III ADSORPTION STUDY OF POROUS GLASS .....</b>	<b>60</b>
3.1 Abstract .....	60
3.2 Introduction .....	60
3.3 Theory and literature reviews .....	63
3.3.1 Adsorption .....	63
3.3.2 Adsorption isotherms .....	69
3.3.3 Adsorption isotherm equations .....	71
3.3.4 Adsorption models of mixtures .....	81
3.3.5 Isosteric heat of adsorption .....	89
3.3.6 Adsorption kinetics .....	90
3.3.7 Surface property of silica .....	96

## TABLE OF CONTENTS (Continued)

	<b>Page</b>
3.3.8 Characterization of porous glass .....	102
3.4 Experimental method .....	104
3.5 Results and discussion .....	111
3.5.1 Adsorbent characterization .....	107
3.5.2 Single component adsorption of heavy metal ions .....	120
3.5.3 Adsorption of binary ions.....	153
3.5.4 Gas-phase adsorption .....	182
3.5.5 Monte Carlo Simulation of CO <sub>2</sub> adsorption on porous glass .....	222
3.6 Conclusion .....	222
3.7 References .....	223
<b>IV REMOVAL OF METHYLENE BLUE IN A FIXED-BED ADSORBER .....</b>	<b>228</b>
4.1 Abstract .....	228
4.2 Introduction .....	228
4.3 Characteristic of fixed-bed adsorption .....	230
4.4 Breakthrough equation .....	233
4.5 Experimental .....	239
4.6 Results and discussion .....	243
4.6.1 Physical and porous properties of porous glass .....	243

## TABLE OF CONTENTS (Continued)

	<b>Page</b>
4.6.2 Batch adsorption tests .....	245
4.6.3 Breakthrough curves .....	247
4.6.4 Breakthrough models .....	254
4.7 Conclusion .....	264
4.8 References .....	265
VCONCLUSION AND RECOMMENDATIONS .....	267
5.1 Conclusion .....	267
5.2 Recommendations for further works .....	274
<b>APPENDICES</b>	
APPENDIX A Monte Carlo Simulation of CO <sub>2</sub> adsorption on porous glass.....	277
APPENDIX B Publication.....	292
BIOGRAPHY .....	297

## LIST OF TABLES

Table	Page
2.1 Typical chemical compositions of ashes produced from burning coals of different ranks .....	12
2.2 Brief historical development of porous glass manufacturing .....	15
2.3 Typical compositions and properties of commercially available porous glass.....	18
2.4 Chemical composition (wt%) of fly ash used in the present work .....	30
2.5 Chemical composition of base glass for porous glass preparation after adding various oxides into the fly ash sample .....	32
2.6 Chemical compositions of molten glass and porous glasses after acid and alkaline treatments (750 °C and 20 hours of heat treatment conditions)....	36
2.7 Physical properties (appearance and weight loss) of prepared porous glass before and after acid leaching.....	37
2.8 Physical properties (appearance and weight loss) of prepared porous glass before and after alkaline leaching.....	39
2.9 Porous and physical properties of porous glasses after acid leaching .....	43
2.10 Porous properties of porous glasses after acid and alkali treatment by mercury intrusion porosimeter (Auto pore III, Micrometrics) .....	49
2.11 Correlation parameters of the relationship between median pore size and heat treatment conditions .....	53

## LIST OF TABLES (Continued)

<b>Table</b>	<b>Page</b>
3.1 Comparison of physical adsorption and chemical adsorption.....	65
3.2 Industrial applications of liquid and gas phase adsorption.....	66
3.3 Frequently used single-component adsorption models in gas phase that can be applied to liquid phase adsorption .....	79
3.4 Porous properties of original and modified porous glass adsorbents.....	112
3.5 Results on point of zero charge and functional group loading of original and modified porous glass adsorbents.....	117
3.6 Adsorbents-adsorbate characterization based on the HSAB theory.....	124
3.7 Adsorption kinetic data of $\text{Cu}^{2+}$ and $\text{Ag}^+$ onto original and modified porous glass at 25 °C.....	128
3.8 Fitted kinetic parameters for the adsorption of $\text{Cu}^{2+}$ and $\text{Ag}^+$ by $\text{PGNH}_2$ and $\text{PGSH}$ at 25 °C.....	130
3.9 Fitted parameters of various isotherm models for single component adsorption of $\text{Cu}^{2+}$ and $\text{Ag}^+$ by modified porous glass at 25 °C.....	135
3.10 Adsorption capacity of copper ions for different common adsorbents....	136
3.11 Adsorption capacity of silver ions for different common adsorbents.....	138
3.12 Fitted parameters of various kinetic models for the adsorption of gold by $\text{PGNH}_2$ and $\text{PGSH}$ at 25 °C.....	146
3.13 Fitting parameters of adsorption models for adsorbed gold by $\text{PG-NH}_2$ and $\text{PG-SH}$ at 25 °C.....	150

## LIST OF TABLES (Continued)

<b>Table</b>	<b>Page</b>
3.14 Adsorption capacity for gold ions of different common adsorbents .....	150
3.15 Calculation scheme for fitting the extended Langmuir isotherm with the experimental isotherm data of $\text{Ag}^+$ - $\text{Cu}^{2+}$ mixture using modified porous glass adsorbents from fly ash of $\text{PGNH}_2$ adsorbent .....	156
3.16 Calculation scheme for fitting the extended Langmuir isotherm with the experimental isotherm data of $\text{Ag}^+$ - $\text{Cu}^{2+}$ mixture using modified porous glass adsorbents from fly ash of $\text{PGSH}$ adsorbent .....	157
3.17 Calculation scheme for fitting the extended Langmuir –Freundlich isotherm with the experimental isotherm data of $\text{Ag}^+$ - $\text{Cu}^{2+}$ mixture using modified porous glass adsorbents from fly ash for $\text{PGNH}_2$ adsorbent ...	163
3.18 Calculation scheme for fitting the extended Langmuir –Freundlich isotherm with the experimental isotherm data of $\text{Ag}^+$ - $\text{Cu}^{2+}$ mixture using modified porous glass adsorbents from fly ash for $\text{PGSH}$ adsorbent ....	166
3.19 Calculated parameters of IAST using the Langmuir isotherm equation for $\text{PG-NH}_2$ .....	175
3.20 Calculated parameters of IAST using the Langmuir isotherm equation for $\text{PG-SH}$ .....	176
3.21 Calculated parameters for IAST using the Freundlich isotherm equation of $\text{PG-NH}_2$ .....	178

## LIST OF TABLES (Continued)

<b>Table</b>	<b>Page</b>
3.22 Calculated parameters for IAST using the Freundlich isotherm equation of PG-NH <sub>2</sub> .....	179
3.33 Fitted parameters of Langmuir and Freundlich equations for the adsorption of carbon dioxide by porous glass from fly ash at various temperatures.....	185
3.34 Adsorption capacity of carbon dioxide by various adsorbents at 1 atm and 30°C.....	186
3.35 Effect of CO <sub>2</sub> adsorption loading on the isosteric heat of adsorption .....	188
3.36 Calculated parameters derived from BET and n-layer BET model for ethanol adsorption on porous glass from coal fly ash .....	196
3.37 Fitted parameters of BET and n-layer BET equations for water vapor adsorption with porous glass from coal fly ash .....	205
3.38 Fitted parameters of adsorption kinetic models at various temperatures.	208
3.39 Effects of temperature and loading for water adsorption by porous glass on the pore and surface diffusivities.....	218
3.40 Effect of water loading on the pre-exponential factor ( $D_{s00}$ ) and activation energy ( $E_a$ ) of surface diffusion equation .....	219
4.1 Experimental conditions for fixed-bed adsorption of methylene blue by porous glass performed at 30°C .....	242



## LIST OF TABLES (Continued)

<b>Table</b>	<b>Page</b>
4.2 Physical and porous properties of porous glass adsorbents used for methylene blue adsorption tests .....	244
4.3 Fitted parameters of isotherm models for the adsorption of methylene blue by porous glass at 30°C.....	247
4.4 Effect of bed height, feed concentration and feed flow rate on the breakthrough parameters for the adsorption of methylene blue by porous glass PG1 at 30°C.....	252
4.5 Effects of pore size and particle size of porous glass on the breakthrough parameters for the adsorption of methylene blue at 30°C .....	253
4.6 Curve fitting schemes for obtaining breakthrough model parameters by regression analysis for the adsorption of methylene blue by porous glass PG1 at 30°C .....	256
4.7 Fitted parameters of breakthrough models for predicting breakthrough curves of methylene blue adsorption by porous glass PG1 at 30°C.....	257
4.8 Sensitivity of parameters of Thomas model on the fitting of breakthrough curve for the adsorption of methylene blue by porous glass PG1 at 30°C	262

## LIST OF FIGURES

Figure	Page
2.1 Pore size distribution of a porous glass having an average median pore diameter of 2.1 nm (21 <sup>o</sup> A).....	19
2.2Preparation method of porous glass .....	20
2.3Ternary Phase diagram for the sodium borosilicate system .....	24
2.4 Three regions of liquid-liquid immiscibility in the SiO <sub>2</sub> - B <sub>2</sub> O <sub>3</sub> - Na <sub>2</sub> O system (wt%).....	25
2.5 Structure of porous glass .....	27
2.6 Scanning Electron Microscope (SEM) photos of fly ash particles at 2,000x magnification. ....	30
2.7 Particle size distribution of calcined fly ash.....	30
2.8 Schematic diagram of the preparation of porous glass from coal fly ash .	33
2.9Equipments used for the characterization of prepared porous glass Samples .....	34
2.10Photographs of base glass, glass after heat treatment at 780 °C and 20 hours conditions and glass after acid leaching with 1 M of HNO <sub>3</sub> solution	40
2.11Relation between pore diameter and heat treatment time at various heat treatment temperatures, after acid leaching .....	45
2.12SEM photos of porous glasses obtained under various heat treatment Conditions.....	46

## LIST OF FIGURES (Continued)

<b>Figure</b>	<b>Page</b>
3.7 Groups on silica surface following modification with 3-aminopropyltriethoxysilane.....	99
3.8 The pH influence on surface charge.....	102
3.9 Schematic diagram of a thermogravimetric system.....	103
3.10 Schematic diagram for grafting 3-aminopropyltriethoxysilane (-NH <sub>2</sub> ) and 3-mercaptopropyl trimethoxysilane (-SH) onto the surface of porous glass.....	105
3.11 Schematic for surface modification.....	106
3.12 N <sub>2</sub> adsorption isotherm plots of obtained porous glass and modified porous glass.....	112
3.13 Pore size distribution of (a) PG (b) PGNH <sub>2</sub> and (c) PGSH by N <sub>2</sub> adsorption from isotherm data.....	113
3.14 FTIR spectra of original and modified porous glass.....	115
3.15 Thermogravimetric analyses of original and modified porous glass.....	117
3.16 Point of zero charge of original and modified porous glass.....	118
3.17 Effect of solution pH on Cu <sup>2+</sup> and Ag <sup>+</sup> adsorption of PGNH <sub>2</sub> and PGSH	125
3.18 Schematic of surface conversion from thiol group to sulfonic group on porous glass when pH solution is below 2.....	126
3.19 Adsorption kinetics of Cu <sup>2+</sup> onto PGNH <sub>2</sub> and Ag <sup>+</sup> by the original porous glass and modified porous glass.....	129

## LIST OF FIGURES (Continued)

<b>Figure</b>	<b>Page</b>
3.20 Comparison of experimental and model predicted adsorption kinetic data of $\text{Cu}^{2+}$ and $\text{Ag}^+$ .....	131
3.21 Adsorption isotherms of $\text{Cu}^{2+}$ and $\text{Ag}^+$ onto $\text{PGNH}_2$ and $\text{PGSH}$ .....	134
3.22 Effect of solution pH on the adsorption of $\text{Au}^{3+}$ onto $\text{PG-NH}_2$ and $\text{PG-SH}$ .....	144
3.23 Adsorption kinetics of gold by $\text{PGSH}$ , $\text{PGNH}_2$ and $\text{PG}$ .....	145
3.24 Comparison of experimental and model predicted adsorption kinetic for gold adsorption by $\text{PGNH}_2$ and $\text{PGSH}$ at $25^\circ\text{C}$ .....	147
3.25 Adsorption isotherms of gold by $\text{PGNH}_2$ and $\text{PGSH}$ at $25^\circ\text{C}$ .....	148
3.26 Proposed mechanism scheme for gold adsorption onto aminopropyls and thiopropyls grafted porous glass.....	151
3.27 Comparison of single component adsorption and binary component adsorption of $\text{Ag}^+$ and $\text{Cu}^{2+}$ onto $\text{PG-NH}_2$ and $\text{PG-SH}$ .....	153
3.28 Predicted and experimental isotherm data for adsorption of $\text{Ag}^+$ - $\text{Cu}^{2+}$ mixture by $\text{PG-NH}_2$ porous glass.....	159
3.29 Predicted and experimental isotherm data for adsorption of $\text{Ag}^+$ - $\text{Cu}^{2+}$ mixture by $\text{PG-SH}$ porous glass.....	160
3.30 Predicted and experimental isotherm data for adsorption of $\text{Ag}^+$ - $\text{Cu}^{2+}$ mixture by $\text{PG-NH}_2$ porous glass.....	165

## LIST OF FIGURES (Continued)

Figure	Page
3.31 Predicted and experimental isotherm data for adsorption of $\text{Ag}^+$ - $\text{Cu}^{2+}$ mixture by PG-SH porous glass.....	168
3.32 Prediction of equilibrium isotherms of $\text{Cu}^{2+}$ - $\text{Ag}^+$ mixture by IAST based on Langmuir equation for pure component adsorption (adsorbent used $\text{PGNH}_2$ ).....	177
3.33 Prediction of equilibrium isotherms of $\text{Cu}^{2+}$ - $\text{Ag}^+$ mixture by IAST based on Langmuir equation for pure component adsorption (adsorbent used PGSH).....	177
3.34 Prediction of equilibrium isotherms of $\text{Cu}^{2+}$ - $\text{Ag}^+$ mixture by IAST based on Freundlich equation for pure component adsorption (adsorbent used $\text{PGNH}_2$ ).....	180
3.35 Prediction of equilibrium isotherms of $\text{Cu}^{2+}$ - $\text{Ag}^+$ mixture by IAST based on Freundlich equation for pure component adsorption (adsorbent used PGSH) .....	180
3.36 Adsorption isotherms of carbon dioxide on porous glass from coal fly ash at various temperatures.....	184
3.37 Isosteric heat of carbon dioxide adsorption onto porous glass.....	188
3.38 Ethanol adsorption/desorption isotherms on porous glass at 20 °C.....	190
3.39 Adsorption isotherms of ethanol on porous glass at various temperatures	193
3.40 Model of ethanol adsorption on silica surface with the presence of silanol group (-OH). .....	193

## LIST OF FIGURES (Continued)

<b>Figure</b>	<b>Page</b>
3.41 Testing BET equation against isotherms of ethanol adsorption on porous glass.....	194
3.42 Testing n-layer BET equation against isotherms of ethanol adsorption on porous glass.....	195
3.43 Isosteric heat of ethanol adsorption onto porous glass.....	197
3.44 Schematic of water adsorption on silica surface.....	199
3.45 Typical isotherm curves for water vapor adsorption on porous glass at 25 °C.....	200
3.46 Effect of temperature on water isotherms using porous glass as Adsorbent.....	201
3.47 Water isotherms of original and nitric oxidized activated carbon from eucalyptus wood .....	202
3.48 Fitting of water isotherms with conventional BET equation.....	203
3.49 Fitting of water isotherms with n-layer BET equation.....	204
3.50 Effect of water loading on isosteric heat of adsorption using porous glass adsorbent.....	206
3.51 Adsorption kinetic data of water vapor by porous glass at 20 °C and various increasing pressures.....	207
3.52 Comparison of adsorption kinetics of water by porous glass from experiments and model prediction (P = 4 mbar and T = 20 °C).....	208

## LIST OF FIGURES (Continued)

Figure	Page
3.53 Effect of water loading and temperature on adsorption with model parameters ( $k_1$ , $k_2$ and $D_e$ ) .....	215
3.54 Schematic of adsorbate diffusion in adsorbent pores.....	216
3.55 Effects of temperature and adsorption loading on surface diffusivity ( $D_s$ ) for water adsorption onto porous glass.....	220
3.56 Linear plots of $\ln D_s$ versus $1/T$ for determining the pre-exponential factor ( $D_{s\infty}$ ) and activation energy for surface diffusion.....	220
4.1 Formation and progression of mass transfer zone (MTZ) within a fixed bed of adsorbent until the breakthrough is reached at the bed exit.....	231
4.2 Breakthrough characteristics of a fixed-bed activated carbon adsorber ...	233
4.3 Nitrogen adsorption isotherms of porous glass samples at 77K.....	244
4.4 Equilibrium isotherms of methylene blue adsorption by different types of porous glass at 30°C ; (a) PG1, (b) PG2, (c) PG3, and (d) PG4.....	246
4.5 Typical breakthrough curve showing the estimation of breakthrough parameters.....	250
4.6 Effects of process variables on the breakthrough curves of methylene blue adsorption by porous glass PG1 at 30°C: (a) bed height, (b) feed concentration, (c) feed flow rate, (d) pore size, and (e) particle size .....	251
4.7 Testing of fitting schemes (Scheme I) of breakthrough models: (a) Klinkenberg model, (b) Bohart and Adams model, and (c) Thomas model.....	260

## LIST OF FIGURES (Continued)

<b>Figure</b>	<b>Page</b>
4.8 Model prediction of breakthrough curve by Scheme II for methylene blue adsorption by porous glass PG1 at 30°C: Effects of (a) bed height, (b) feed concentration, and (c) feed flow rate .....	261
4.9 Sensitivity of parameters of Thomas model for breakthrough prediction of methylene blue adsorption by porous glass PG1 at 30°C.....	263





# CHAPTER I

## INTRODUCTION

### 1.1 Background and significance of the study

In Thailand, the amounts of fly ash generated from coal-fired power plants have been increasing every year due to the consequent increase in the electricity demand of the country. It is estimated that approximately 13 Mt of fly ash is produced annually from which around 2 Mt is used directly in the cement industry (Electricity Generating Authority of Thailand, 2010). The rest is disposed through land fill which creates both environmental and ecological problems. The other possible utilizations of coal fly ash are to use it as a raw material for brick and tile fabrication (C. Ferreira et al., 2003), as filler in plastic and paint (S.M. Kutuarni and Kishore, 2002), in wastewater treatment (J.R. Kastner, K.C. DAs and N.D. Melear, 2002) and as a starting material for glass-ceramic production (E. Waraporn, 2005).

In recent years, many researches and investigations have been directed towards the utilization of fly ash as a raw material for adsorbent preparation, for example, zeolite adsorbents (X. Querol et al. ,2002). Another potential adsorbent that can be produced from coal fly ash is silica-based porous glass, because fly ash contains a major portion of  $\text{SiO}_2$  and  $\text{Al}_2\text{O}_3$ . The porous glass possesses a number of advantageous properties including, thermal stability, high mechanical strength, resistance to bacteria and virus, chemical stability, narrow pore size distribution and excellent shaping ability. With these favorable characteristics, porous glass has also

been employed in many other applications such as in the area of biotechnology (M. Hermann and U. Gottschalk, 2003), membrane technology (K. Kuraoka et al., 2001), dental industry (D. Heindl, 1999), heterogeneous catalyst and its supports (T. Takahashi et al., 1996), as starting materials for the preparation of new inorganic/inorganic composites (zeolite/PG) (W. Schwieger, 2000), and as components for optical chemosensors (M.P. Xavier, 2000), etc.

Porous glass can be conventionally formed by two different methods, namely the thermal phase separation and the sol-gel method. For the phase separation method, two different interconnected phase of borate and silicate glass are first formed by the high-temperature melting of a proper composition of raw mix. By further heat treating the glass product over the temperature range from 180 to 700 °C, the separation of these two glassy phases will occur. By leaching out the alkali-rich borate phase with a hot mineral acid, for example, nitric acid solution, the skeleton of almost pure porous silica can be obtained (D. enke, F. Janowski and W.Schwiger, 2003). It is further noted that due to the very low solubility of silica in the acid solution, silica-gel still remains in the structure cavities. Thus, the remaining colloidal silica is further removed by treatment with dilute basic solution (e.g. sodium hydroxide solution). Preparation of porous glass by the sol-gel process can be achieved by the hydrolysis of tetraethyl orthosilicate, TEOS,  $\text{Si}(\text{OC}_2\text{H}_5)_4$ , under acidic conditions to yield  $\text{SiO}_2$  in the form of a “glass material” (L. L Hench and J. K. West, 1990). However, the quality and shaping ability of porous glass obtained by the sol-gel process is not as good as by the phase separation, because the difficulty in controlling the required pore size and operating conditions. In this work, porous glass will be prepared by the thermal phase-separation of alkali borosilicate glasses. The

structural and textural properties of porous glasses are to be controlled by varying the conditions of heat treatment (temperature and time) which is the key factor in controlling the pore size distribution of porous glass.

To illustrate the potential use of porous glass in the area of adsorption, it was decided to apply the prepared porous glass from coal fly ash for wastewater treatment, that is, for the removal of heavy metal ions and dyes molecules from aqueous solutions. The existence of polar silanol group (Si-OH) on the porous glass surface makes it ideal for the capture of metal ions by ion-exchange process. The mesoporous nature of porous glass is also advantageous for effective adsorption of large dye molecules.

For heavy metal adsorption, the purpose is either to remove the unwanted pollutant species or to recover the precious metal species from the solution. Presently, the recovery of precious material is more interesting and challenging, examples are silver and gold. In this work, the prepared porous glass was utilized as an effective adsorbent to remove and recover a number of precious metal ions from aqueous solutions. In addition, the adsorption of single component in gas phase, including carbon dioxide, ethanol and water which possess different polarity, was also studied with the porous glass adsorbent.

As to the adsorption of dye molecules, the prepared porous glass was employed for the adsorption of methylene blue as a model commercial dye in a fixed-bed adsorption system. The fixed-bed column is able to treat wastewater with large quantity and low operating cost.

This research is divided into 5 chapters. Chapter I is introduction part; it describes the motivation, objectives of this research, scope and limitation of the

research work. Chapter II reports an investigation on the preparation and characterization of porous glass from coal fly ash. For this part, porous glass was prepared from coal fly ash by thermal phase-separation of alkali borosilicate glasses and the effects of temperature and time of heat treatment conditions were investigated. In Chapter III, the application of porous glass in adsorption field was focused on metal ions adsorption onto porous glass adsorbents. The single component adsorption ( $\text{Cu}^{2+}$ ,  $\text{Ag}^+$  and  $\text{Au}^{3+}$ ) and binary adsorption ( $\text{Cu}^{2+}/\text{Ag}^+$ ) were studied. The comparison of adsorption by the original porous glass and surface modified porous glass were made. Various adsorption models were also tested against the experimental isotherm data. Furthermore, gas adsorption studies of  $\text{CO}_2$ , water vapor and ethanol vapor were also investigated and compared with experimental isotherm data as well as the testing of various well known adsorption models. Chapter IV is concentrated on studying the adsorption of methylene blue in a fixed-bed adsorber. Column breakthrough curves were determined as a function of process variables such as feed flow rate, static bed height and particle size and pore size of porous glass. Breakthrough curve models were tested by validating with the experimental results. Finally, Chapter V is the conclusion of the research work from this dissertation and some recommendations for future study are suggested.

## **1.2 Research objectives**

The followings are the specific objectives of this thesis:

1.2.1 To prepare porous glass from non-porous fly ash derived from a coal-fired power plant by the phase-separation technique.

1.2.2 To characterize for the physical, chemical and porous properties of the prepared porous glass.

1.2.3 To study the influence of preparation conditions on the properties of porous glass.

1.2.4 To study the modification of surface groups on the surface of porous glass by chemical treatment.

1.2.5 To study adsorption equilibrium and kinetics of metal ions and gas adsorbates by porous glass adsorbent.

1.2.6 To study fixed bed adsorption of methylene blue from aqueous solution by porous glass adsorbent.

## **1.3 Scope and limitation of the research**

1.3.1 The fly ash as was used as a raw material and was obtained from Rayong coal burning thermal power plant in Rayong, Thailand

1.3.2 For the preparation step of porous glass, the heat treatment conditions (temperature and time) are varied.

1.3.3 Characterization of prepared porous glass is performed by various techniques including:

1.3.3.1 The mean pore diameter by Mercury Intrusion Porosimetry (Auto Pore III, Micromeritics) and true density by a helium pycnometer.

1.3.3.2 The pore volume and surface area by employing N<sub>2</sub> adsorption isotherm data.

1.3.3.3 The chemical compositions of fly ash and prepared porous glass by X-Ray Fluorescence Spectrometry (XRF).

1.3.3.4 The images of surface structure of porous glass by scanning electron microscope (SEM).

1.3.3.5 The identification of functional group on porous glass surface by Fourier Transform Infrared Spectroscopy (FTIR).

1.3.3.6. The surface charge by determining the point of zero charge (p.z.c.).

1.3.4 Study the surface modification by converting the silanol group on the surface of porous glass to amino group by reacting the porous glass with 3-aminopropyltriethoxysilane and 3-mercaptopropyltrimethoxysilane.

1.3.5 Study the adsorption equilibria of heavy metal ions both as single and binary components from aqueous solution onto the modified and unmodified porous glass.

1.3.6 Study the equilibria and kinetics of gas adsorption of CO<sub>2</sub>, C<sub>2</sub>H<sub>5</sub>OH and H<sub>2</sub>O onto the porous glass from coal fly ash.

1.3.7 Study the fixed-bed adsorption of methylene blue from solution in a fixed-bed of porous glass. Prediction of breakthrough curves by various breakthrough models is also attempted.

## 1.4 References

- D. Enke, F. Janowski and W.Schwiger. (2003). Porous glass in the 21<sup>st</sup> century a short review.**Micropore and Mesopore Materials**. 60:19-30.
- J. Nawrocki. (1991). Silica Surface Controversies, Strong Adsorption Sites, their Blockage and Removal.Part I.**Chromatographia**. 31.
- K. Kuraoka, Y. Chujo and T. Yazawa.(2001). Hydrocarbon separation via porous glass membranes surface-modified using organosilane compounds.**Journal of Membrane Science**. 182:139-149.
- M. Hermann and U. Gottschalk. (2000).**Bioforum** 3:172.
- MahittiP.andFuangfa U. (2006). Chemically modified MCM-41 and silica gel as adsorbents for Hg (II) ions.**Science and Technology of Thailand**. pp. 1–4.
- RungrojChanajaree. (2006).**Computational Chemistry Unit Cell:Zeolites**.
- S. Iwaishi, Y. Yanagimoto and T. Kai. (1996). Hydrogenation activity of benzenes on nickel catalysts supported on porous glass prepared from borosilicate glass with small amounts of metal oxides.**Microporous Materials**. 6:189-194.
- S. Morimoto.(1996).Porous glass: preparation and properties.**Key Engineering Materials**.115:147-158.
- Shaobin W., Mehdi S., Li L. and Z.H. Zhu. (2006). Coal ash conversion into effective adsorbents for removal of heavy metal and dyes from wastewater.**Journal of Hazardous Materials**. B133:243-251.
- Thomas H. E. (1992), Porous and Reconstructed Glasses, **Engineered Materials Handbook volume 4: Ceramic and glasses, United States of America**.
- T. Takahashi, Ruthven D. M. (1997), **Encyclopedia of Separation Technology**. 95, New York: John Wiley.

T. Yazawa. (1996). Present status and future potential of preparation of porous glass and its application. **Key Engineering Materials**. 115:123-146.

Waraporn E. (2005). Effective utilization of coal fly ash for high thermal shock resistance glass-ceramic ware. **Master Thesis**. Suranaree university of technology.

W. Schwieger, M. Rauscher, R. Monnig, F. Scheffler, D. Freude. (2000). in: A. Sayari, M. Jaroniec, T.J. Pinnavaia (Eds.). Nanoporous Materials II, Studies in Surface Science and Catalysis. **Elsevier**. Amsterdam.129:121.





## **CHAPTER II**

# **PREPARATION AND CHARACTERIZATION OF POROUS GLASS FROM COAL FLY**

### **2.1 Abstract**

Porous glasses were prepared by a conventional phase separation method using coal fly ash as a raw material, and the properties of these porous glasses were determined. The composition of coal fly ash, consisting basically of  $\text{SiO}_2$ ,  $\text{Al}_2\text{O}_3$ ,  $\text{Fe}_2\text{O}_3$  and  $\text{CaO}$ , was adjusted by oxide addition to meet the target base glass system of  $\text{SiO}_2$ - $\text{B}_2\text{O}_3$ - $\text{Al}_2\text{O}_3$ - $\text{CaO}$ - $\text{Na}_2\text{O}$  for porous glass preparation. It was found that the mean pore diameter of the prepared porous glass increased proportionally to the cube root of heat treatment time ( $t^{1/3}$ ), although this correlation was not observed at the early stage of the phase separation. With this finding, it was hypothesized that the rate determining step of the phase separation process may be the diffusion process of structural units involving oxygen ions and the phase separation takes place by the nucleation and growth mechanism. The relatively large pores of greater than  $1 \mu\text{m}$  can be obtained easily, giving the glass to have similar chemical composition to the commercial Shirasu porous glass which also contains  $\text{Al}_2\text{O}_3$  and  $\text{B}_2\text{O}_3$ . From the obtained results, it can be concluded that the synthesis of porous glass from coal fly ash by the phase-separation technique, consisting of three consecutive steps of glass forming by melting, binary glassy phase separation by heat treating and acid leaching

to remove the borate rich phase, can yield an excellent porous silica adsorbent with well controlled pore size distribution.

## 2.2 Introduction

The generation of fly ash in large quantities from coal-fired power plants has created a serious disposal problem. Most of fly ash is traditionally disposed of through land filling (Cheerarot and Jaturapitakkul, 2004), which requires relatively large land area and without proper handling this could create both ecological and environmental problems. Until recently, steadily increasing portion of fly ash has been directly utilized in cement industry to augment the pozzolanic action of the cement (Hurley and Pritchard, 2005). In addition, fly ash also finds applications in construction-related industries, including the manufacture of insulation bricks and light aggregates, glass ceramics in floor tile and side-wall production industries, etc. However, there are still some inherent problems associated with the use of coal fly ash. That is, ash properties are highly heterogeneous as affected by such factors as coal compositions, types of furnaces and firing conditions, and this may be the main reason that still prevents the wider application and effective utilization of coal fly ash.

Porous glass is one of inorganic porous materials that can be produced from coal fly ash. The important features of this material are as follows: high thermal and chemical stability, high mechanical strength, resistance for bacteria, very narrow pore size distribution, excellent shaping ability, well controlled pore size range and transparency (Shelby, 1997). Porous glass is manufactured mainly by three processes, namely thermal-phase separation, sol-gel and crystallized process. The thermal-phase separation method is most widely used due to its ease of operation and

the flexibility in controlling the pore size of porous glass. Applications of porous glasses are of very wide range. It is used, for example, as a separation membrane, catalyst and its support, enzyme support, packing material for chromatography, support for DNA synthesis and a chemical durable resistor(Enke et al., 2003a). However, the many potential applications of porous glass have not yet been fully utilized and this should open up further research challenges for product development from porous glass.

In this work, porous glasses were prepared using fly ash as a raw material by a conventional phase-separation method and the effect of heat treatment conditions on the properties of porous glasses as well as product characterization were investigated.

## **2.3 Theory and general background of porous glass**

### **2.3.1 Fly ash**

Fly ash is the finely divided mineral residue resulting from the combustion of coal in electricity generating plants. Fly ash consists of inorganic, incombustible matter presenting in the coal that has been fused during combustion into a glassy, amorphous structure. It consists mostly of silica ( $\text{SiO}_2$ ), alumina ( $\text{Al}_2\text{O}_3$ ), iron oxides ( $\text{FeO}+\text{Fe}_2\text{O}_3$ ), alkali and alkaline earth oxides with a small amount of various heavy metals and transition metal oxides (Barbieri et al., 2000). Coal burning generates heat and residue that contains 80 per cent fly ash and 20 percent bottom ash which can be classified by the location and methods of recovery. Fly ash particles are generally spherical in shape and range in size from 0.5  $\mu\text{m}$  to 100  $\mu\text{m}$ . They are also pozzolanic in nature and can react with calcium hydroxide and alkali to form calcium silicate hydrates (cementitious compounds).

### 3.2.2.1 Classification of fly ash

Fly ash can be classified into two types that depend on the chemical compositions and source of fly ash. The two classes of fly ash are defined according to ASTM C618 (ISG resources, Headwater Company): Class F fly ash and Class C fly ash. The main difference between these classes is the differing amount of calcium, silica, alumina, and iron content in the ash. The chemical properties of fly ash are largely determined by the chemical content of the coal burned. **Table 2.1** shows typical examples of ash compositions resulting from the burning of various types of coals. (Zimmer F., 1970)

**Table 2.1** Typical chemical compositions of ashes produced from burning coals of different ranks. (Zimmer, 1970)

Components	Anthracite	Bituminous	Subbituminous	Lignite
SiO <sub>2</sub> (%)	80-90	20-60	40-60	15-45
Al <sub>2</sub> O <sub>3</sub> (%)	0-5	5-35	20-30	20-25
Fe <sub>2</sub> O <sub>3</sub> (%)	0-3	10-40	4-10	4-15
CaO (%)	0-1	1-10	5-30	15-40
SO <sub>3</sub> (%)	0-1	0-5	2-7	5-10
LOI* (%)	0-2	0-15	0-3	0-5

\*LOI = Loss of ignition

- **Class F fly ash**

The burning of harder, older anthracite and bituminous coal typically produces Class F fly ash. This fly ash is pozzolanic in nature, and contains less than 10% lime (CaO). This is aluminosilicate material which has pozzolanic properties: a material such as certain fly ash and blast furnace slag which is finely divided will exhibit certain cementitious properties. (Loran, 1994)

- **Class C fly ash**

This is the fly ash produced from the burning of lignite or subbituminous coal. It is calcium sulphate ash which also has pozzolanic and some cementitious properties.

#### **2.2.2.2 Disposal and the reuse of fly ash**

The generation of electricity and process heat from coal combustion without proper and efficient handling of emitted ash particles will cause severe impact to the environment. In the past, fly ash was generally released into the atmosphere, but pollution control equipment mandated in recent decades now requires that it be captured prior to release. Electrostatic precipitators are typically used to control the entrained particulates while the reduction of SO<sub>2</sub> emission is achieved with flue gas desulfurization equipment (scrubbers). Worldwide, more than 65% of the captured fly ash from coal fired power stations is disposed of in landfill and ash ponds. In Thailand, almost all power plants are a thermal power plant that burns lignite coal to produce electrical energy. During the early of 1970–2000,

approximately 50 million tons of fly ash and bottom ash were disposed by the open landfill method (Cheerarat and Jaturapitakkul, 2004).

However, in recent years many researches and investigations have been directed towards the exploitation of collected fly ash from landfills (Cheerarat, R. and C. Jaturapitakkul 2004) by using it as a raw material for the cement industry (M. Erol et al., 2003), brick and tile fabrication (C. Ferreira et al., 2003), filler in plastic (S.M. Kutuarni and Kishore, 2002), as a starting material for glass-ceramic production (E. Waraporn, 2005) and in waste treatment processes (J.R. Kastner, K.C. DAs and N.D. Melear, 2002).

Moreover, special effort has been made on utilizing fly ash in the area of adsorption. It is well known that fly ash contains a large amount of  $\text{SiO}_2$  and  $\text{Al}_2\text{O}_3$ . Therefore, fly ash can be used as a raw material for adsorbent synthesis such as porous glass, zeolite, silica-gel, etc. (Chaturaporn Nimjaroen, Shigeki Morimoto and Chaiyot Tangsathitkulchai, 2009; Querol and Moreno, 2002). Particularly, porous glass from fly ash is an attractive adsorbent with its many superior properties and its containing silanol group (Si-OH) that can be chemically modified to increase the selectivity for a particular adsorbate species.

### 2.3.2 Porous glass

Porous glass is one of inorganic porous materials that has been recognized for nearly 80 years. **Table 2.2** outlines its brief historical development. Porous glass is mostly produced by phase separation couple with acidic extraction or a combined acidic and alkaline extraction of alkali borosilicate glasses. Porous glass is a porous material containing approximately 96% silica, a specific surface area

varying from 10 to 300 m<sup>2</sup>/g and an average pore size in the range from 0.4 and 1000 nm with a very narrow pore size distribution. For commercial porous glasses, Porous VYCOR-Glass (PVG) and Controlled Pore Glass (CPG) have been manufactured by Corning Glass Works (Corning Glass Work company, 2000); they are manufactured by acid leaching of phase-separated Na<sub>2</sub>O-B<sub>2</sub>O<sub>3</sub>-SiO<sub>2</sub> glasses.

**Table 2.2** Brief historical development of porous glass manufacturing. (T. Yazawa, 1996)

<b>Porous glass</b>	<b>Year of production</b>	<b>Research group</b>
SiO <sub>2</sub>	1934	Corning (Nordberg and Hood, 1944)
Developing SiO <sub>2</sub>	1974	Pittsburgh Plate Glass, PPG(J.J. Hammel and T.Allersma, 1974)
Shirasu system	1981	Industrial Research Institute of Miyazaki Prefecture (T. Nakashima and Y. Kuroki, 1981)
TiO <sub>2</sub> system	1985	Miakonojo College (T. Kokubu and M.Yamane, 1985)
ZrO <sub>2</sub> system	1986	Nanotechnology Research Institute , Osaka (Y. Mori and K. Eguchi, 1986)
PO <sub>4</sub> system	1990	Nagoya Institute of Technology (H. Hosono et al., 1993)

The advantages and characteristic features of these porous glasses are:

1. Thermal stability
2. High mechanical strength
3. High resistance for bacteria and viruses
4. Chemical stability
5. Very narrow pore size distribution
6. Excellent shaping ability into various forms: irregular particles (powder, granulate), spheres, plates, sticks, fibers, ultra-thin membranes, tubes and rings.
7. Easy control of pore size by heat treating

In the 19th century, Nordberg and Hood (Nordberg and Hood, 1940) at Corning group discovered that alkali borosilicate glasses can be separated into soluble (sodium borate rich) and insoluble (silica rich) phases if the glass is thermally treated. By leaching with mineral acids, the soluble phase can be removed and a porous silica network remains. During a sintering process after acid leaching extraction, a silica glass is generated, which has properties approaching those of quartz glass. The manufacturing of such high-silica glasses has been referred to as the VYCOR-process. There are also many other new types of porous glass that possess a special property of chemical durability. They are

- **SiO<sub>2</sub>-AlPO<sub>4</sub> porous glass** (S. Morimoto, 1990)

The base glass is SiO<sub>2</sub>(AlPO<sub>4</sub>)-B<sub>2</sub>O<sub>3</sub>-Na<sub>2</sub>O system. The phase separated glasses is leached out by hot water or dilute organic acids, following the heat treatment process.

- **SiO<sub>2</sub> – Al<sub>2</sub>O<sub>3</sub> porous glass, Shirasu porous glass** (T. Nakashima and Y. Kuroki, 1981)



This porous glass was developed by IRI Miyaki (Industrial Research Institute of Miyaki, Japan) and the name of this glass is Shirasuporous glass. The base glass is  $\text{SiO}_2\text{-Al}_2\text{O}_3\text{-B}_2\text{O}_3\text{-RO-R}_2\text{O}_3$  system. Shirasu porous glass contains about 10% of  $\text{Al}_2\text{O}_3$  and 15% of  $\text{B}_2\text{O}_3$ . Pore diameter is usually large pore size of silica glass, ranging from nanometer to micrometer level. The alkaline resisting durability is also greater than other porous silica glasses. The Shirasu porous glass is usually applied in the area of liquid phase separation.

-  **$\text{SiO}_2\text{-P}_2\text{O}_5$  porous glass** (E.M.Rabinobitch, 1980)

The base glass is  $\text{SiO}_2\text{-P}_2\text{O}_5\text{-RO-R}_2\text{O}$  system. This porous glass contains a few percent of  $\text{P}_2\text{O}_5$  and is obtained by phase separation followed by acid leaching.

-  **$\text{SiO}_2\text{-TiO}_2$  porous glass** (T. Kokubu and M. Yamane, 1985)

This glass contains about 50% of  $\text{TiO}_2$  and is obtained from  $\text{SiO}_2\text{-B}_2\text{O}_3\text{-RO-Al}_2\text{O}_3\text{-TiO}_2$  base glass system. This material has high thermal resistance and chemical durability.

-  **$\text{SiO}_2\text{-ZrO}_2$  porous glass** (S.Morimoto, 1990)

This porous glass contains about 10% of  $\text{ZrO}_2$  and it is obtained by using the base glass of  $\text{SiO}_2\text{-ZrO}_2\text{-Al}_2\text{O}_3\text{-B}_2\text{O}_3\text{-RO-R}_2\text{O}$  system. This material has higher chemical durability.  $\text{SnO}_2$  can be used instead of  $\text{ZrO}_2$

### 3.2.2.1 Properties of porous glass

Porous glass is a predominantly amorphous solid with high thermal stability and chemical resistance. **Table 2.3** shows some properties of commercially available porous glass (Thomas H. E., 1992) which is an intermediate glass prepared by heat treating and leaching a special alkali-borosilicate glass. It has a surface area of

150 to 200 m<sup>2</sup> /g as determined by the Brunauer-Emmett-Teller (BET) method (Duong D.Do, 1998) using nitrogen as the adsorbate gas, and an internal porosity of 28%. Its pore size distribution is generally very narrow (**Figure 2.1**), with the average median pore radius of about 2.1 nm (21°A).

**Table 2.3** Typical compositions and properties of commercially available porous glass (Thomas H. E., 1992)

Properties	Value
Composition on basis weight (%)	
SiO <sub>2</sub>	96.3
B <sub>2</sub> O <sub>3</sub>	2.95
Na <sub>2</sub> O	0.04
Al <sub>2</sub> O <sub>3</sub> +ZrO <sub>2</sub>	0.72
Appearance	Opal color
Refractive index	1.33
Apparent density (g/cm <sup>3</sup> )	1.5
Porosity, (%)	28
Average pore radius, nm	2.1

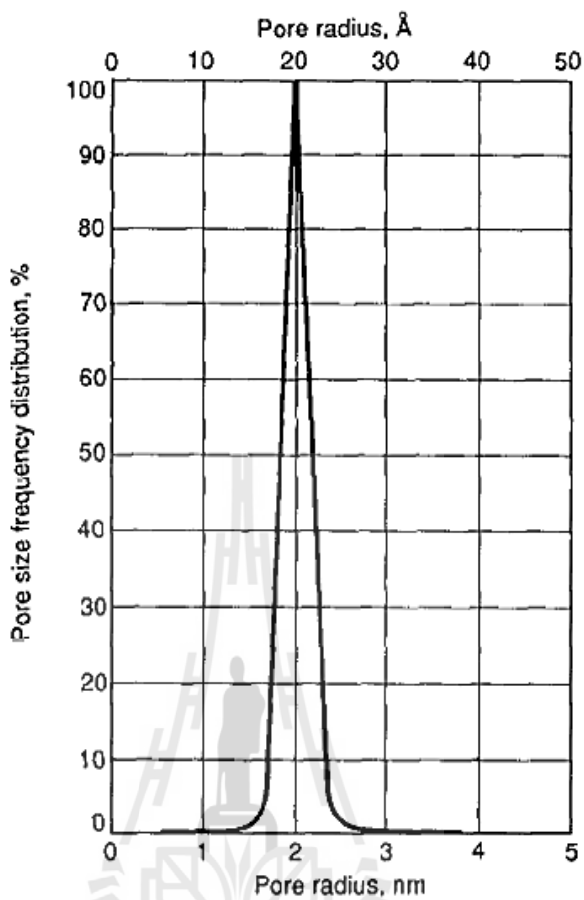


**Figure 2.1** Pore size distribution of a porous glass having an average median pore diameter of 2.1 nm (21 °A) (Thomas H. E., 1992).

### 2.3.2.2 Preparation of porous glass.

The preparation of porous glass can be commonly obtained by three different techniques: phase separation by thermal treatment, sol-gel process and crystallized glass process(Enke et al., 2003b). The technique that is widely used and easy to prepare is the phase separation by thermal treatmentprocess. It is easy to operate and well controlled pore size of porous glass can be achieved byphase separation of the molten base glass followed by leaching with acid and alkaline solution. When atypical phase separated compositions of borosilicate glass (e.g. 69

$\text{SiO}_2$  - 1  $\text{Al}_2\text{O}_3$  - 21.8  $\text{B}_2\text{O}_3$  - 8.2  $\text{Na}_2\text{O}$  mol%) is immersed in acid solution, one of the separated rich phase ( $\text{B}_2\text{O}_3$  -  $\text{Na}_2\text{O}$ ) is then leached out into the hot acid solution, giving the framework of silica rich phase. Finally, porous silica glass having interconnected pores of small diameter and large pore volume is obtained. **Figure 2.2** shows the schematic of the preparation method.

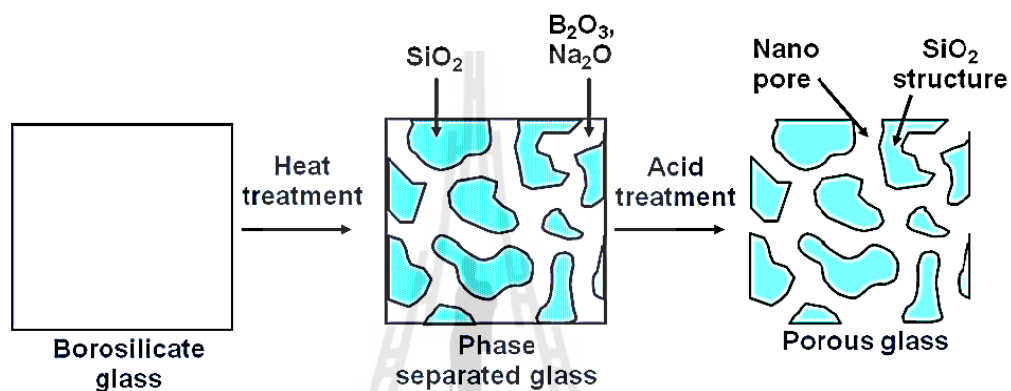


**Figure 2.2** Preparation method of porous glass.

During the acid leaching process,  $\text{SiO}_2$  in  $\text{B}_2\text{O}_3$  -  $\text{Na}_2\text{O}$  phase is not entirely leached out but some still remain in the pores as silica colloids. Many methods have been tried to remove silica colloids from these pores and the method of immersion in dilute alkaline solution has been found to be most effective.

The raw materials used for the preparation of porous glass are extremely important, especially for the proper control of pore size distribution. The chemical components of the base glass can also affect the properties of the final porous glass product as outlined below.

- **Sand ( $\text{SiO}_2$ )**, high  $\text{SiO}_2$  content imparts high strength to glass product and high resistance to heat and chemicals, but it is difficult to process because of the higher melting temperature and high viscosity.

- **Soda ash ( $\text{Na}_2\text{CO}_3$ )**,  $\text{Na}_2\text{O}$  imparts low melting point characteristic to glass, more brittle mass and high resistance to chemicals.
- **Potassium oxide ( $\text{K}_2\text{O}$ )**, it helps to slow the crystallization and makes a good arrangement of crystals.
- **Calcium ( $\text{CaO}$ ), Magnesium oxide ( $\text{MgO}$ ), or Barium oxide ( $\text{BaO}$ )**, they could assist in glass forming by speeding up the cooling down period of molten glass as well as increasing its chemical resistance. The  $\text{CaO}$  and  $\text{MgO}$  also assist in the arrangement of crystals by decreasing temperature at a slower rate.
- **Aluminum oxide ( $\text{Al}_2\text{O}_3$ )**, the glasses with high  $\text{Al}_2\text{O}_3$  content has higher resistance to corrosion and chemicals.
- **Boron compounds**, borosilicate glass is highly resistant to acid and base and thermal resistance of glass due to the decrease in thermal expansion coefficient. These types of glasses are used for laboratory glassware and microwave ovens.
- **Lead oxide ( $\text{PbO}$ )**, the glass containing lead components (Lead glass) gives clear glass luster due to the high refractive index of the light.
- **Ferric oxide ( $\text{Fe}_2\text{O}_3$ )**,  $\text{Fe}_2\text{O}_3$  can reduce the melting point of glass. In addition, it makes the color of glass to change from clear to dark brown color.

The structural and textural properties of the porous glasses prepared by the phase separation are controlled by three factors: (i) the initial composition of base glass, (ii) the conditions of heat treatment and (iii) the leaching conditions (including acid and alkaline solution). The widely used means for controlling the pore size of

porous glass are the conditions of the heat treatment process and leaching condition. The cracking of porous glass during the acid leaching is sometime observed and is related to the stretching of glass in this process due to the generated stress between the leached and unleached layers. The development of stretching condition is caused by the leach out of  $B_2O_3$ - $Na_2O$  from  $SiO_2$  rich phase and also from the remaining  $SiO_2$  colloids in the pores. Although, the leaching method can be additionally applied for control of the pore size of porous glass but it is not practically stable because the remaining of alkaline phase can be easily dissolved into the acid solution while the silica phase can dissolve in alkali solution.

T. Yazawa (1996) studied the preparation of porous glass by thermal heat treatment with the purpose to investigate the effect of base glass composition on glass forming region. The initial heat-treatment temperature conditions studied was in the range of 730 – 760 °C. Normally, the pore size of porous glass is controlled by heat treatment conditions, especially P-Zn glass ( $SiO_2$ - $B_2O_3$ - $ZnO$ - $ZrO_2$  compositions as mother glass). However, the limit of the available median pore diameter of prepared porous glass covered the range of 4 – 150 nm of silica porous glass.

S. Morimoto (2001) studied the preparation and properties of porous glass by thermal phase separation and found that the pore structure was controlled by heating temperature and time; higher heat treatment temperature and longer time conditions gave porous glass with relatively larger pore diameter.

The initial raw mix composition for the production of porous glass has been developed by Corning Glass Works (1996) which is presented as chemical composition of the base glass on ternary phase diagram of  $Na_2O$ - $B_2O_3$ - $SiO_2$

glass system as shown in **Figure 2.3**. The corresponding formulating equation can be expressed as.

$$(\text{Na}_2\text{O}_3) = 9.5 - 0.1[\text{S}] - 0.17[\text{A}]^2$$

where  $[\text{S}] = (\text{SiO}_2) - 55$  in percentage of composition mass

$[\text{A}] = \text{Al}_2\text{O}_3$  in percentage of composition mass

$(\text{B}_2\text{O}_3) = \text{Balance up to } 100\%$ , by wt%

To achieve phase separation, the initial glass composition must lie in the miscibility gap of the ternary  $\text{Na}_2\text{O}-\text{B}_2\text{O}_3-\text{SiO}_2$  glass system, shown as Vycor glass and Pyrex glass area in **Figure 2.3**. As both phases (Vycor and Pyrex glass) have different resistances to water, mineral acids, and inorganic salt solutions, the sodium-rich borate phase in these mediums can be removed by hot acid solution. The structural and textural properties of porous glass are controlled by the initial base glass composition, conditions of heat treatment (temperature, time) and leaching conditions (type of acid and concentration).

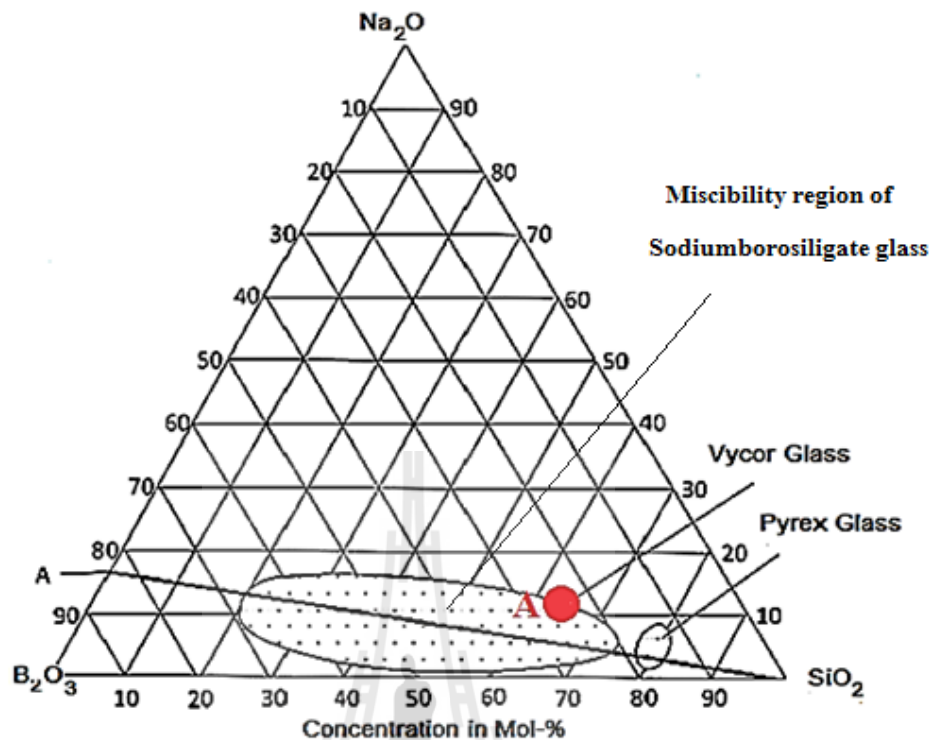


**Figure 2.3** Ternary Phase diagram for the sodium borosilicate system  
 ([http://commons.wikimedia.org/wiki/File:Phasendiagramm\\_natriumborosilikat.jpg](http://commons.wikimedia.org/wiki/File:Phasendiagramm_natriumborosilikat.jpg)).

Phase separation in the region of liquid-liquid immiscibility has an adverse effect on the physical properties of glass. Phase separation in glasses generally takes the form of two immiscible glass phases which differ in chemical composition, density, and surface tension. **Figure 2.4** shows three regions (I, II and III) of liquid-liquid immiscibility for the  $\text{SiO}_2 - \text{B}_2\text{O}_3 - \text{Na}_2\text{O}$  system. The upper critical temperature is at about  $760^\circ\text{C}$  and the lower one at about  $500^\circ\text{C}$ . The ranges of immiscibility in two commercially important systems of  $\text{Na}_2\text{O}-\text{B}_2\text{O}_3-\text{SiO}_2$  have been investigated. In these systems, it is shown that three region of immiscibility or



separated phase (I, II and III regions) can exist. Glasses of the Pyrex and the Vycor type occur in the different parts of immiscibility region II in this system, the Pyrex glasses exhibit phase separation in region I. Furthermore, colloidal silica is dissolving in the sodium-rich borate phase, when time and temperature of thermal treatment are increased. This process is called secondary decomposition. The solubility of colloidal silica in alkaline solutions is higher than that of the network silica, and thus can be removed by the alkaline after heat treatment.

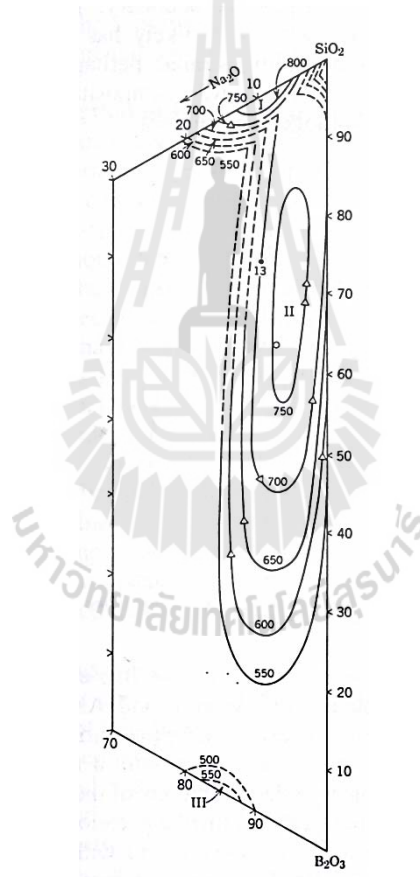


**Figure 2.4** Three regions of liquid-liquid immiscibility in the SiO<sub>2</sub> - B<sub>2</sub>O<sub>3</sub> - Na<sub>2</sub>O system (wt%). (W. Haller, D.H. Blakburn, F.E. Wastaff, and R.J. Charles, 1970).

### 2.3.3 Mechanisms of phase separation in porous glass

As already mentioned porous glasses can be prepared by an acid or combined acid/alkaline leaching treatment of the phase-separated alkali borosilicate glasses. The interconnected pore structure of prepared porous glass is almost a pure SiO<sub>2</sub> phase. Theoretically, there are two types of mechanism describing this phenomenon of phase separation in porous glass. One is nucleation and growth mechanism and the other is the spinodal decomposition.

#### 2.3.3.1. Nucleation and growth mechanism

Nucleation and growth closely resemble crystallization; the microstructure formed by this process has some similarities to that found in crystallizing samples. Growth occurs on individual, isolated nuclei, so that the region of phase is a liquid. The surface energy will be minimized for spheres, so the second phase will occur as isolated spheres of one equilibrium composition randomly dispersed through a matrix of the other equilibrium composition. The growth behavior will be such that the spheres will have composition of the phase with the lesser volume fraction, since nucleation occurs randomly. Local connectivity of spheres may exist when two neighboring spheres intersect, but the connectivity of the minor phase will generally be quite low. The structure and texture obtained from this mechanism is shown in **Figure 2.5 (a)**.

#### 2.3.3.2 Spinodal decomposition mechanism

The spinodal decomposition mechanism differs from the nucleation and growth mechanism in that there is no nucleation of the second-phase composition. Both phases will gradually and continually change in composition until they reach the composition of the equilibrium liquid. The second phase will be

regularly distributed in space and characterized by a regular size. The distance between centers of either phase is sometimes termed the wavelength of the microstructure. Finally, both phases will have high degree of connectivity so that continuous pathways through the material exist for each phase. Morphology of this type are said to be interconnected and the region beneath the spinodal boundary is sometimes referred to as the interconnected region. **Figure 2.5 (b)** shows the structure and texture of porous glass resulting from this mechanism.

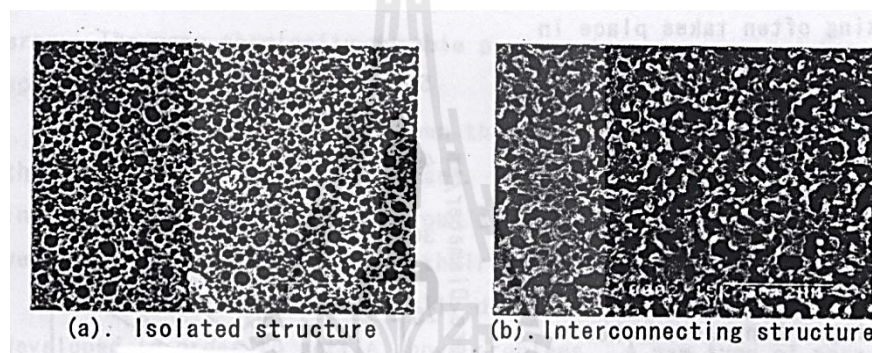


**Figure 2.5** Structure of porous glass (a) Isolated structure occurred by nucleation and growth mechanism (b) Interconnecting structure occurred by spinodal decomposition mechanism (S. Morimoto, 1996).

#### 2.3.4 Application of porous glass

Porous glasses have many advantageous features including their high mechanical strength, thermal and chemical stability, excellent shaping ability, a wide range of pore sizes with a narrow pore size distribution and capability of surface modifications. Also, Porous glass can be used in a variety of applications. It is used in the area of biotechnology (M. Hermann and U. Gottschalk, 2003), membrane technology (K. Kuraoka et al., 2001), dental industry (D. Heindl, 1999),

heterogeneous catalyst and its supports (T. Takahashi et al., 1996), as starting materials for the preparation of new inorganic/inorganic composites (zeolite/PG) (W. Schwieger, 2000), and as components for optical chemo sensors (M.P. Xavier, 2000).

Porous glasses are ideal for material separation because of the narrow pore size distribution. This is why they are used in gas chromatography, thin layer chromatography and affinity chromatography. Moreover, an adaptation of stationary phase for a separation problem is possible by a specific modification of the surface of the porous glass.

In biotechnology, porous glasses give benefits for the cleaning of DNA and the immobilization of enzymes or microorganisms. Porous glass can be used to remove virus and bacteria which can be easily eliminated by thermal cleaning.

In addition, porous glasses have been used for manufacturing implants, especially dental implants, for which porous glass powder is processed with plastics to form a composite. The particle size and pore size influence the elasticity of the composite so as to fit the optical and mechanical properties to surrounding tissue.

With the ability of porous glass to form platelets, membrane technology is another important area of application. Additionally, porous glasses are often appropriate to be employed as a carrier in catalysts. For example, the olefin – metathesis was realized on the system of metal – metal oxide/porous glass (Amir H. Hoveyda and Adil R. Zhugralin, 2007).

Porous glasses can be used as membrane reactors as well, again because of their high mechanical, thermal and chemical stability. Membrane reactors can improve conversion of limited balance reactions, when one reaction product is removed by a selective membrane.

## 2.3 Experimental

### 3.3.1. Preparation and characterization of coal fly ash

The coal fly ash used in this study was supplied by “BLCP Coal Power Plant Thailand” in Rayong province, Thailand. The as-received fly ash appeared to be dark grey in color. Since fly ash sometimes contains a small amount of organic materials or reducing materials which can attack a Pt/Rh alloy crucible used during the glass melting quite severely, it was thus first calcined at 900°C for 10 h in an electric furnace in air to remove those reducing materials. The calcined ash sample was then cooled to room temperature and stored in a desiccator. The Scanning Electron Microscope (SEM) photo of fly ash particles is given in **Figure 2.6**, showing that fly ash is spherical in shape and non-porous in nature.

The chemical composition of fly ash was analyzed by XRF (X-ray fluorescence) method and the results are shown in **Table 2.4**. It is clear that this fly ash is basically composed of  $\text{SiO}_2$ – $\text{Al}_2\text{O}_3$ – $\text{CaO}$  system with relatively large contents of  $\text{Fe}_2\text{O}_3$  and  $\text{SO}_3$ . Based on XRD (X-ray diffraction) analysis, this fly ash consists mainly of glassy phase (~75 %) with crystalline phases (~25 %) of  $\alpha$ -quartz, anorthite ( $\text{CaAl}_2\text{Si}_2\text{O}_8$ ) and gehlenite ( $\text{Ca}_2\text{Al}_2\text{SiO}_7$ ) (Waraporn, 2005). The particle size distribution was determined by a laser diffraction particle size analyzer (Mastersizer Malvern, United Kingdom), and is displayed in **Figure 2.7**. The

average particle size was  $46.11\mu\text{m}$  with a small amount of fine powder (smaller than  $1\mu\text{m}$ ).

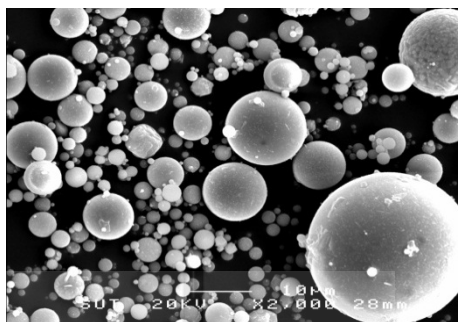


**Figure 2.6** Scanning Electron Microscope (SEM) photos of fly ash particles at 2,000x magnification.

**Table 2.4** Chemical composition (wt%) of fly ash used in the present work.

$\text{SiO}_2$	$\text{Al}_2\text{O}_3$	$\text{CaO}$	$\text{Fe}_2\text{O}_3$	$\text{K}_2\text{O}$	$\text{MgO}$	$\text{Na}_2\text{O}$	$\text{SO}_3$	<i>Ig. loss</i>
41.62	23.11	14.92	6.03	1.92	1.59	1.15	0.77	2.60

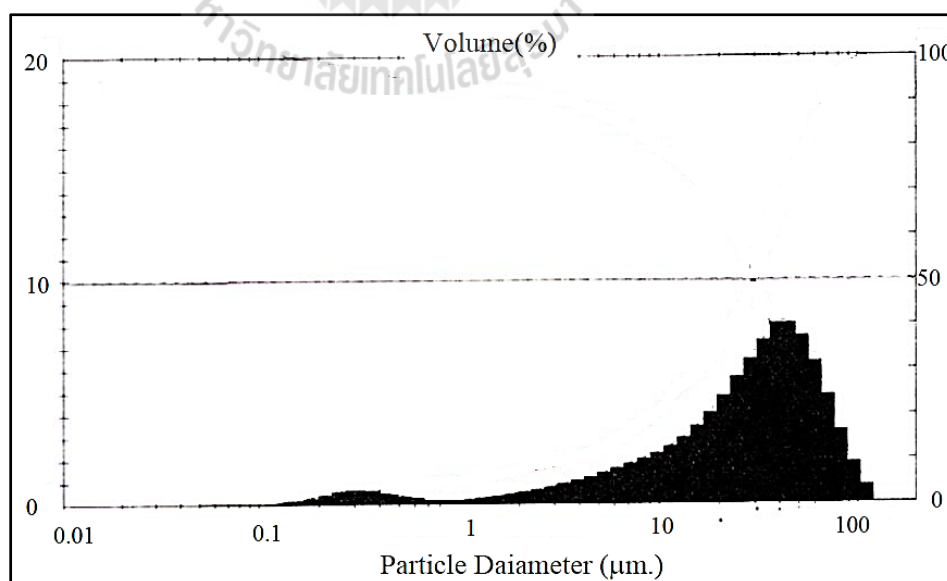


**Figure 2.7** Particle size distribution of calcined fly ash.

### 2.3.2 Preparation of porous glass from fly ash

In order to use this fly ash as a raw material for the preparation of porous glass, the chemical composition of fly ash needs to be considered. According to **Table 2.4**, this fly ash is basically composed of  $\text{SiO}_2\text{-Al}_2\text{O}_3\text{-CaO}$  system, and hence the required base glass of  $\text{SiO}_2\text{-B}_2\text{O}_3\text{-Na}_2\text{O}$  system for phase separation cannot be directly obtained from the as-received fly ash. Therefore, it is suggested that the chemical composition of fly ash needs to be adjusted such that the obtained molten glass be in the Vycor glass region of the ternary phase diagram (**Figure 2.3**) to affect the phase separation. An arbitrary composition of base glass for  $\text{SiO}_2\text{-B}_2\text{O}_3\text{-Na}_2\text{O}$  system was chosen for this study and is shown as red point A in **Figure 2.3**. The calculated final composition of the raw mix after adding various oxides into the flyash, to be used for porous glass preparation, is listed in Table 2.5.

Silica sand ( $\text{SiO}_2$ ), fly ash, and reagent grade chemicals of  $\text{CaCO}_3$  (laboratory reagent, Unilab),  $\text{H}_3\text{BO}_3$  (purity 99.5%, Carlo Erba Reagenti) and  $\text{Na}_2\text{B}_4\text{O}_7 \cdot 10\text{H}_2\text{O}$  (RPE for analysis, Carlo Erba Reagenti) were used as starting raw materials. A batch of 150 g of the synthetic raw mix was melted in a 100 cc Pt/Rh crucible at  $1450^\circ\text{C}$  for 2 h in an electric furnace in air. The molten glass obtained was poured onto an iron plate and pressed by another one to form a thin sheet and then heat treated under various conditions ( $650^\circ\text{-}800^\circ\text{C}$ , 10–150 h) to induce the phase separation. After heat treatment, they were crushed and sieved to obtain powder samples of 0.5 - 1 mm in size. After obtaining the phase separated glass by heat treatment process, it was acid leached by 1N of  $\text{HNO}_3$  solution, using the amount of acid to glass ratio of 10 (ml/g) as suggested by Morimoto (2005). Then it was washed and rinsed by running water for 24 hours and dried at  $120^\circ\text{C}$  for 24 hours. Afterwards,

the glass was treated with a dilute alkali solution (1N-NaOH) at room temperature for 5 hours to remove any SiO<sub>2</sub> colloids remaining inside the pores following the acid leaching step. On acid leaching, O.E. Lebedeva (2000) discovered that the textural properties of prepared porous glass depended on the nature of the acid used. Overall, HNO<sub>3</sub> acid solution gave clearer structure and less slag than other types of acid solutions; slag contains CaO and SiO<sub>2</sub> as major components and it always remain in pore after acid leaching. For this reason, nitric acid was thus selected as a leaching solution in this study. Schematic diagram of the preparation of porous glass from coal fly ash used in this work is shown in **Figure 2.8**.

**Table 2.5** Chemical composition of base glass for porous glass preparation after adding various oxides into the fly ash sample.

Chemical composition	% wt
SiO <sub>2</sub>	51.7
Al <sub>2</sub> O <sub>3</sub>	9.2
B <sub>2</sub> O <sub>3</sub>	17.6
Fe <sub>2</sub> O <sub>3</sub>	2.4
MgO	0.6
CaO	13.2
Na <sub>2</sub> O	4.5
K <sub>2</sub> O	0.8



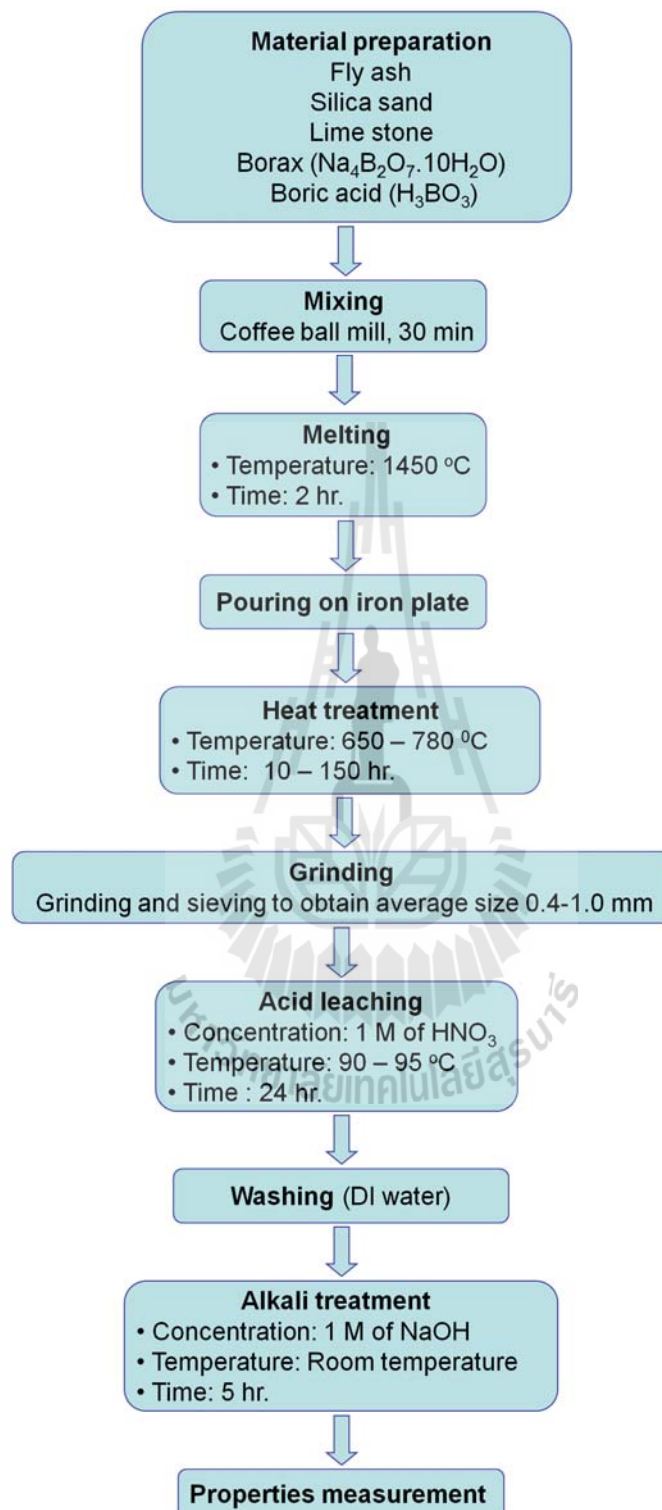


**Figure 2.8** Schematic diagram of the preparation of porous glass from coal fly ash.

#### 2.4.4. Characterization of porous glass

The oxide composition of prepared porous glasses was determined by XRF method. The wet chemical analysis was applied for the determination of  $B_2O_3$  and this was performed by The National Metal and Materials Technology Center, MTEC(Thailand). The surface structures of porous glasses were observed by scanning electron microscopy (SEM, JEOL JSM 6400). The pore size distribution, specific surface area, pore volume, porosity, bulk density and apparent density of porous glasses were determined by a mercury intrusion porosimeter (Auto pore III, Micrometrics). **Figure 2.9** shows the equipment used for the characterization of prepared porous glass.

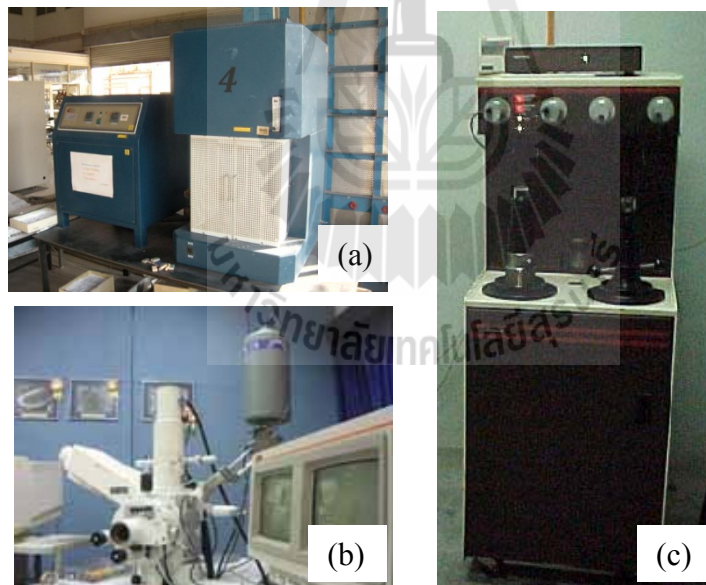


**Figure 2.9** Equipments used for the characterization of prepared porous glass samples, (a) glass melting furnace (b) scanning electron microscopy (SEM, JEOL JSM 6400) (c) mercury intrusion porosimeter (Auto pore III, Micrometrics).

## 2.5 Results and discussion

### 2.5.1 Compositions and properties of porous glasses

**Table 2.6** shows typically the chemical composition of molten glass and the prepared porous glasses following acid and alkaline treatments for heat treatment conditions of 750 °C and 20 hour. The initial base glass system is SiO<sub>2</sub>-B<sub>2</sub>O<sub>3</sub>-(Al<sub>2</sub>O<sub>3</sub>-CaO)-Na<sub>2</sub>O system. The weigh percentage of SiO<sub>2</sub> was found to increase after acid leaching while those of other oxides tended to decrease, due mainly to the removal of sodium – rich borate phase of B<sub>2</sub>O<sub>3</sub>, CaO, Al<sub>2</sub>O<sub>3</sub>, MgO, Na<sub>2</sub>O and K<sub>2</sub>O, and left behind the frame work of silica rich phase. In addition, about 26% of SiO<sub>2</sub> was further removed after alkaline leaching since alkaline solution can remove silica colloid and silica structure phase. Furthermore, around 74 % of Fe<sub>2</sub>O<sub>3</sub> was leached out by the acid leaching process, which indicates that Fe<sub>2</sub>O<sub>3</sub> moves to the soluble borate phase during the phase separation process. The chemical composition of porous glass after acid treatment as shown in **Table 2.6** is similar to that of Shirasu porous glass (SPG); chemical composition of SPG is around 75 % of SiO<sub>2</sub>, 10% of Al<sub>2</sub>O<sub>3</sub>, 5 % of B<sub>2</sub>O<sub>3</sub> and 10 % of other compositions) (S. Morimoto, 1995). The SPG is highly resistant to bacteria, virus, acid and alkali solution, and capable of pore diameter design in a wide range. Therefore, porous glass obtained from this work should have properties and capability comparable to the commercial Shirasu porous glass.

**Table 2.6** Chemical compositions of molten glass and porous glasses after acid and

alkaline treatments (750 °C and 20 hours of heat treatment conditions)

Porous glass composition	Base glass (after glass melting)	After acid treatment		After alkali treatment	
	gram( %wt)	gram	%wt	gram	%wt
<b>SiO<sub>2</sub></b>	41.18	40.51	69.85	29.83	63.57
<b>B<sub>2</sub>O<sub>3</sub></b>	17.97	3.59	5.90	3.40	7.24
<b>CaO</b>	17.53	1.73	2.85	1.72	3.66
<b>Na<sub>2</sub>O</b>	12.21	2.79	4.59	2.70	5.75
<b>Al<sub>2</sub>O<sub>3</sub></b>	7.37	5.60	9.20	5.45	11.61
<b>Fe<sub>2</sub>O<sub>3</sub></b>	1.93	0.50	0.82	0.47	1.00
<b>MgO</b>	0.99	0.12	0.20	0.11	0.24
<b>K<sub>2</sub>O</b>	0.83	0.66	1.08	0.65	1.38

**Table 2.7** shows physical properties of the prepared porous glass after acid leaching as a function of heat treatment conditions. The weight loss percentage of porous glass after acid leaching varied in the range from 39 – 48%. The longer time and higher treatment temperature had no significant effect on the amount of weight loss since acid solution dissolved only the borate rich phase. In principle, the weight loss should depend on the chemical composition of the original base glass. The appearance of porous glass depends on the heat treatment conditions, for example, porous glass was transparent at 650°C which was the lowest heat treatment temperature used, while white opaque and gray opaque colors were obtained at the high temperature range of 700 - 750°C and 750 - 780°C, respectively.

**Table 2.7** Physical properties (appearance and weight loss) of prepared porous glass

before and after acid leaching

Batch No.	Heat treatment conditions	Weight (g)		Appearance of porous glass after acid leaching	Weight loss after acid leaching	
		Before acid leaching	After acid leaching		$\Delta W$ (g)	$\Delta W$ (%)
1	650 °C – 150 hr.	3.3313	1.9035	Transparent	1.4278	42.86
2	650 °C – 120 hr.	1.7676	0.9949	Transparent	0.7728	43.72
3	650 °C – 90 hr.	2.2036	1.2242	Transparent	0.9794	44.44
4	650 °C – 50 hr.	1.4615	0.8165	Transparent	0.6450	44.13
5	650 °C – 20 hr.	6.9425	3.8406	Transparent	3.1019	44.68
6	700 °C – 120 hr.	2.2439	1.2581	White opaque	0.9858	43.93
7	700 °C – 72 hr.	2.4208	1.4641	White opaque	0.9567	39.52
8	700 °C – 90 hr.	1.8128	1.0293	White opaque	0.7836	43.22
9	700 °C – 50 hr.	2.1058	1.2468	White – Partly Pale blue	0.8590	40.79

**Table 2.7** Physical properties (appearance and weight loss) of prepared porous glass

before and after acid leaching. (continued)

Batch No.	Heat treatment conditions	Weight (g)		Appearance of porous glass after acid leaching	Weight loss after acid leaching	
		Before acid leaching	After acid leaching		$\Delta W$ (g)	$\Delta W$ (%)
10	700 °C – 20 hr.	3.1332	1.7369	White – Partly Pale blue	1.3963	44.56
11	725 °C – 120 hr.	7.0079	3.8585	White opaque	3.1494	44.94
12	725 °C – 90 hr.	8.8913	4.9311	White opaque	3.9602	44.54
13	725 °C – 72 hr.	7.7965	4.3550	White opaque	3.4415	44.14
14	750 °C – 40 hr.	4.1157	2.4545	Gray opaque	1.6612	40.36
15	750 °C – 20 hr.	5.5493	3.3774	White opaque	2.1719	39.14
16	750 °C – 10 hr.	2.0960	1.2351	White opaque	0.8609	41.07
17	780 °C – 20 hr.	7.7846	4.7159	Gray opaque	3.0687	39.42
18	780 °C – 10 hr.	8.6081	4.4556	Gray opaque	4.1525	48.24
19	780 °C – 5 hr.	8.3699	5.1166	White opaque	3.2533	38.87

**Table 2.8** Physical properties (appearance and weight loss) of prepared porous glass

before and after alkaline leaching

No.	Heat treatment conditions	Weight (g)		Appearance after alkaline leaching process	Weight loss	
		Before alkaline leaching after acid leaching	After alkaline leaching		$\Delta W$ (g)	$\Delta W$ (%)
1	650 °C – 120 hr.	1.0245	0.2547	Transparent	0.7698	75.14
2	650 °C – 90 hr.	1.0406	0.1839	Transparent	0.8567	82.33
3	650 °C – 50 hr.	0.9510	0.1389	Transparent	0.8121	85.39
4	650 °C – 20 hr.	1.2617	0.3215	Transparent	0.9402	74.52
5	700 °C – 120 hr.	0.9820	0.7082	White	0.2738	27.88
6	700 °C – 90 hr.	1.0270	0.7259	White	0.3011	29.32
7	700 °C – 72 hr.	1.0625	0.6272	White	0.4353	40.97
8	700 °C – 50 hr.	1.0184	0.5427	White	0.4757	46.71
9	700 °C – 20 hr.	0.8180	0.3364	White	0.4816	58.88
10	750 °C – 40 hr.	1.0124	0.7273	White opaque	0.2851	28.16
11	750 °C – 20 hr.	1.3777	1.0172	White opaque	0.3605	26.17

The physical appearances of glasses are shown in **Figure 2.10**. The mother glass in **Figure 2.10a** (glass after the melting process) changed from dark brown to gray color after heat treatment process (**Figure 2.10b**). The color of porous glass after acid leaching following heat treatment was transparent and finally turned to white opaque as shown in **Figure 2.10c**. Therefore, the different colors of porous

glass are dependent on the heat treatment conditions and the structure of porous glass itself.

**Table 2.8** shows physical properties of the prepared porous glass after the final alkali leaching. The weight loss observed is the result of the removal of silica colloid from the pores; the higher the weight loss, the more transparency of the glass. The weight loss percentage of porous glass after alkali leaching at 650 °C is around 74 – 85% and 26 – 59 % at higher temperatures (700 - 750 °C) as shown in **Table 2.8**.

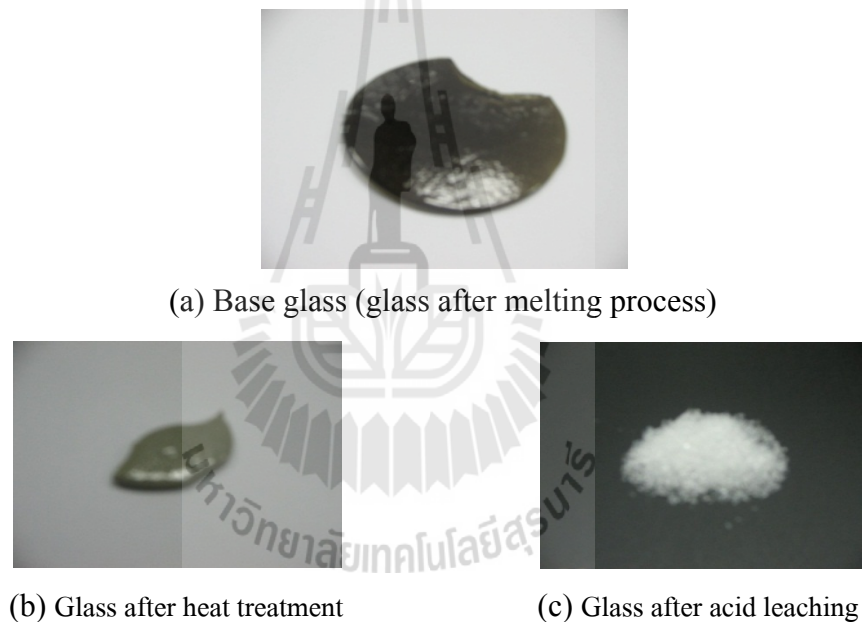


**Figure 2.10** Photographs of (a) base glass (glass after melting process) (b) glass after heat treatment at 780 °C and 20 hours conditions (c) glass after acid leaching with 1 M of HNO<sub>3</sub> solution.



### 3.4.2 Pore structure of porous glass

#### 3.4.2.1 Effect of acid leaching

The appearances of glass after heat treatment were transparent, white opaque and gray color depending on the temperature range from 650 °C to 800°C of the heat treatment process and finally turned to colorless transparent to white color after acid leaching. Presumably, this final appearance is caused by the removal of  $\text{Fe}_2\text{O}_3$  into the soluble phase due to the action of acid leaching as summarized in **Table 2.7 -2.8.**

The surface area (A), pore volume (V) average pore size in terms of median pore diameter, porosity, bulk density and apparent density of the final porous glasses obtained in this study were measured by Mercury porosimetry and are summarized in **Table 2.9**. The variation of median pore size as a function of heat treatment condition is shown plotted in **Figure 2.11**. It is seen that the pore diameter increased sharply over a brief heat treatment time for heat treatment temperatures above 750°C. Below 700 °C, there is no development of internal pore being observed at any heat treatment time. The controlled pore sizes are crucial for a specific application of porous glass. The results showed pore structure to be controlled to a greater extent by heating temperature and to a lesser extent by heating time with higher temperature and longer time resulting in the larger pore diameter of porous glass. Also, the effect of heating time on the mean pore size is more pronounced at higher treatment temperature. As an example, results from **Table 2.9** show that the median pore diameter at 650 , 700 and 725 °C for 90 hours were 9.1 nm., 71.1 nm. and 544 nm., respectively. On the other hand, the median pore diameter at 650 °C for 90 , 120 and 150 hours of treatment time were 9.1 nm., 9.5 nm., and 11.4

nm., respectively. The bulk density of derived porous glass is in the range of 1.5 – 2.0 g/cm<sup>3</sup>, while the apparent density varies from 2.0 – 3.0 g/cm<sup>3</sup>. There appears to be no clear indication as to the effect of heat treatment conditions on the bulk density of porous glass product. There is a tendency that porosity of porous glass increases with increasing treatment temperature, for example, at 90 hour and treatment temperatures of 650 , 700 and 725 °C, the porosity are 27.59, 40.21 and 48.65%, respectively. However, the effect of treatment time on the porosity of glass is not clear as shown in **Table 2.9**. The SEM photographs of the obtained porous glass are shown in **Figure 2.12** based on the same magnification. There is clear evidence that the mean pore size of porous glass increased with increasing heat treatment time and temperature, as previously discussed.

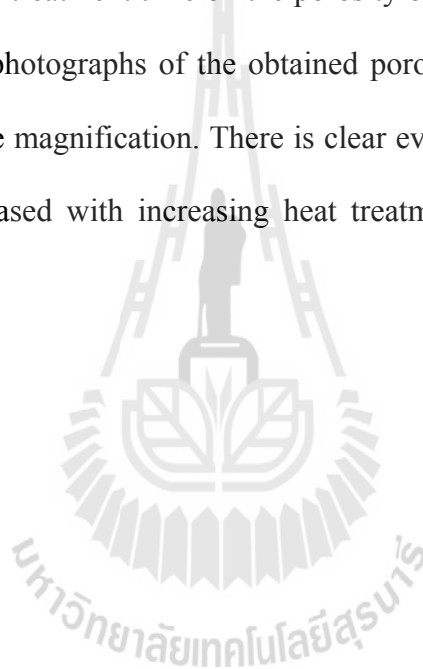


**Table 2.9** Porous and physical properties of porous glasses after acid leaching.

Heat treatment		Surface area	Pore volume	Median pore diameter	Bulk density	Apparent density	Porosity
Temperature °C	Time hour	m <sup>2</sup> /g	cm <sup>3</sup> /g	nm	(g/cm <sup>3</sup> )	(g/cm <sup>3</sup> )	%
650	90	51	0.16	9.1	1.7365	2.3983	27.59
	120	65.9	0.18	9.5	1.7853	2.6379	32.32
	150	29.3	0.13	11.4	1.7102	2.1832	21.67
700	50	13.2	0.15	52.1	1.7321	2.3278	25.59
	90	16.3	0.16	71.1	1.6901	2.8268	40.21
	120	13.3	0.24	95.9	1.7864	2.4911	28.29

**Table 2.9** Porous and physical properties of porous glasses after acid leaching.

Heat treatment		Surface area m <sup>2</sup> /g	Pore volume cm <sup>3</sup> /g	Median pore diameter nm	Bulk density (g/cm <sup>3</sup> )	Apparent density (g/cm <sup>3</sup> )	Porosity %
Temperature °C	Time hour						
725	72	9	0.29	296	1.6334	3.1155	47.57
	90	9.6	0.18	544	1.6251	3.165	48.65
	120	8.1	0.3	581	1.6224	2.3063	29.65
750	10	17.9	0.26	159	1.8442	3.5223	47.64
	20	11.5	0.32	467	1.6510	3.5406	53.37
	40	6.7	0.32	1123	1.6006	3.2669	51.01
780	5	14	0.32	565	1.5239	2.2609	32.60
	10	15.4	0.16	1615	1.5625	3.3803	53.78
	20	3.5	0.34	2097	1.9773	2.8609	30.89

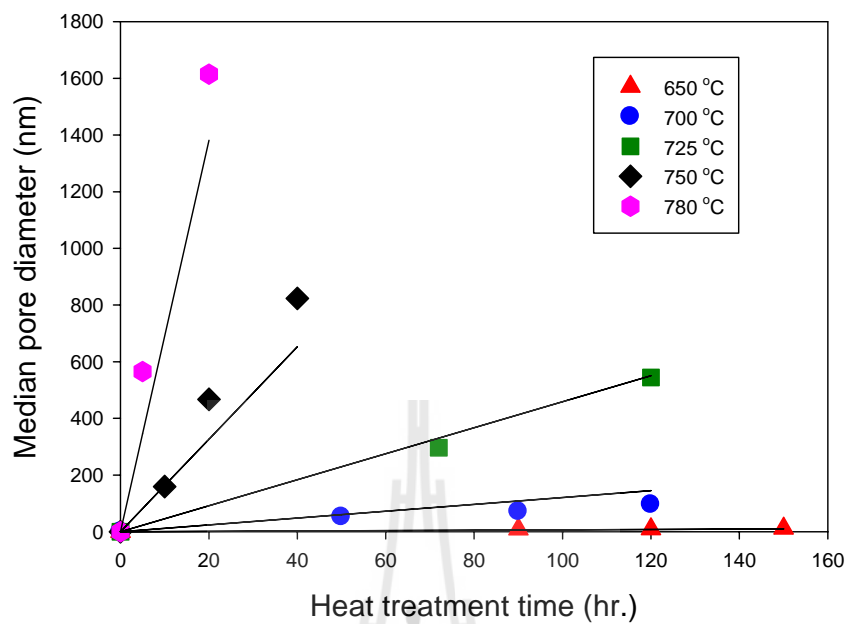
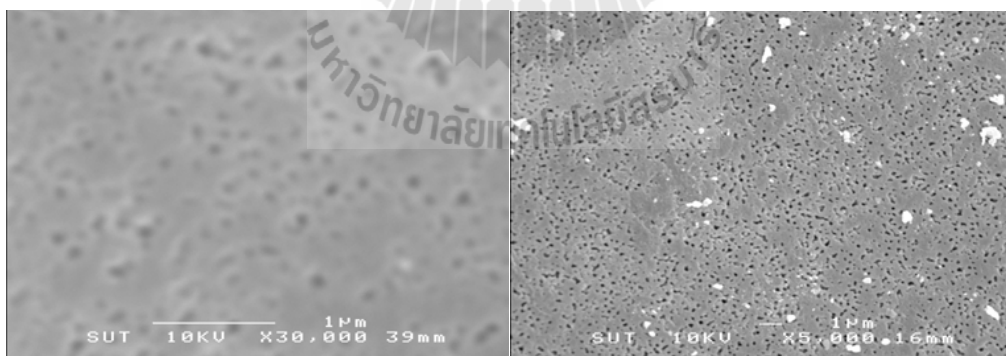


**Figure 2.11** Relation between pore diameter and heat treatment time at various heat treatment temperatures, after acid leaching.



700°C– 20 h

700°C–90 h

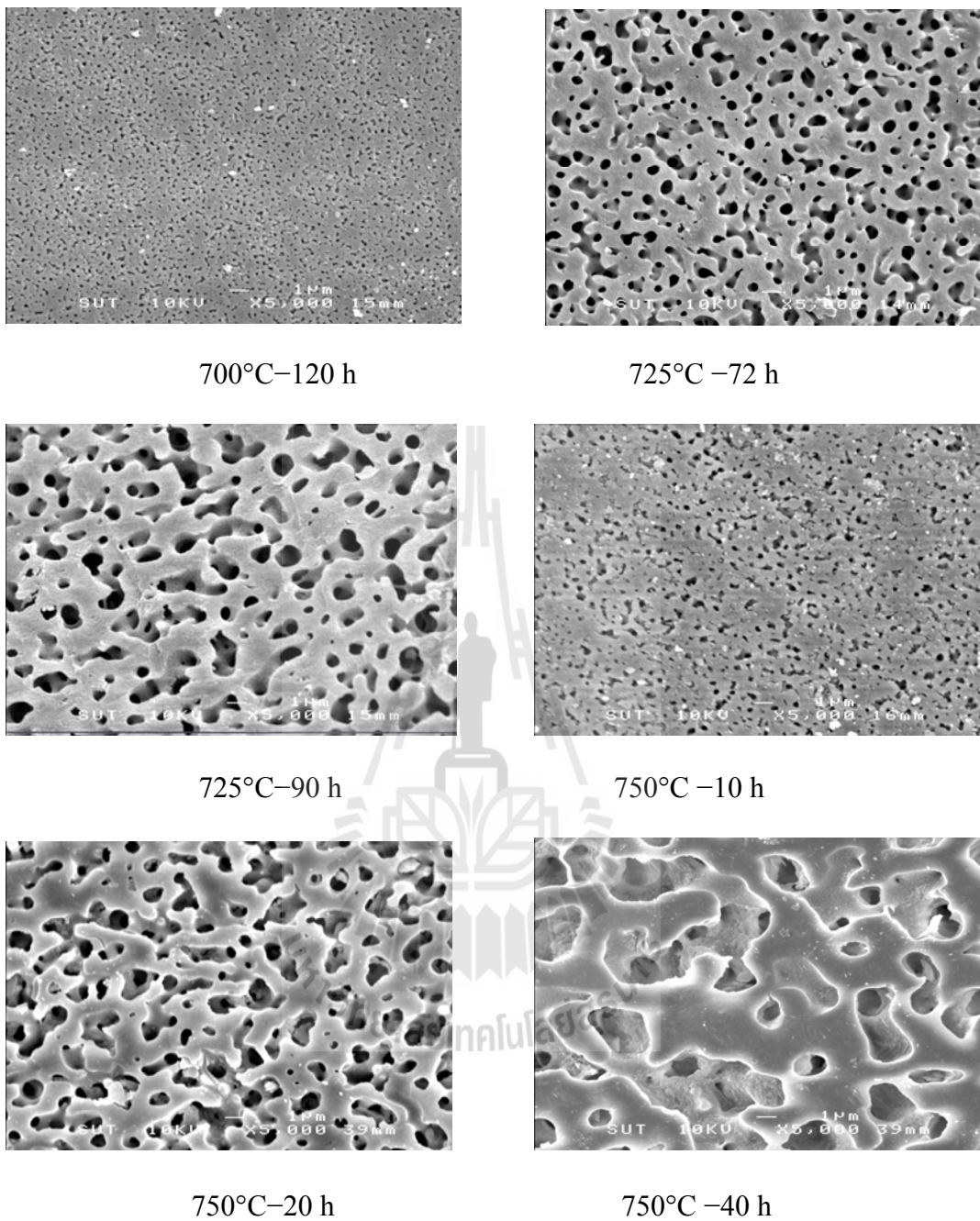
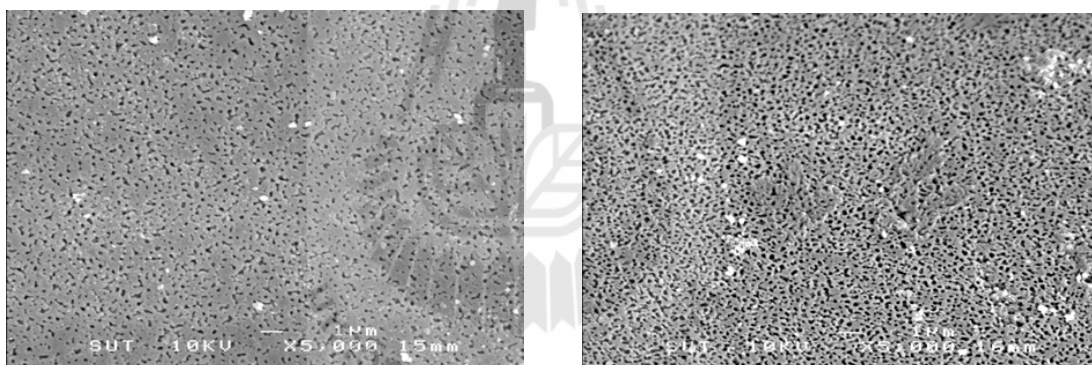


**Figure 2.12** SEM photos of porous glasses obtained under various heat treatment conditions.

### 2.5.2.2 Effect of alkali leaching

Usually, acid soluble phase ( $B_2O_3$ -RO- $R_2O$  rich phase) contains a considerable amount of  $SiO_2$  and the solubility of this  $SiO_2$  component in acid solution is very low. As a result,  $SiO_2$  colloids tends to remain inside the pores after acid leaching. These  $SiO_2$  colloids can be removed by treating the acid – leached glasses with alkali solution. **Figure 2.13** shows the SEM photos of porous glass before and after alkali treatment. The interconnected pore structure can be clearly seen after alkali treatment. It is seen that the pore diameter increases slightly and the pore volume increases markedly after alkali treatment.



(a) Before alkali treatment (b) After alkali treatment

**Figure 2.13** SEM photographs of porous glass (a) before alkali solution treatment (b) after alkali solution treatment for the 700 °C and 120 hour heat treatment conditions.

It is also seen that a slight amount of spherical particles remains inside the pores, especially in the center part of porous glass. These particles may be silica colloids. However, the pore structure of porous glass is still clear before alkali

treatment and the pore size distribution shows that these pores are through pores as shown in **Figure 2.14b** which represents the center part of fractured surface of porous glass. The pore size distributions of porous glass after acid and after alkali treatment are shown in **Figure 2.15**. Table 2.10 shows the porous properties of porous glass after alkali treatment; the median pore diameter and porosity were increased after alkali treatment and this implies that the colloidal silica was readily removed by the action of alkali solution.

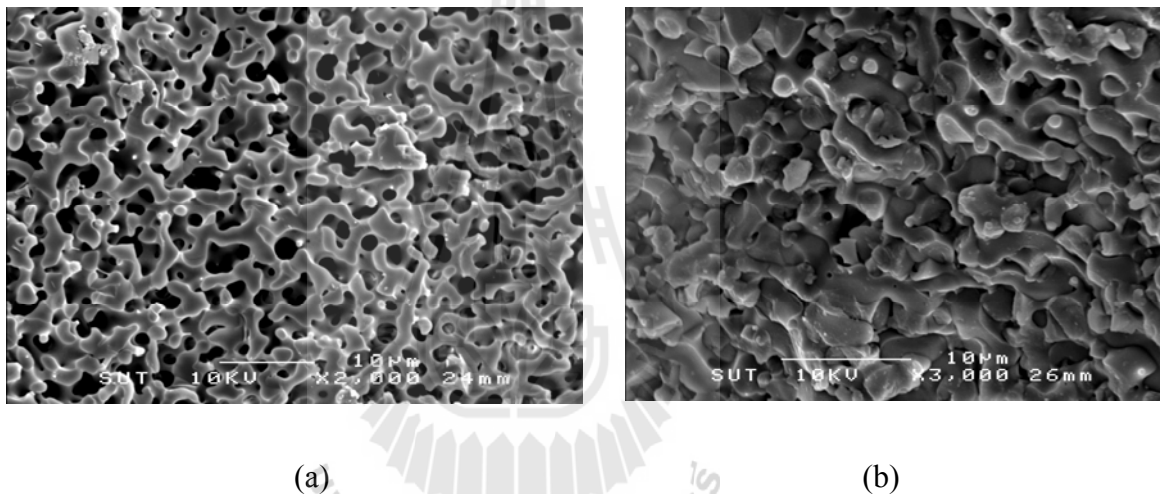


**Figure 2.14** SEM photos of porous glass plate with positions of (a) top surface and (b) center part of a fractured surface for the 700 °C and 120 hour heat treatment conditions, showing interconnected pore structure.



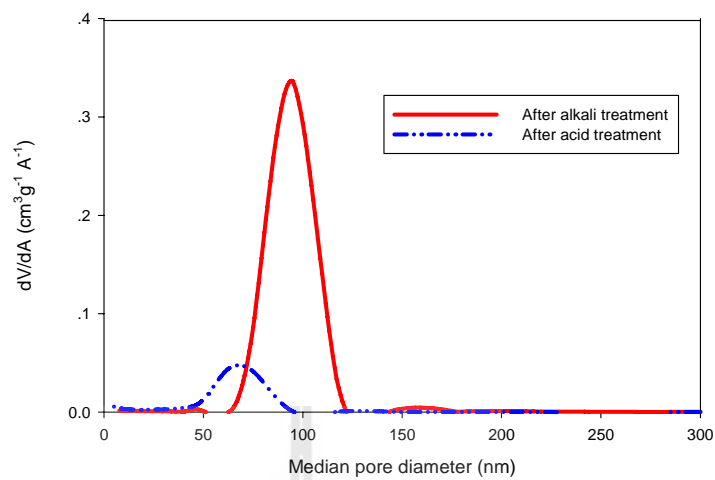


**Figure 2.15** Pore size distributions of (a) after acid treatment (b) after alkali treatment at 700 °C and 120 hour heat treatment conditions.

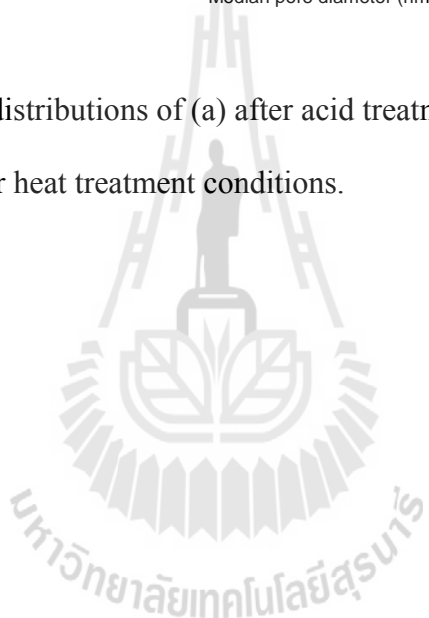


**Table 2.10** Porous properties of porous glasses after acid and alkali treatment by mercury intrusion porosimeter (Auto pore III, Micrometrics).

Condition treatment	Heat treatment		Surface area m <sup>2</sup> /g	Pore volume cm <sup>3</sup> /g	Median pore diameter nm	Bulk density (g/cm <sup>3</sup> )	Apparent density (g/cm <sup>3</sup> )	Porosity %
	Temperature °C	Time hour						
After acid treatment	700	120	13.30	0.24	95.9	1.7864	2.4911	28.29
	750	20	11.50	0.32	467.0	1.6510	3.5406	53.37
		40	6.70	0.32	1123.0	1.6006	3.2669	51.01
After alkali treatment	700	120	20.75	0.50	103.1	1.3274	3.9508	66.40
	750	20	5.37	0.36	486.4	1.3968	2.7941	50.01
		40	4.04	0.36	1083.0	1.2744	2.3674	46.17

### 2.5.3 Pore diameter equation

It has been found that the conditions of heat treatment, including temperature and time of the phase separation process affect directly the pore size distribution of the prepared porous glass. In this section a general correlation was proposed to predict the median pore size of porous glass as a function of heat treatment parameters.

A general equation relating the median pore diameter ( $D_p$ ) of porous glass after acid treatment with time ( $t$ ) and temperature ( $T$ ) of the heat treatment conditions can be written as

$$D_p = k f(t) \quad (2.3)$$

where  $k$  = rate constant, and  $f(t)$  is a function of heat treatment time in the form,

$$f(t) = t^n \quad (2.4)$$

where  $n$  is a constant indicating the nature of mass transfer for the phase separation

**Equation 2.3** can now be written as

$$D_p = kt^n \quad (2.5)$$

If  $k$  depends on heat treatment temperature only, the Arrhenius equation can be applied,

$$k = k_0 e^{-\frac{E_a}{RT}} \quad (2.6)$$

where  $k_0$  = pre-exponential factor

$E_a$  = activation energy of the phase-separation process

$R$  = universal gas constant

$T$  = absolute temperature

There are two mechanisms for the formation of three dimensional interconnected structures of porous glasses that have been previously proposed; one is the spinodal decomposition (J. W. Cahn and R. J. Charles, 1965) and the other is the nucleation and growth (W. Haller, 1965). In the latter process, the pore diameter increases proportional to the square root of heat treatment time ( $t^{1/2}$ ) until the volume fraction of the two phases reaches a constant (S. M. Ohlberg, H. R. Golob, J. J. Hammel and R. R. Lewchuck, 1965). After reaching the constant volume fraction, the pore diameter now increases proportionally to the cube root of heat treatment time ( $t^{1/3}$ ) (Y. Moriya, D. H. Warrington and R. W. Douglas, 1981). From the plotted results in **Figure 2.16**, although the initial stage of phase separation is not clear, the pore diameter increases proportionally to the cube root of heating time ( $t^{1/3}$ ) at the later stage. This implies that the small particles melt again and grow to larger particles. Then, the large particles contact each other and form the three dimensional interconnected structure. As shown in **Figure 2.12**, the structure of porous glass is seen like droplet type structure (750°C–10 h) in the early stage, and after that this structure grows to interconnected structure with an increase in heating time (750°C–20 h and 750°C–40 h). This result indicates that the interconnected structure observed in this study may be formed by the spinodal decomposition at heat treatment temperatures in the range of 750 – 780 °C.

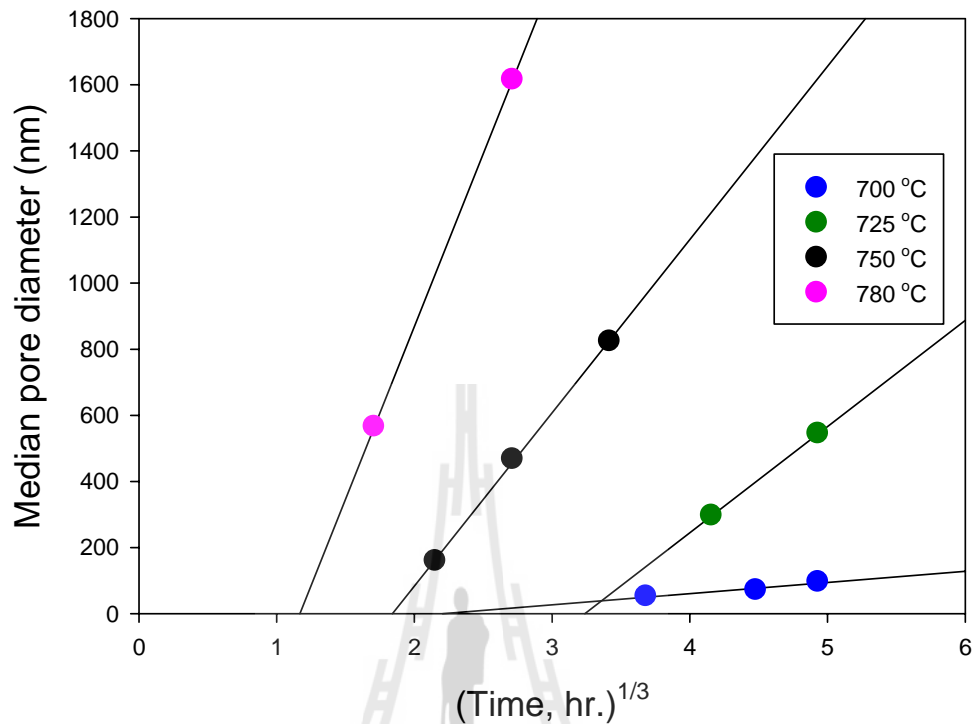


**Figure 2.16** Relation between pore diameter and cube root of heating time at various temperatures, before alkali treatment.

**Figure 2.16** shows the relationship between median pore diameter and cube root of heating time ( $t^{1/3}$ ) according to **Equation 2.5** with  $n=1/3$ , and the values of rate constant  $k$  determined from the slope of the linear plot of **Equation 2.5**. The pre-exponential factor ( $k_0$ ) and activation energy for the phase separation ( $E_a$ ) were obtained from the intercept and slope of the Arrhenius plot, respectively, as shown in **Figure 2.17**, to give the values of  $7.921 \text{ nm}\cdot\text{hour}^{1/3}$  for  $k_0$  and  $419.18 \text{ kJ/mol}$  for  $E_a$ , respectively. The rate constant,  $k$ , decreases markedly with decreasing treatment temperature from  $780$  to  $700$  °C as shown in **Table 2.11**.

**Table 2.11** Correlation parameters of the relationship between median pore size and heat treatment conditions

Treatment temperature (°C)	$D_p$ and time <sup>(1/3)</sup>	
	$k$ (nm.hr <sup>1/3</sup> )	$R^2$
780	567	0.9009
750	280	0.6906
725	97	0.8972
700	18	0.9451

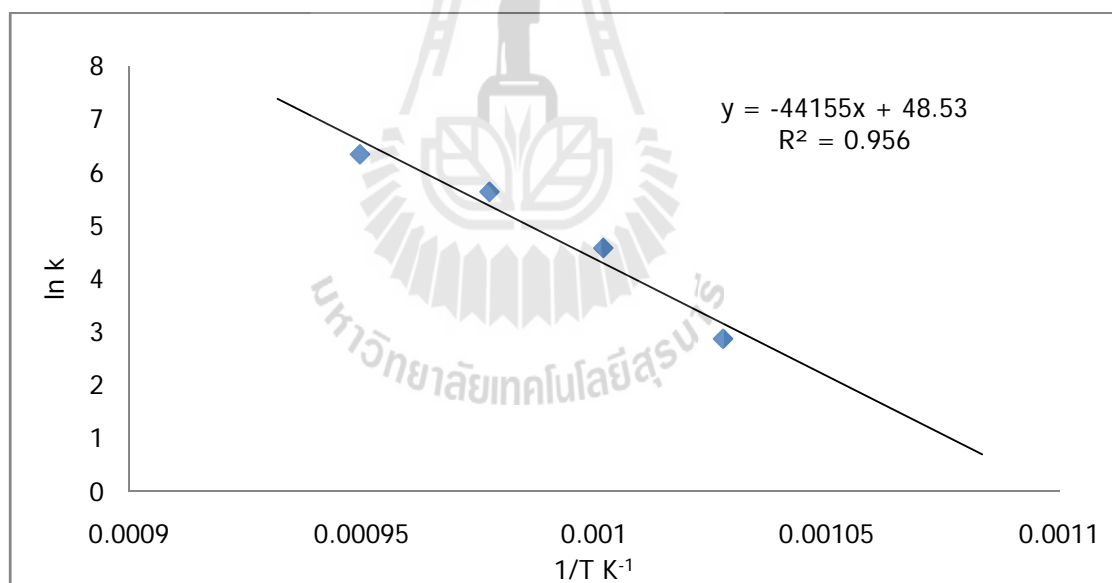


**Figure 2.17** Arrhenius plot for determining kinetic parameters ( $k_0$  and  $E_a$ ) for pore size development of porous glass.

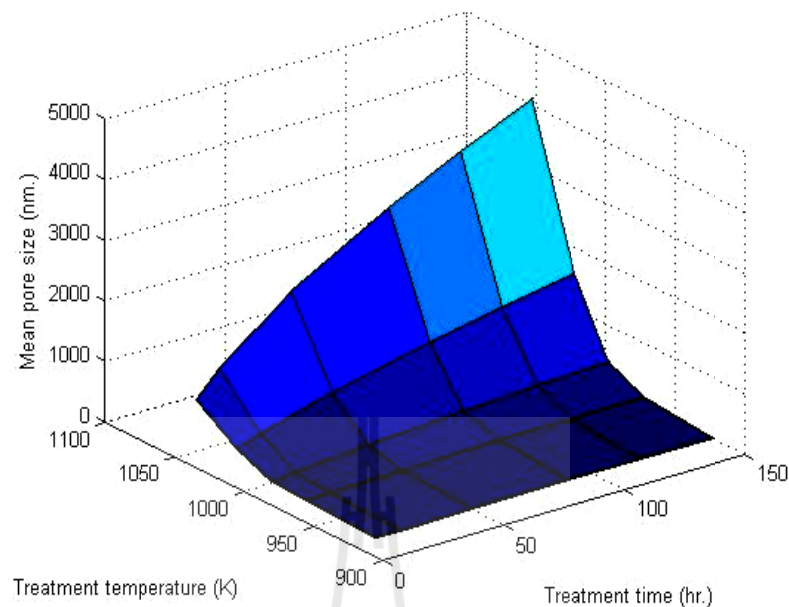


**Figure 2.18** Relationship between median pore size of porous glass and heat treatment conditions from the correlation model.

The final correlation relating the median pore diameter ( $D_p$  in nm.) with time ( $t$  in hour) and temperature ( $T$  in  $^{\circ}\text{C}$ ) of the heat treatment process is presented as in **Equation 2.7**.

$$D_p = 7.92 \text{ nm.hour}^{1/3} \exp\left(\frac{-419.18 \text{ kJ/mol}}{8.314 T}\right) t^{1/3} \quad (2.7)$$

with heat treatment temperature ( $T$ ) ranging between  $700 - 780^{\circ}\text{C}$  and  $10 - 150$  hours of heat treatment time ( $t$ ).

The numerical values of Equation 2.7 are graphically displayed in **Figure 2.18**. Again, it is observed that the higher treatment temperature and longer treatment time increase the pore size of porous glass. Furthermore, the higher

treatment temperature appears to show a more pronounced effect on the pore size distribution of porous glass as compared to the variation of heat treatment time.

## 2.6 Conclusion

In this work, porous glasses were prepared by the thermal phase separation technique using coal fly ash as a raw material. The composition of coal fly ash is basically composed of  $\text{SiO}_2\text{-Al}_2\text{O}_3\text{-Fe}_2\text{O}_3\text{-CaO}$  and the  $\text{SiO}_2\text{-B}_2\text{O}_3\text{-(Al}_2\text{O}_3\text{-CaO)-Na}_2\text{O}$  system was chosen as a base glass composition in this work to affect the phase separation of boron and silica based glass. The obtained porous glasses were characterized for pore size distribution, specific surface area, pore volume, porosity, bulk density and apparent density using a mercury intrusion porosimeter. Furthermore, the pore structure of porous glass was ascertained from SEM photomicrographs. The heat treatment conditions were found to directly influence the pore size of porous glass; the mean pore size of porous glass increased with increasing heat treatment temperature and treatment time and this result was also supported by SEM photographs.

The alkaline solution treatment was applied after acid leaching of the phase – separated glass to leach out silica colloids remaining inside the pore structure. However, the acid leaching process using 1M- $\text{HNO}_3$  solution could also reduce effectively the silica colloids, and hence only acid leaching is sufficient for the preparation of the porous glasses. A correlation was developed to correlate the mean pore size of porous glass with heat treatment conditions, such that the median pore diameter increased proportionally to the cube root of heating time ( $t^{1/3}$ ) at relatively long treatment times. It is hypothesized that the rate determining step could be the



diffusion process of structural units involving oxygen ions and the phase separation may take place by the nucleation and growth mechanism. Porous glass with pores larger than 1  $\mu\text{m}$  can be obtained easily and has chemical composition similar to the commercial Shirasu porous glass.

## 2.7 References

- A. Garea, J. R. Viguri and A. Irabien. (1997). Kinetic of the flue gas desulphurization at low temperature: fly ash/calcium (31) sorbent behavior. **Chemical Engineering Science**. 52: 715-732.
- Barbieri, L., Corradi Bonamartini, A. and Lancellotti, I. (2000). Alkaline and alkaline-earth silicate glasses and glass-ceramics from municipal and industrial wastes. **Journal of the European Ceramic Society**. 20(14–15): 2477-2483.
- C. Ferricia, A. Ribeiro and L. Ottosen. (2003). **Journal Hazardous Material**. B96 201-206.
- Barbieri, L., Corradi Bonamartini, A. and Lancellotti, I., (2000). Alkaline and alkaline-earth silicate glasses and glass-ceramics from municipal and industrial wastes. **Journal of the European Ceramic Society**, 20(14–15): 2477-2483.
- Bois, L., Bonhommé, A., Ribes, A., Pais, B., Raffin, G. and Tessier, F., (2003). Functionalized silica for heavy metal ions adsorption. **Colloids and Surfaces A: Physicochemical and Engineering Aspects**, 221(1–3): 221-230.
- Cheerarat, R. and Jaturapitakkul, C., (2004). A study of disposed fly ash from landfill to replace Portland cement. **Waste Management**, 24(7): 701-709.

- Enke, D., Janowski, F. and Schwieger, W., (2003a). Porous glasses in the 21st century--a short review. **Microporous and Mesoporous Materials**, 60(1-3): 19-30.
- Enke, D., Janowski, F. and Schwieger, W., (2003b). Porous glasses in the 21st century—a short review. **Microporous and Mesoporous Materials**, 60(1–3): 19-30.
- Hurley, P.W. and Pritchard, R.G., (2005). CEMENT. In: W. Editors-in-Chief: Paul, T. Alan and P. Colin (Editors), **Encyclopedia of Analytical Science (Second Edition)**. Elsevier, Oxford, pp. 458-463.
- Shelby, J.E., 1997. Introduction to glass science and technology. **The Royal Society of Chemistry**.
- T. W. Cheng and Y. S. Cheng.(2003).**Chemosphere**, 51:817-824.
- T. Yazawa (1995), “Present Status and Future Potential of Preparation of Porous Glass and Its Application”, in “Porous Ceramic Materials”, **Ed. D-M. Liu**, Trans Tech Publications, Switzerland, pp.125-146.
- W. Emem (2005)., “Effective Utilization of coal fly ash for high thermal shock resistance Glass-ceramic ware”, **Master Thesis**, Suranaree University of Technology.
- W. Haller. (1965).**Journal Chemical Physic**, 42, 686-693.

## CHAPTER III

### ADSORPTION STUDY OF POROUS GLASS

#### 3.1 Abstract

Porous glass prepared from coal fly ash by the phase-separation technique was used to study the adsorption behavior in both liquid and gas systems. The liquid-phase adsorption was carried out with single component of  $\text{Cu}^{2+}$ ,  $\text{Ag}^+$  and  $\text{Au}^{3+}$  as well as the binary adsorption of  $\text{Cu}^{2+}$  and  $\text{Ag}^+$ , using both the virgin and chemically grafted porous glass as the adsorbents. Selective adsorption of  $\text{Cu}^{2+}$  and  $\text{Ag}^+$  could be achieved with porous glass containing amino ( $-\text{NH}_2$ ) and thiol ( $-\text{SH}$ ) groups, respectively. The analysis of adsorption equilibrium and kinetics of the single and binary adsorption were also made employing the well accepted adsorption models. Gas-phase adsorption of  $\text{CO}_2$ , water and ethanol vapors was investigated using the virgin porous glass adsorbent. It was found that the silanol groups plays a significant role in the adsorption of water and ethanol molecules which are polar adsorbates through hydrogen bonding whereas the adsorption of non-polar  $\text{CO}_2$  relies on the dispersive force interaction.

#### 3.2 Introduction

It is realized that the discharge of wastewater containing heavy metals (Cu, Cr, Ni, Ag, Au, etc) from many industries can cause serious environmental problem because

of the toxic nature of the metals (Fu and Wang, 2011) and thus the separation of these metal species to an acceptable level is of prime importance. In particular, heavy metals from mining, electronics and electroplating industries, which are precious metals and in strong demand such as Au and Ag, have made the removal and recovery of these metals even more attractive. The removal and recovery methods of heavy metal ions include chemical precipitation, ion-exchange, membrane filtration, electrochemical treatment and adsorption (Wan Ngah and Hanafiah, 2008). Of these methods, the adsorption process is an interesting choice because of its relatively low cost and ease of operation. For example, activated carbon is one of the effective adsorbents used to recover precious gold from mining operations (Rees and van Deventer, 2000). However, the non-selective adsorption of metal species by a given adsorbent makes their recovery for reuse difficult and expensive. The search for low cost adsorbents with relatively high capacity of separation for metal recovery from solution is a promising area of work aimed in the present study. Porous glass is one of such alternative adsorbents which possesses characteristics of effective adsorption, separation and regeneration (Enke et al., 2003). Porous glass is a mesoporous material with good thermal resistance, high mechanical strength and capability of fixing various functional groups onto its surface. For separation by the adsorption process, surface modification of porous material is necessary for increased adsorption capacity and selectivity. The use of mesoporous materials with surface modification has been mostly studied with a specific purpose to remove heavy metal ions from aqueous solution. One of the theories which describes the separation of heavy metals by surface functionalization is the hard-soft acid-base principle (HSAB) known as

Pearson's HSAB principle (Pearson, 1963). It states that hard (Lewis) acids prefer to bind to hard (Lewis) bases and soft (Lewis) acids prefer to bind to soft (Lewis) bases.

In this study, the equilibrium adsorption of single metal ions ( $\text{Ag}^+$ ,  $\text{Cu}^{2+}$  and  $\text{Au}^{3+}$ ) and a binary component mixture ( $\text{Cu}^{2+}/\text{Ag}^+$ ) from aqueous solution by porous glass prepared from coal fly ash was investigated. On the adsorption of  $\text{Cu}^{2+}$  and  $\text{Ag}^+$  from aqueous solution, the  $\text{Cu}^{2+}$  cation is considered to be hard Lewis acid and the  $\text{Ag}^+$  cation to be a soft Lewis acid, according to Pearson's HSAB principle. The grafting of adsorbents with a hard Lewis base aminopropyl group ( $-\text{NH}_2$ ) should create an adsorbent for  $\text{Cu}^{2+}$  adsorption, while the soft base mercaptopropyl group ( $-\text{SH}$ ) grafted on the adsorbent surface should give good affinity for  $\text{Ag}^+$  adsorption. Based on this consideration, the surface modification was studied by grafting aminopropyl ( $\text{R}-\text{NH}_2$ ) and thiolpropyl ( $\text{R}-\text{SH}$ ) groups on the surface of porous glass (PG) samples and were designated as  $\text{PGNH}_2$  and  $\text{PGSH}$  adsorbents, respectively. The adsorption equilibrium and kinetics of single component metal ion were performed in batch mode to study the effects of solution pH and initial solute concentration on adsorption efficiency and the measured isotherms were tested with various adsorption models (Freundlich, Langmuir, and Sips) based on the regression analysis of the data. For the batch adsorption of the binary system of  $\text{Cu}^{2+}$  and  $\text{Ag}^+$ , the Ideal Adsorption Solution Theory (IAST) and the well-known empirical isotherm equations were adopted for the analysis of the experimentally obtained isotherm data. Furthermore, the single component adsorption in gas phase of adsorbates with varying degree of polarity (water, ethanol and carbon dioxide) by the prepared porous glass was also investigated.

### 3.3 Theory and literature reviews

#### 3.3.1 Adsorption

Adsorption process employing porous solids is one of the most widely used methods for removing substances from both gas and liquid systems. The process of adsorption involves the separation of a substance from a fluid phase by accumulation or concentration of molecules at the surface of a solid. The adsorbing phase is called adsorbent, and the material concentrated or adsorbed at the surface of the solid phase is termed adsorbate.

Overall, the adsorption process consists of 4 consecutive steps that include

1. Transfer of the adsorbate molecules from interparticle void space by convection and dispersion to the external film surrounding the adsorbent particle (interparticle mass transfer).
2. Transfer of the adsorbate molecules by diffusion through a stagnant fluid film that surrounds the adsorbent (interphase mass transfer).
3. Diffusion through the internal pores (intraparticle mass transfer) by pore and surface diffusion processes.
4. Uptake of the adsorbate molecules on the active surface (adsorption) by adsorbent-adsorbate interactions.

The rate of adsorption depends on the rate at which the molecules can reach the available internal surface by diffusion from the interparticle bulk fluid through the external film and inside the pores.

A diagram representing an adsorption process and concentration profile of adsorbate are displayed in **Figure 3.1**.

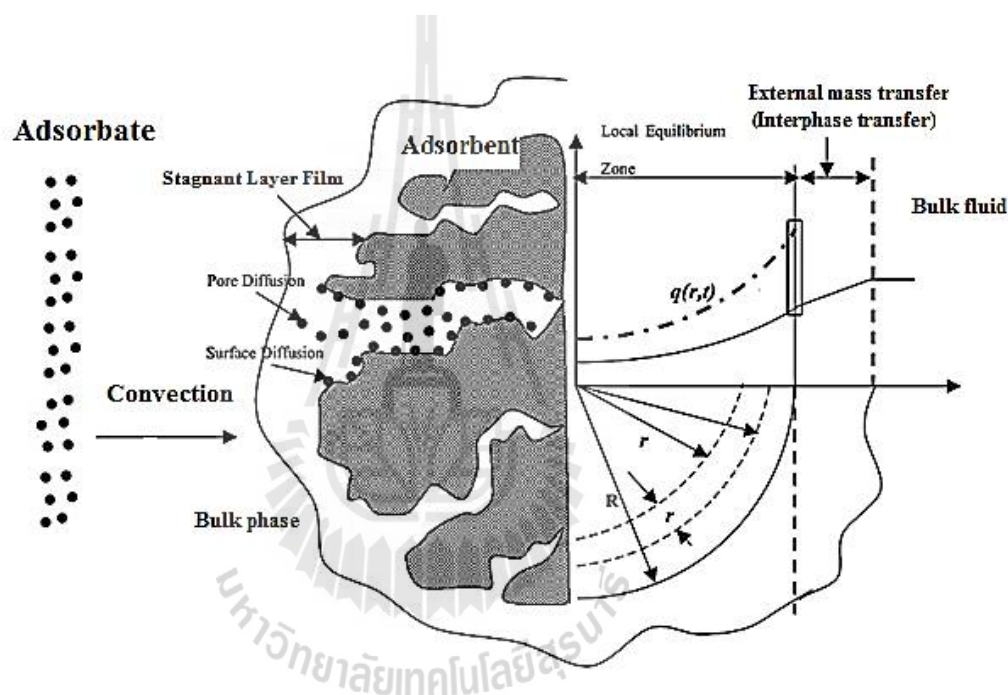


**Figure 3.1** Concentration profile of adsorbate in an adsorption process.

(Badruzzaman et al., 2004).

Generally, adsorption process can be classified into two types,

1. Physical adsorption
2. Chemical adsorption

Physical adsorption or physisorption involves Van der Waals attractive forces and is a reversible process. The adsorbate is adsorbed onto the adsorbent surface when the forces of attraction between the adsorbate and the adsorbent are greater than the forces of attraction between the adsorbate themselves.

Chemical adsorption or chemisorption occurs as a result of chemical interaction between the solid and the adsorbed molecules and the process is usually irreversible. The differences between physisorption and chemisorption process are summarized in **Table 3.1** and **Table 3.2** shows the applications of liquid and gas phase adsorption in industries.

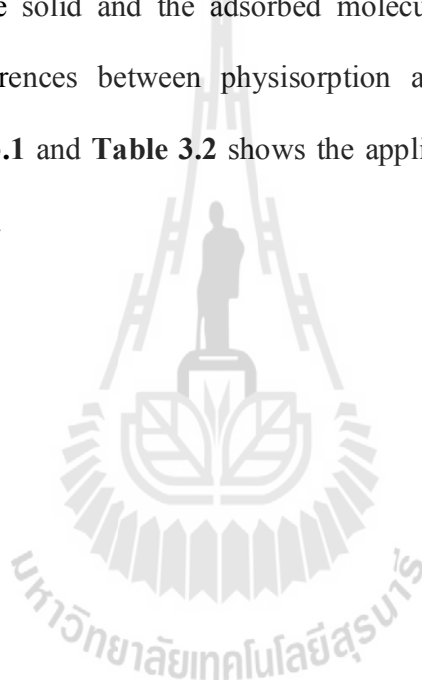




**Table 3.1** Comparison of physical adsorption and chemical adsorption. (Ruthven D. M., 1997)

<b>Parameter</b>	<b>Physical adsorption</b>	<b>Chemical adsorption</b>
Heat of adsorption	<ul style="list-style-type: none"> <li>• Low</li> <li>• &gt; 1-5 times latent heat of evaporation</li> </ul>	<ul style="list-style-type: none"> <li>• High</li> <li>• &gt; 1-5 times latent heat of evaporation</li> </ul>
Specificity	<ul style="list-style-type: none"> <li>• Nonspecific</li> </ul>	<ul style="list-style-type: none"> <li>• Highly specific</li> </ul>
Nature of adsorbed phase	<ul style="list-style-type: none"> <li>• Monolayer or multilayer</li> <li>• No dissociation of adsorbed species</li> </ul>	<ul style="list-style-type: none"> <li>• Monolayer only</li> <li>• May involve dissociation</li> </ul>
Temperature range	<ul style="list-style-type: none"> <li>• Only significant at relative low temperatures</li> </ul>	<ul style="list-style-type: none"> <li>• Possible over a wide range of temperature</li> </ul>
Forces of adsorption	<ul style="list-style-type: none"> <li>• No electron transfer, although polarization of adsorbate may occur</li> </ul>	<ul style="list-style-type: none"> <li>• Electron transfer leading to bond formation between adsorbate and surface</li> </ul>
Reversibility	<ul style="list-style-type: none"> <li>• Rapid</li> <li>• Reversible</li> </ul>	<ul style="list-style-type: none"> <li>• May be slow</li> <li>• Irreversible</li> </ul>

**Table 3.2** Industrial applications of liquid and gas phase adsorption. (Y. Ngenyen, 2007)

<b>Adsorption</b>	<b>Applications</b>
Liquid phase adsorption	<ul style="list-style-type: none"> <li>• <i>Potable water treatment</i>: remove toxic and organic materials</li> <li>• <i>Groundwater remediation</i>: adsorb contaminants</li> <li>• <i>Industrial and municipal wastewater treatment</i>: remove residual toxic and organic compounds after the primary filtration and secondary biological treatment</li> <li>• <i>Sweetener decolorization</i>: purify of sugar and corn syrup</li> <li>• <i>Chemical processing</i>: removes impurities to achieve high quality, for example, remove organic contaminants from solution in the production of alum, soda ash and potassium hydroxide</li> <li>• <i>Food, beverage and cooking oil production</i>: for example, remove taste and odor from vodka and in the production of alcoholic beverage</li> </ul>

**Table 3.2** Industrial applications of liquid and gas phase adsorption (continued).

(Y. Ngenyen, 2007)

<b>Adsorption</b>	<b>Applications</b>
Gas phase adsorption	<ul style="list-style-type: none"> <li>• <i>Solvent recovery</i></li> <li>• <i>Gasoline emission control</i>: capture gasoline vapors that escape from vents in automotive fuel systems</li> <li>• <i>Adsorption of radio nuclides</i>: control krypton and xenon radio nuclides from nuclear power plants</li> <li>• <i>Protection against atmospheric contaminants</i>: filter breathing air to protect against a variety of toxic or noxious vapors, including war gases, industrial chemicals, solvents and odorous compounds</li> <li>• <i>Process stream separations</i>: separate aromatic compounds from lighter vapors in petroleum refining process streams and to recover gasoline components from natural and manufactured gas</li> </ul>

### 3.3.2 Adsorption isotherms

The equilibrium relationship between an adsorbate and adsorbent is usually defined in terms of an adsorption isotherm which expresses the amount of adsorbate being adsorbed at equilibrium as a function of the fluid-phase concentration (partial pressure for gases and vapors) at a constant temperature. **Figure 3.2** shows the IUPAC classification of adsorption isotherms for gas adsorption system (Do Duong, 1998). They are

*Type I* isotherm where the isotherm is concave to the relative pressure ( $p/p^o$ ) axis. It rises sharply at low relative pressures and reaches a plateau as  $p/p^o$  approaches 1.

*Type II* isotherm where the isotherm is concave to the  $p/p^o$  axis, then increases almost linearly and finally convex to the  $p/p^o$  axis. It indicates the formation of an adsorbed layer whose thickness increases progressively with increasing relative pressure until  $p/p^o$  approaches 1. When the equilibrium pressure equals the saturation vapor pressure, the adsorbed layer becomes a condensed bulk liquid. If the knee of the isotherm (point B) is sharp, the uptake at point B is usually considered to represent the completion of the monomolecular layer (monolayer) and the beginning of the formation of the multimolecular layer (multilayer) adsorption. The ordinate of point B gives an estimation of the amount of adsorbate required to cover the unit mass of solid surface with a complete monomolecular layer (monolayer capacity). Type II isotherms are obtained with non-porous or macroporous adsorbents, which allow unrestricted monolayer-multilayer adsorption to occur at high  $p/p^o$ .

*Type III* isotherm where the isotherm is convex to the  $p/p^0$  axis and therefore showing no point B. This feature is indicative of weak adsorbent-adsorbate interactions.

*Type IV* isotherm is similar to Type II isotherm but with the presence of a hysteresis loop. The lower branch of loop represents measurements obtained by progressive addition of gas on the adsorbent, and the upper branch by the progressive withdrawal (desorption). The hysteresis loop is usually associated with the filling and emptying of the mesopore by capillary condensation. Type IV isotherms are common but the exact shape of the hysteresis loop varies from one system to another.

*Type V* isotherm is similar to Type III isotherm but exhibits a hysteresis loop which is associated with the mechanism of pore filling and emptying. This isotherm is relatively rare.

*Type VI* isotherm, or stepped isotherm, is also relatively rare and is associated with layer-by-layer adsorption on a highly uniform surface. The sharpness of the steps is dependent on the adsorption system and the temperature.

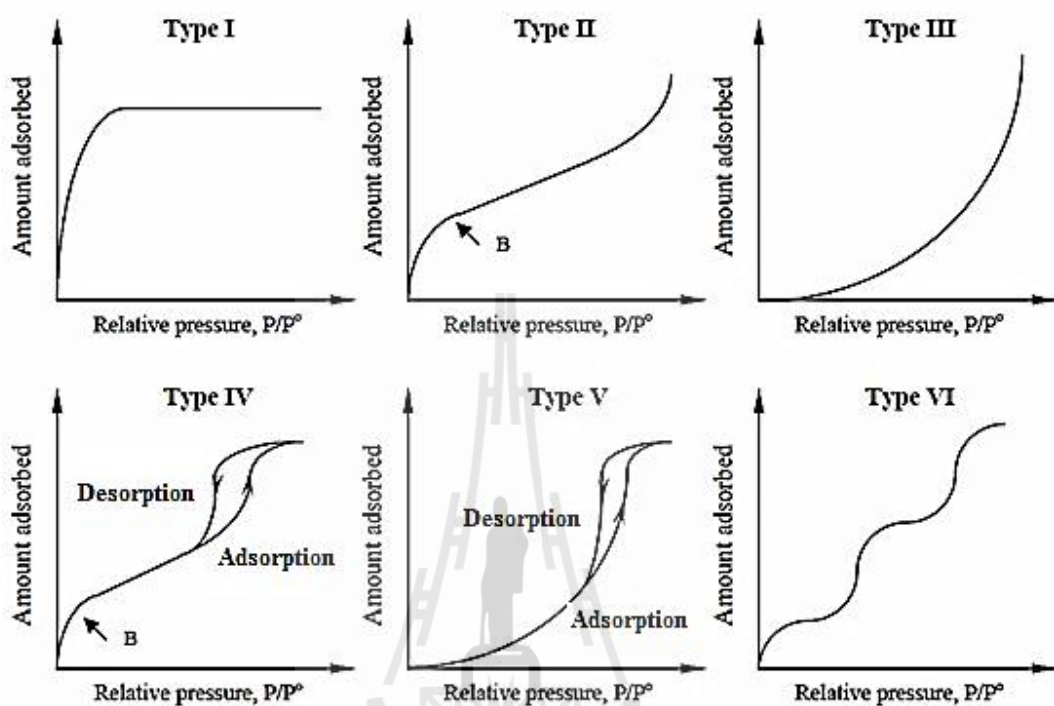


**Figure 3.2** Classification of adsorption isotherms (Do Duong, 1998).

### 3.3.3 Adsorption isotherm equations

The quantity of adsorbate that can be taken up by an adsorbent is a function of both the characteristics and concentration of adsorbate and the temperature. Generally, the amount of material being adsorbed at equilibrium is determined as a function of the adsorbate concentration in the bulk fluid at a constant temperature, and the resulting function is called an adsorption isotherm. Normally, the bulk adsorbate concentration at equilibrium is symbolized by  $C_e$  (mass/volume) and relative pressure ( $P/P^0$ ) for the liquid and gas adsorption system, respectively.

The following isotherm equations are commonly used to describe the experimental isotherm data and are briefly discussed here.

### 3.3.3.1 Linear isotherm

This is the simplest adsorption isotherm that is applied for adsorption in a relatively low concentration region. The linear correlation of the concentrations in the fluid phase and the adsorbed phase inside the particle is expressed by

$$q = K_H C_e \quad (3.1)$$

where

$q$  = concentration of adsorbate in the solid phase or adsorbed phase

$C_e$  = concentration of adsorbate in the fluid phase

$K_H$  = equilibrium distribution coefficient or Henry constant

### 3.3.3.2 Langmuir adsorption isotherm

The Langmuir adsorption isotherm was developed based on the monolayer adsorption of gas on a flat surface based on the following assumptions (Do Duong, 1998):

1. The surface of the adsorbent is uniform, that is, the adsorption energy is constant independent of adsorption loading.
2. No interaction among the adsorbed molecules.
3. Each adsorbed molecule occupies only one site and the adsorption is localized.

The Langmuir theory is based on a kinetic principle, that is, the rate of adsorption (which is the striking rate at the surface multiplied by a sticking coefficient, sometime called the accommodation coefficient) is equal to the rate of desorption from the surface.

The rate of striking the surface, in mole per unit time and unit area, obtained from the kinetic theory of gas is:

$$R_s = \frac{P}{\sqrt{2\pi MR_g T}} \quad (3.2)$$

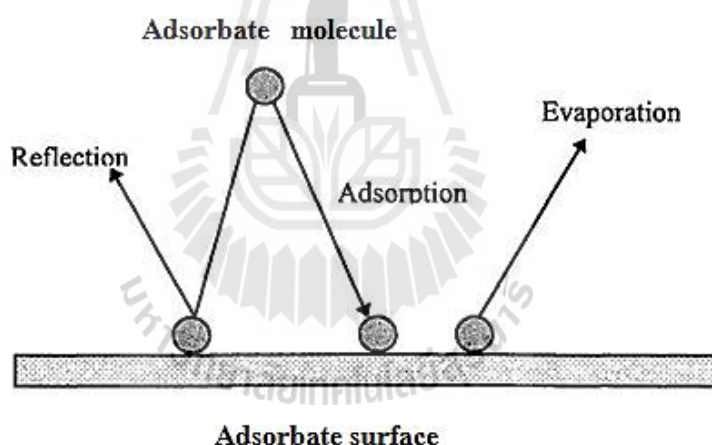


**Figure 3.3** Schematic diagram of Langmuir adsorption mechanism on a flat surface. (Moradi, 2011).

A fraction of gas molecules striking the surface will condense and is held by the surface force until these adsorbed molecules evaporate again (see **Figure 3.3**). Langmuir (1918) quoted that there is good experimental evidence that this



fraction is unity, but for a real surface which is usually far from ideal this fraction could be much less than unity. Allowing for the sticking coefficient (which accounts for non-perfect sticking), the rate of adsorption in mole adsorbed per unit bare surface area per unit time is

$$R_a = \frac{\alpha P}{\sqrt{2\pi MR_g T}} \quad (3.3)$$

Therefore, the rate of adsorption on an occupied surface is equal to the rate given by **Equation (3.3)** multiplied by the fraction of empty sites, that is:

$$R_a = \frac{\alpha P}{\sqrt{2\pi MR_g T}} (1 - \theta) = k_a P (1 - \theta) \quad (3.4)$$

where  $\theta$  is the fractional coverage of molecules on the surface and  $k_a$  is the rate constant of adsorption.

The rate of desorption from the surface is equal to the rate of evaporation, which corresponds to fully covered surface ( $k_d$ ), multiplied by the fractional coverage, that is

$$R_d = k_d \theta = k_{d\infty} \exp\left(-\frac{E_d}{R_g T}\right) \theta \quad (3.5)$$

where  $E_d$  is the activation energy for desorption and  $k_{d\infty}$  is the rate constant for desorption at infinite temperature.

Equating the rate of adsorption and desorption (**Equation 3.4 and 3.5**), we obtain the following famous Langmuir isotherm written in terms of fractional loading:

$$\theta = \frac{bP}{1 + bP} \quad (3.6)$$

where

$$b = \frac{k_a}{k_d} = \frac{\alpha \exp(Q/R_g T)}{k_{d\infty} \sqrt{2\pi MR_g T}} = b_{\infty} \exp(Q/R_g T) \quad (3.7)$$

Q is the heat of adsorption and is equal to the activation energy for desorption,  $E_d$ , and parameter b is called the affinity constant or Langmuir constant.

The Langmuir isotherm can also be applied for liquid system and is written as,

$$\theta = \frac{q}{q_m} = \frac{bC_e}{1 + bC_e} \quad (3.8)$$

where

$q$  is the adsorbed amount at equilibrium,

$q_m$  is the maximum amount adsorbed or monolayer capacity,

$C_e$  is the adsorbate concentration in the solution at equilibrium

The constants in the Langmuir equation ( $q_m$  and b) can be determined from **Equation 3.8** by plotting  $C_e/q$  versus  $C_e$ , making use of the following linear form,

$$\frac{C_e}{q} = \frac{1}{q_m b} + \frac{C_e}{q_m} \quad (3.9)$$

where slope (S) =  $\frac{1}{q_m}$ , y - intercept (I) =  $\frac{1}{q_m b}$ ,

$$\text{giving } q_m = \frac{1}{S} \text{ and } b = \frac{S}{I}$$

### 3.3.3.3 Freundlich adsorption isotherm

Freundlich adsorption isotherm is popularly used in the description of monolayer adsorption in gas and liquid phase systems provided the range of fluid phase concentration is not too wide. It is obtained based on the assumption that the adsorption takes place on a heterogeneous surface, that is, the adsorption energy of adsorbent-adsorbate interaction is distributed (not constant). Adsorption sites having the same adsorption energy are grouped into one patch and there is no interaction between each patch. Each adsorbate molecule in each patch occupies only one adsorption site (monolayer adsorption). The isotherm equation does not have a proper Henry law behavior at low concentration, and it does not have a finite limit when the concentration is sufficiently high. Therefore, it is generally valid in the narrow range of the adsorption data (Do Duong, 1998).

The empirically derived Freundlich isotherm is as follows,

$$q = K_F C_e^{1/n_F} \quad (3.10)$$

where  $q$  is the adsorbed amount of adsorbate at equilibrium,  $C_e$  is the adsorbate concentration in the bulk fluid, and  $K_F$  and  $n_F$  are Freundlich constants for each adsorbent-adsorbate system

The constants in the Freundlich isotherm can be determined by plotting  $(q)$  versus  $C_e$  on a log-log scale, using the following equation.

$$\log q = \log K_F + \frac{1}{n_F} \log C_e \quad (3.11)$$

where

$$\text{slope (S)} = \frac{1}{n_F}, \quad \text{y - intercept (I)} = \log(K_F),$$

giving

$$n_F = \frac{1}{S} \quad \text{and} \quad K_F = 10^I$$

### 3.3.3.4 Sips adsorption isotherm

Sips adsorption isotherm is another empirical adsorption equation that is widely used for the interpretation of adsorption data. Sips (1948) proposed an equation similar in form to the Freundlich equation, but it has a finite limit when the pressure is sufficiently high. This model which contains three constants ( $q_m$ ,  $K_s$  and  $n_s$ ) can be considered as a combination of Langmuir and Freundlich equation, and is represented for a gas system by

$$q = \frac{q_{ms} (K_s P / P_0)^{1/n_s}}{1 + (K_s P / P_0)^{1/n_s}} \quad (3.12)$$

The difference between this equation and the Langmuir equation is the additional parameter “ $n_s$ ” in the Sips equation. If this parameter “ $n_s$ ” is unity, we recover the Langmuir equation that is applicable for an ideal surface. Hence the parameter “ $n_s$ ” could be regarded as the parameter characterizing the surface heterogeneity. The parameter “ $n_s$ ” is usually greater than unity, and therefore the larger is this parameter the more heterogeneous is the surface.

**Equation 3.12** can be applied to a liquid system from which the pressure  $P$  and  $P_0$  in the equation are replaced with solute concentration ( $C_e$ ) and solute solubility ( $C_s$ ), respectively, to give

$$q = \frac{q_{ms} (K_s C_e)^{1/n_s}}{1 + (K_s C_e)^{1/n_s}} \quad (3.13)$$

### 3.3.3.5 Brunauer-Emmett-Teller (BET)

In 1938, Brunauer et al. (Brunauer et al., 1938) first developed the BET theory for gas adsorption on a flat surface with no limit in the number of layers that can be accommodated on the surface. The surface is energetically homogeneous (adsorption energy does not change with the progress of adsorption in the same layer) and there is no interaction among the adsorbed molecules. The BET equation is an extension of Langmuir equation for multilayer adsorption and the equation reads

$$\theta = \frac{q}{q_m} = \frac{CP}{(P_0 - P)[1 + (C - 1)(P/P_0)]} \quad (3.14)$$

where  $P$  is the pressure of gas adsorbed,  $P_0$  is the saturation vapor pressure of gas adsorbed at the temperature of adsorption,  $q$  is the amount of gas adsorbed at pressure  $P$ ,  $q_m$  is the monolayer amount adsorbed,  $C$  is the nondimensional constant, and  $\theta$  is the fractional coverage of the surface.

When applied to a liquid system, the pressure  $P$  and  $P_0$  in the above equation are replaced with solute concentration ( $C_e$ ) and solute solubility ( $C_s$ ), respectively. **Equation 3.14** is used extensively for the determination of specific surface area of the adsorbent, when the monolayer coverage  $q_m$  and the area occupied by one adsorbate molecule are known.

The pressure range of validity of the BET equation covers the relative pressure ( $P/P_0$ ) from 0.05 - 0.3. For relative pressures above 0.3, there exists capillary condensation, which is not amenable to multilayer analysis. A plot of  $(P/(V(P_0 - P)))$  versus  $P/P_0$  would yield a straight line with a slope  $((C-1)/CV_m)$  and an intercept  $(1/CV_m)$ , according to the following linear form of BET equation,

$$\frac{P}{V(P_0 - P)} = \frac{1}{CV_m} + \frac{(C-1)}{CV_m} \frac{P}{P_0} \quad (3.15)$$

Once  $q_m$  in mol/g is obtained from the slope, the surface area ( $A$ ,  $m^2/g$ ) is calculated from:

$$A = V_m N_A a_m \quad (3.16)$$

where  $N_A$  is the Avogadro number and  $a_m$  is the molecular project area, for example, for nitrogen  $a_m$  is equal to  $16 \text{ \AA}^2/\text{molecule}$  at 77 K (Do Duong, 1998). **Table 3.3** summarizes the form and assumptions associated with the previously mentioned isotherm equations.

**Table 3.3** Frequently used single-component adsorption models in gas phase that can be applied to liquid phase adsorption (Do Duong, 1998).

Isotherm	Equation	Assumption/ Advantage or disadvantage
Henry	$q = K_H P$	<ul style="list-style-type: none"> <li>• Simple and linear form</li> </ul>
Langmuir	$q = \frac{b q_m P}{1 + b P}$	<ul style="list-style-type: none"> <li>• A uniform surface and constant temperature</li> <li>• Monolayer adsorption</li> <li>• Interpretable parameters</li> <li>• A good representation of chemisorption</li> </ul>
Freundlich	$q = K P^{1/n_F}$	<ul style="list-style-type: none"> <li>• Power's law model</li> </ul>
Sips	$q = \frac{q_{mS} (K_S C P)^{1/n_s}}{1 + (K_S C P)^{1/n_s}}$	<ul style="list-style-type: none"> <li>• Combining Langmuir and Freundlich model</li> </ul>

**Table 3.3** Frequently used single-component adsorption models in gas phase that can be applied to liquid phase adsorption (continued) (Duong D. Do, 1998).

<b>Isotherm</b>	<b>Equation</b>	<b>Assumption/ Advantage or disadvantage</b>
Brunauer- Emmett- Teller (BET)	$\frac{q}{q_m} = \frac{CP}{(P_0 - P)[1 + (C - 1)(P/P_0)]}$	<ul style="list-style-type: none"> <li>• An extension of the Langmuir relationship</li> <li>• Multilayer adsorption</li> <li>• enthalpy of adsorption is the same for any layer</li> <li>• energy of adsorption is the same for layers other than the first</li> <li>• A new layer can start before another is finished</li> </ul>

### 3.3.4 Adsorption models of mixtures

Due to the time consuming problem in the measurement of multicomponent mixture adsorption, the prediction of multicomponent equilibria from single component isotherms has received considerable attention. The adsorption theories and models have been developed especially for gas mixture adsorption which can be categorized into three approaches, namely kinetic models, thermodynamics models and potential-theory models (Parida et al., 2006). Only the first two approaches will be used for the adsorption analysis in the present work and are briefly presented as follows.



### 3.3.4.1 Kinetic Approach

#### -Extended Langmuir equation

The Langmuir isotherm equation for single-gas adsorption can be readily extended to binary or multicomponent mixtures.

The adsorption rate of species  $i$  onto the adsorbent surface is

$$R_{a,i} = k_{a,i} P_i (1 - \sum_{i=1}^N \theta_i) \quad (3.17)$$

where  $\theta_i$  is the fractional coverage of species  $i$  and  $k_{a,i}$  is the rate constant for adsorption of species  $i$

The rate of desorption of species  $i$  is proportional to the fractional loading, that is

$$R_{d,i} = k_{d,i} \theta_i \quad (3.18)$$

**Equating (3.17) and (3.18)** for condition at equilibrium to give

$$b_i P_i (1 - \theta_T) = \theta_i \quad (3.19)$$

where  $R_i = \frac{k_{a,i}}{k_{d,i}}$  and  $\theta_T = \sum_{i=1}^N \theta_i$

Summing **Equation (3.19)** for all species, we obtain the total fractional coverage in terms of partial pressure. Thus

$$\theta_T = \frac{\sum_{i=1}^N b_i P_i}{1 + \sum_{i=1}^N b_i P_i} \quad (3.20)$$

or in terms of functional unoccupied sites,

$$1 - \theta_T = \frac{1}{1 + \sum_{i=1}^N b_i P_i} \quad (3.21)$$

Combining **Equations (3.19) and (3.21)**, we obtain the fractional coverage for the adsorption of species  $i$  as

$$\theta_i = \frac{q_i}{q_T} = \frac{b_i P_i}{1 + \sum_{i=1}^N b_i P_i} \quad (3.22)$$

where  $q_{mi}$  is the monolayer capacity of species  $i$  in the mixture.

**Equation (3.22)** is known as “extended Langmuir isotherm equation”. It should be noted that in order to meet the thermodynamic consistency, it requires that the monolayer capacity is the same for all species, that is,

$$q_i = q_j = q_m \quad (3.23)$$

For a binary gas mixture, we have

$$\theta_1 = \frac{q_1}{q_{m1}} = \frac{b_1 P_1}{1 + b_1 P_1 + b_2 P_2} \quad (3.24)$$

and

$$\theta_2 = \frac{q_2}{q_{m2}} = \frac{b_2 P_2}{1 + b_1 P_1 + b_2 P_2} \quad (3.25)$$

For liquid adsorption, the extended Langmuir isotherm is written as

$$q_1 = \frac{q_{m1} b_1 C_1}{1 + b_1 C_1 + b_2 C_2} \quad (3.26)$$

and

$$q_2 = \frac{q_{m2} b_2 C_2}{1 + b_1 C_1 + b_2 C_2} \quad (3.27)$$

where  $C_1$  and  $C_2$  are equilibrium adsorbate concentration of component 1 and 2 in the liquid phase.

- **Extended Langmuir-Freundlich isotherm**

As in the case of extended Langmuir equation for multicomponent mixtures, the mixed Langmuir-Freundlich equation for pure-component adsorption can also be extended to multicomponent systems and the equation reads

$$\theta_i = \frac{q_i}{q_{mi}} = \frac{b_i P_i^{1/n_i}}{1 + \sum_{i=1}^N b_i P_i^{1/n_i}}, \text{ for gas adsorption} \quad (3.28)$$

and

$$\theta_i = \frac{q_i}{q_{mi}} = \frac{b_i C_i^{1/n_i}}{1 + \sum_{i=1}^N b_i C_i^{1/n_i}}, \text{ for liquid adsorption} \quad (3.29)$$

where the parameters  $n_i$  indicate the surface heterogeneity for the adsorption of species  $i$ .

If lateral interactions exist among the adsorbed molecules, the equation is modified by incorporating a lateral interaction parameters,  $\eta_i$ , to obtain

$$\theta_i = \frac{q_i}{q_{mi}} = \frac{(b_i / \eta_i) P_i^{1/n_i}}{1 + \sum_{i=1}^N (b_i / \eta_i) P_i^{1/n_i}}, \text{ for gas adsorption} \quad (3.28)$$

and

$$\theta_i = \frac{q_i}{q_{mi}} = \frac{(b_i/\eta_i)C_i^{1/n_i}}{1 + \sum_{i=1}^N (b_i/\eta_i)C_i^{1/n_i}}, \text{ for liquid adsorption} \quad (3.29)$$

### 3.3.4.2 Thermodynamic approach

Realizing the shortcoming of the extended Langmuir equation and the empiricism of the extended Langmuir-Freundlich isotherm equation, the analysis of multicomponent mixture adsorption has been attempted using thermodynamic approaches which include, the ideal adsorbed solution theory of Myers and Prausnitz (Myers and Prausnitz, 1965) (IAST), the real adsorbed solution theory (RAST) and the vacancy solution model (VSM).

Of these thermodynamic models, the IAST has been successfully used for a number of gaseous mixtures (Hand et al., 1985) (Hand et al., 1985; Wang et al., 2008) and will be applied for the prediction of adsorption equilibrium of a binary metal ion system in the present study.

The IAST considers the mixed adsorbates as an ideal solution in equilibrium with the bulk gas phase and the basic thermodynamic relationships for liquids are applied to the adsorbed phase. The adsorbed phase is viewed as a two dimensional surface with surface area  $A$  and pressure  $\Pi$ , called spreading pressure, which are equivalent to volume  $V$  and pressure  $P$  of the bulk gas phase. Spreading pressure ( $\Pi$ ) is considered as the change in surface energy due to adsorption analogous to a monomolecular film at the gas-liquid interface.

The ideal adsorbed solution theory contains a set of equations as follows.

1. At equilibrium, the chemical potential for each adsorbed species is equal to that in the gas phase so that it can be shown that,

$$Py_i = P_i^o(\pi)x_i, \quad i = 1, 2, \dots, N \quad (3.32)$$

where

$P$  = total pressure of the gas phase

$x_i, y_i$  = mole fraction of adsorbed species  $i$  in the adsorbed phase and in the gas phase, respectively.

$P_i^o(\Pi)$  = equilibrium “vapor pressure” or hypothetical pressure of pure component  $i$  at the same spreading pressure ( $\Pi$ ) and the same temperature ( $T$ ) as the adsorbed mixture.

2. The surface potential of the adsorbed mixture is the same as the surface potential of all pure components, leading to the following relation

$$\frac{\phi_m}{R_g T} = \frac{\phi_i^o}{R_g T} = - \int_0^{P_i^o} \frac{q_i^o}{P_i^o} dP_i^o = \frac{\pi A}{R_g T} \quad (3.33)$$

where

$\phi_m$  = surface potential of gas mixture

$\phi_i^o$  = surface potential of pure component  $i$

$q_i^o$  = equilibrium adsorbed-phase concentration of pure component  $i$  which can be obtained from isotherm data of pure component adsorption

$P_i^o$  = pressure of the gas phase in the pure component adsorption of species i

3. Based on the condition of an ideal adsorbed phase that there is no change in the specific adsorption area upon mixing of various adsorbed species in the adsorbed phase, the following relationship is obtained

$$\frac{1}{q_t} = \sum_{i=1}^N \frac{x_i}{q_i^o} \quad (3.34)$$

where  $q_t$  is the total amount adsorbed and  $x_i$  is the mole fraction of species i in the adsorbed phase

4. The amount of adsorption of species i is given by

$$q_i = q_t x_i \quad (3.35)$$

5. Mass balance give

$$\sum x_i = \sum y_i = 1 \quad (3.36)$$

where  $y_i$  is the mole fraction of adsorbed species i in the gas phase.

It is seen that we have  $(2N+1)$  equations from the IAST, that is, N equation from Eq. (3.32), N-1 equations from Eq. (3.33), 1 equation from Eq. (3.34) and 1 equation from Eq. (3.36), but there are  $3N+2$  unknowns to be determined which include 1 unknown for P, N unknown for  $P_i^o$ , N unknown for  $x_i$ , N unknown for  $y_i$  and 1

unknown for  $q_t$ . Generally, we can specify the system total pressure ( $P$ ) and a set of mole fraction in the gas phase ( $y_i$ ). As a result, the number of unknowns now reduces to  $(2N+1)$  unknowns which are equal to the number of the available equations and thus all other unknowns can now be directly solved.

### 3.3.5 Isosteric heat of adsorption

The adsorption of an adsorbate on a solid surface is generally associated with the liberation of heat, resulting from adsorbent-adsorbate interaction. The equation used for the estimation of heat of adsorption from adsorption isotherms is the well-known van't Hoff equation for gas adsorption which reads

$$\frac{\Delta H^{st}}{R_g T^2} = \left( \frac{\partial \ln P}{\partial T} \right)_\theta \quad (3.37)$$

where  $\Delta H$  is the isosteric enthalpy of adsorption or isosteric heat of adsorption,  $R_g$  is the gas constant,  $T$  is the absolute temperature,  $P$  is the pressure and  $\theta$  is the fractional coverage representing a fixed amount of adsorbate being adsorbed.

Thus, the isosteric heat of adsorption can be obtained directly from **Equation 3.37** by determining the slope of a plot of  $\ln P$  versus  $T$  as a function of surface coverage ( $\theta$ ). Alternatively, it can be determined from the linear plot ( $\ln P$  versus  $1/T$ ) of the integral form of **Equation (3.37)**, as shown in **Equation (3.38)**.



$$(\ln P)_\theta = -\frac{\Delta H^{st}}{R_g T} + c \quad (3.38)$$

where  $c$  is the constant

For liquid adsorption, van't Hoff equation is expressed as

$$\frac{\Delta H^{st}}{R_g T^2} = \left( \frac{\partial \ln C_e}{\partial T} \right)_\theta \quad (3.39)$$

or

$$\Delta H^{st} = R_g \left( \frac{-\partial \ln C_e}{\partial (1/T)} \right)_\theta \quad (3.40)$$

where  $C_e$  is the adsorbate concentration in the liquid phase.

### 3.3.6 Adsorption kinetics

Apart from adsorption equilibrium data, information on the kinetics of adsorption is also significant for evaluating the performance of a given adsorbent and gaining insight into the underlying adsorption mechanisms. There have been a number of studies available in the literature concerning adsorption kinetics and some of the commonly used kinetic models for data analysis are presented as follows.

#### 3.3.6.1 Pseudo-first-order rate equation

Lagergren (1898) presented a first-order rate equation to describe the kinetic process of liquid-solid phase adsorption, which is believed to be the earliest

model pertaining to the adsorption rate based on the adsorption capacity. It is represented by the following equation.

$$\frac{dq_t}{dt} = k_{p1}[q_e - q_t] \quad (3.41)$$

where  $q_e$  and  $q_t$ (mmol/g) are the adsorption capacities at equilibrium and time  $t$  (min), respectively.  $k_{p1}$  ( $\text{min}^{-1}$ ) is the pseudo-first-order rate constant for the kinetic model.

Integrating **Equation 3.41**, with the boundary conditions of  $q_t=0$  at  $t=0$  and  $q_t=q_t$  at  $t=t$ , yields

$$\ln\left(\frac{q_e}{q_e - q_t}\right) = k_{p1}t \quad (3.42)$$

which can be rearranged to

$$\log(q_e - q_t) = \log q_e - \frac{k_{p1}}{2.303}t \quad (3.43)$$

In recent years, pseudo-first-order equation has been widely used to describe the adsorption of pollutants from wastewater in different fields, such as the adsorption of methylene blue from aqueous solution by broad bean peels and the removal of malachite green from aqueous solutions using oil palm trunk fiber(Hameed, 2008).

### 3.3.6.2 Pseudo-second-order rate equation

In 1998, Ho described a kinetic process of the adsorption of divalent metal ions onto peat (Ho and McKay, 1998)in which the chemical bonding among divalent metal ions and polar functional groups on peat, such as aldehydes,

ketones, acids, and phenolics are responsible for the cation-exchange capacity of the peat. As a result, the peat-metal reaction may be presented as shown in **Equation (3.44) and (3.45)**, which can be dominant in the adsorption of  $\text{Cu}^{2+}$  ions onto peat (Coleman *et al.*, 1956):



and



where  $\text{P}^-$  and HP are active sites on the peat surface.

The main assumptions for the above two equations were that the adsorption may be second-order, and the rate limiting step may be chemical adsorption involving valent forces through sharing or the exchange of electrons between the peat and divalent metal ions. In addition, the adsorption was assumed to follow the Langmuir equation (Ho and McKay, 2000).

The rate of adsorption described by **Equation (3.44) and (3.45)** is dependent upon the amount of divalent metal ions on the surface of peat at time  $t$  and that adsorbed at equilibrium. Therefore the rate expression may be given as (Ho and McKay, 1998).

$$\frac{d(P)_t}{dt} = k_{p2}[(P)_0 - (P)_t]^2 \quad (3.46)$$

or

$$\frac{d(HP)_t}{dt} = k_{p2}[(HP)_0 - (HP)_t]^2 \quad (3.47)$$

where  $(P)_0$  and  $(HP)_0$  denote the amount of equilibrium sites available on the peat,  $(P)_t$  and  $(HP)_t$  denote the amount of active sites occupied on the peat at time  $t$ , and  $k_{p2}$  (g/(mg·min)) is the pseudo-second-order rate constant of adsorption

The amount adsorbed on the active sites, is proportional to the available fraction of active sites (Ho and McKay, 1998). Then, **Equation 3.44** can be written as

$$\frac{dq_t}{dt} = k_{p2}[q_e - q_t]^2 \quad (3.48)$$

**Equation 3.48** can be rearranged as follows:

$$\frac{dq_t}{(q_e - q_t)^2} = k_{p2} dt \quad (3.49)$$

Integrating **Equation 3.49**, with the boundary conditions of  $q_t=0$  at  $t=0$  and  $q_t=q_t$  at  $t=t$ , yields

$$\frac{1}{(q_e - q_t)} = \frac{1}{q_e} + k_{p2}t \quad (3.50)$$

which can be rearranged to give:

$$\frac{t}{q_t} = \frac{1}{V_0} + \frac{1}{q_e}t \quad (3.51)$$

with

$$V_0 = k_{p2}q_e^2 \quad (3.52)$$

where  $V_0$  (mg/(g·min)) means the initial adsorption rate, and the constants ( $k_{p2}$  and  $q_e$ ) can be determined experimentally by plotting of  $t/q_t$  against  $t$ .

Similarly, Ho's second-order rate equation has been called pseudo-second-order rate equation to distinguish the kinetic equations based on adsorption capacity from the concentration of solution (Ho and McKay, 1998).. This equation has been successfully applied to the adsorption of metal ions, dyes, herbicides, oils, and organic substances from aqueous solutions (Yan and Viraraghavan, 2003; Al-Ashehet *al.*, 2004).

### 3.3.6.3 Intraparticle diffusion or pore diffusion model

A typical intraparticle diffusion model is the so-called homogeneous solid diffusion model (HSDM) (Cooney, 1999). The HSDM equation can be presented as

$$\frac{\partial q_t}{\partial t} = \frac{D_e}{r^2} \frac{\partial}{\partial r} \left( r^2 \frac{\partial q_t}{\partial r} \right) \quad (3.53)$$

where  $D_e$  is intraparticle diffusion coefficient,  $r$  is the radial position of a spherical adsorbent,  $q_t$  is the adsorption quantity of solute in the adsorbed phase which varies with radial position and time  $t$ . This mass balance equation neglects the accumulation term of adsorbate in the pore space of the adsorbent particle.

The average value of  $q$  in a spherical particle at any particular time, defined as  $\bar{q}$ , can be determined from the following equation:

$$\bar{q} = \frac{3}{R^3} \int_0^R q(r) r^2 dr \quad (3.54)$$

where  $q(r)$  is the local value of the solid-phase concentration and  $R$  is the particle radius.

The following solution equation can be finally obtained

$$\frac{\bar{q}}{q_\infty} = 1 - \frac{6}{\pi^2} \sum_{n=1}^{\infty} \frac{1}{n^2} \exp\left(\frac{-D_e n^2 \pi^2 t}{R^2}\right) \quad (3.55)$$

where  $q_\infty$  represents the average concentration in the solid at infinite time or at equilibrium ( $q_e$ ).

For a short adsorption time, when  $\frac{\bar{q}}{q_\infty} < 0.3$ , **Equation 3.55** can be simplified to yield

$$\frac{\bar{q}}{q_\infty} = 6 \left( \frac{D_e}{R^2 \pi} \right)^{1/2} t^{1/2} \quad (3.56)$$

For a long time ( $\frac{\bar{q}}{q_\infty} > 0.7$ ), only the first term of the summation in **Equation 3.55** is important, therefore we have

$$\frac{\bar{q}}{q_\infty} = 1 - \frac{6}{\pi^2} e^{-\pi^2 D_e t / R_p^2} \quad (3.57)$$

The linearization of **Equation 3.57** gives

$$\ln \left( 1 - \frac{\bar{q}}{q_\infty} \right) = \frac{-D_e \pi^2}{R^2} t + \ln \frac{6}{\pi^2} \quad (3.58)$$

The value of  $D_e$  from long-time adsorption data can be determined by plotting of  $\ln \left( 1 - \frac{\bar{q}}{q_\infty} \right)$  versus  $t$  and the slope of straight line determined.

### 3.3.7 Surface property of silica

Silica porous glass is mostly composed of  $\text{SiO}_2$  and the detection of surface of porous glass is in effect the same as those of silica surface. In previous study, J. Nawrocki and B. Buszewski (1988) showed that some of the properties of silica can be explained by different reactivities of the various silanol adsorption sites. The

silanol or hydroxyl groups (Si-OH) are the key elements to determine the adsorption and diffusion behavior of guest molecules on the surfaces. Furthermore, silanols exist not only as chemical compounds but also on the surface of silica. Their presence is responsible for the adsorption properties, for example, derivitization of accessible silanol groups in a bonded stationary phase with trimethylsilyl groups is referred to as endcapping in chromatography system. In recent study, Wu Chen (2009) showed that a typical silica surface of porous silica microspheres with organosilane modified surfaces can be represented as in **Figure 3.4**. The Si atom shows tetrahedral coordination, with oxygen atoms, hydroxide group (OH) and organosilane functional group (R) surrounding a central Si atom.

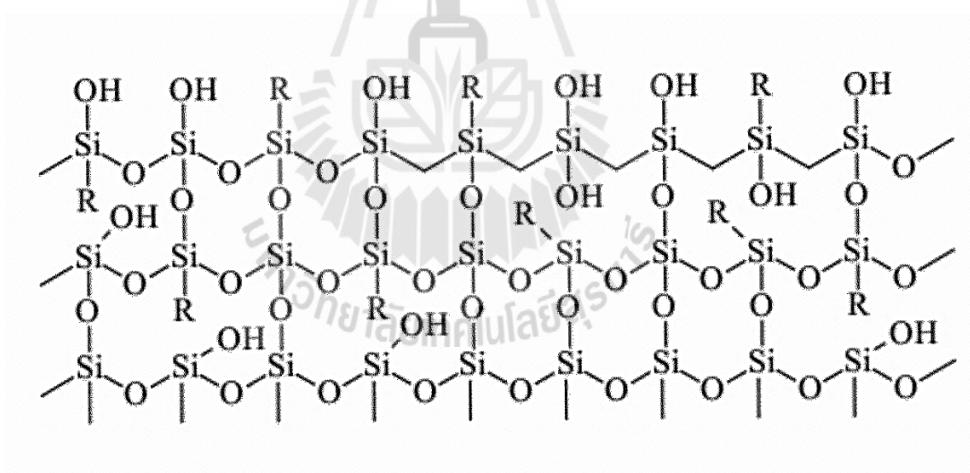


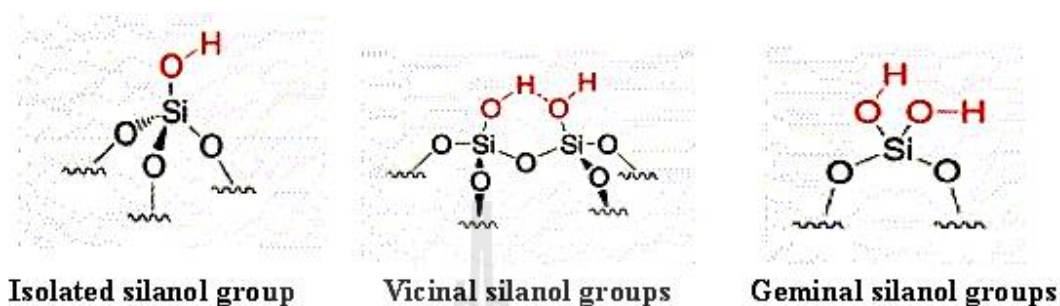
**Figure 3.4** Graphical representation of porous silica surface (Wu Chen, 2009).

### 3.3.7.1 Surface silanol (Si-OH)

As in **Figure 3.5**, silanol group on the surface of porous glass can be classified into three types, namely isolated silanol groups, vicinal silanol group (paired



type) where silanol groups can form hydrogen bonds with each other and geminal silanol groups where two hydroxyls sit on the same Si atom.



. **Figure 3.5** Type of silanol groups on the surface of porous glass (R. Chanajaree, 2006).

### 3.3.7.2 Surface modification

Surface modification of porous glass is of significance because it could affect the adsorption capacity and selectivity. The modification results in products with new functional groups on their surface that is capable of interaction with a number of adsorbates. For example, the presence of aminosilane ( $R-NH_2$ ) is capable of reacting with carbonyl groups of aldehydes, ketones, esters, amine groups as well as with halides, multiple bonds  $C=C$ , epoxy bridges, etc. Aminosilane molecules may interact with silica surface silanol groups in various ways (Van Der Voort and Vansant, 1997), as illustrated in **Figure 3.6**. In addition, the increasingly hydrophilic surface of silica, as modified with various aminosilane types, reflects the ability of amine groups to form hydrogen bonds with silanol groups (hydroxy groups) of silica surface or  $Si-OH$  groups in molecules of the hydrolyzed silane.

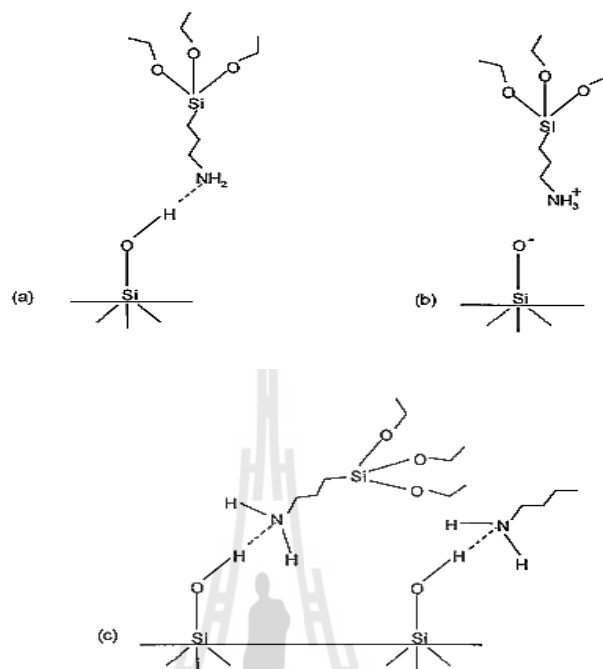


**Figure 3.6** Three types of interactions between an aminosilane molecule and silica surface: a) hydrogen bonds (H-N), b) proton transfer, c) condensation with silanol groups. (A. Krysztafkiewicz and S. Binkowski, 1995).

According to Ishida and Koenig and Chiang et al. (1982) the silica surface, modified with, for example, 3-aminopropyltriethoxysilane, may be presented as shown in **Figure 3.7**. Aminosilane-modified silicas find multiple applications in industries. They can be used as fillers of several polymers, in particular of polyurethanes and polyamides. With increasing frequency they are used as coupling agents in combination with organic pigments (e.g. those containing azo groups). The water soluble organic pigments can be transformed to water insoluble systems following adsorption on a modified silica surface (Simonin et al., 1995).

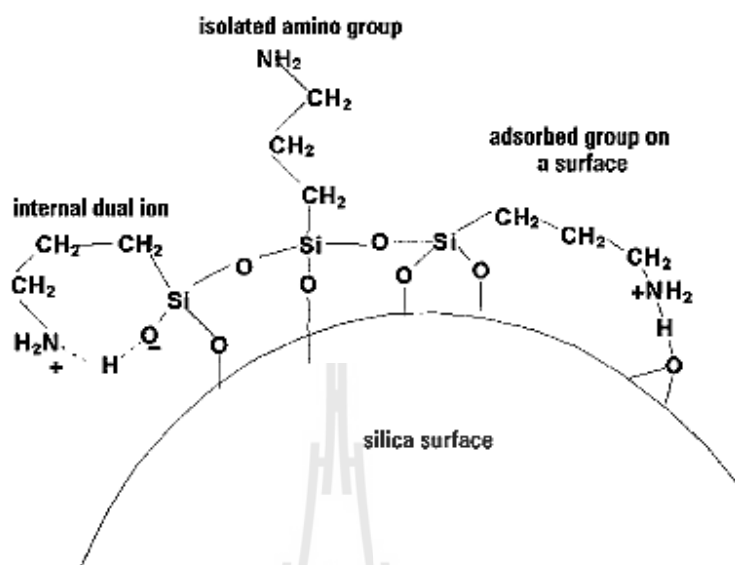


**Figure 3.7** Groups on silica surface following modification with 3 - aminopropyltriethoxysilane. (A. Krysztafkiewicz and S. Binkowski, 1995).

There is a growing interest in the metal ions adsorption of mesoporous materials, especially on silica surface. The report of selective metal ions adsorption using 3-aminopropyltriethoxysilane and mercaptopropyl grafting on surface are briefly presented as follows.

Mahitti P. and Fuangfa U. (2006) studied adsorption of Hg(II) ion by modified MCM-41 (mesoporous adsorbent of silica). The modified MCM-41 is obtained by grafting 2-(3-(2-aminoethylthio)propylthio) ethanamine onto the silica surface. 3-aminopropyltriethoxysilane was first immobilized onto the silica via reaction with silanol groups on the surface followed by ethyl-2-bromopropionate and 2-(3-(2-

amino ethylthio)propylthio)ethanamine, respectively. The results indicate that the structure of the reagents affects the adsorption behavior. These reagents show potential for the application as effective and selective adsorbents for Hg(II) removal from water.

Koon et al. (2006) studied the adsorption of  $\text{Cr}_2\text{O}_7^{2-}$  and  $\text{Cu}^{2+}$  by modified MCM-41. The modified MCM-41s were prepared by grafting aminopropyl and propionates on the pore wall of mesoporous silica. The MCM-41 adsorbent containing aminopropyls,  $\text{NH}_2\text{-MCM-41}$ , was prepared by refluxing of 2.5 g MCM-41 powder in 250 ml dry toluene (>99.5%, Mallinckrodt) containing 0.4 M 3-aminopropyltriethoxysilane (97%, Aldrich) for 18 h. The  $\text{NH}_2\text{-MCM-41}$  powder was filtered, washed with toluene and dried in an oven at 383 K overnight. The dried adsorbent was ground and sieved to obtain a free flowing powder. Single and binary component adsorptions show that  $\text{NH}_3^+\text{-MCM-41}$  has a 100% selectivity for  $\text{Cr}_2\text{O}_7^{2-}$  adsorption at low pH (<3.5 i.e., point of zero charge, p.z.c.). The results showed that  $\text{NH}_2\text{-MCM-41}$  adsorbs only  $\text{Cr}_2\text{O}_7^{2-}$  and does not adsorb  $\text{Co}^{2+}$ ,  $\text{Cu}^{2+}$ ,  $\text{Ni}^{2+}$ ,  $\text{Zn}^{2+}$ ,  $\text{Ag}^+$ ,  $\text{Pb}^{2+}$ ,  $\text{Hg}^{2+}$  and  $\text{Cd}^{2+}$  below pH 3.5. The regenerated  $\text{NH}_2\text{-MCM-41}$  could be reused with no loss in its performance.

L. Bois and co-workers (Bois et al., 2003) studied adsorption capacity of heavy metal solution [ $\text{Cu}^{2+}$ ,  $\text{Ni}^{2+}$ ,  $\text{Co}^{2+}$ ,  $\text{Cd}^{2+}$  and the anion Cr(VI)] by MCM-41 with mercaptopropyl and aminopropyl group, giving the prepared adsorbents with mercaptopropyl group having a high loading capacity for  $\text{Cd}^{2+}$ . Later, K. F. Lam and co-workers (Lam et al., 2008) studied the selectivity of mesoporous material for  $\text{Cr}_2\text{O}_7^{2-}$  and  $\text{Cu}^{2+}$  solution by grafting aminopropyl and propionated on the MCM-41. The results

showed that NH<sub>2</sub>-MCM-41 adsorbed only Cr<sub>2</sub>O<sub>7</sub><sup>2-</sup> and does not adsorb Cu<sup>2+</sup>, while COONa-MCM-41 could separate Cu<sup>2+</sup> from solution containing Cr<sub>2</sub>O<sub>7</sub><sup>2-</sup>.

### 3.3.8 Characterization of porous glass

#### 3.3.8.1 pH at the point of zero charge (pH<sub>p.z.c.</sub>)

The pH<sub>pzc</sub> is the pH at which porous glass has equal amount of positive and negative charges on the surface, resulting in a net zero charge. In other words, the total charge from the cations and anions at the surface is equal to zero but this does not mean that the number of cations versus anions are equal. The surface charges on the porous glass are important in determining particle interactions. **Figure 3.8** shows the influence of pH on the surface charge. When the pH value of the solution containing porous glass is below the pH<sub>pzc</sub> (pH < pH<sub>pzc</sub>), the porous glass surface becomes positively charged and exhibit an anion exchange capacity. This favors the adsorption of anionic species (**Figure 3.8a**). When the pH of the solution equals to the pH<sub>pzc</sub> (pH = pH<sub>pzc</sub>), the porous glass surface contains a balance of positive and negative charges and exhibit no exchange capacity (**Figure 3.8b**). At the pH of the solution above the pH<sub>pzc</sub> (pH > pH<sub>pzc</sub>), the porous glass surface becomes negatively charged and exhibit a cation exchange capacity. This favors the adsorption of cationic species (**Figure 3.8c**) (Radovic et al., 1997).

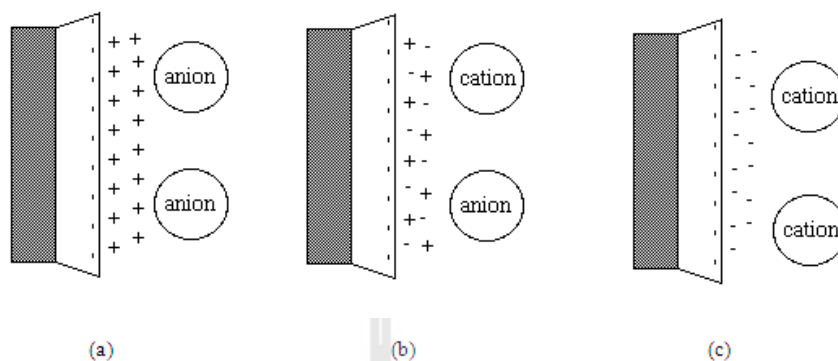


**Figure 3.8** The pH influence on surface charge; (a)  $\text{pH} < \text{pH}_{\text{pzc}}$ , (b)  $\text{pH} = \text{pH}_{\text{pzc}}$ , (c)  $\text{pH} > \text{pH}_{\text{pzc}}$

### 3.3.8.2 Thermogravimetric analysis (TGA)

Thermogravimetric analysis (TGA) is the most commonly used thermal analysis technique for studying the thermal behavior of porous materials. This technique is used to monitor the mass of sample in a specified atmosphere against the time or temperature which is programmed. The instrument used for this measurement is called a thermobalance, or a thermogravimetric analyzer. In general, a thermogravimetric analyzer has four major parts; the electrobalance and its controller, the furnace and temperature sensors, the program or computer and the recorder, plotter or data acquisition device (Haines, 1995). The schematic diagram of the thermogravimetric analyzer is shown in **Figure 3.9**. In this work, TGA was used to analyze the amount of various functional groups residing on the surface of porous glass.

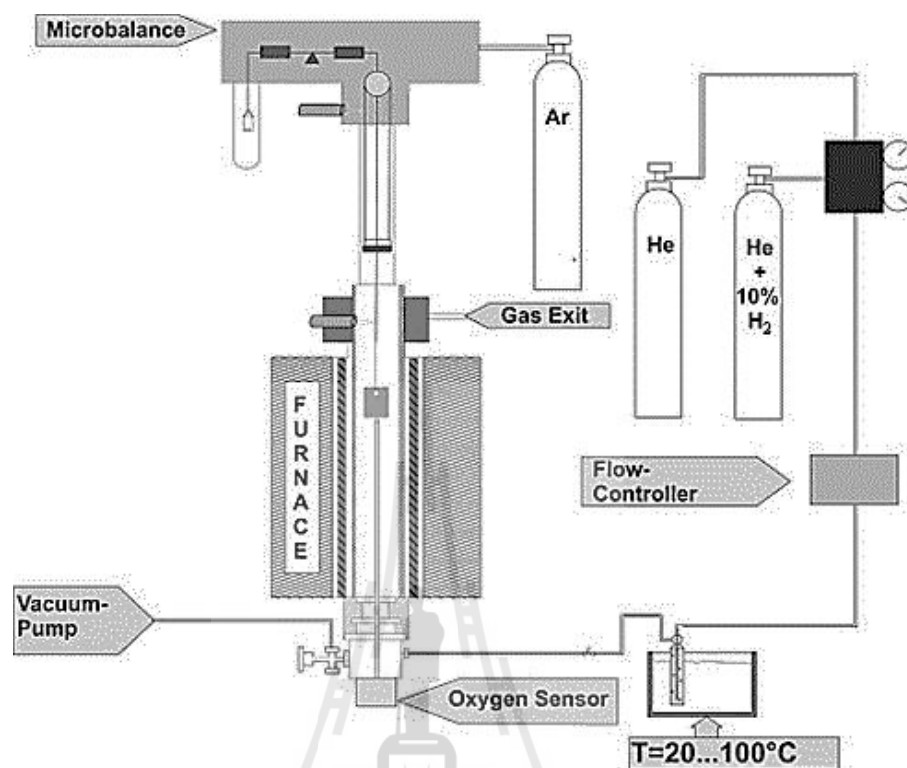


Figure 3.9 Schematic diagram of a thermogravimetric system. (Burk et al., 2010).

## 3.4 Experimental method

### 3.4.1 Preparation of fly ash

The porous glasses were prepared from the coal fly ash obtained from “BLCP Coal Power Plant Thailand” in Rayong province, Thailand. The fly ash was calcined at 900 °C for 10 h in an electric furnace and cooled down to room temperature in the furnace and stored in a desiccator.

### 3.4.2 Preparation of porous glass from fly ash

A total of 150 grams of raw mix with the following composition in wt%, 31.25% fly ash, 27.34% silica sand, 10.16% lime stone ( $\text{CaCO}_3$ ), 19.53% sodium tetraborate ( $\text{Na}_4\text{B}_2\text{O}_7 \cdot 10\text{H}_2\text{O}$ ) and 11.72% boric acid ( $\text{H}_3\text{BO}_3$ ), was prepared and melted at  $1450^\circ\text{C}$  for 2 hours in an electrically controlled furnace. The molten glass was poured onto an iron plate and heat treated at  $650^\circ\text{C}$  for 20 hours to allow for the phase separation of borosilicate glass. Following the phase separation, the product sample was broken and ground into granular form and sieved to obtain the size fraction of 0.1 mm in average screen size. The phase separated glass was acid leached by 1M of nitric acid solution at  $95^\circ\text{C}$  for 24 hours. Then, the sample was rinsed with deionized (DI) water and dried at  $120^\circ\text{C}$  for 24 hours. The obtained porous glass sample was designated as PG.

### 3.4.3 Surface modification of porous glass

Surface silanol group of silica can be involved in a chemical reaction with various organic and inorganic compounds which make it possible to graft to the silica surface different functional groups aimed to increase effective separation and adsorption capacity. The porous glasses from coal fly ash with attached thiolpropyl and aminopropyl groups were prepared using 3-mercaptopropyltrimethoxysilane and 3-aminopropyltriethoxysilane, respectively. The thiolpropyl and aminopropyl groups were grafted by refluxing the porous glass sample in a 50 ml dry toluene solution containing 0.01 mol of 3-mercaptopropyltrimethoxysilane (98%, Fluka) per gram of adsorbent and 0.01 mole of 3-aminopropyltriethoxysilane (97%, Aldrich) per gram of adsorbent at  $120^\circ\text{C}$  for 24 hours, respectively. The modified porous glass was washed by fresh toluene



several times and dried in an oven at 40 °C for 24 hours. The schematic diagram of surfacemodificationof porous glass is shown in **Figure 3.10**. The modified porous glass samples with aminopropyl and thiolpropyl groups were designated as PGNH<sub>2</sub> and PGSH, respectively. **Figure3.11** shows the incorporation of aminopropyl and thiolpropyl groups onto the surface of porous glass.

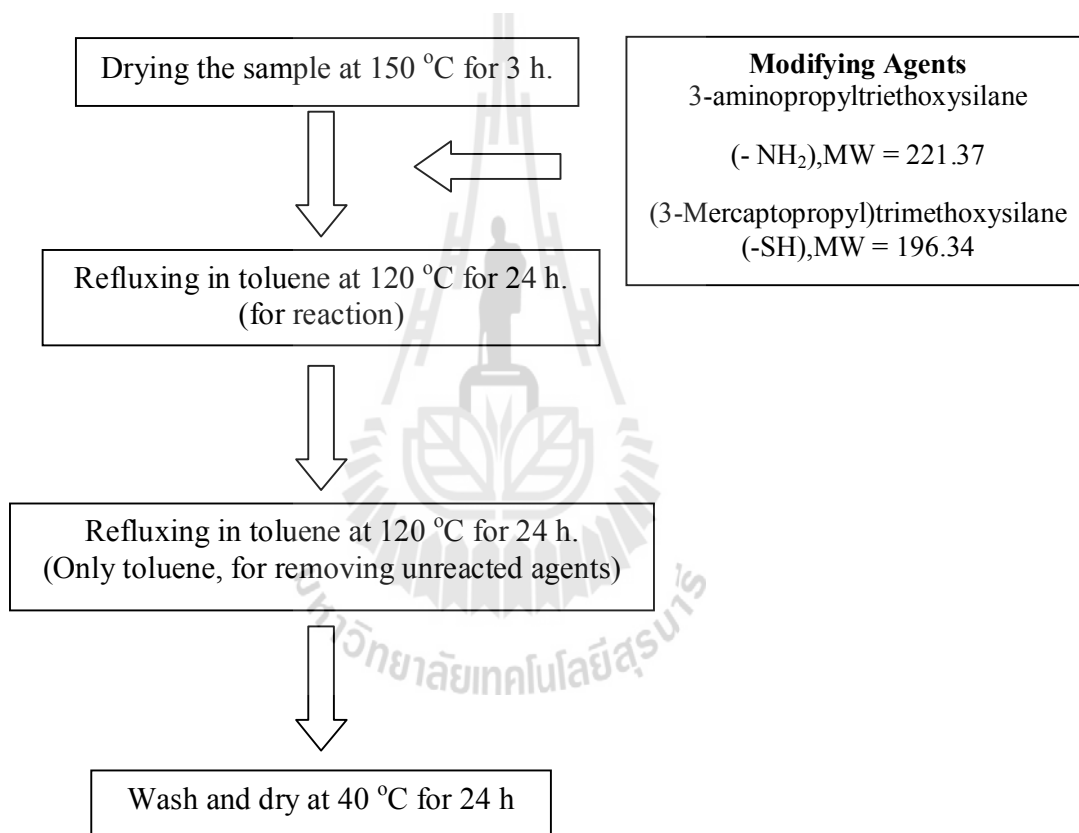


**Figure 3.10** Schematic diagram for grafting 3-aminopropyltriethoxysilane (-NH<sub>2</sub>) and 3-mercaptopropyl trimethoxysilane (-SH) onto the surface of porous glass.

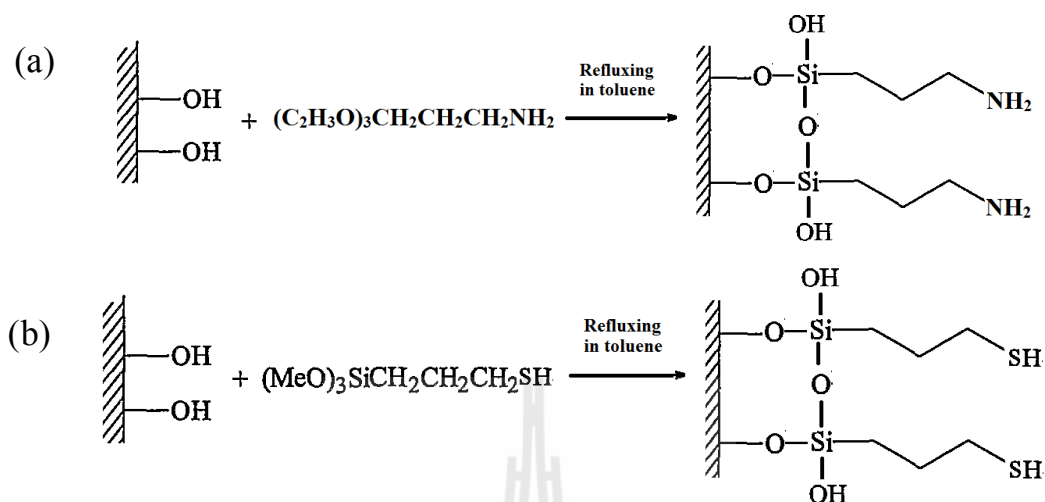


**Figure 3.11** Schematic for surface modification of (a) aminopropyl and (b) thiolpropyl groups on porous glass. (El-Nahhal and El-Ashgar, 2007).

### 3.4.4 Adsorbent characterization

The functional group loadings of the prepared and modified porous glasses were determined by thermogravimetric and differential thermal analyzer (TGA/DTA, Rigaku TG8120). The specific surface area and pore volume of porous glass adsorbents were calculated from nitrogen isotherm data obtained from a high precision surface area and pore size analyzer (Belsorp, Japan). Fourier Transform Infrared and Raman spectroscopy were used to identify the type of functional groups present on the adsorbent surface. The  $\text{pH}_{\text{pzc}}$  was determined using the pH drift method. The following gives details of the measurements.

Porous properties of the porous glasses were determined using  $\text{N}_2$  adsorption isotherm data at  $-196^\circ\text{C}$  acquired by the automated adsorption apparatus. The

porous glass was first degassed at 250 °C under vacuum ( $< 50\mu\text{mHg}$ ) for 12 hours to remove moisture and other volatiles. From the obtained isotherm data, the specific surface area,  $S_{\text{BET}}$ , was estimated by applying Brunauer-Emmett-Teller (BET) equation (Do, 1998). The total pore volume,  $V_{\text{T}}$ , was found from the amount of  $\text{N}_2$  gas adsorbed at the relative pressure of 0.99 and converted it to the corresponding volume in liquid state. The mesopore volume was determined by BJH theory (Barrett, Joyner, and Halenda theory).

The FTIR spectrometer was used to measure the infrared spectrum of the porous glass and to identify their chemical functionality. The porous glass was mixed with KBr powder and the pellet formed by compressing it at 10 tons for 2 min in a hydraulic press. Before measurement, the instrument was run to collect the background, which was automatically subtracted from the sample spectrum.

The pH at the point of zero charge ( $\text{pH}_{\text{pzc}}$ ) value was used to compare the extent of acidic surface functional groups on porous glass. By definition,  $\text{pH}_{\text{pzc}}$  is the pH of the solution in contact with solid at which the net surface charge on the surface of an adsorbent particle is zero. Therefore, the porous glass that contains acidic surface functional groups will exhibit a low value of  $\text{pH}_{\text{pzc}}$  whereas high value of  $\text{pH}_{\text{pzc}}$  is observed for the basic surface. The  $\text{pH}_{\text{pzc}}$  of the porous glass was measured by the pH drift method. In this method, at the solution pH above the  $\text{pH}_{\text{pzc}}$  the porous glass with acidic functional groups on surface releases protons into a solution. If the solution pH is lower than the  $\text{pH}_{\text{pzc}}$  the porous glass with acidic functional groups on surface receives protons from the solution. A point is reached at which the acidic functional groups are in

equilibrium with protons in solution so that the final pH of solution does not change. This point is defined as the point of zero charge. Under this condition, all surface charges are effectively neutralized so that the net surface charge of the porous glass is zero. The determination of  $\text{pH}_{\text{pzc}}$  was done by adjusting the pH of 0.01 M NaCl (50 cm<sup>3</sup>) to values between 1 to 10 obtained by adding either 0.1 M HCl or NaOH. About 0.15 g of porous glass was added into each stock solution at room temperature (25°C) and then shaken for 48 hours. The final pH was measured and plotted against the initial pH. The pH at which the plotted curve intersects the line of  $\text{pH}(\text{final}) = \text{pH}(\text{initial})$  was taken as the  $\text{pH}_{\text{pzc}}$  of the porous glass surface.

#### 3.4.5 Single metal ion adsorption

Batch experiments of metal ion adsorption were conducted by using 0.1 g of porous glass or surface modified porous glass and 50 ml of aqueous solutions containing 0.5 to 3 mM metal ions. For aqueous metal solutions, copper sulfate ( $\text{CuSO}_4 \cdot 5\text{H}_2\text{O}$ ),  $\text{AgNO}_3$ ,  $\text{AuCl}_4$  were obtained from Wako pure chemical industries, Japan. The pH of solutions was adjusted with dilute nitric acid and sodium hydroxide solutions. The batch adsorption experiments were performed in a shaker bath at room temperature (25 °C). The adsorption kinetics was performed by taking the sample solution for determining metal ion concentration at a fixed time interval with equilibrium adsorption being measured at the end of 5 days adsorption period. The initial and final concentrations of the metal in the solution were analyzed by a UV-visible spectrophotometer (V-650, Jasco). The wavelength for maximum absorbance was

observed at  $\lambda_{\max} = 212$  nm, perfectly served as a measure of  $\text{Cu}^{2+}$  concentration in the solution since the absorbance at this wavelength gives a linear dependence on  $\text{Cu}^{2+}$  concentration (V. Pautieniene, 2004). For  $\text{Ag}^+$  and  $\text{Au}^{3+}$  concentration, the wavelength for maximum absorbance was observed at  $\lambda_{\max} = 233$  nm and  $\lambda_{\max} = 250$  nm, respectively.

The adsorption capacity of porous glass was calculated from the following equation,

$$q_e = \frac{(C_o - C_e)V}{m} \quad (3.48)$$

where  $q_e$  (mmol/g) is the adsorption capacity,  $C_o$  (mM) and  $C_e$  (mM) are the initial and equilibrium concentrations of metal in solution, respectively,  $V$  (L) is the volume of solution,  $m$  (g) is the mass of adsorbent.

### 3.4.6 Adsorption of binary metal ions

Binary  $\text{Cu}^{2+}/\text{Ag}^+$  system was prepared from  $\text{CuSO}_4/\text{AgNO}_3$ . Aqueous solution with different metal ions concentrations were prepared by diluting the initial stock solution and 0.05 g of porous glass sample was added into 50  $\text{cm}^3$  of the respective solution. The mixture was shaken and allowed to equilibrate at 30°C for 24 hours without adjusting the pH. Competitive adsorption is the usual situation encountered in real applications and therefore the competitive adsorption of binary aqueous metal ions in mixtures of  $\text{Cu}^{2+}/\text{Ag}^+$  was investigated under the molar ratio of 1:1. The remaining metal ions in the solution after adsorption were measured by Atomic Absorption

Spectroscopy (AAS). Three measurements were performed and averaged, and the equilibrium adsorption capacity was calculated.

### 3.4.7 Gas adsorption experiments

The gas adsorption tests with porous glass adsorbents were also performed using CO<sub>2</sub>, C<sub>2</sub>H<sub>5</sub>OH and water vapor as adsorbates in an Intelligent Gravimetric Analyzer (IGA) supplied by Hiden Analytical, UK. This apparatus allows the measurement of adsorption and desorption isotherms of gas adsorbates via the gravimetric system. Initially, the porous glass sample weighting about 0.2 grams was outgassed at 300 °C for 12 hours. The numbers of pressure points were specified and the measurement of the adsorbed amount at equilibrium performed for each scan of adsorption and desorption steps.

## 3.5 Results and discussions

### 3.5.1 Adsorbent characterization

In this section the characterization of the original and surface modified porous glasses are presented.

#### 3.5.1.1 Porous properties of prepared porous glass

**Figure 3.12** shows the N<sub>2</sub> adsorption of the original and modified porous glass adsorbents. It is clear that these adsorbents show the typical type IV isotherm (Type II with hysteresis loop) which is indicative of a mesoporous material. This means that the adsorption of N<sub>2</sub> by this type of adsorbent is associated with the

phenomenon of capillary condensation. It is observed that capillary condensation effect commences at the relative pressure ( $P/P_0$ ) around 0.3 for all the adsorbents. It is further noted that both of the modified porous glass give much less amount of adsorbed nitrogen as compared with the adsorption by the original unmodified porous glass, for example, 20 versus 80 mL(STP)/g adsorbent at  $P/P_0 = 0.30$ . The decrease in the amount adsorbed should be due to the inaccessibility of  $N_2$  to the adsorption sites caused by the presence of introduced function groups on the pore surface. When comparing the two modified adsorbents, the results indicate that the porous glass with amine group (PGNH<sub>2</sub>) give slightly higher adsorbed amount than the porous glass with thiol group (PGSH) over the relative pressure range up to 0.70. It is probable that the presence of thiol group could impart greater hindrance or blocking effect than the presence of amine group. In addition, PGNH<sub>2</sub> shows a larger hysteresis loop in comparison with that of PG-SH. **Table 3.4** compares the porous properties of the modified and unmodified porous glass adsorbents, calculated from  $N_2$  isotherm data at  $-196^\circ\text{C}$  (77K). As expected from the isotherm data, all calculated porous properties of the original porous glass, including specific surface area, total pore volume, micropore volume and mesopore volume and average pore size, decrease significantly after introducing the surface functional groups. The comparison of pore size distribution between PG, PGNH<sub>2</sub> and PGSH samples are displayed in **Figure 3.13**. It is observed that there is virtually no change in the pore size distribution of modified porous glass samples compared to the virgin porous glass.

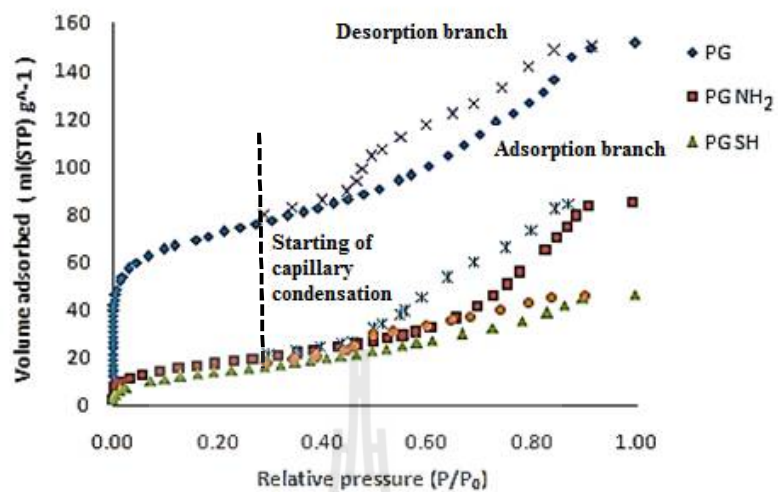
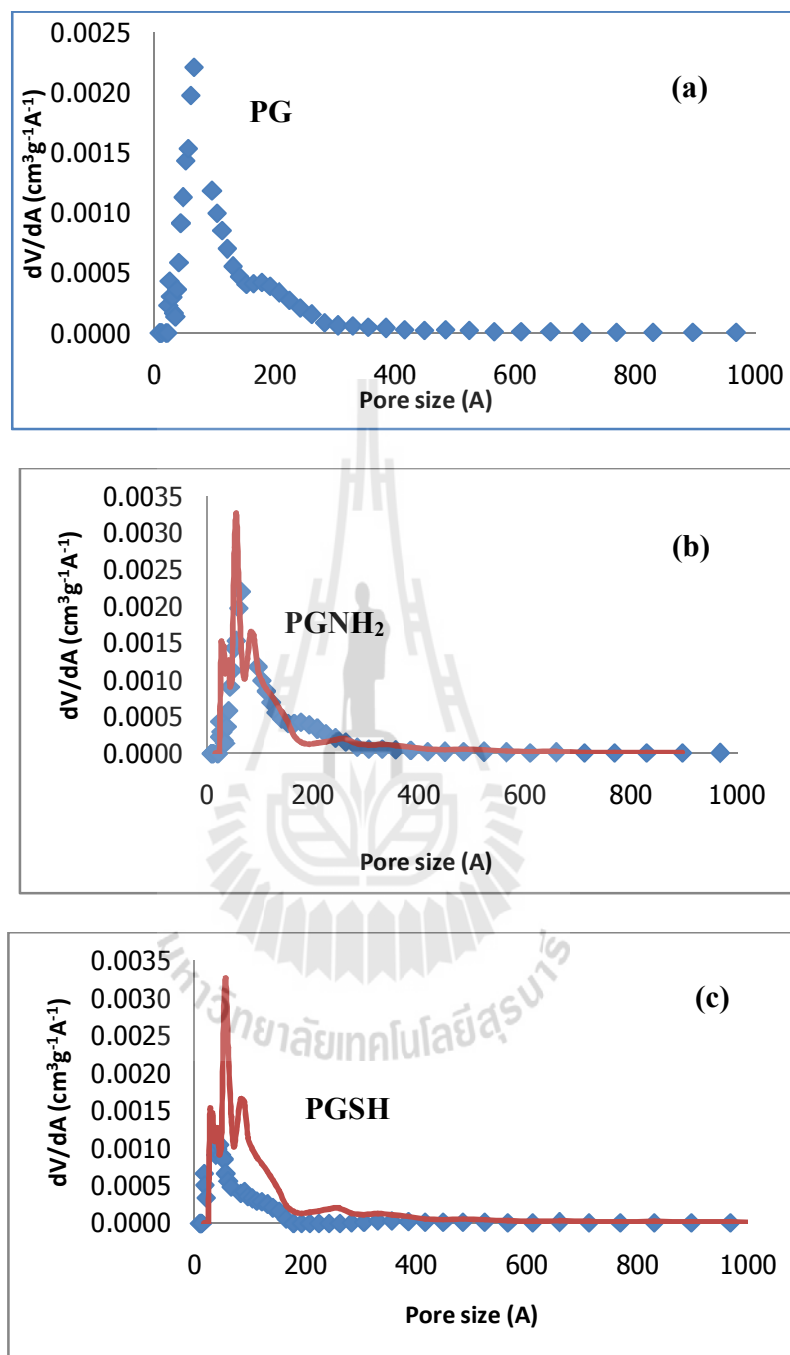


**Figure 3.12**  $N_2$  adsorption isotherm plots of obtained porous glass and modified porous glass.

**Table 3.4** Porous properties of original and modified porous glass adsorbents.

Adsorbents	Specific surface area ( $m^2/g$ )	Pore volume ( $cm^3/g$ )	Micropore volume ( $cm^3/g$ )		Mesopore volume ( $cm^3/g$ )		Average pore size (nm)
			$cm^3/g$	%	$cm^3/g$	%	
PG	237	0.29	0.039	13.30	0.254	86.70	3.80
PG $NH_2$	64	0.15	0.0016	1.05	0.154	98.95	3.53
PG SH	51	0.084	0.0001	0.15	0.083	99.85	3.29

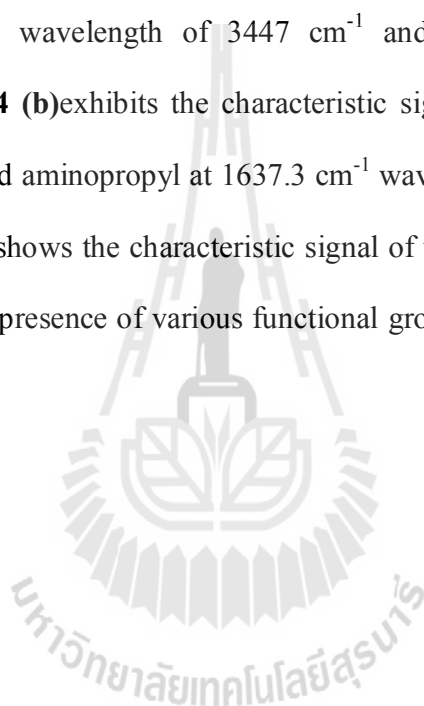




**Figure 3.13** Pore size distribution of (a) PG (b) PGNH<sub>2</sub> and (c) PGSH by N<sub>2</sub> adsorption from isotherm data.

### 3.5.1.2 Confirmation of surface functional groups by FTIR

The existence of functional groups on the silica surface was ascertained from the FTIR spectrum of the original (PG) and modified (PGNH<sub>2</sub> and PGSH) porous glass adsorbents and the results are displayed in **Figure 3.14**. For the original porous glass (PG), **Figure 3.14(a)** shows the characteristic signal of silanol group on the surface at the wavelength of 3447 cm<sup>-1</sup> and Si-O-Si bond at 1078 cm<sup>-1</sup> wavelength. **Figure 3.14 (b)** exhibits the characteristic signals of n-propyl group on the surface at 2900 cm<sup>-1</sup> and aminopropyl at 1637.3 cm<sup>-1</sup> wavelength for the PGNH<sub>2</sub> sample. Finally, **Figure 3.14(c)** shows the characteristic signal of thiol group at 2571 cm<sup>-1</sup> for the PGSH. As a result, the presence of various functional groups on the porous glass surface is confirmed.



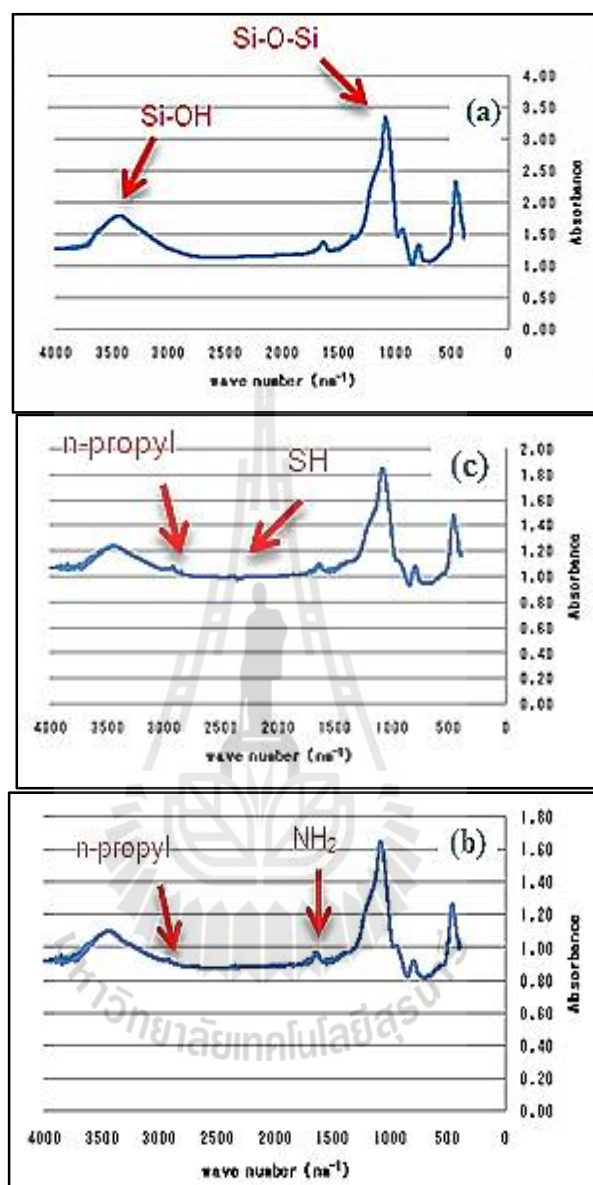


**Figure 3.14** FTIR spectra of (a) PG (b) PGNH<sub>2</sub> and (c) PGSH

### 3.5.1.3 Surface group loading by TGA

Thermogravimetric analysis (TGA) was adopted in this study for the determination of the concentration of silanol group (-OH) on the surface of silica porous glass. The non-isothermal heating by TGA on the porous glass samples was programmed from room temperature to the final temperature of 1000 °C. **Figure 3.15** shows the obtained results for PG, PGNH<sub>2</sub> and PGSH samples. As shown, all the weight loss curves can be divided into three consecutive regions based on the difference in the slope of the curve. According to Lam (Lam et al., 2006), the weight loss in Region I (<400 K) and Region II (400 – 670 K) correspond to the liberation of adsorbed water on the adsorbent surface and the hydrogen bond water molecules, respectively. The samples weight in Region III starts to fall continuously from 670 K to a constant value at 1070 K. The weight loss during this period represents the amount of released functional groups existing on the adsorbent surface. It is implicitly assumed that the weight loss in Region III is due solely to the release of hydroxyl group (-OH), hence the concentration (in mmol/g adsorbent) of hydroxyl or silanol group can be readily estimated. The weight loss in Region III of sample PGNH<sub>2</sub> is attributed to the liberation of both the hydroxyl and the attached amine functional groups. Thus, the concentration of the amine surface group (-NH<sub>2</sub>) can be determined by subtracting the total weight loss in Region III by the amount of hydroxyl group obtained from sample PG. Similar to sample PGNH<sub>2</sub>, the amount of thiol containing surface group (-SH) can be derived from the weight loss of PGSH on Region III. The surface group loadings of the above three samples of porous glass are listed in **Table 3.5**.

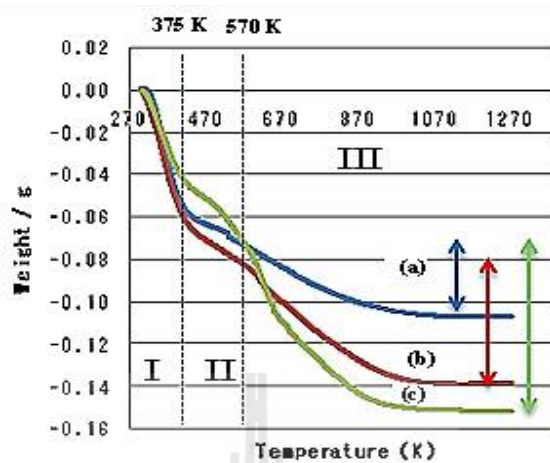


**Figure 3.15** Thermogravimetric analyses of (a) PG (b) PGNH<sub>2</sub> and (c) PGSH.

**Table 3.5** Results on point of zero charge and functional group loading of original and modified porous glass adsorbents.

Adsorbents	Point of zero charge	Functional group loading, mmol/g		
		Hydroxyl (-OH)	Amino (-NH <sub>2</sub> )	Thiol (-SH)
PG	2.5	1.82	-	-
PG NH <sub>2</sub>	2.0	-	0.86	-
PG SH	2.0	-	-	0.77

### 3.5.1.4 Point of zero charge ( $\text{pH}_{\text{p.z.c.}}$ )

The plotted pH results for determining point of zero charge ( $\text{pH}_{\text{p.z.c.}}$ ) of PG,  $\text{PGNH}_2$  and  $\text{PGSH}$  samples are shown in **Figure 3.16** and the results of  $\text{pH}_{\text{p.z.c.}}$  are listed in **Table 3.5**. It was found that the  $\text{pH}_{\text{p.z.c.}}$  of the original porous glass was 2.5 and those of modified porous glass ( $\text{PGNH}_2$  and  $\text{PGSH}$ ) were 2.0. According to Dietrich (Dietrich et.al., 1997), the pH of zero charge on silica surface varies between 1.5 and 3.0. This signifies that adsorption of metal ions can take place at pH above 2.5 and 2.0 for the original and modified porous glasses, respectively, since at this condition the adsorbent surface becomes negatively charged, or in other words there is less number of  $\text{H}^+$  as the solution pH is increased above  $\text{pH}_{\text{p.z.c.}}$ .

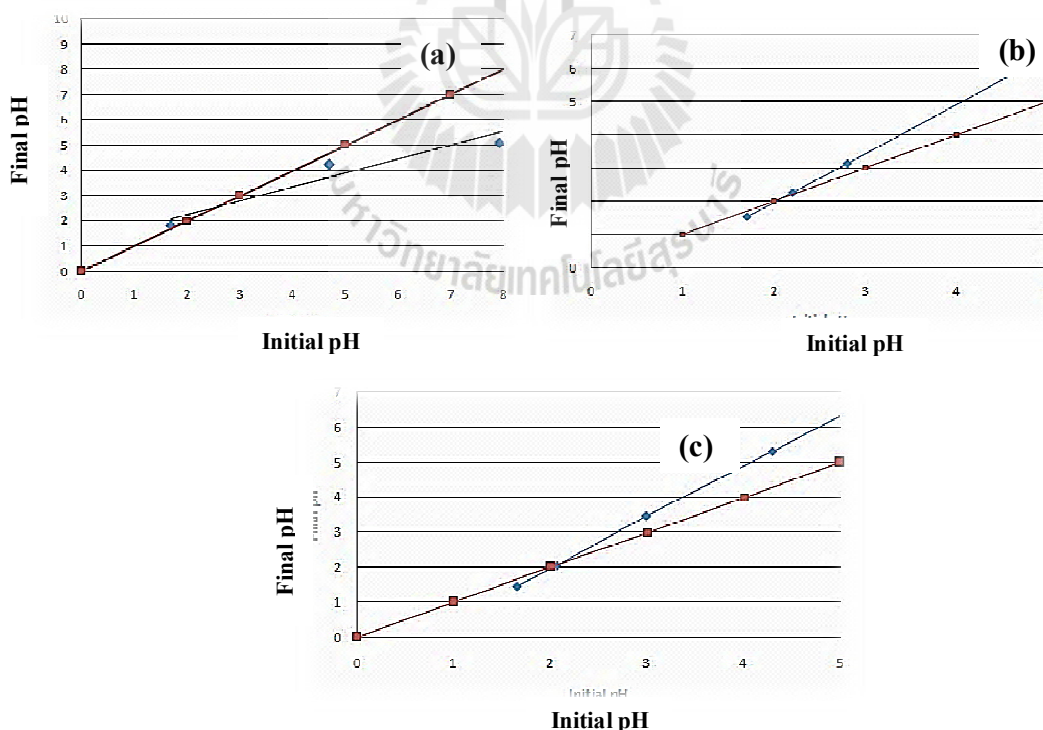


**Figure 3.16** Point of zero charge ( $\text{pH}_{\text{p.z.c.}}$ ) of (a)PG, (b) $\text{PGNH}_2$  and (c) $\text{PGSH}$ .

### **3.5.2 Single component adsorption of heavy metal ions**

This section reports on the adsorption equilibrium and kinetics of single metal ions, including  $\text{Cu}^{2+}$ ,  $\text{Ag}^+$  and  $\text{Au}^{3+}$  by the prepared porous glass adsorbents.

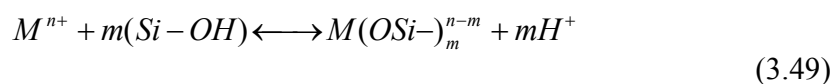
#### **3.5.2.1 Adsorption of $\text{Cu}^{2+}$ and $\text{Ag}^+$**

##### **3.5.2.1.1 Effect of pH and functional group type on the adsorption of $\text{Cu}^{2+}$ and $\text{Ag}^+$**

Porous silica glass consists essentially of a three-dimensional net work of silica,  $\text{SiO}_2$ , in which each silicon atom is connected to four oxygen atoms forming a tetrahedron structure. At the glass surface, the structure exists as siloxane links, Si-O-Si. The surface oxygen can form two covalent bonds, one with the interior silicon atom and the other with a suitable external agent. When silica is in contact with water, the most suitable agent that can associate with the surface oxygen is proton ( $\text{H}^+$ ) from water, leading to the forming of hydroxyl group (-OH) or silanol group. In effect, the surface nature of porous glass can thus be visualized as consisting of siloxane links interrupted by sites of exposing silanol groups which can vary in both the type and distribution on the surface. This hydrous form of silica surface is considered most important as far as the process of adsorption is concerned, since the surface hydroxyls can play a key role in determining the reactivity of silica at the surface (Parida et al., 2006). In this work, the acquisition of surface hydroxyls on the porous glass surface by protonation should occur during the leaching step of the phase-separated glass by dilute nitric acid solution.

The effect of solution pH on the equilibrium uptake of  $\text{Cu}^{2+}$  and  $\text{Ag}^+$  by both the original and surface modified porous glass adsorbents is shown in **Figure 3.17**. First, it is observed that the adsorption of the original unmodified porous glass (PG) is extremely low for  $\text{Cu}^{2+}$  and almost negligible for  $\text{Ag}^+$ . To explain this behavior the polar nature of the surface hydroxyls needs to be considered. The degree of surface polarity can be determined from the value of ionic character which correlates with the difference in electronegativity of two atoms forming a single chemical bond (Lam et al., 2006). The electronegativities of oxygen and hydrogen atom are 3.5 and 2.1, respectively, and this gives the electronegativity difference of 1.4, corresponding to the ionic character of 67%. This number substantiates that the presence of hydroxyl or silanol group on the glass surface shows a reasonable degree of surface polarity that enable the surface group to attract metal ions by electrostatic interaction. Therefore, it is likely that the relatively low adsorption of  $\text{Cu}^{2+}$  and  $\text{Ag}^+$  by the original porous glass (sample PG) is probably due to the low surface concentration of the silanol group itself.

Another mechanism of metal ion uptake by silica surface has been proposed to result from the exchange of metal ion with the weak acidic silanol group, as shown in the following equation (E. Papirer, 2000)



However, the equilibrium constant of this reaction for  $\text{Cu}^{2+}$  and  $\text{Ag}^+$  are extremely low in the order of  $10^{-11}$  and  $10^{-7}$  at 20 °C, respectively. Therefore, it is



less likely that the uptake of both metal ions by sample PG is by ion-exchange mechanism. It is further argued that the hydroxyl group could be protonated by the reaction,



so that its exchange capacity for metal ions may be reduced. However, the estimated proton association constant for the silanol links was found to be  $\log K = -16.9$ , which indicates that this group can be considered inert toward the protonation process (Lam et al., 2006).

Results in **Figure 3.17** further illustrates that pH has a profound effect on the adsorption of metal ion by PGNH<sub>2</sub> and PGSH samples. There is a general tendency for the amounts of both metal ions to increase with increasing pH above the pH at point of zero charge (pH<sub>p.z.c.</sub>). This is simply explained by the competitive effect between H<sup>+</sup> and metal ions (Cu<sup>2+</sup> and Ag<sup>+</sup>) towards the adsorption sites. That is, as the pH is increased above pH<sub>p.z.c.</sub> the concentration of H<sup>+</sup> in the solution decreases, thus increasing the likelihood for the association of both metal ions with the polar parts of the modified porous glass (-NH<sub>2</sub> and -SH) by electrostatic forces or possibly by chemical bonding.

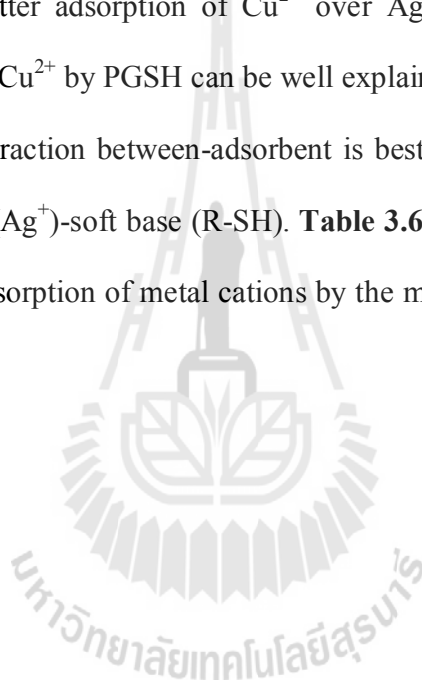
Further examination of **Figure 3.17** shows that after introducing the functional groups of -NH<sub>2</sub> and -SH onto the glass surface, the adsorbed amounts of metal ions by these two adsorbents increase significantly. Obviously, this increase is the

result from the consequent increase in the number of adsorption sites due to the addition of introduced surface groups, as can be seen from **Figure 3.14**.

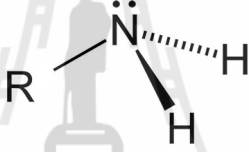
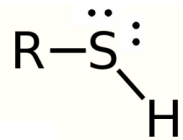
It is also noticed that the adsorption behavior of metal ions is strongly influenced by the types of surface groups. While sample PGNH<sub>2</sub> could effectively adsorb Cu<sup>2+</sup>, its adsorbed capacity for Ag<sup>+</sup> is surprisingly low. On the other hand, the adsorption of metal ions by PGSH shows the opposite trend, that is, it could adsorb Ag<sup>+</sup> much higher than Cu<sup>2+</sup>. This adsorption behavior of the modified porous glass could be explained by the HSAB concept which is an initialism for “Hard and Soft (Lewis) Acids and Bases”, also known as the Pearson acid and base concept (Pearson, 1963).

The HSAB theory is widely used for qualitative explanation of the interaction, stability, reaction mechanism and reaction pathway of chemical species, and was used in this study to explain the adsorption between the surface modified porous glass and metal cations. This theory employs the term “hard” or “soft” and “(Lewis) acid” or “(Lewis) base” to describe the chemical species. The term “Lewis acid” refers to any species that can accept an electron lone pair from another molecule to complete its stable form, while “Lewis base” is the one that donates a pair of electrons to a Lewis acid. The term “hard” applies to species which are small (atomic or ionic radius), high oxidation state, and weakly polarizable and high electronegativity (for bases). The term “soft” refers to species that are big (atomic or ionic radius), low or zero oxidation state, strongly polarizable and low electronegativity.

Concerning the HSAB theory, it states that soft acids react faster and form stronger bonds with soft bases, whereas hard acids react faster and form stronger bonds with hard bases. In summary, hard acid-hard base interactions are stronger than hard acid-soft base or soft acid-hard base interactions, and soft acid-soft base interactions are stronger than soft acid-hard base or hard acid-soft base interactions. It was found that the better adsorption of  $\text{Cu}^{2+}$  over  $\text{Ag}^+$  by  $\text{PGNH}_2$  and the superior adsorption of  $\text{Ag}^+$  over  $\text{Cu}^{2+}$  by  $\text{PGSH}$  can be well explained and supported by the HSAB concept in that the interaction between-adsorbent is best for hard acid ( $\text{Cu}^{2+}$ )-hard base ( $\text{R-NH}_2$ ) and soft acid ( $\text{Ag}^+$ )-soft base ( $\text{R-SH}$ ). **Table 3.6** gives details of applying of the HSAB theory to the adsorption of metal cations by the modified porous glass adsorbents in the present study.



**Table 3.6** Adsorbents-adsorbate characterization based on the HSAB theory.

Characteristics	Adsorbate	
	Hard Lewis acid	Soft Lewis acid
Atomic radius, pm	Cu <sup>2+</sup> 91 (small)	Ag <sup>+</sup> 129 (large)
Oxidation state	+2 (high)	+1 (low)
Characteristics	Functional group	
	Hard Lewis acid	Hard Lewis acid
Electronegativity	 <p>N = 3.0 H = 2.1 Diff. = 0.9 (high)</p>	 <p>S = 2.5 H = 2.1 Diff. = 0.4 (low)</p>

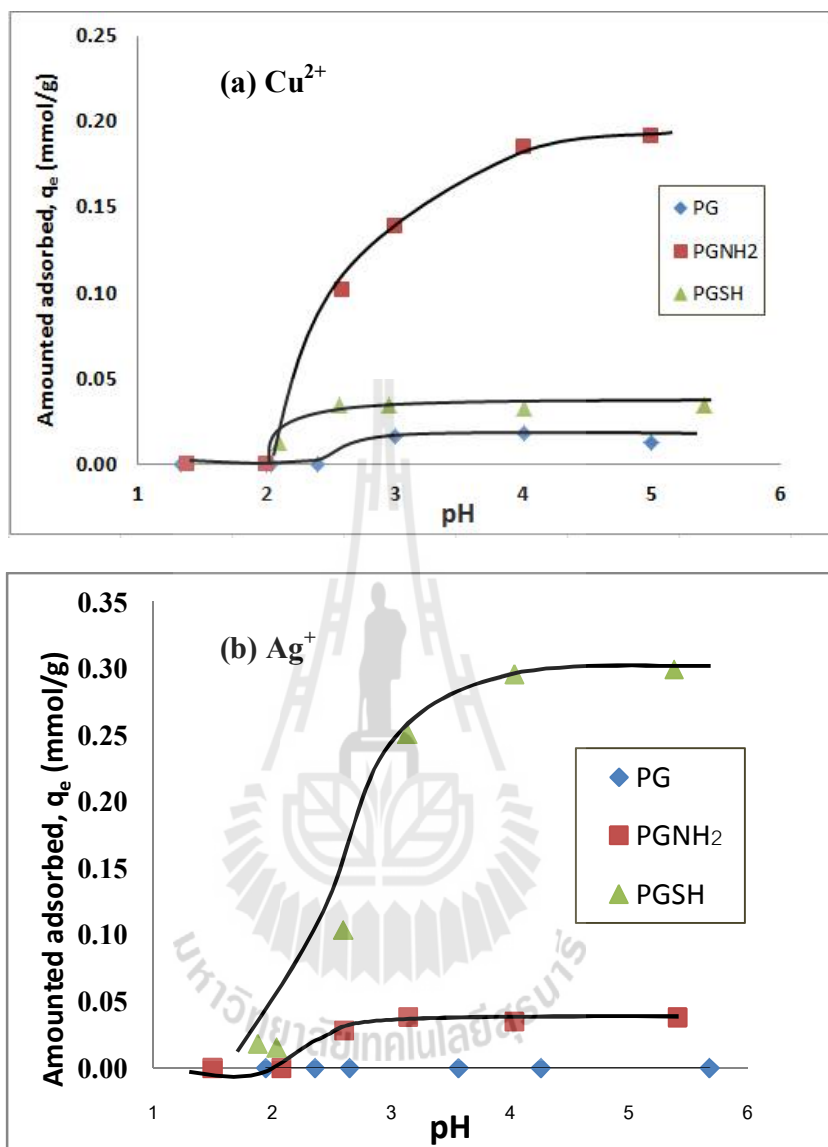


**Figure 3.17** Effect of solution pH on (a) Cu<sup>2+</sup> and (b) Ag<sup>+</sup> adsorption of PGNH<sub>2</sub> and PGSH ([Cu<sup>2+</sup>] = [Ag<sup>+</sup>] = 1.0 mM, Temperature = 25 ± 5 °C, adsorption time = 24 hours).

Finally, it is need from **Figure 3.17** that at pH below  $pH_{pzc}$  ( $<2$ ) at which the porous glass surface becomes positively charged, sample PGSH was still able to adsorb small amount of metal ions. This could be explained by the conversion of thiol group (-SH) to sulfonic group (-SO<sub>3</sub>H) by oxidation reaction with acid in the solution at such a low pH (Kikukawa et al., 2005), as schematically illustrated in **Figure 3.18**. With stronger acidity, sulfonic group is able to attract more metal ions by electrostatic interaction.

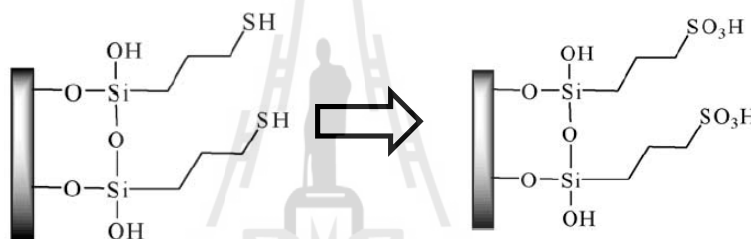


**Figure 3.18** Schematic of surface conversion from thiol group to sulfonic group on porous glass when pH solution is below 2.

#### 3.5.2.1.2 Adsorption kinetics of Cu<sup>2+</sup> and Ag<sup>+</sup>

Single ion adsorption of Cu<sup>2+</sup> and Ag<sup>+</sup> by porous glass adsorbents was studied as a function of time at 25°C and the results are listed in **Table 3.7** and graphically displayed in **Figure 3.19**. As observed, samples PGNH<sub>2</sub> and PGSH were able to selectively adsorb copper ion and silver ion from solution, respectively, while the original unmodified porous glass showed almost negligible metal ion adsorption. The kinetic data show similar rapid increase of adsorbed ions by both grafted adsorbents over

the first 10 min of adsorption time, and followed by a plateau of relatively constant ion uptake. **Table 3.8** shows the fitted parameters of the three kinetic models tested, namely the pseudo first-order, the pseudo second-order and the pore or intraparticle diffusion models. The comparison between the experimental and the predicted kinetic data for the adsorption of  $\text{Cu}^{2+}$  and  $\text{Ag}^+$  by the modified porous glass (PHNH<sub>2</sub> and PGSH) is presented in **Figure 3.20**.

Based on the values of the regression coefficient of curve fitting ( $R^2$ ), the predictive capabilities of the kinetic models are as follows: pseudo second-order > pseudo first-order > pore diffusion model. The equilibrium adsorption capacities ( $q_e$ ) estimated by both the pseudo first-order and the pseudo second-order models agree with each other quite well. The selective adsorption of each metal ion is clearly indicated by the mole ratio of selective to non-selective ion that is greater than one, that is, the ratio of adsorbed  $\text{Cu}^{2+}$  to  $\text{Ag}^+$  is 3.7 for PGNH<sub>2</sub> and 8.7 for the ratio of  $\text{Ag}^+$  to  $\text{Cu}^{2+}$  for PGSH. On the other hand, the value of the rate constant ( $k_{p2}$ ) are less for the selectively adsorbed metal ion as compared to the non-selective one. Considering the values of effective pore diffusivity ( $D_e$ ) derived from the pore diffusion model, the diffusivities of both metal ions for each adsorbent are considered relatively constant. However, the diffusivities of  $\text{Cu}^{2+}$  and  $\text{Ag}^+$  in PGNH<sub>2</sub> is about twice higher than those for the transport of these ions in the pores of PGSH. This indicates the difference in the resistance of pore structure for mass transport when different functional groups are grafted on the porous glass surface. It is also interesting to note that the ionic size has no direct bearing on the pore diffusivity since the effective ionic radius of  $\text{Ag}^+$  is twice as much compared to that of  $\text{Cu}^{2+}$  (100

versus 57 pm) but the pore diffusivities of both ions for the same adsorbent are about the same. This signifies that the passage of metal ions through pores is not obstructed by pore wall since the mesopore size of porous glass is much larger than the size of the diffusing ions.

**Table 3.7** Adsorption kinetic data of  $\text{Cu}^{2+}$  and  $\text{Ag}^+$  onto original and modified porous glass at 25 °C.

Time (min)	Amount adsorbed of $\text{Cu}^{2+}$ onto			Amount adsorbed of $\text{Ag}^+$ onto		
	PG (mmol/g)	PGNH <sub>2</sub> (mmol/g)	PGSH (mmol/g)	PG (mmol/g)	PGNH <sub>2</sub> (mmol/g)	PGSH (mmol/g)
5	0.0000	0.0127	0.1136	0.0000	0.0290	0.1960
10	0.0050	0.0263	0.1227	0.0001	0.0320	0.2691
15	0.0060	0.0280	0.1300	0.0001	0.0340	0.2581
20	0.0060	0.0336	0.1292	0.0001	0.0350	0.2538
30	0.0080	0.0279	0.1207	0.0001	0.0362	0.2724
40	0.0090	0.0315	0.1305	0.0002	0.0360	0.2755
60	0.0090	0.0392	0.1377	0.0002	0.0377	0.2919
90	0.0090	0.0245	0.1384	0.0002	0.0360	0.2857
120	0.0090	0.0315	0.1481	0.0002	0.0355	0.2937



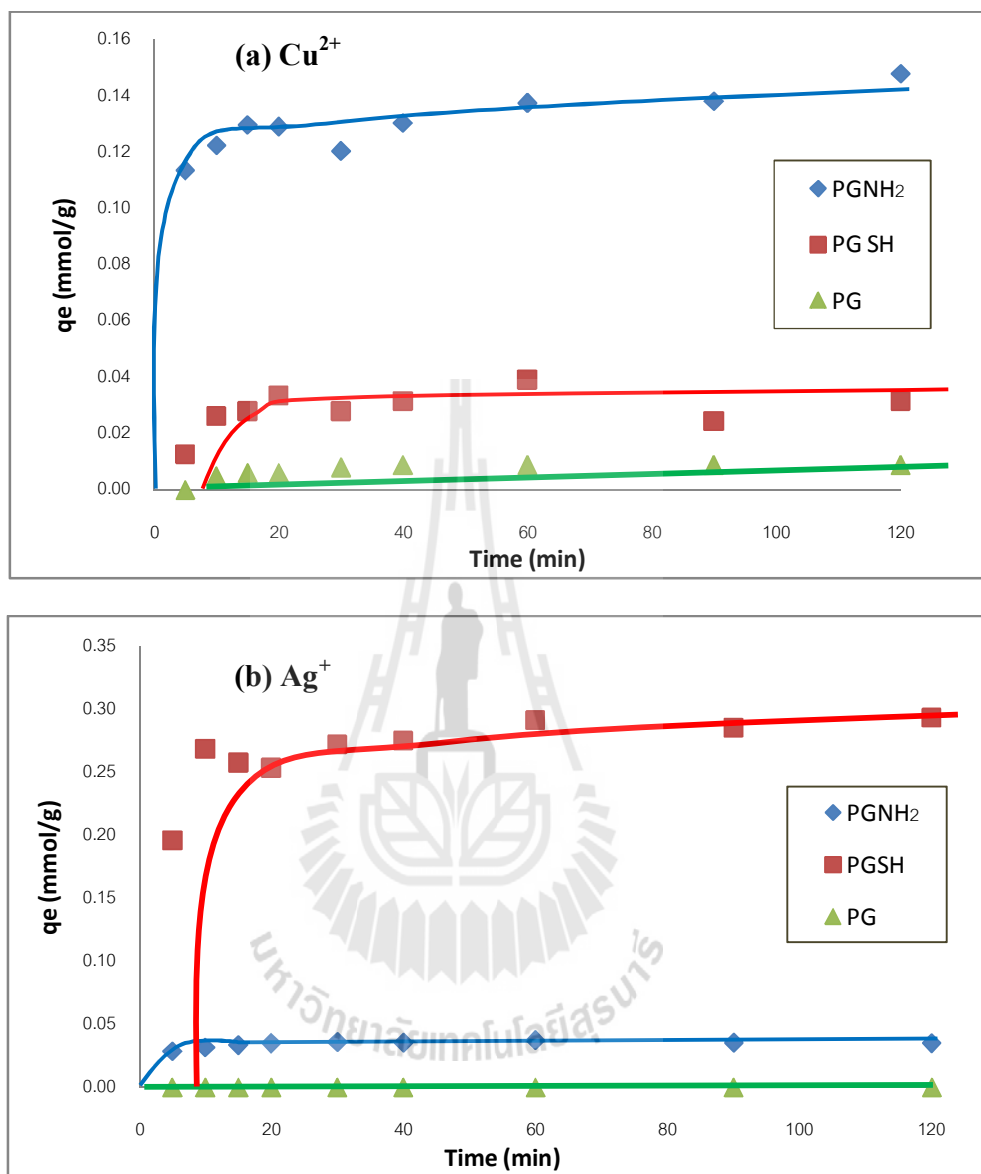


**Figure 3.19** Adsorption kinetics of (a) Cu<sup>2+</sup> onto PGNH<sub>2</sub> and (b) Ag<sup>+</sup> by the original porous glass (PG) and modified porous glass (PGNH<sub>2</sub> and PGSH) (0.1 g adsorbent: 50 ml solution, pH = 5, 25 °C).

**Table 3.8** Fitted kinetic parameters for the adsorption of  $\text{Cu}^{2+}$  and  $\text{Ag}^+$  by  $\text{PGNH}_2$  and  $\text{PGSH}$  at 25 °C.

Kinetic model	Model parameters	Adsorbent-Metal ions		Adsorbent-Metal ions	
		$\text{PGNH}_2\text{-Cu}^{2+}$	$\text{PGNH}_2\text{-Ag}^+$	$\text{PGSH-Cu}^{2+}$	$\text{PGSH-Ag}^+$
Pseudo 1 <sup>st</sup> order	$k_{p1}, \text{min}^{-1}$	0.368	0.306	0.142	0.2288
	$q_e, \text{mmol/g}$	0.132	0.036	0.032	0.2783
	$R^2$	0.9915	0.9895	0.8699	0.9836
Pseudo 2 <sup>nd</sup> order	$k_{p2}, \text{mmol}^{-1}\text{min}^{-1}$	6.448	19.00	6.591	1.2816
	$q_e, \text{mmol/g}$	0.138	0.037	0.034	0.2972
	$R^2$	0.9980	0.9958	0.8303	0.9973
Pore diffusion	$D_e, \text{m}^2/\text{s}$	$5.74 \times 10^{-9}$	$4.21 \times 10^{-9}$	$1.94 \times 10^{-9}$	$2.61 \times 10^{-9}$
	$q_e, \text{mmol/g}$	0.129	0.035	0.031	0.2748
	$R^2$	0.8168	0.8283	0.7022	0.8204

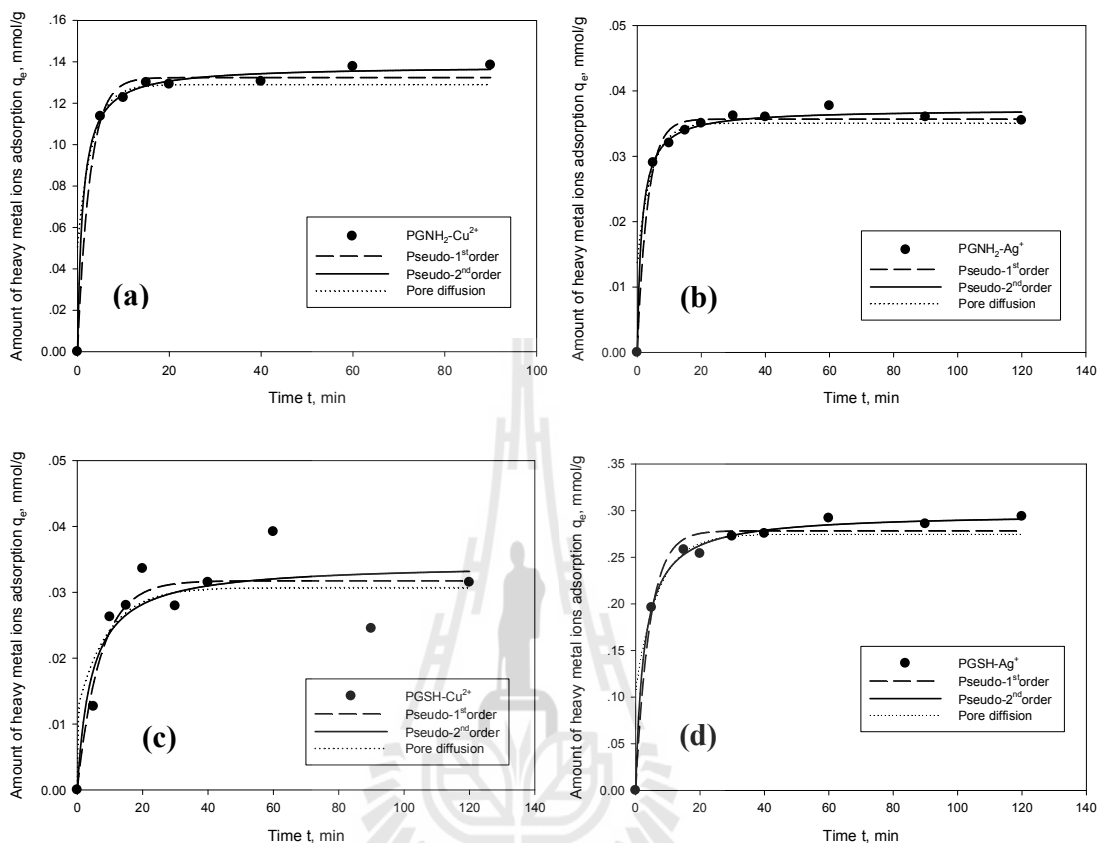


**Figure 3.20** Comparison of experimental and model predicted adsorption kinetic data of  $\text{Cu}^{2+}$  and  $\text{Ag}^+$ , (a)  $\text{PGNH}_2\text{-Cu}^{2+}$  (b)  $\text{PGNH}_2\text{-Ag}^+$  (c)  $\text{PGSH-Cu}^{2+}$  and (b)  $\text{PGSH-Ag}^+$  solution onto porous glass (0.1 g of adsorbent: 50 ml of solution, pH= 5.0, 25 °C).

### 3.5.2.1.3 Adsorption equilibrium of $\text{Cu}^{2+}$ and $\text{Ag}^+$

**Figure 3.21** shows the single adsorption isotherms of  $\text{Cu}^{2+}$  and  $\text{Ag}^+$  in solution by  $\text{PGNH}_2$  and  $\text{PGSH}$  adsorbents, covering the equilibrium ion concentration up to 2.0 mmol/L. Three well known isotherm equations, including

Langmuir, Freundlich, and Sips models were tested against the experimental isotherm data using regression analysis for data fitting and the derived model parameters are listed in **Table 3.9**. Based on the regression coefficient ( $R^2$ ), the three-parameter Sips model can predict the isotherms of metal ions most accurately, followed by Langmuir and Freundlich equations, respectively. The comparison of adsorption isotherms derived from the experiment and model prediction is displayed in **Figure 3.21**. Although the Sips model is slightly more accurate, the Langmuir model is considered to be more convenient for describing the equilibrium adsorption of  $\text{Cu}^{2+}$  and  $\text{Ag}^+$  by porous glass since it contains only two parameters. The selective adsorption of metal ion by each adsorbent can be quantified by determining the ratio of monolayer capacity of Langmuir model ( $q_e$ ) between the selective and non-selective ion to give the values of 3.8 for copper ion adsorbed by  $\text{PGNH}_2$  and 5.6 for the adsorption silver ion by  $\text{PGSH}$ . Also, it can be seen from **Table 3.9** that the selective adsorption of metal ion is accompanied by a larger value of Langmuir constant ( $K_L$ ) which is a measure of surface affinity, for example, the selective adsorption of metal ions by  $\text{PGNH}_2$  gives  $K_L$  for  $\text{Cu}^{2+}$  and  $\text{Ag}^+$  to be 71.8 and 56.6 L/mmol, respectively.

For the purpose of comparison, the adsorption capacities of  $\text{Cu}^{2+}$  and  $\text{Ag}^+$  by various adsorbents, including porous glass from the present work, mesoporous silica adsorbent (MCM), activated carbon and zeolite, are summarized as shown in **Table 3.10** and **Table 3.11**, respectively. Since each adsorbent has different density, the adsorption capacity usually expressed as the amount adsorbed per unit mass of adsorbent is also presented based on a unit surface area, in order that the comparison

can be made on the same basis of adsorbed area. **Table 3.10** indicates that mesoporous silica adsorbent (MCM) gives the same adsorption behavior as porous glass from the present work as follows: (i) virgin silica adsorbent cannot adsorb any copper ion on the surface, (ii) silica adsorbent attached with aminopropyls group can selectively adsorb  $\text{Cu}^{2+}$  from solution, and (iii) increasing surface group loading enhances the adsorbed capacity of copper ion. It is interesting to observe that eucalyptus based activated carbon, after fixing the oxygen functional groups by surface oxidation, is able to effectively adsorb more ion from solution. Zeolite adsorbent, despite its low specific surface area, shows impressive adsorption capacity for  $\text{Cu}^{2+}$  compared to other types of listed adsorbents. **Table 3.11** shows that the virgin MCM or virgin porous glass from the present work cannot specifically adsorb silver ion. However, once they are grafted with thiolpropyls group (-SH) the uptake of  $\text{Ag}^+$  increase considerably. In contrast to the present study, MCM grafted with aminopropyls ( $-\text{NH}_2$ ) shows a strong affinity for  $\text{Ag}^+$  with adsorption capacity of 0.62 mmol/g for functional group loading of 2.26 mmol/g. Interestingly, the adsorption of  $\text{Ag}^+$  by a rather new adsorbent of carbon nanospheres gives excellent adsorption capacity even with a very low particle surface area. Finally, it is observed that when expressed the adsorption capacity based on a unit surface area of adsorbent, the adsorption capacities of both ions for most common adsorbents are relatively low and vary in a narrow range from  $1 \times 10^{-3}$ - $5 \times 10^{-3}$  mmol/  $\text{m}^2$ .

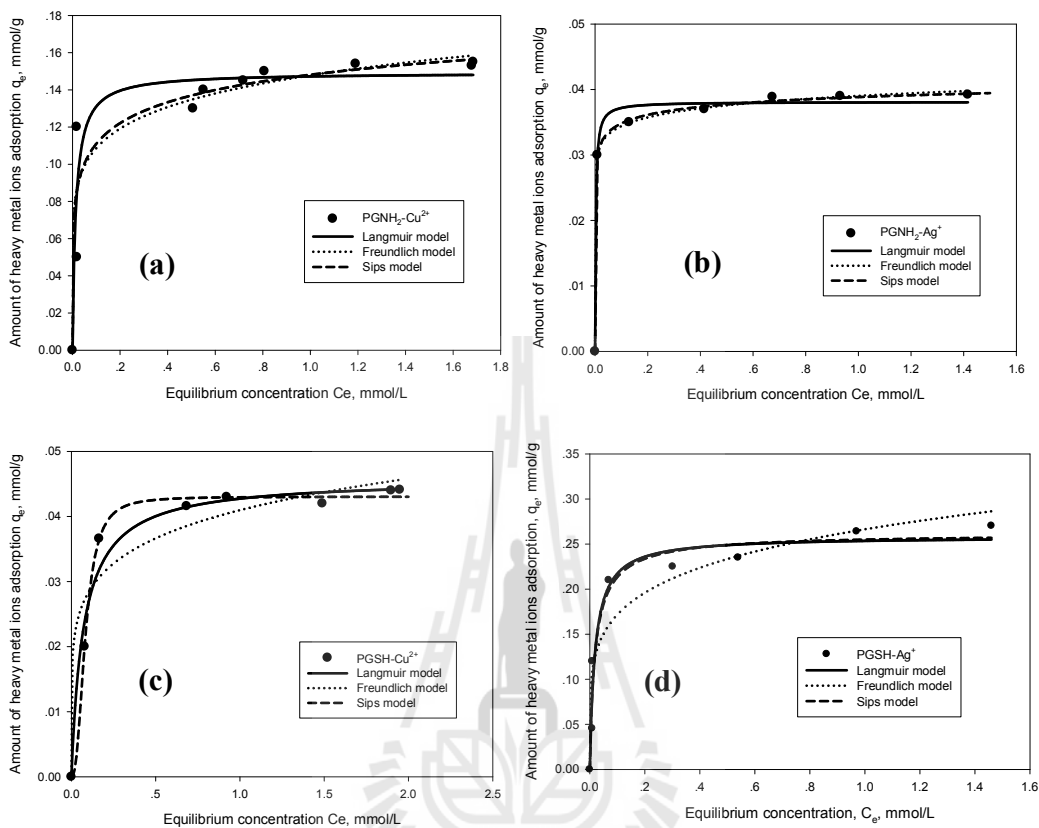


**Figure 3.21** Adsorption isotherms of  $\text{Cu}^{2+}$  and  $\text{Ag}^+$  onto  $\text{PGNH}_2$  and  $\text{PGSH}$ , (a)  $\text{PGNH}_2\text{-Cu}^{2+}$ , (b)  $\text{PGNH}_2\text{-Ag}^+$  (c)  $\text{PGSH-Cu}^{2+}$  and (d)  $\text{PGSH-Ag}^+$  (0.1 g of adsorbent: 50 ml of solution,  $\text{pH}= 5.0$ ,  $25^\circ\text{C}$ ).

**Table 3.9** Fitted parameters of various isotherm models for single component adsorption of Cu<sup>2+</sup> and Ag<sup>+</sup> by modified porous glass at 25 °C.

Adsorbent	Metal ion	Langmuir			Freundlich			Sips			
		q <sub>m</sub> (mmol/g)	K <sub>L</sub>	R <sup>2</sup>	K <sub>F</sub>	n <sub>F</sub>	R <sup>2</sup>	q <sub>ms</sub> (mmol/g)	K <sub>S</sub>	n <sub>S</sub>	R <sup>2</sup>
PG NH <sub>2</sub>	Cu <sup>2+</sup>	0.149	71.8	0.8812	0.148	7.46	0.8940	0.167	7.15	1.42	0.9956
PG SH	Cu <sup>2+</sup>	0.046	13.8	0.9769	0.041	6.21	0.9375	0.005	6.52	1.36	0.9654
PG NH <sub>2</sub>	Ag <sup>+</sup>	0.039	56.6	0.9991	0.039	19.67	0.9994	0.004	132	1.71	0.9996
PG SH	Ag <sup>+</sup>	0.258	52.8	0.9506	0.266	5.24	0.9059	0.320	4.50	1.66	0.9691

**Table 3.10** Adsorption capacity of copper ions for different common adsorbents

Adsorbate	Adsorbents	Adsorption capacity (mmol/g)	Specific surface area (m <sup>2</sup> /g)	Adsorption capacity (mmol/m <sup>2</sup> )	Conditions	Ref.
Cu <sup>2+</sup>	PG-NH <sub>2</sub>	0.15	64	0.0029	T = 30 °C, 50 ml: 0.1 g (ratio solution:adsorbent)	This work
	Zeolite P from Fly ash	0.13	25.7	0.0051	T= 30 °C, 100 mL:0.05 g	Shaobin, 2006
		1.0	25.7	0.0389	T= 40 °C, 100 mL:0.05 g,	Shaobin, 2006
	MCM-41	0	1070	0.0000	T= 22 °C, 100 ml:0.1g, 0.5-4mM, function loading = 2.53 mmol/g	K.F.Lam, 2006
	COONa-MCM-41	0.28	679	0.0004	T= 22 °C, 100 ml:0.1g, 0.5-4mM, function loading = 1.46 mmol/g	K.F.Lam, 2006
	NH <sub>2</sub> -MCM-41	0.25	772	0.0003	T= 22 °C, 100 ml:0.1g, 0.5-3mM, function loading = 1.01 mmol/g	K.F.Lam, 2006
		0.84	774	0.0011	T= 22 °C, 100 ml:0.1g, 0.5-3mM, function loading = 2.26 mmol/g	K.F.Lam, 2006



**Table 3.10** Adsorption capacity of copper ions for different common adsorbents(continued).

Adsorbate	Adsorbents	Adsorption capacity (mmol/g)	Specific surface area (m <sup>2</sup> /g)	Adsorption capacity (mmol/m <sup>2</sup> )	Conditions	Ref.
Cu <sup>2+</sup>	SH-MCM-41	0.02	990	0.0000	T= 22°C, 100 ml:0.1g, 0.5-3mM, function loading = 1.00 mmol/g	K.F.Lam, 2006
	AC (Eucalyptus wood)	0.06	1200	0.0001	T=30 °C, 50 ml:0.1g)	Yuvarat, 2007
	AC (H <sub>2</sub> O <sub>2</sub> 24 h.)	0.13	689	0.0002	T=30 °C, 50 ml:0.1g)	Yuvarat, 2007
	AC (HNO <sub>3</sub> re 1M 24h)	0.43	523	0.0008	T=30 °C, 50 ml:0.1g)	Yuvarat, 2007

**Table 3.11** Adsorption capacity of silver ions for different common adsorbents.

Adsorbate	Adsorbents	Adsorption capacity (mmol/g)	Specific surface area (m <sup>2</sup> /g)	Adsorption capacity (mmol/m <sup>2</sup> )	Conditions	Ref.
Ag <sup>+</sup>	PG-SH	0.30	51	0.0059	T = 30 °C, 50 ml: 0.1 g (ratio solution:adsorbent)	This work
	MCM-41	0	1070	0.0000	T=22C, 100 ml:0.1g, 0.5-4mM, function loading = 2.53 mmol/g	K.F.Lam, 2006
	NH <sub>2</sub> -MCM-41	0.11	772	0.0001	T=22C, 100 ml:0.1g, 0.5-3mM, function loading = 1.01 mmol/g	K.F.Lam, 2006
	NH <sub>2</sub> -MCM-41	0.62	774	0.0008	T=22C, 100 ml:0.1g, 0.5-3mM, function loading = 2.26 mmol/g	K.F.Lam, 2006

**Table 3.11** Adsorption capacity of silver ions for different common adsorbents(continued).

<b>Adsorbate</b>	<b>Adsorbents</b>	<b>Adsorption capacity (mmol/g)</b>	<b>Specific surface area (m<sup>2</sup>/g)</b>	<b>Adsorption capacity (mmol/m<sup>2</sup>)</b>	<b>Conditions</b>	<b>Ref.</b>
Ag <sup>+</sup>	SH-MCM-41	0.97	990	0.0010	T=22C, 100 ml:0.1g, 0.5-3mM, function loading = 1.00 mmol/g	K.F.Lam, 2006
	AC (colloidal carbon nanosphere with 0.5 M NaOH	1.41	12.7	0.1110	T=25 C, 100 ml:0.1g,	Xianghua, 2011

### 3.5.2.2 Adsorption of gold ion

The adsorption of gold onto porous glass surface is separately presented in this section due to the fact that the adsorption mechanism of gold is different and more complex than that of copper and silver ions (Lam et al.).

Similar to  $\text{Cu}^{2+}$  and  $\text{Ag}^+$  adsorption, it was discovered that the adsorption capacity of gold in solution by the original porous glass was extremely low despite its reasonable surface area of  $237 \text{ m}^2/\text{g}$  (Table 3.4). Figure 3.22 shows the effect of solution pH on the adsorption capacity of gold at  $25^\circ\text{C}$  by the grafted porous glass,  $\text{PGNH}_2$  and  $\text{PGSH}$ . Over a relatively narrow range of pH from 2 to 4, the amount of gold adsorbed appeared to increase by about twofold with increasing pH from 2 to around 3.4, and became constant at higher pH values. The maximum adsorption capacities of gold on  $\text{PGNH}_2$  and  $\text{PGSH}$  are 0.83 and 0.98 mmol/g, respectively. It appears that both adsorbents give comparable adsorption capacity for gold. It should be further noted that over the pH range from 2-4, the glass surface is negatively charged since the pH at point of zero charge ( $\text{pH}_{\text{pzc}}$ ) of both adsorbents has the value of about 2, thus allowing a strong interaction between the solid surface and the positive gold ion. It should be noted also that according to Murphy and Lagrange (Murphy and LaGrange, 1998) gold can only exist in solution as  $\text{AuCl}_4^-$  at pH below 4.

Figure 3.23 shows the effect of adsorption time on the uptake of gold by the original and grafted porous glass. It is clear that the adsorption time to reach equilibrium is relatively long; it takes about 300 and 600 min for  $\text{PGNH}_2$  and  $\text{PGSH}$ , respectively. To increase the adsorption rate, it is obvious that the surface concentration

of the grafted functional groups needs to be increased. The kinetic data of gold adsorption were fitted with the three common kinetic models, namely the pseudo first-order, the pseudo second-order, and the pore diffusion models. The fitted model parameters are listed in **Table 3.12** and the fitting accuracy can be observed from the plots in **Figure 3.24** for the  $\text{PGNH}_2$  and PGSH adsorbents. Based on the values of regression coefficient ( $R^2$ ), it can be inferred that the pseudo second-order kinetic model gives the best fit to experimental data, followed by the pseudo first-order model and the pore diffusion model, respectively. The model rate constants,  $k_{p1}$  and  $k_{p2}$ , indicate that  $\text{PGNH}_2$  has higher uptake rate of gold than the PGSH adsorbent, although the final amounts adsorbed by the two adsorbents are not greatly different. Similar results are obtained from the pore diffusion model in that the effective pore diffusivity ( $D_e$ ) of  $\text{PGNH}_2$  is higher than that of PGSH by about an order of magnitude ( $3 \times 10^{-10}$  vs.  $7.86 \times 10^{-11}$ ).

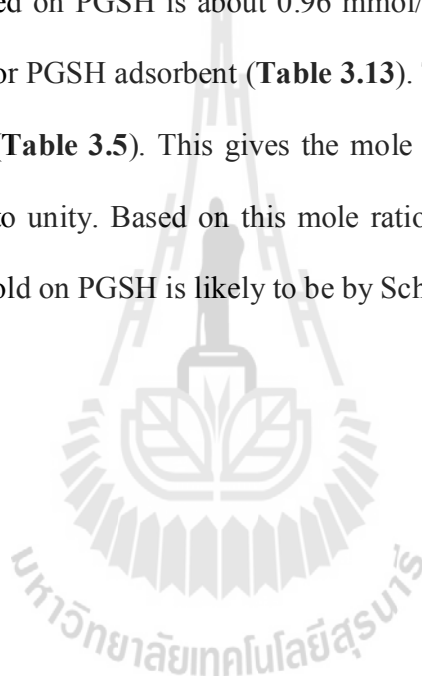
**Figure 3.25** shows the equilibrium adsorption isotherms of gold by porous glass adsorbents,  $\text{PGNH}_2$  and PGSH. The two-parameter adsorption models of Langmuir and Freundlich and the three-parameter Sips model were tested against the experimental isotherm data and the results are illustrated in **Figure 3.25**. **Table 3.13** lists the derived model parameters:  $q_m$  and  $K_L$  for Langmuir model,  $n_F$  and  $K_F$  for Freundlich model, and  $q_{ms}$ ,  $K_s$  and  $n_s$  for the Sips model, along with the regress coefficient of curve fitting ( $R^2$ ). Again, based on  $R^2$ , the Sips model with three adjustable parameters gives the best description of gold adsorption isotherm by  $\text{PGNH}_2$  and PGSH, followed by Langmuir and Freundlich models, respectively. The maximum adsorbed amounts of gold ( $q_{ms}$ ) predicted by the Sips model have the values of 1 and 0.96 mmol/g for  $\text{PGNH}_2$  and

PGSH, respectively. **Table 3.14** compares the adsorption capacities of gold from the present work and those by several different potential adsorbents. It is noticed that the reported adsorption capacities of gold among various adsorbents vary widely from 0.5 to 6.5 mmol/g and this should result from the differences in their porous structure ( surface area and pore volume) and surface functionalities (type, concentration and distribution).

On the adsorption mechanism of gold, Trokhimchuk and co-workers (Trokhimchuk et al., 2004) have proposed several schemes for gold ion adsorption on aminopropyls and thiopropyls, as depicted in **Figure 3.26**. The gold ions can adsorb on  $\text{PGNH}_2$  by two possible mechanisms, that is, by ion exchange mechanism (Scheme 1) or by complexation mechanism (Scheme 2). The functional group loading of aminopropyls ( $\text{R-NH}_2$ ) on  $\text{PGNH}_2$  was found to be 0.86 mmol/g (**Table 3.5**) and the maximum adsorption capacity of gold ion by  $\text{PGNH}_2$  is around 1 mmol/g, taken from the fitted equilibrium capacity,  $q_{\text{ms}}$ , of the Sips model in **Table 3.13**. As a result, the mole ratio of  $\text{Au}^{3+}$ :  $\text{R-NH}_2$  is around 1.16 which is close to one. This number agrees reasonably well with 1:1 mole ratio of Scheme 1 for which one gold ion is attached by one aminopropyls group on the glass surface. It is therefore reasonable to deduce that the adsorption of gold ion by  $\text{PGNH}_2$  adsorbent is by ion exchange mechanism where the protonated amino group ( $\text{R-NH}_3^+$ ) interacts with  $\text{AuCl}_4^-$  anions existing at solution pH lower than 4.

There are several proposed schemes for gold adsorption on thiolpropyls ( $\text{R-SH}$ ) of PGSH surface, as illustrated in **Figure 3.26**. Gold which is present as  $\text{AuCl}_4^-$  at pH below 4 can form complexes with the thiol groups by Scheme 3a and 3b,

depending on the number of thiol and gold atoms involved. There is a possibility that  $\text{Au}^{3+}$  in Scheme 3a to be reduced to  $\text{Au}^+$  with the oxidation of thiolpropyls to dithiolpropyls, shown as Scheme 4. At the same time,  $\text{Au}^+$  atoms can transform to metallic gold ( $\text{Au}^0$ ) and attach to the thiolpropyls groups as in Scheme 5. Finally, gold can also be adsorbed by the dithiolpropyls according to Scheme 6. The equilibrium amount of gold adsorbed on PGSH is about 0.96 mmol/g, as derived from the value of  $q_{ms}$  of the Sips model for PGSH adsorbent (**Table 3.13**). The functional group loading of R-SH is 0.77 mmol/g (**Table 3.5**). This gives the mole ratio of  $\text{Au}^{3+}$ : R-SH to be 1.25 which is at best close to unity. Based on this mole ratio number, **Figure 3.26** suggests that the adsorption of gold on PGSH is likely to be by Scheme 3b.



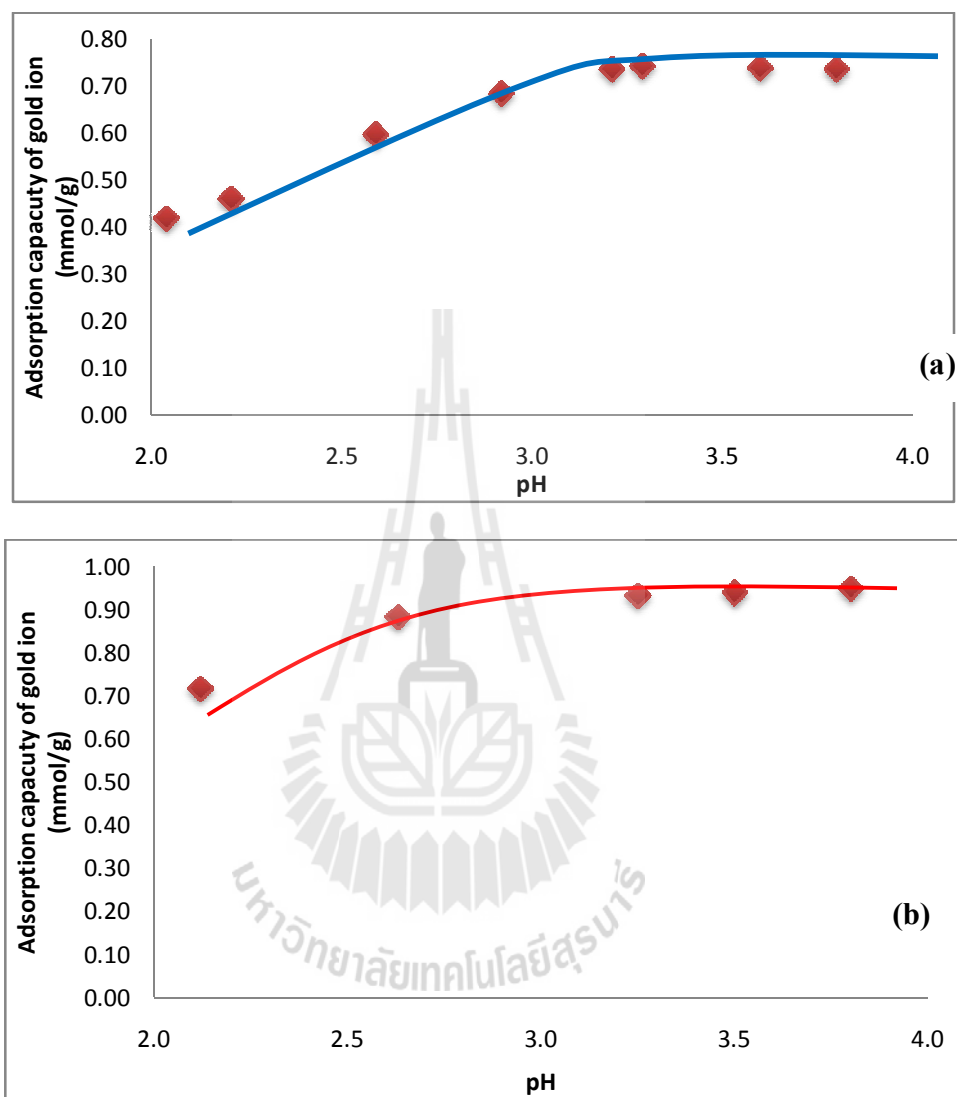


**Figure 3.22** Effect of solution pH on the adsorption of  $\text{Au}^{3+}$  onto (a) PG-NH<sub>2</sub> and (b) PG-SH ( $\text{AuCl}_4^- = 1\text{mM}$ , 5 day for measuring concentration, 0.1 g of adsorbent: 50 ml of solution, 25 °C).



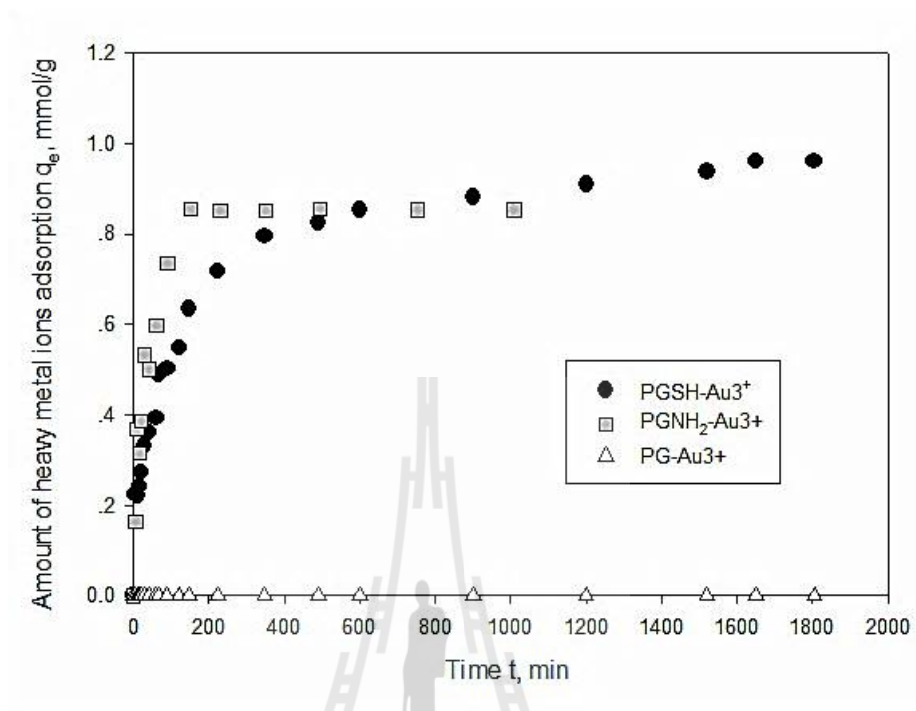


**Figure 3.23** Adsorption kinetics of gold by PGSH, PGNH<sub>2</sub> and PG. ( $[Au^{3+}]$  1.0 mM, pH = 5, 25 °C)

**Table 3.12** Fitted parameters of various kinetic models for the adsorption of gold by PGNH<sub>2</sub> and PGSH at 25 °C.

Kinetic model	Model parameters	Adsorbent-Metal ions	
		PGNH <sub>2</sub> -Au <sup>3+</sup>	PGSH-Au <sup>3+</sup>
Pseudo 1 <sup>st</sup> order	$k_{p1}, \text{min}^{-1}$	0.0303	0.0107
	$q_e, \text{mmol/g}$	0.8446	0.8802
	$R^2$	0.9550	0.9272
Pseudo 2 <sup>nd</sup> order	$k_{p2}, \text{mmol}^{-1}\text{min}^{-1}$	0.0492	0.0156
	$q_e, \text{mmol/g}$	0.9097	0.9564
	$R^2$	0.9571	0.9676
Pore diffusion	$D_e, \text{m}^2/\text{s}$	$3.00 \times 10^{-10}$	$7.86 \times 10^{-11}$
	$q_e, \text{mmol/g}$	0.8277	0.8693
	$R^2$	0.8255	0.8710

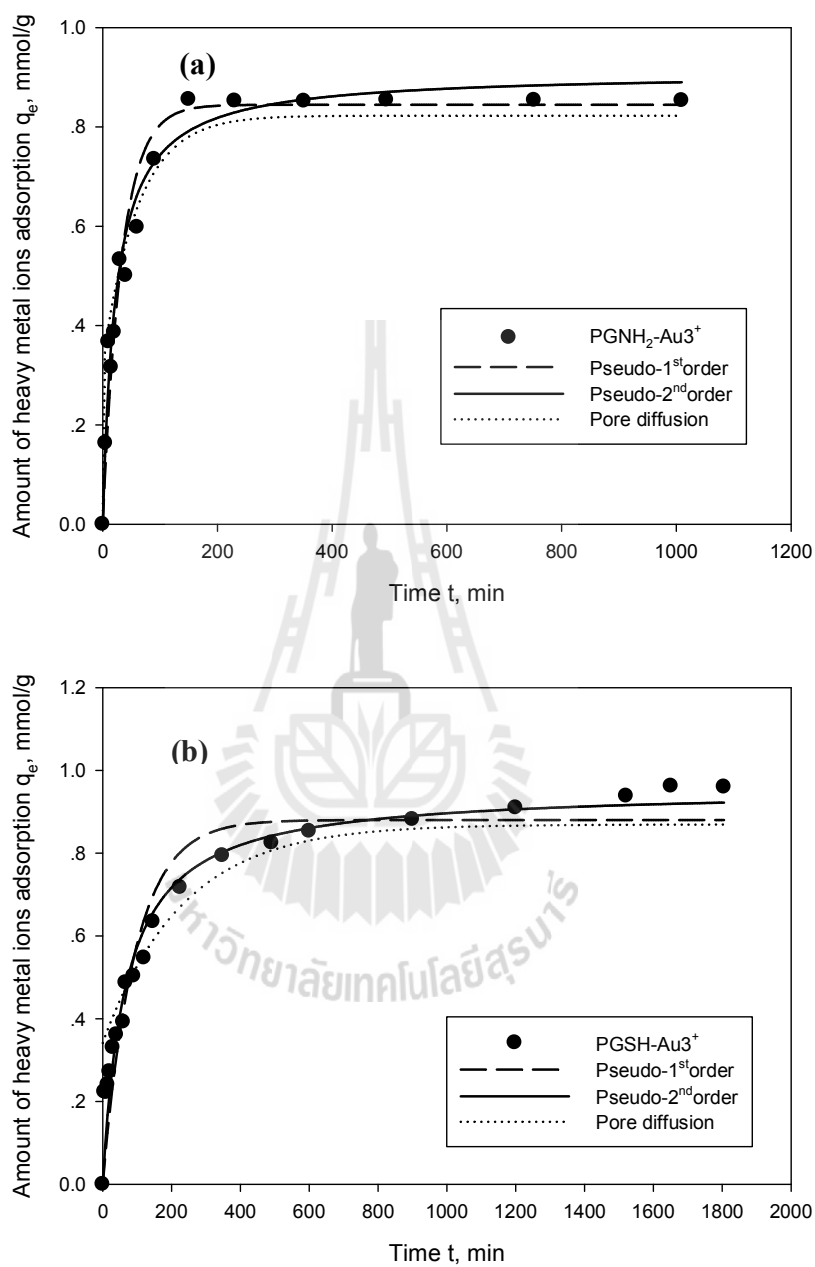


**Figure 3.24** Comparison of experimental and model predicted adsorption kinetic for gold adsorption by (a)  $\text{PGNH}_2$  and (b)  $\text{PGSH}$  at  $25^\circ\text{C}$ .

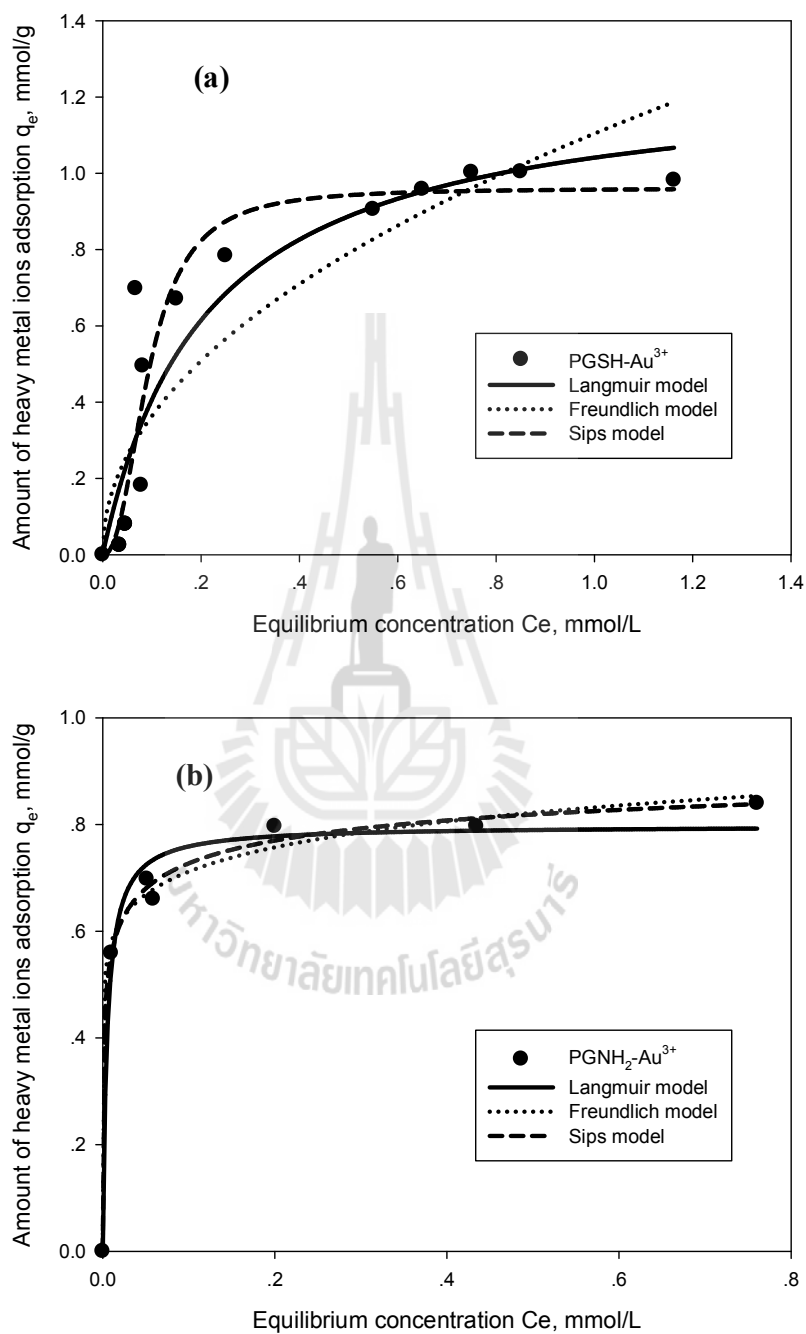


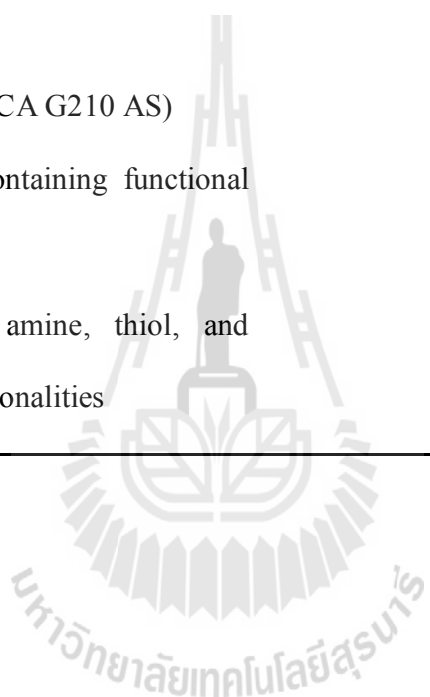
**Figure 3.25** Adsorption isotherms of gold by PGNH<sub>2</sub> and PGSH at 25 °C.

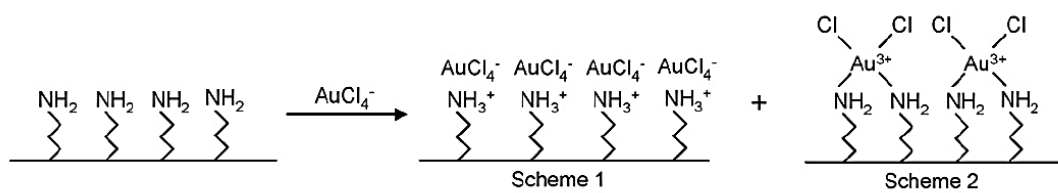
**Table 3.13** Fitting parameters of adsorption models for adsorbed gold by PG-NH<sub>2</sub> and PG-SH at 25 °C.

Isotherm equation	Parameters	Adsorbent	
		PG-NH <sub>2</sub>	PG-SH
Langmuir model	q <sub>m</sub> , mmol/g	0.7978	1.2594
	K <sub>L</sub>	195.8428	4.7673
	R <sup>2</sup>	0.9806	0.8669
Freundlich model	n <sub>F</sub>	11.1563	2.0729
	K <sub>F</sub>	0.8747	1.1039
	R <sup>2</sup>	0.9932	0.8013
Sips model	q <sub>ms</sub> , mmol/g	0.9991	0.9608
	K <sub>S</sub>	199.7577	10.6883
	n <sub>S</sub>	3.0432	0.4254
	R <sup>2</sup>	0.9957	0.9105

**Table 3.14 Adsorption capacity for gold ions of different common adsorbents**

<b>Adsorbents</b>	<b>Maximum adsorption capacity, mmol/g</b>
PG-NH <sub>2</sub> (in this work)	0.99
PG-SH (in this work)	0.83
NH <sub>2</sub> -MCM-41	1.40
Activated carbon	0.18
Commercial carbon (PICA G210 AS)	0.51
Polymer with sulfur-containing functional groups	0.4-6.5
Different resin with amine, thiol, and amine-mercaptan functionalities	2.2





Ion exchange

Complexion

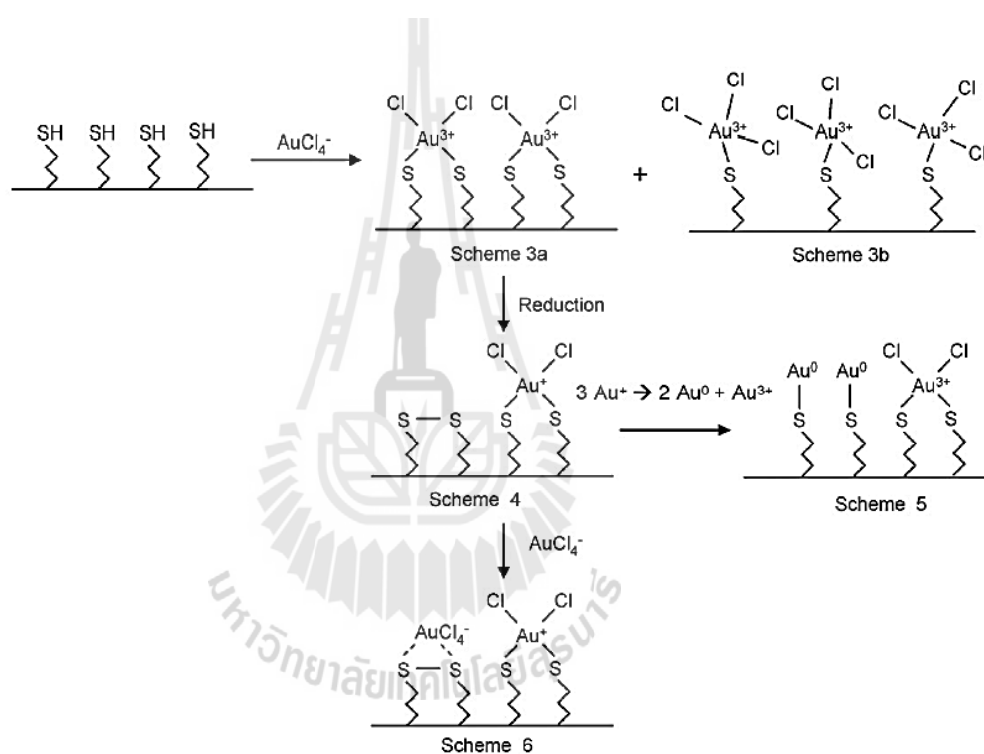


**Figure 3.26** Proposed mechanism scheme for gold adsorption onto aminopropyls and thiopropyls grafted porous glass. (Trokhimchuk et al., 2004)

### 3.5.3 Adsorption of binary ions ( $\text{Cu}^{2+}/\text{Ag}^+$ )

In this section, the study on the adsorption of binary metal ions of  $\text{Cu}^{2+}/\text{Ag}^+$  by the modified porous glass adsorbents ( $\text{PGNH}_2$  and  $\text{PGSH}$ ) is presented.

**Figure 3.27** shows the adsorption isotherms of  $\text{Cu}^{2+}$  and  $\text{Ag}^+$  in single and binary systems. It is surprising to observe that there is virtually no difference in the adsorbed capacity of  $\text{Cu}^{2+}$  by  $\text{PGNH}_2$  and  $\text{Ag}^+$  by  $\text{PGSH}$  in the two adsorption systems. This indicates that the introduced functional group on the porous glass surface is able to impart a characteristic of strong specificity to the respective adsorbent so that the selective adsorption of a given species can take place irrespective of the presence of other metal ions in the solution. In other words, there is a strong definite affinity of adsorption sites toward a specific species without competing with other available metal ion species. Although it was found that the isotherm of a preferable metal ion in a binary mixture of  $\text{Cu}^{2+}$  and  $\text{Ag}^+$  was the same as that in the pure component system, it might be worthwhile to analyze the equilibrium adsorption of  $\text{Cu}^{2+}/\text{Ag}^+$  mixture by the theories of mixture adsorption.

As a result, the experimental isotherms of a binary mixture of  $\text{Cu}^{2+}/\text{Ag}^+$  were tested against those predicted by three adsorption models, namely the extended Langmuir equation, the hybrid Langmuir-Freundlich equation and the ideal adsorption solution theory. The first two models are considered as empirical ones in that the model parameters are optimally searched by applying the regression analysis to minimize the total sum of square error (SSE) between the experimental and the calculated results, defined according to the following objective function,



$$SSE = \sum_{i=1}^N [(q_{1,\text{exp}} - q_{1,\text{cal}})^2 + (q_{2,\text{exp}} - q_{2,\text{cal}})^2] \quad (3.51)$$

where  $q_{1,\text{exp}}$  and  $q_{2,\text{exp}}$  are the experimental amounts adsorbed at equilibrium for component 1 and 2, respectively,  $q_{1,\text{cal}}$  and  $q_{2,\text{cal}}$  are the corresponding values obtained from the model calculation, and  $N$  is the number of data points.

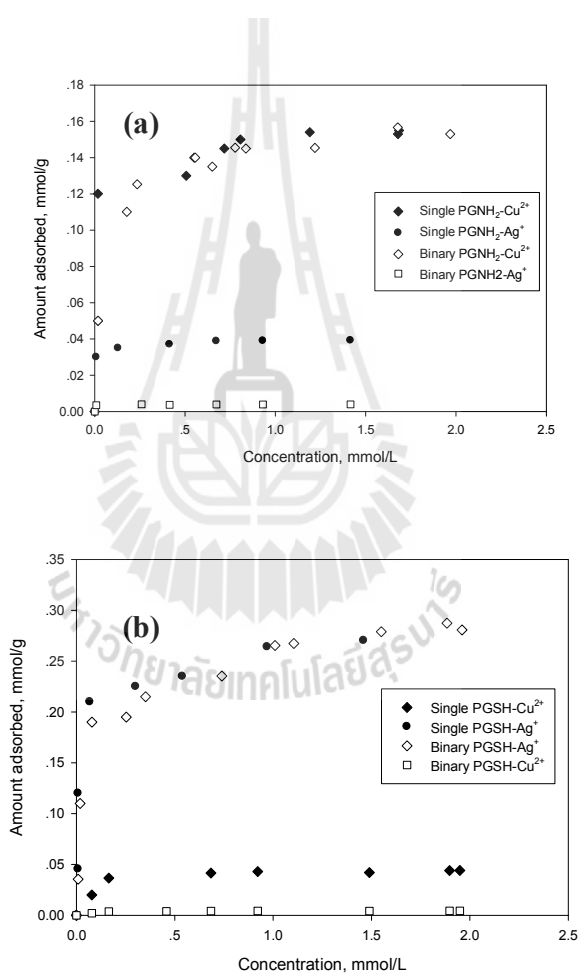


**Figure 3.27** Comparison of single component adsorption (filled symbol) and binary component (open symbol) adsorption of Ag<sup>+</sup> and Cu<sup>2+</sup> onto (a) PG-NH<sub>2</sub> and (b) PG-SH

### 3.5.3.1 The extended Langmuir equation

Starting with the extended Langmuir equation, which for binary adsorption of  $\text{Ag}^+(1)$  and  $\text{Cu}^{2+}(2)$ , it reads

$$q_1 = \frac{V_{m1}K_{L1}C_e}{1 + V_{m1}K_{L1} + V_{m2}K_{L2}} \quad (3.52)$$

and

$$q_2 = \frac{V_{m2}K_{L2}C_e}{1 + V_{m1}K_{L1} + V_{m2}K_{L2}} \quad (3.53)$$

There are five proposed fitting schemes to be tested, as shown in **Table 3.15 and Table 3.16** for  $\text{PGNH}_2$  and  $\text{PGSH}$  samples along with the values of fitted parameters of each scheme and the corresponding sum of square error (SSE) used for checking the goodness of data fitting. Comparison between the experimental and predicted isotherm data based on the various calculation schemes is shown plotted in **Figure 3.28 and Figure 3.29**.

Scheme I is a straightforward data fitting using the direct value of pure component parameters ( $K_{L1}$ ,  $K_{L2}$ ,  $V_{m1}$  and  $V_{m2}$ ). Scheme II is similar to Scheme I but imposing a criteria of equal monolayer capacity for component 1 and 2 ( $V_{m1} = V_{m2} = V_m$ ), allowing only one parameter to be optimized. Scheme III utilizes the affinity constants ( $K_{L1}$  and  $K_{L2}$ ) from the pure component adsorption data but requires the

optimized parameters of  $V_{m1}$  and  $V_{m2}$ . Scheme IV is a 3-parameter equation from which the affinity or Langmuir constants ( $K_{L1}$  and  $K_{L2}$ ) and a constant monolayer capacity ( $V_{m1} = V_{m2} = V_m$ ) need to be optimized. Finally, Scheme V required the best fitted parameters for both the Langmuir constants ( $K_{L1}$  and  $K_{L2}$ ) and the monolayer capacity parameters ( $V_{m1}$  and  $V_{m2}$ ).

Based on the value of SSE in **Table 3.15** and **Table 3.16** and **Figure 3.28** and **Figure 3.29**, the simplest Scheme I and Scheme II cannot correctly predict the isotherm results. They both over predict and under predict the adsorption of  $Ag^+$  and  $Cu^{2+}$  in the mixture, respectively, for  $PGNH_2$  adsorbent. The same is true for  $PGSH$  in over predicting and under predicting the amount adsorbed of  $Cu^{2+}$  and  $Ag^+$ , respectively. Scheme III shows reasonable data fitting to the experimental isotherms although the same deviation can still be observed. Scheme IV and V can predict the adsorption isotherms equally well. However, since Scheme V contains four parameters, it is suggested that Scheme IV, a 3-parameters equation, should be most appropriate for describing the adsorption isotherm data for  $Ag^+ - Cu^{2+}$  system by both the  $PGNH_2$  and  $PGSH$  adsorbents.

**Table 3.15** Calculation scheme for fitting the extended Langmuir isotherm with the experimental isotherm data of  $\text{Ag}^+$ - $\text{Cu}^{2+}$  mixture using modified porous glass adsorbents from fly ash of (PGNH<sub>2</sub> adsorbent).

Method	Fixed parameters	Floated parameters	Number of parameters	Sum of square error (SSE)
I	$K_{L1} = 56.6527$ $K_{L2} = 71.8022$ $V_{m1} = 0.0395$ $V_{m2} = 0.1493$ (from pure component isotherm data)	-	-	0.0178
II	$K_{L1} = 56.6527$ $K_{L2} = 71.8022$ (from pure component isotherm data)	$V_{m1} = V_{m2} = 0.1505$	1	0.0366
III	$K_{L1} = 56.6527$ $K_{L2} = 71.8022$ (from pure component isotherm data)	$V_{m1} = 0.0091$ $V_{m2} = 0.2334$	2	0.0047
IV	-	$K_{L1} = 0.6956$ $K_{L2} = 25.7438$ $V_{m1} = V_{m2} = 0.1522$	3	0.0006

**Table 3.15** Calculation scheme for fitting the extended Langmuir isotherm with the experimental isotherm data of  $\text{Ag}^+$ - $\text{Cu}^{2+}$  mixture using modified porous glass adsorbents from fly ash of (PGNH<sub>2</sub> adsorbent). (continued).

Method	Fixed parameters	Floated parameters	Number of parameters	Sum of square error (SSE)
V	-	$K_{L1} = 0.1343$ $K_{L2} = 26.4474$ $V_{m1} = 0.0001$ $V_{m2} = 0.1488$	4	0.0001

**Table 3.15** Calculation scheme for fitting the extended Langmuir isotherm with the experimental isotherm data of  $\text{Ag}^+$ - $\text{Cu}^{2+}$  mixture using modified porous glass adsorbents from fly ash of (PGSH adsorbent).

Method	Fixed parameters	Floated parameters	Number of parameters	Sum of square error (SSE)
I	$K_{L1} = 52.8128$ $K_{L2} = 13.8076$ $V_{m1} = 0.2583$ $V_{m2} = 0.0458$ (from pure component isotherm data)	-	-	0.0253

**Table 3.15** Calculation scheme for fitting the extended Langmuir isotherm with the experimental isotherm data of  $\text{Ag}^+$ - $\text{Cu}^{2+}$  mixture using modified porous glass adsorbents from fly ash of (PGSH adsorbent).(continued).

Method	Fixed parameters	Floated parameters	Number of parameters	Sum of square error (SSE)
II	$K_{L1} = 52.8128$ $K_{L2} = 13.8076$ (from pure component isotherm data)	$V_{m1} = V_{m2} = 0.2963$	1	0.0414
III	$K_{L1} = 52.8128$ $K_{L2} = 13.8076$ (from pure component isotherm data)	$V_{m1} = 0.3218$ $V_{m2} = 0.0161$	2	0.0073
IV	-	$K_{L1} = 21.4046$ $K_{L2} = 0.1851$ $V_{m1} = V_{m2} = 0.2732$	3	0.0043
V	-	$K_{L1} = 21.6262$ $K_{L2} = 0.0001$ $V_{m1} = 0.2708$ $V_{m2} = 0.0715$	4	0.0043

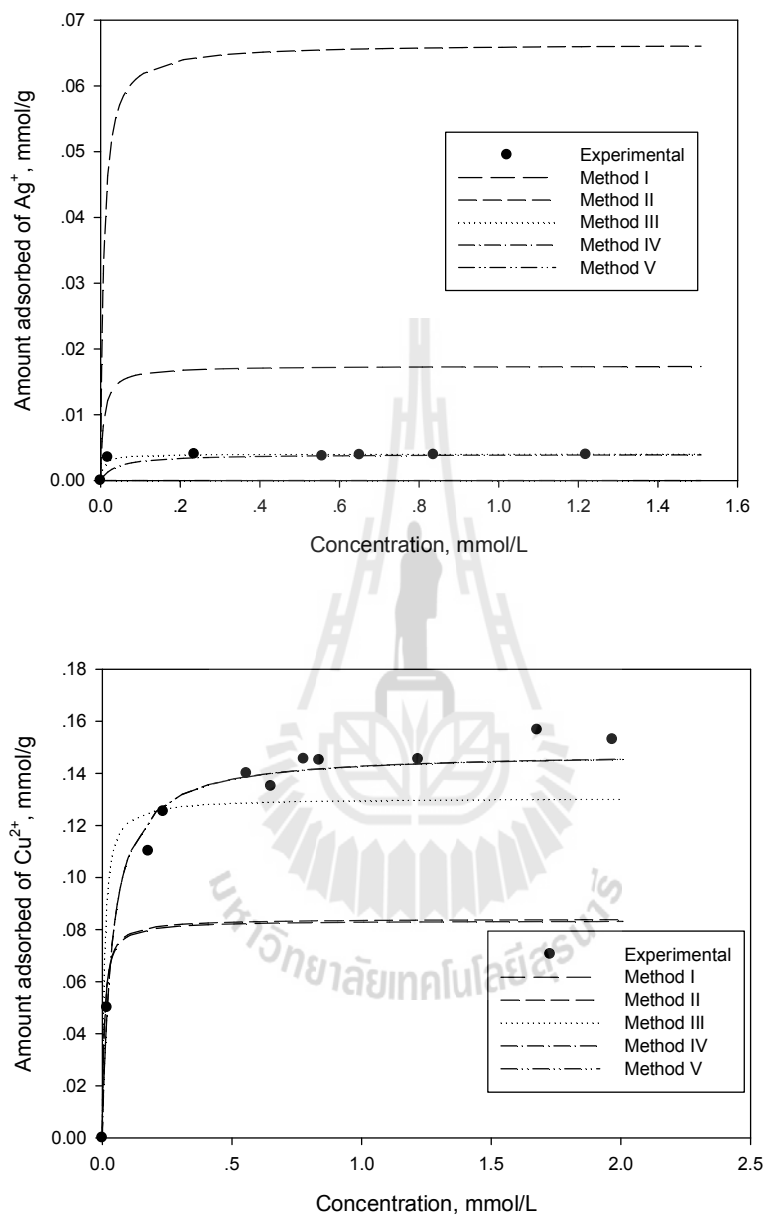


**Figure 3.28** Predicted and experimental isotherm data for adsorption of  $\text{Ag}^+$  -  $\text{Cu}^{2+}$  mixture by PG- $\text{NH}_2$  porous glass.

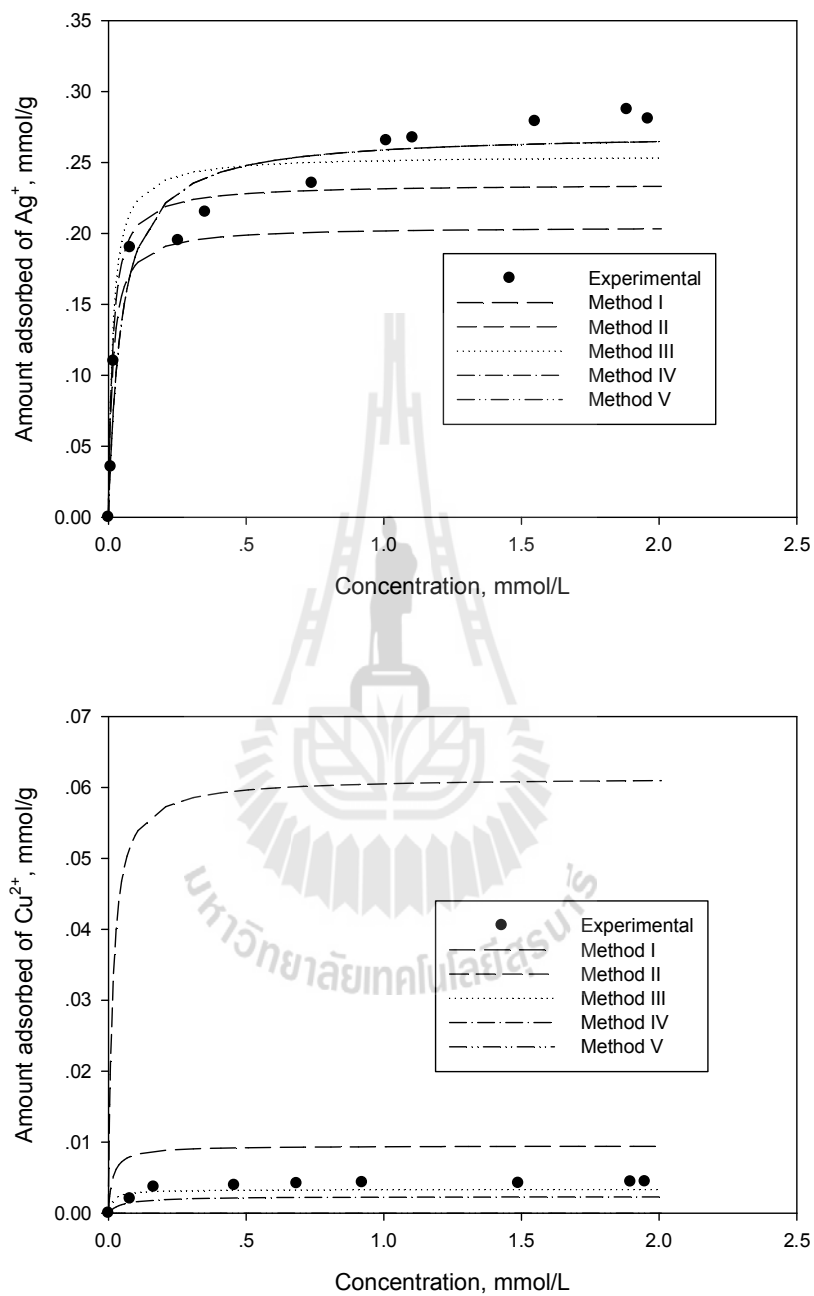


**Figure 3.29** Predicted and experimental isotherm data for adsorption of  $\text{Ag}^+$  -  $\text{Cu}^{2+}$  mixture by PG-SH porous glass.



### 3.5.3.2 The extended Langmuir-Freundlich isotherm

Next, the Langmuir-Freundlich isotherm or Sips isotherm for pure component adsorption was extended to predict the adsorption of binary metal ions of  $\text{Ag}^+$ (1) and  $\text{Cu}^{2+}$ (2) using  $\text{PGNH}_2$  and  $\text{PGSH}$  as adsorbents. The extended Langmuir-Freundlich isotherm is a three-parameter adsorption model and reads

$$\frac{q_1}{q_{S1}} = \frac{K_{S1} C_e^{1/n_{S1}}}{1 + K_{S1} C_e^{1/n_{S1}} + K_{S2} C_e^{1/n_{S2}}} \quad (3.54)$$

and

$$\frac{q_2}{q_{S2}} = \frac{K_{S2} C_e^{1/n_{S2}}}{1 + K_{S1} C_e^{1/n_{S1}} + K_{S2} C_e^{1/n_{S2}}} \quad (3.55)$$

**Table 3.17** and **Table 3.18** show the six fitting parameters of Sips equation for pure component adsorption of  $\text{Ag}^+$  and  $\text{Cu}^{2+}$  by the porous glass adsorbents ( $\text{PGNH}_2$  and  $\text{PGSH}$ ). **Table 3.17** and **Table 3.18** also lists the proposed six calculation schemes and the derived parameters of each scheme. Starting with Scheme I, it computes the mixture isotherms from the direct values of pure component parameter ( $K_{S1}$ ,  $K_{S2}$ ,  $q_{S1}$ ,  $q_{S2}$ ,  $n_{S1}$ ,  $n_{S2}$ ). Scheme II fixes the 4 parameters of the pure component adsorption ( $K_{S1}$ ,  $K_{S2}$ ,  $n_{S1}$ ,  $n_{S2}$ ) constants and optimizes the monolayer capacity ( $q_{S1}$ ,  $q_{S2}$ ). Scheme III is similar to Scheme II but the surface heterogeneity parameter ( $n_{S1}$ ,  $n_{S2}$ ) are optimized instead. Scheme IV optimized four model parameters ( $K_{S1}$ ,  $K_{S2}$ ,  $q_{S1}$ ,  $q_{S2}$ ) holding the parameters  $n_{S1}$ ,  $n_{S2}$  constants. Scheme V optimizes four model parameters ( $K_{S1}$ ,  $K_{S2}$ ,  $n_{S1}$ ,

$n_{S2}$ ) holding the adsorption capacity parameters,  $q_{S1}$ ,  $q_{S2}$  constants. The last calculation scheme, Scheme VI, involves the optimization of all six model parameters of the isotherm equation.

The fitting accuracy of each calculation scheme is decided from the value of sum of square error (SSE) shown in **Table 3.17** and **Table 3.18**. **Figure 3.30** and **Figure 3.31** compares the isotherms derived from experiments and model prediction. Based on the overall fitting accuracy of both metal ions ( $Ag^+$  and  $Cu^{2+}$ ) by both adsorbents, it can be reasonably inferred that Scheme II computing is most suitable for the prediction of adsorption of a binary mixture of  $Ag^+$  and  $Cu^{2+}$  in solution by the  $PGNH_2$  and  $PGSH$  adsorbents. Furthermore, the values of all model parameters derived from Scheme II are in the same order of magnitude as the corresponding values of pure component adsorption system. However, if the fitting accuracy is based on the data most of adsorbed species that is, adsorption of  $Cu^{2+}$  by  $PGNH_2$  and adsorption of  $Ag^+$  by  $PGSH$ , it is clearly seen that Scheme IV, V and VI are most appropriate.

**Table 3.17** Calculation scheme for fitting the extended Langmuir–Freundlich isotherm with the experimental isotherm data of  $\text{Ag}^+$ - $\text{Cu}^{2+}$  mixture using modified porous glass adsorbents from fly ash for  $\text{PGNH}_2$  adsorbent.

Calculation Scheme	Fixed parameters	Floated parameters	SSE
I	$K_{S1} = 132.1$ , $K_{S2} = 7.1468$ $q_{s1} = 0.0039$ , $q_{s2} = 0.1673$ $n_{s1} = 1.7085$ , $n_{s2} = 1.4152$ (from pure component isotherm data)	-	0.0087



**Table 3.17** Calculation scheme for fitting the extended Langmuir –Freundlich isotherm with the experimental isotherm data of  $\text{Ag}^+$ - $\text{Cu}^{2+}$  mixture using modified porous glass adsorbents from fly ash for  $\text{PGNH}_2$  adsorbent

Calculation Scheme	Fixed parameters	Floated parameters	SSE
II	$K_{S1} = 132.1, K_{S2} = 7.1468$ $n_{s1} = 1.7085, n_{s2} = 1.4152$ (from pure component isotherm data)	$q_{s1} = 0.0041$ $q_{s2} = 0.2686$	0.0055
III	$K_{S1} = 132.1, K_{S2} = 7.1468$ $q_{s1} = 0.0039, q_{s2} = 0.1673$ (from pure component isotherm data)	$n_{s1} = 1.7103$ $n_{s2} = 1.4348$	0.0867
IV	$n_{s1} = 1.7085, n_{s2} = 1.4152$ (from pure component isotherm data)	$K_{S1} = 0.4348, K_{S2} = 7.2610$ $q_{s1} = 0.0775, q_{s2} = 0.1749$	0.0000 7
V	$q_{s1} = 0.0039, q_{s2} = 0.1673$ (from pure component isotherm data)	$K_{S1} = 0.1315, K_{S2} = 7.5298$ $n_{s1} = 1.7103, n_{s2} = 1.4348$	0.0000 15
VI	-	$K_{S1} = 1.2839, K_{S2} = 12.1321$ $q_{s1} = 0.0043, q_{s2} = 0.1720$ $n_{s1} = 1.2837, n_{s2} = 1.1953$	0.0000 14

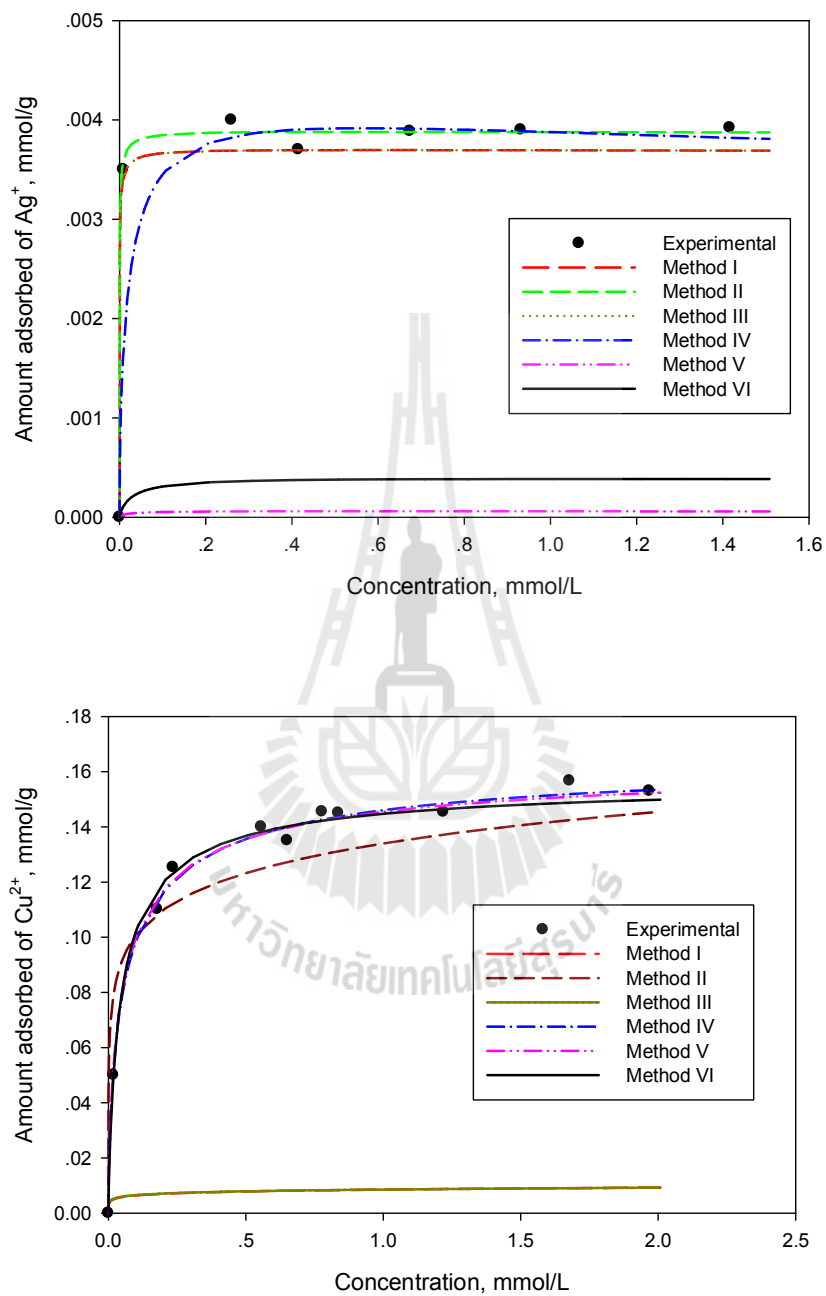


**Figure 3.30** Predicted and experimental isotherm data for adsorption of  $\text{Ag}^+$  -  $\text{Cu}^{2+}$  mixture by PG- $\text{NH}_2$  porous glass.

**Table 3.18** Calculation scheme for fitting the extended Langmuir –Freundlich isotherm with the experimental isotherm data of  $\text{Ag}^+$ - $\text{Cu}^{2+}$  mixture using modified porous glass adsorbents from fly ash for PGSH adsorbent.

Method	Fixed parameters	Floated parameters	SSE
I	$K_{S1} = 4.4972, K_{S2} = 6.5203$ $q_{s1} = 0.3203, q_{s2} = 0.0049$ $n_{s1} = 1.6591, n_{s2} = 1.3605$ (from pure component isotherm data)	-	0.1313
II	$K_{S1} = 4.4972, K_{S2} = 6.5203$ $n_{s1} = 1.6591, n_{s2} = 1.3605$ (from pure component isotherm data)	$q_{s1} = 0.6611, q_{s2} = 0.0076$	0.0118
III	$K_{S1} = 4.4972, K_{S2} = 6.5203$ $q_{s1} = 0.3203, q_{s2} = 0.0049$ (from pure component isotherm data)	$n_{s1} = 5.2245, n_{s2} = 4.9121$	0.1278
IV	$n_{s1} = 1.6591, n_{s2} = 1.3605$ (from pure component isotherm data)	$K_{S1} = 4.1290, K_{S2} =$ $0.0001$ $q_{s1} = 0.3233, q_{s2} = 0.0054$	0.0012
V	$q_{s1} = 0.3203, q_{s2} = 0.0049$ (from pure component isotherm data)	$K_{S1} = 4.1058, K_{S2} =$ $0.0001$ $n_{s1} = 1.7875, n_{s2} = 4.3193$	0.0011

**Table 3.18** Calculation scheme for fitting the extended Langmuir –Freundlich isotherm with the experimental isotherm data of  $\text{Ag}^+$ - $\text{Cu}^{2+}$  mixture using modified porous glass adsorbents from fly ash for PGSH adsorbent (continued).

Method	Fixed parameters	Floated parameters	SSE
VI	-	$K_{S1} = 0.8914$ $K_{S2} = 0.0004$ $q_{s1} = 0.5446$ $q_{s2} = 0.0044$ $n_{s1} = 3.1049$ $n_{s2} = 2.0048$	0.0003



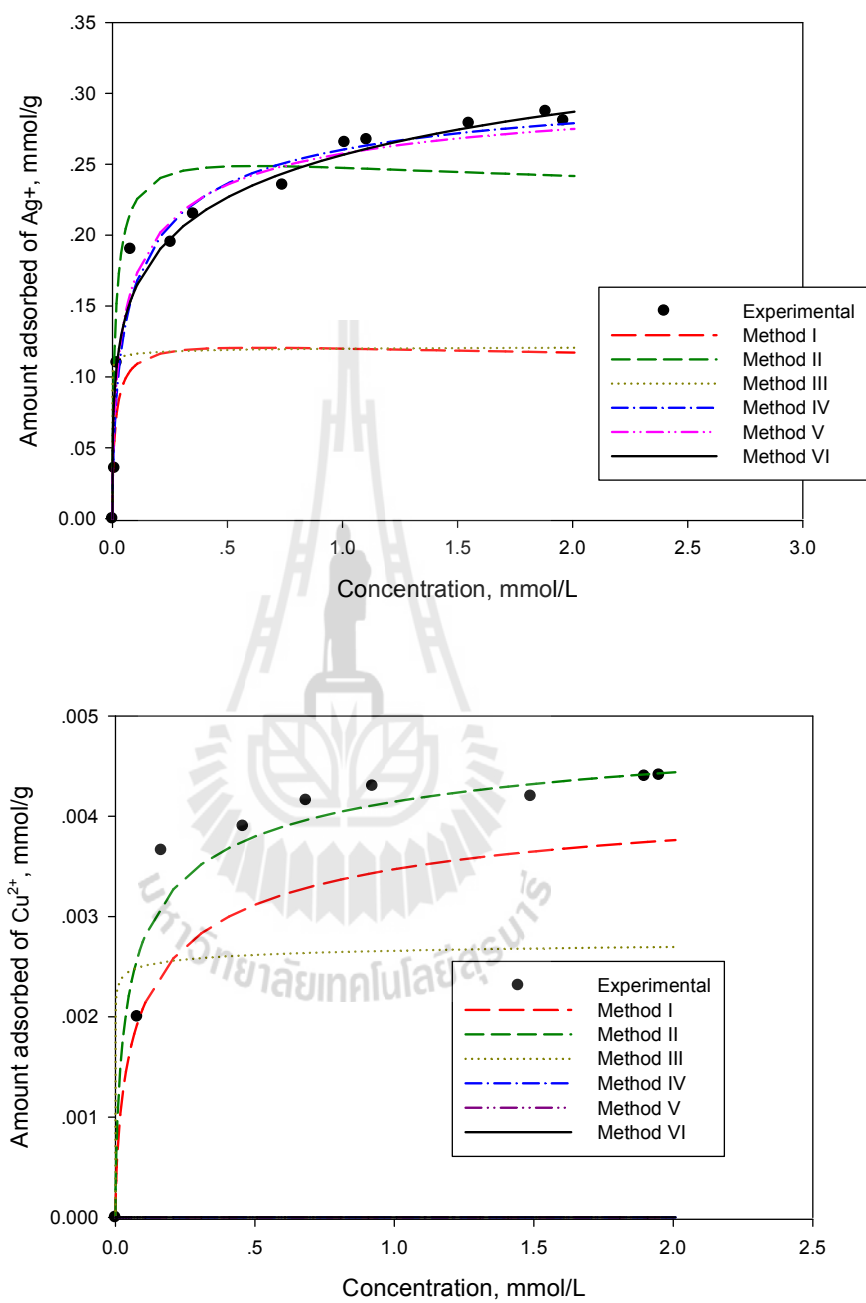


**Figure 3.31** Predicted and experimental isotherm data for adsorption of  $\text{Ag}^+$  -  $\text{Cu}^{2+}$  mixture by PG-SH porous glass.



### 3.5.3.3 The Ideal Adsorption Solution Theory (IAST)

Next, the equilibrium isotherms for the adsorption of a mixture of  $\text{Cu}^{2+}$ - $\text{Ag}^+$  mixture by the modified porous glass  $\text{PGNH}_2$  and  $\text{PGSH}$  were analyzed with the Ideal Adsorption Solution Theory (IAST). When applying this theory to a liquid adsorption system, the relevant equations and symbolism are as follows.

(1) The sum of the individual loading,  $q_i$ , gives the total surface loading,  $q_T$ . That is

$$q_t = \sum_{i=1}^N q_i \quad (3.56)$$

(2) Definition of the mole fraction of adsorbed component  $i$  on the adsorption surface gives

$$x_i = \frac{q_i}{q_t} \quad (3.57)$$

(3) Equation that relates adsorbate concentration in the liquid mixture and the hypothetical concentration in pure state ( $C_i^o$ ) analogous to the Raoult's law.

$$C_i = x_i C_i^o (II) \quad (3.58)$$

(4) Lewis equation relating total loading ( $q_t$ ) in the mixture and loading in pure state ( $q_i^o$ )

$$\frac{1}{q_t} = \sum_{i=1}^N \frac{Z_i}{q_i^o} \quad (3.59)$$

(5) Equation of equal spreading pressure of individual component, thus for a binary mixture, we have

$$\frac{\pi_1^o A}{RT} = \frac{\pi_2^o A}{RT} = \frac{\pi_m A}{RT}$$

or

$$\int_0^{q_1^o} \frac{d \ln C_1^o}{d \ln q_1^o} dq_1^o = \int_0^{q_2^o} \frac{d \ln C_2^o}{d \ln q_2^o} dq_2^o \quad (3.60)$$

A straightforward calculation can be performed by solving the above set of equations, knowing the pure component isotherm data. Now, if the isotherms of component 1 and 2 can be represented by the Langmuir equation,

$$q_1^o = \frac{q_{m1} b_1 C_1^o}{1 + b_1 C_1^o} \quad (3.61)$$

and

$$q_2^o = \frac{q_{m2} b_2 C_2^o}{1 + b_2 C_2^o} \quad (3.62)$$

Then, the IAST equations can be directly solved to predict the adsorption isotherm of each component in the mixture, according to the following steps.

(i) Combining Equation (3.60) with Equations (3.61) and (3.62),

we obtain

$$\left[1 + \frac{b_1 C_1}{x_1}\right]^{q_{m1}} = \left[1 + \frac{b_2 C_2}{x_2}\right]^{q_{m2}} \quad (3.63)$$

with  $x_1 + x_2 = 1$

(ii) Given the values of  $C_{1,\text{exp}}$ ,  $C_{2,\text{exp}}$ ,  $b_1$ ,  $b_2$ ,  $q_{m1}$  and  $q_{m2}$ , the values of corresponding  $x_1$  can be obtained and the mole fraction of the second component follows from,  $x_2 = 1 - x_1$

(iii) The hypothetical solute concentrations of pure component  $C_1^o$  and  $C_2^o$  are derived from Equation (3.58), that is,

$$C_1^o = \frac{C_1}{x_1}$$

$$C_2^o = \frac{C_2}{x_2}$$

(iv)  $q_1^o$  and  $q_2^o$  are now obtained from Equation (3.61) and (3.62) and the total adsorbed phase concentration is readily obtained from Equation (3.59).

Thus,

$$q_t = \left[ \frac{x_1}{q_1^o} + \frac{x_2}{q_2^o} \right]^{-1}$$

(v) The amount adsorbed for component 1 and 2 are calculated from Equation (3.57)

$$q_1 = x_1 q_t$$

$$q_2 = x_2 q_t$$

The model accuracy can be determined by computing the sum of square error (SSE), defined as

$$SSE = \sum_{i=1}^N (q_{1,\text{exp}} - q_{1,\text{model}})^2 + (q_{2,\text{exp}} - q_{2,\text{model}})^2$$

where

N is the number of data points.

If the pure component isotherms can be described by the

Freundlich equation which reads

$$q_1^o = K_{F1} (C_1^o)^{1/n_1}$$

$$q_2^o = K_{F2} (C_2^o)^{1/n_2}$$

and when combined with Equation (3.60), we have

$$n_1 K_{F1} \left( \frac{C_1}{x_1} \right)^{1/n_1} = n_2 K_{F2} \left( \frac{C_2}{1-x_1} \right)^{1/n_2} \quad (3.64)$$

The calculation step can be made just the same as in the case of using Langmuir equation to arrive at adsorption isotherms of a binary mixture adsorption system.

**Table 3.9** shows the Langmuir parameters ( $K_L$  and  $q_m$ ) for pure component adsorption of  $\text{Cu}^{2+}$  and  $\text{Ag}^+$  by  $\text{PGNH}_2$  and  $\text{PGSH}$  adsorbents. **Table 3.19 and 3.20** list the calculated results from IAST using Langmuir model and **Figures 3.32 and 3.33** compare the experimental and calculated amount of  $\text{Cu}^{2+}$  and  $\text{Ag}^+$  adsorbed by the two porous glass samples. In general, the overall fitting is reasonable for both adsorbents up to the bulk solute concentration of 2.0 mM, with the values of SSE being 0.17 and 0.59 for  $\text{PGNH}_2$  and  $\text{PGSH}$ , respectively, indicating a better fit of the former.

**Table 3.9** lists the Freundlich parameters ( $K_F$  and  $n_F$ ) for the adsorption of  $\text{Cu}^{2+}$  and  $\text{Ag}^+$  by the two modified porous glasses. **Tables 3.21 and 3.22** show the calculated results from IAST using the Freundlich equation. **Figure 3.34 and 3.35** shows the model fitting to the experimental isotherms of  $\text{Cu}^{2+}$  and  $\text{Ag}^+$  in the solution mixture by  $\text{PGNH}_2$  and  $\text{PGSH}$ , respectively. It is clearly observed that the model prediction is excellent, giving SSE to be 0.0004 and 0.00067 for  $\text{PGNH}_2$  and  $\text{PGSH}$ , respectively. The superiority of Freundlich isotherm over the Langmuir isotherm in fitting a binary adsorption of  $\text{Cu}^{2+}$  and  $\text{Ag}^+$  by IAST is obvious, although both adsorption models can describe the pure-component isotherm data equally well. Finally, It can be concluded that IAST, which is the thermodynamic approach, is more effective than the empirical approach (Extended Langmuir and Extended Langmuir-Freundlich isotherms) in predicting the binary adsorption isotherms of  $\text{Cu}^{2+}$  and  $\text{Ag}^+$  by porous glass with introduced thiol and amine functional groups. The IAST has many advantages including, it is based on sound thermodynamic consideration, the computation is straightforward using a set of equations without the need to optimized the model parameters, the

calculation requires only the pure component isotherm data and it works well for both gas and liquid adsorption systems.



**Table 3.19** Calculated parameters of IAST using the Langmuir isotherm equation for PG-NH<sub>2</sub> (1=Ag<sup>+</sup>, 2=Cu<sup>2+</sup>)

Given		Experimental		x <sub>1</sub>	x <sub>2</sub>	C <sub>1</sub> <sup>0</sup> (mmol/L)	C <sub>2</sub> <sup>0</sup> (mmol/L)	q <sub>1</sub> <sup>0</sup> (mmol/g)	q <sub>2</sub> <sup>0</sup> (mmol/g)	q <sub>t</sub> (mmol/g)	q <sub>1,model</sub> (mmol/g)	q <sub>2,model</sub> (mmol/g)
C <sub>e1</sub> (mmol/L)	C <sub>e2</sub> (mmol/L)	q <sub>1,exp</sub> (mmol/g)	q <sub>2,exp</sub> (mmol/g)									
0.0000	0.0000	0.0000	0.0000	0.0000	0.0000	0.0000	0.0000	0.0000	0.0000	0.0000	0.0000	0.0000
0.0090	0.0185	0.0035	0.0500	0.0029	0.9971	3.0903	0.0185	0.0393	0.0853	0.0850	0.0002	0.0847
0.2597	0.2356	0.0040	0.1253	0.0001	0.9999	2449.85	0.2356	0.0395	0.1410	0.1409	0.0000	0.1409
0.4149	0.5567	0.0037	0.1400	0.0001	0.9999	5412.21	0.5568	0.0395	0.1457	0.1456	0.0000	0.1456
0.6740	0.6508	0.0039	0.1350	0.0000	1.0000	14314.65	0.6508	0.0395	0.1462	0.1462	0.0000	0.1461
0.9313	0.8368	0.0039	0.1450	0.0000	1.0000	34764.68	0.8368	0.0395	0.1469	0.1468	0.0000	0.1468
1.4160	1.2190	0.0039	0.1454	0.0001	0.9999	14159.91	1.2192	0.0395	0.1476	0.1476	0.0000	0.1476

**Table 3.20** Calculated parameters of IAST using the Langmuir isotherm equation for PG-SH (1=Ag<sup>+</sup>, 2=Cu<sup>2+</sup>)

Given		Experimental		x <sub>1</sub>	x <sub>2</sub>	C <sub>1</sub> <sup>0</sup> (mmol/L)	C <sub>2</sub> <sup>0</sup> (mmol/L)	q <sub>1</sub> <sup>0</sup> (mmol/g)	q <sub>2</sub> <sup>0</sup> (mmol/g)	q <sub>t</sub> (mmol/g)	q <sub>1,model</sub> (mmol/g)	q <sub>2,model</sub> (mmol/g)
C <sub>e1</sub> (mmol/L)	C <sub>e2</sub> (mmol/L)	q <sub>1,exp</sub> (mmol/g)	q <sub>2,exp</sub> (mmol/g)									
0.0000	0.0000	0.0000	0.0000	0.0000	0.0000	0.0000	0.0000	0.0000	0.0000	0.0000	0.0000	0.0000
0.0190	0.0787	0.1100	0.0020	0.9793	0.0207	0.0194	3.8033	0.1308	0.0449	0.1258	0.1232	0.0026
0.2540	0.1651	0.1950	0.0037	0.9999	0.0001	0.2540	1650.55	0.2404	0.0458	0.2403	0.2403	0.0000
0.3517	0.4576	0.2150	0.0039	0.9999	0.0001	0.3518	4576.00	0.2451	0.0458	0.2450	0.2450	0.0000
0.7393	0.6839	0.2354	0.0042	0.9999	0.0001	0.7393	6838.91	0.2519	0.0458	0.2517	0.2517	0.0000
1.0097	0.9219	0.2654	0.0043	0.9999	0.0001	1.0098	9219.11	0.2535	0.0458	0.2534	0.2534	0.0000
1.5498	1.4893	0.2789	0.0042	0.9999	0.0001	1.5500	14893.47	0.2552	0.0458	0.2551	0.2550	0.0000
1.8834	1.8967	0.2873	0.0044	0.9999	0.0001	1.8836	18967.37	0.2557	0.0458	0.2556	0.2556	0.0000
1.9601	1.9489	0.2807	0.0044	0.9999	0.0001	1.9603	19489.32	0.2558	0.0458	0.2557	0.2557	0.0000



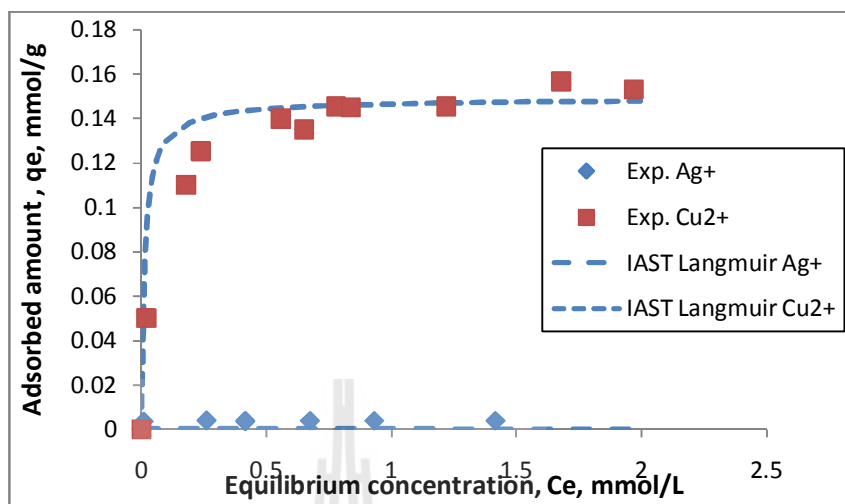


**Figure 3.32** Prediction of equilibrium isotherms of  $\text{Cu}^{2+}$ - $\text{Ag}^+$  mixture by IAST based on Langmuir equation for pure component adsorption (adsorbent used  $\text{PGNH}_2$ )

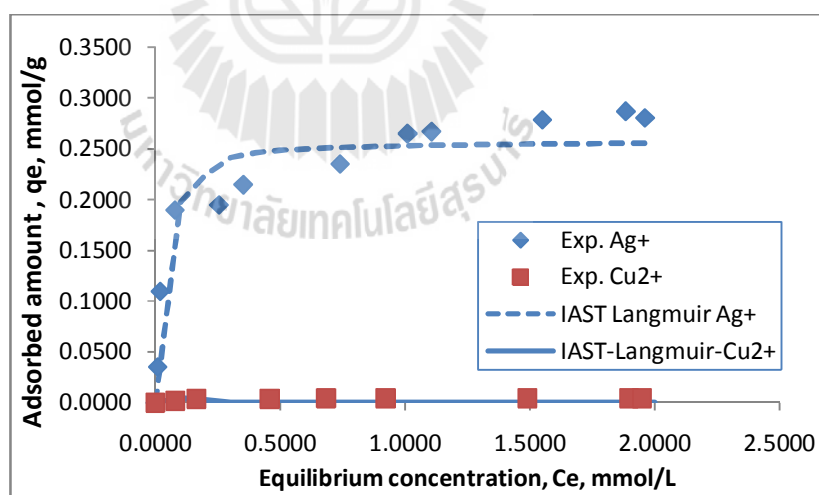


**Figure 3.33** Prediction of equilibrium isotherms of  $\text{Cu}^{2+}$ - $\text{Ag}^+$  mixture by IAST based on Langmuir equation for pure component adsorption (adsorbent used  $\text{PGSH}$ )

**Table 3.21** Calculated parameters for IAST using the Freundlich isotherm equation of PG-NH<sub>2</sub> (1=Ag<sup>+</sup>, 2=Cu<sup>2+</sup>)

Given		Experimental		x <sub>1</sub>	x <sub>2</sub>	C <sub>1</sub> <sup>o</sup> (mmol/L)	C <sub>2</sub> <sup>o</sup> (mmol/L)	q <sub>1</sub> <sup>o</sup> (mmol/g)	q <sub>2</sub> <sup>o</sup> (mmol/g)	q <sub>t</sub> (mmol/g)	q <sub>1,model</sub> (mmol/g)	q <sub>2,model</sub> (mmol/g)
C <sub>e1</sub> (mmol/L)	C <sub>e2</sub> (mmol/L)	q <sub>1,exp</sub> (mmol/g)	q <sub>2,exp</sub> (mmol/g)									
0.0000	0.0000	0.0000	0.0000	0.0000	0.0000	0.0000	0.0000	0.0000	0.0000	0.0000	0.0000	0.0000
0.0090	0.0185	0.0035	0.0500	0.1629	0.8371	0.0550	0.0221	0.0337	0.0887	0.0700	0.0114	0.0586
0.2597	0.1780	0.0040	0.1101	0.0001	0.9999	2596.88	0.1780	0.0582	0.1173	0.1173	0.0000	0.1173
0.4149	0.2356	0.0037	0.1253	0.0142	0.9858	29.13	0.2390	0.0463	0.1220	0.1192	0.0017	0.1175
0.6740	0.5567	0.0039	0.1400	0.0025	0.9975	272.40	0.5581	0.0519	0.1367	0.1361	0.0003	0.1358
0.9313	0.6508	0.0039	0.1350	0.0001	0.9999	7768.44	0.6509	0.0615	0.1395	0.1395	0.0000	0.1395
1.4160	0.7777	0.0039	0.1455	0.0022	0.9978	656.81	0.7794	0.0542	0.1429	0.1424	0.0003	0.1421

**Table 3.22** Calculated parameters for IAST using the Freundlich isotherm equation of PG-NH<sub>2</sub> (1=Ag<sup>+</sup>, 2=Cu<sup>2+</sup>)

Given		Experimental		x <sub>1</sub>	x <sub>2</sub>	C <sub>1</sub> <sup>o</sup> (mmol/L)	C <sub>2</sub> <sup>o</sup> (mmol/L)	q <sub>1</sub> <sup>o</sup> (mmol/g)	q <sub>2</sub> <sup>o</sup> (mmol/g)	q <sub>t</sub> (mmol/g)	q <sub>1,model</sub> (mmol/g)	q <sub>2,model</sub> (mmol/g)
C <sub>e1</sub> (mmol/L)	C <sub>e2</sub> (mmol/L)	q <sub>1,exp</sub> (mmol/g)	q <sub>2,exp</sub> (mmol/g)									
0.0000	0.0000	0.0000	0.0000	0.0000	0.0000	0.0000	0.0000	0.0000	0.0000	0.0000	0.0000	0.0000
0.0090	0.0787	0.0355	0.0020	0.9994	0.0006	0.0090	139.61	0.1084	0.0908	0.1084	0.1083	0.0001
0.0190	0.1651	0.1100	0.0037	0.9995	0.0005	0.0190	345.16	0.1251	0.1051	0.1251	0.1250	0.0001
0.0789	0.4576	0.1900	0.0039	0.9998	0.0002	0.0790	1920.52	0.1641	0.1386	0.1641	0.1641	0.0000
0.2540	0.6839	0.1950	0.0042	0.9999	0.0001	0.2540	6838.91	0.2051	0.1700	0.2051	0.2051	0.0000
0.3517	0.9219	0.2150	0.0043	0.9999	0.0001	0.3518	9219.11	0.2183	0.1784	0.2183	0.2182	0.0000
0.7393	1.4893	0.2354	0.0042	0.9999	0.0001	0.7393	14893.47	0.2515	0.1927	0.2515	0.2515	0.0000
1.0097	1.8967	0.2654	0.0044	0.9999	0.0001	1.0098	18967.37	0.2669	0.2004	0.2669	0.2669	0.0000
1.1052	1.9489	0.2674	0.0044	0.9999	0.0001	1.1054	19489.32	0.2715	0.2013	0.2715	0.2715	0.0000

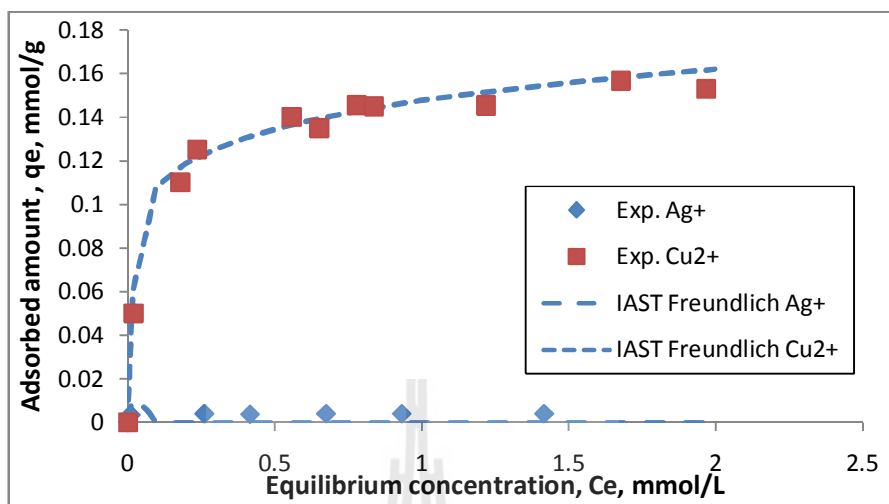


**Figure 3.34** Prediction of equilibrium isotherms of  $\text{Cu}^{2+}$ - $\text{Ag}^{+}$  mixture by IAST based on Freundlich equation for pure component adsorption (adsorbent used  $\text{PGNH}_2$ )

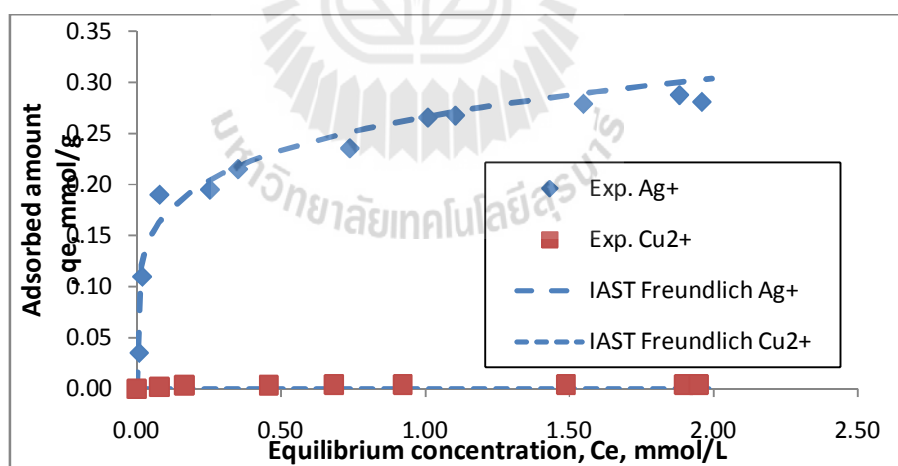


**Figure 3.35** Prediction of equilibrium isotherms of  $\text{Cu}^{2+}$ - $\text{Ag}^{+}$  mixture by IAST based on Freundlich equation for pure component adsorption (adsorbent used  $\text{PGSH}$ )

### 3.5.3 Gas-phase adsorption

The virgin non-grafted porous glass (sample PG) with 240 m<sup>2</sup>/g surface area and 1.82 mmol/g silanol group loading was employed for the study of adsorption in gas phase. Three adsorbates with increasing degree of molecular polarity were tested, including carbon dioxide (dipole moment = 0 D(debye), ethanol (dipole moment = 1.69 D) and water (dipole moment = 1.85 D). It should be noted that no attempt was made at this stage to study the effect of silanol group (loading and distribution) and the type of grafted functional groups on the adsorbent-adsorbate interactions. In general, depending on the nature of glass surface the adsorption behavior on porous glass will be dictated by the interaction between the adsorbate molecules and the siloxanes (Si-O-Si) and silanol groups (-OH) existing on the solid surface.

#### 3.5.3.1 Carbon dioxide adsorption

Adsorption isotherms of carbon dioxide on porous glass at three adsorption temperatures of 283K, 293K and 303K are shown in **Figure 3.36**. Over the pressure up to 1 atm, the amount of CO<sub>2</sub> adsorbed at each temperature increases with increasing pressure and the shape of isotherm resembles the initial part of Type II isotherm according to IUPAC classification, thus indicating a characteristic of multilayer adsorption on a mesoporous glass adsorbent. It is seen that the amount adsorbed decreases with increasing in the adsorption temperature which signifies that CO<sub>2</sub> adsorption on the porous glass surface is an exothermic process. Since there would be no contribution by electrostatic interaction owing to the symmetrical molecular structure of CO<sub>2</sub>, it can thus be inferred that the adsorption should occur by dispersive attraction

forces between CO<sub>2</sub> molecules and adsorbent molecules of siloxanes (Si-O-Si) and silanol groups (-OH).

From the shape of the measured isotherms two types of isotherm models, namely the Langmuir and Freundlich equations, were tested to check for the validity of model prediction. The model equations are as follows.

Langmuir equation:

$$q = \frac{q_m bP}{1 + bP}$$

where  $q$  is the amount adsorbed in mmol/g adsorbent,  $q_m$  is monolayer capacity in mmol/g,  $b$  is the Langmuir constant or affinity constant and  $b = b_\infty \exp(Q/R_gT)$ ,  $Q$  is the heat of adsorption, and  $P$  is the pressure in Pascal (Pa).

Freundlich equation :

$$q = K_F (P)^{1/n_F}$$

where  $K_F$  and  $n_F$  is the affinity constant and surface heterogeneity parameter, respectively, and  $P$  is in Pa.

**Table 3.33** lists the best fit values of model parameters along with the regression coefficients ( $R^2$ ) and the comparison of the isotherm curves from experiments and model calculation is shown plotted in **Figure 3.37**. Based on the value of regression coefficient as the fitting criterion, it was found that the measured isotherms are best described by the Freundlich equation, with  $R^2$  very close to unity at all

temperatures. On the adsorbed capacity, there is a tendency for both  $q_m$  and  $K_F$  to decrease with the increase in adsorption temperature, as to be expected. However, the affinity coefficient,  $b$ , and the surface heterogeneity parameter,  $n_F$ , appear to be insensitive to change in temperature over the range from 10-30°C.

The comparison of adsorbed amount of CO<sub>2</sub> by various adsorbents at 1 atm and 30°C is typically shown in **Table 3.34**. From these limited data, it can be seen that the adsorbed capacities of CO<sub>2</sub> differ widely for microporous adsorbents as compared to those of mesoporous silicas. This should be predominantly attributed to the differences in their chemical and porous properties. The amount of CO<sub>2</sub> adsorbed by porous glass from this study is comparable to other types of porous silica adsorbents. It is also noted that the increase in silanol content on porous silica surface from 3.19 to 5.80 mmol/g help increase the amount adsorbed by around 30% and the grafting of silica with aminopropyl group imparts strong affinity for CO<sub>2</sub> adsorption.

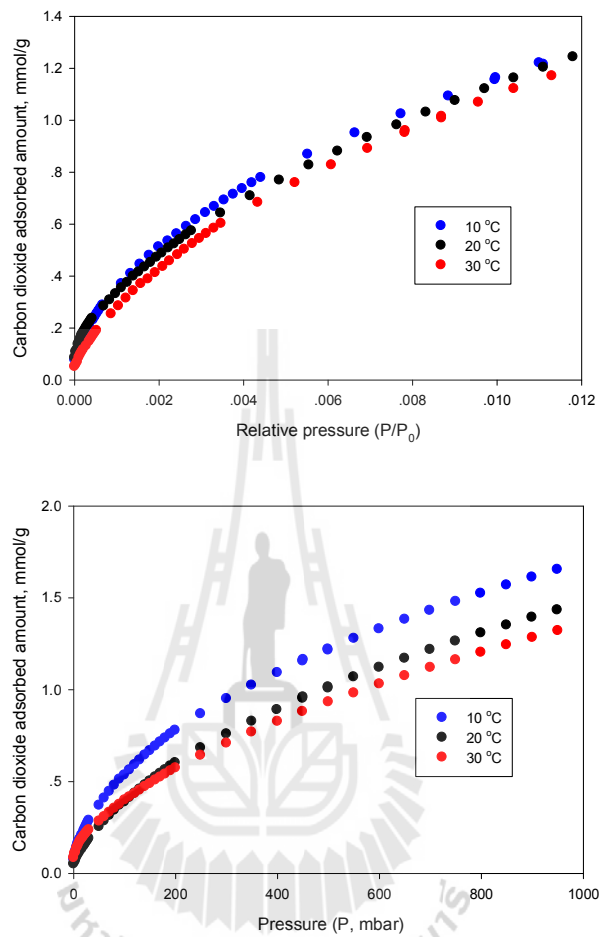


**Figure 3.36** Adsorption isotherms of carbon dioxide on porous glass from coal fly ash at various temperatures.



**Table 3.33** Fitted parameters of Langmuir and Freundlich equations for the adsorption of carbon dioxide by porous glass from fly ash at various temperatures.

Temperature °C	CO <sub>2</sub> vapor pressure MPa	Langmuir model			Freundlich model		
		q <sub>m</sub> (mmol/g)	b (Pa <sup>-1</sup> )	R <sup>2</sup>	K <sub>F</sub>	n <sub>F</sub>	R <sup>2</sup>
10	4.502	2.013	3.43x10 <sup>-3</sup>	0.9712	5.51x10 <sup>-3</sup>	2.066	0.9991
20	5.729	1.998	2.24x10 <sup>-3</sup>	0.9891	2.30x10 <sup>-3</sup>	1.746	0.9993
30	7.214	1.658	2.96x10 <sup>-5</sup>	0.9610	3.69x10 <sup>-3</sup>	1.954	0.9961

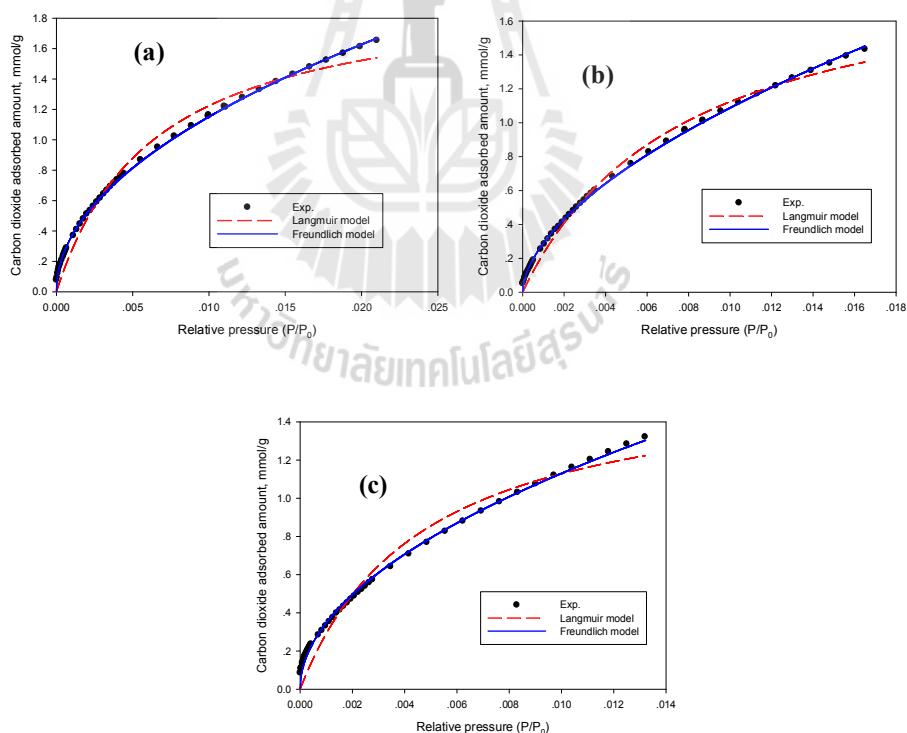


**Figure 3.37** Fitting of Langmuir and Freundlich isotherm equation to isotherm data of carbon dioxide on porous glass, (a) 10 °C, (b) 20 °C and (c) 30 °C.

**Table 3.34** Adsorption capacity of carbon dioxide by various adsorbents at 1 atm and 30°C.

Type	Adsorbent	CO <sub>2</sub> loading (mmol/g)	Reference
Microporous	Activated carbon	0.41	B. Guo et. al , 2006
	Silica gel	0.80	K. Berlier and M. Frere, 1997
	Zeolite 5A	2.51	Coring PG, 2001
	Zeolite 5A	1.0	S. Bourrel and et. al, (2005)
Mesoporous	MCM-41	0.80	Y.He, 2003
	Porous glass -silanol 1.82 mmol/g	1.33	This work
	Porous silica -silanol 3.19 mmol/g	0.84	T. Witoon and M. Chareonpanich, 2012
	-silanol 5.80 mmol/g	1.10	
	Mesoporous silica (aminopropyl group grafted)	2.13	G. Zhao and et.al., 2010

Heat of adsorption is an important parameter in any adsorption processes, since it indicates how much heat needs to be dissipated from the adsorption zone and may elucidate the underlying mechanism of adsorption. In this work, the isosteric heat of adsorption ( $\Delta H^{st}$ ) for carbon dioxide adsorbed by porous glass was calculated from the isotherm data using the following well known van't Hoff equation,

$$(\ln P)_{n_a} = -\frac{\Delta H^{st}}{R_g T} + C$$

where

$n_a$  is the amount of adsorbate adsorbed and C is a constant.

The effect of CO<sub>2</sub> adsorption loading on the isosteric heat of adsorption is numerically shown in **Table 3.35** and displayed in **Figure 3.37**. It is observed that the heat of adsorption decreases continuously from 21.7 to 17.4 kJ/mol with increasing carbon dioxide loading from 0.2 to 1.6 mmol/g and there is a tendency to approach a constant value at higher loading. The isosteric heat of adsorption at zero coverage is obtained by extrapolation to be 22.7 kJ/mol. Heat of adsorption is high initially owing to the strong interaction between the adsorbate molecules and the surface adsorption sites. At higher surface coverage, however, weak dispersive forces among adsorbate molecules start to play an important role, thus releasing less amount of heat of adsorption. The slow decrease of heat of adsorption with increased surface loading could result from the large value of permanent quadrupole moment of CO<sub>2</sub> ( $-13.71 \times 10^{-40}$  Coulomb-m<sup>2</sup>) that could promote additional interaction with the polar surface of porous glass by electrostatic contribution. It is noted that the gradual decreasing of heat of

adsorption with increased loading has also been observed in activated carbon and zeolite adsorbents (G. Zhao et.al, 2010; A. Romeo-Perez, 2010). In comparison with other types of adsorbents, the data on limiting heat of adsorption were reported to be in the range from 15-30 kJ/mol for activated carbons, depending on the types of precursors and the porous structure and chemical modification of carbons (B.B. Saha et.al., 2011; S. Himeno, 2005), and a higher value of around 40 kJ/mol for zeolite 13X and zeolite 4A (J-S Lee et.al., 2002).

**Table 3.35** Effect of CO<sub>2</sub> adsorption loading on the isosteric heat of adsorption ( $\Delta H^{st}$ ).

<b>CO<sub>2</sub> loading (mmol/g)</b>	<b>Isosteric heat of adsorption (kJ/mol)</b>
0.2	21.7
0.4	20.3
0.6	19.4
0.8	18.8
1.0	18.4
1.2	18.0
1.4	17.7
1.6	17.4

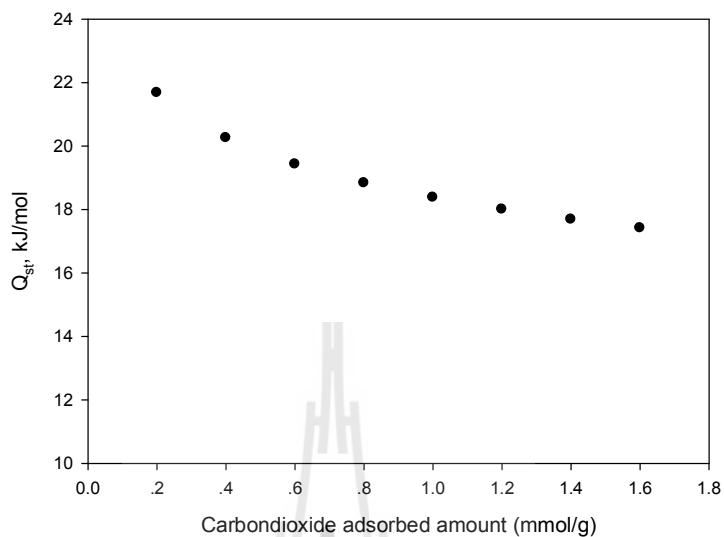


**Figure 3.37** Isosteric heat of carbon dioxide adsorption onto porous glass.

### 3.5.3.2 Ethanol adsorption

Ethanol adsorption with the prepared porous glass from coal fly ash (sample PG) was also studied in an intelligent gravimetric analyzer (IGA) at 10, 20 and 40°C. **Figure 3.38** shows typical adsorption/desorption isotherms of ethanol at 20°C. The result shows that the isotherm can be classified as Type II isotherm according to the IUPAC classification (S.J. Gregg, 1982). This type of isotherm was also observed for the adsorption of ethanol by acid-catalyzed silica gels (K. Nakanishi, 1988) and CPG-10 Corning porous glass (M.S. Nadiye, 2009). The isotherm in **Figure 3.38** exhibits a rapid increase in the amount adsorbed with a sharp curvature over a relatively narrow range of relative pressure from 0- 0.1, then it increases almost linearly with increasing relative pressure up to the value of 0.5, and followed by a final sharp increase when the relative

pressure approaches one. The amount of ethanol adsorbed at the knee of isotherm curve (point B) indicates the monolayer capacity before the multilayer adsorption starts to occur. It is further noted that a hysteresis loop exists which indicates that the adsorption is associated with the capillary condensation mechanism, typical of adsorption in a mesoporous adsorbent like the porous glass studied in this work. The loop is found to close at the relative pressure of about 0.1, coinciding with the starting of multilayer adsorption at point B in **Figure 3.38**.

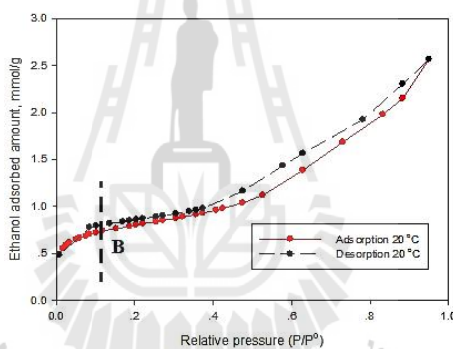


**Figure 3.38** Ethanol adsorption/desorption isotherms on porous glass at 20 °C

**Figure 3.39** shows the effect of temperature on the adsorption isotherms of ethanol, presented both as a function of the vapor pressure and the relative pressure. It is clear that the adsorption favorably increases with the decrease in the adsorption temperature, thus indicating that the adsorption occurs by physical adsorption. The adsorption mechanism of ethanol onto porous glass surface can be visualized as depicted in **Figure 3.40**. Ethanol molecules can first interact with the silanol active sites

through the hydrogen bonding (hydrogen from silanol and oxygen from alcohol). When all the surface active sites are engaged in the monolayer adsorption, the next multilayer adsorption could occur by self-interaction among the ethanol molecules, also by hydrogen bonds. It is interesting to note that the monolayer capacity at point B for each adsorption temperature varies from 0.7-1.0 mmol/g which is less than the silanol surface content of 1.82 mmol/g. This indicates that there must be a distribution of active site activation energy so that not all the active sites are available for the adsorption process. However, this conclusion does not take into account the possible interaction of ethanol with the surface siloxanes (Si-O-Si), the importance of which depends on the content of surface silanols; the high density of silanol group could prevent the access of ethanol to interact with the siloxanes on the solid surface due to the hindrance effect.

Attempt was made to fit the ethanol isotherms with available isotherm models. The shape of adsorption branch in **Figure 3.39** suggests that BET equation for multilayer gas adsorption

$$\frac{q}{q_m} = \frac{Cx}{(1-x)} [1 + (C-1)x]$$

where  $x$  is the relative pressure ( $P/P_0$ ), could be a possible choice. After applying the BET isotherm to experimental data, as shown in **Figure 3.41**, it was found that the BET equation could not properly describe the derived ethanol isotherms. It was then decided to try another version of BET equation, known as the n-layer equation, which has the following form:

$$\frac{q}{q_m} = \frac{Cx}{(1-x)} \left[ \frac{1 - (n-1)x^n + nx^{n+1}}{1 + (C-1)x - Cx^{n+1}} \right] \quad (3.65)$$

where  $x$  is the relative pressure ( $P/P_0$ ) and  $n$  is the number of adsorbed layer.

**Figure 3.42** shows the model fitting to the isotherm data and **Table 3.36** lists the fitting parameters of the BET isotherm model. It is seen that the  $n$ -layer BET equation can fit the isotherm results very well with the regression coefficient ( $R^2$ ) being greater than 0.98, as compared to the traditional BET equation. Surprisingly, adsorption temperature has no definite effect on the values of monolayer capacity ( $q_m$ ) and number of adsorbed layers ( $n$ ), with the values varying from 0.56-0.60 mmol/g and 6.7-9.2, respectively. However, the value of constant  $C$ , which is a measure of surface affinity, appears to decrease with the increase in temperature, thus giving the same effect of temperature on the amount of ethanol adsorbed. The parameter  $C$  can be correlated with adsorption temperature through the Arrhenius equation, that is,

$$C = C_0 \exp(E/RgT) \quad (3.66)$$

Where  $C_0$  is the apparent adsorption rate constant (-),  $E$  is the characteristic energy of interaction,  $Rg$  is the gas constant (8.314kJ/mol-K),  $T$  is the absolute temperature (K). By linear regression, the best fitting values of  $C_0$  and  $E$  are  $6.18 \times 10^{-8}$  and 58.6 kJ/mol, respectively, with regression coefficient ( $R^2$ ) of 0.85.



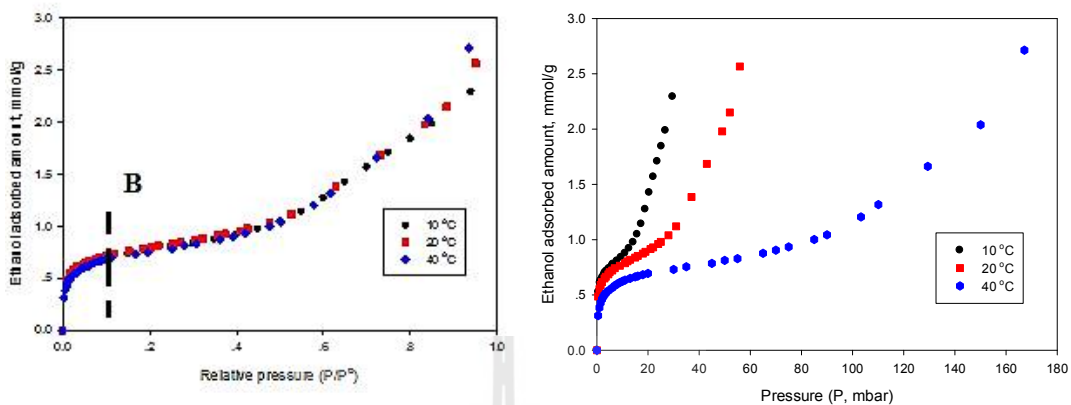


**Figure 3.39** Adsorption isotherms of ethanol on porous glass at various temperatures.

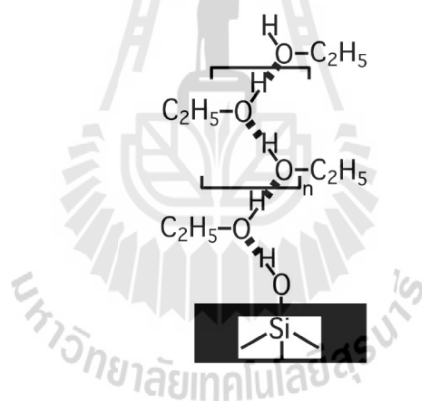


**Figure 3.40** Model of ethanol adsorption on silica surface with the presence of silanol group (-OH).

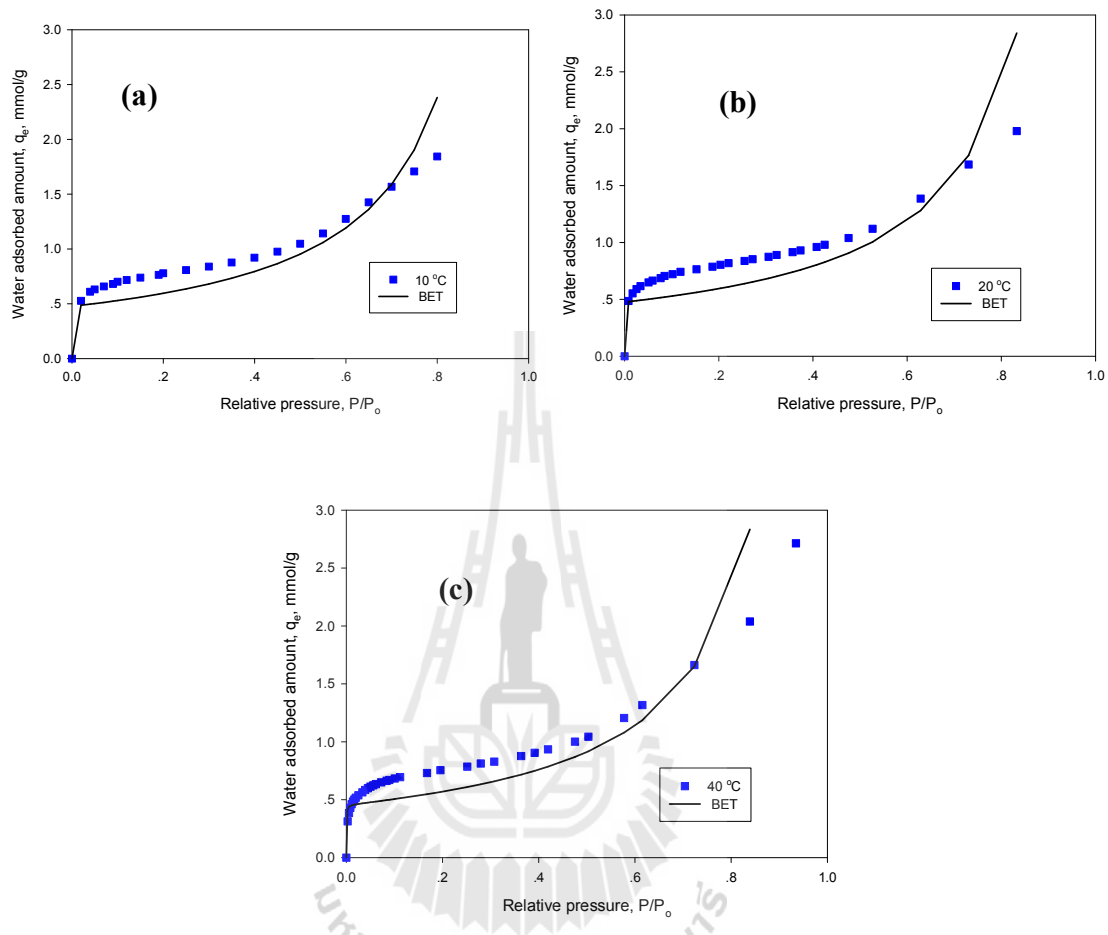


**Figure 3.41** Testing BET equation against isotherms of ethanol adsorption on porous glass (a) 10 °C, (b) 20 °C and (c) 40 °C.

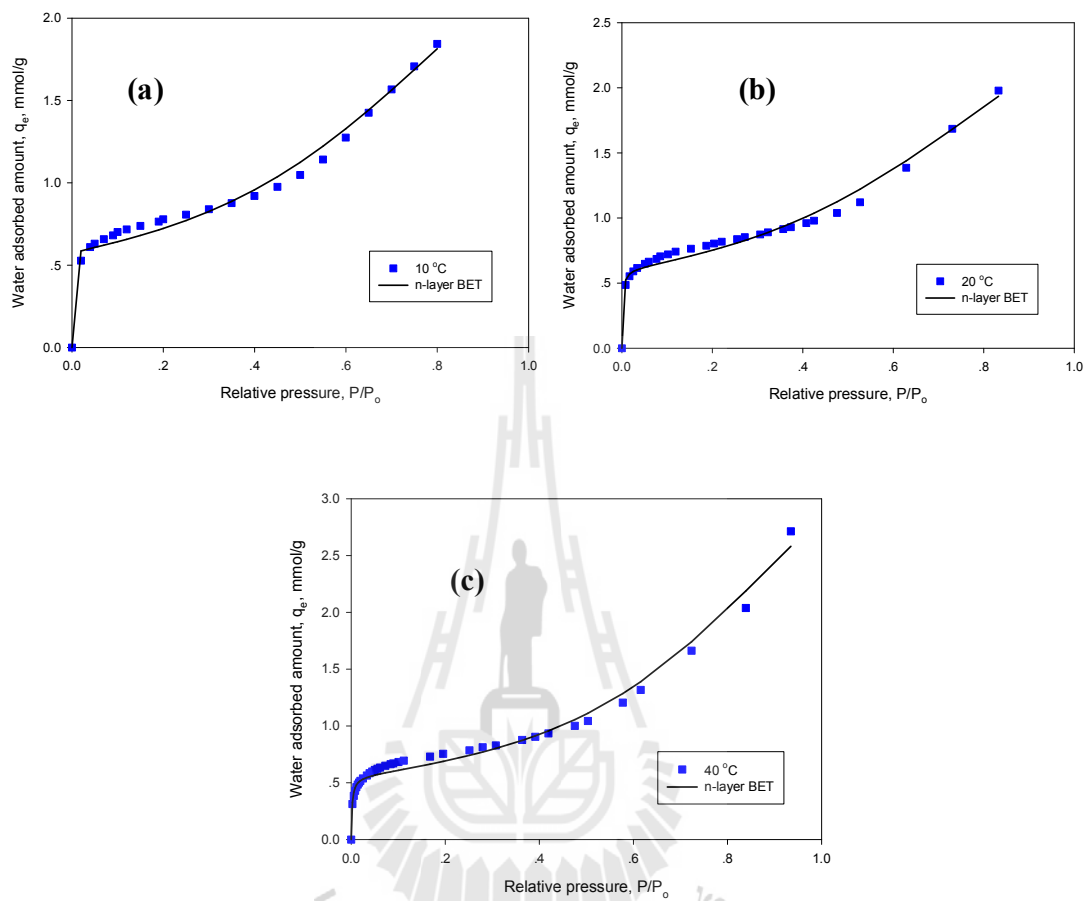


**Figure 3.42** Testing n-layer BET equation against isotherms of ethanol adsorption on porous glass (a) 10 °C, (b) 20 °C and (c) 40 °C.

**Table 3.36** Calculated parameters derived from BET and n-layer BET model for ethanol adsorption on porous glass from coal fly ash.

Temperature °C	Vapor Pressure (mbar)	BET			n-layer BET			
		$q_m$ (mmol/g)	C	$R^2$	$q_m$ (mmol/g)	C	n	$R^2$
10	30.83	0.4765	$1.51 \times 10^6$	0.8775	0.5788	7168	6.97	0.9883
20	58.12	0.4356	$1.76 \times 10^6$	0.7917	0.6053	713	6.70	0.9855
40	178.68	0.4561	$3.76 \times 10^3$	0.8365	0.5579	505	9.19	0.9963

**Figure 3.43** shows the isosteric heat of ethanol adsorption by porous glass as a function of adsorption loading. Over the loading from 0.60 to 2.25 mmol/g ethanol, the isosteric heat of adsorption decreases continuously from 49.3 to 41.7 kJ/mol and tends to approach the value of 40.5 kJ/mol for bulk condensation of ethanol at 1 atm pressure (I.Y. Babkin, 1962). The extrapolated heat of adsorption of ethanol at zero loading is estimated to be 55.6 kJ/mol. Compared to carbon dioxide adsorption with the same porous glass, this limiting heat of adsorption for ethanol is about 2.5 times higher, hence emphasizing the stronger interaction of silanols with the ethanol molecules.

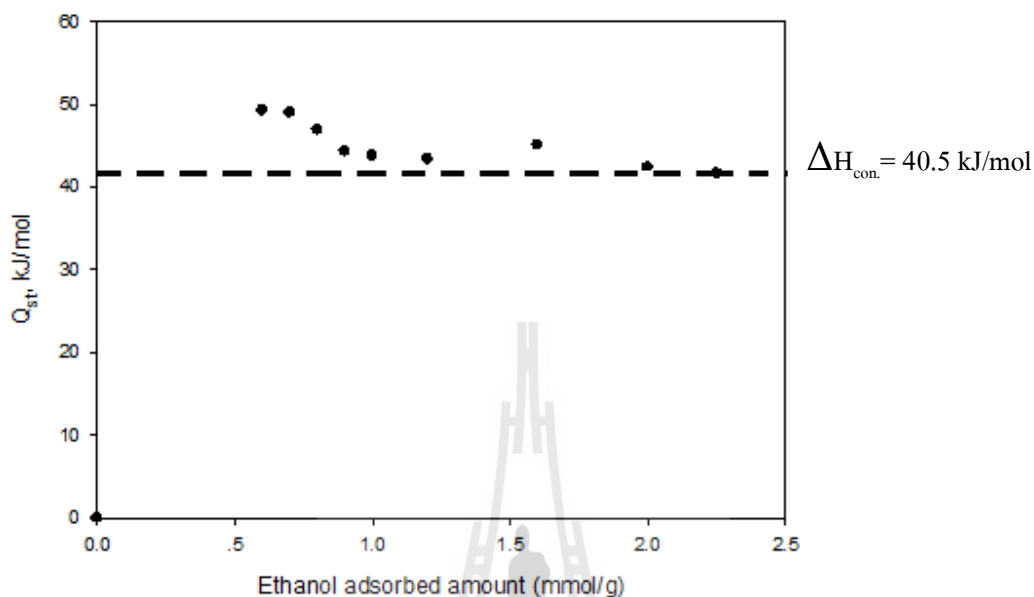


**Figure 3.43** Isosteric heat of ethanol adsorption onto porous glass.

### 3.5.3.3 Water adsorption

Adsorption behavior of water vapor, an adsorbate with strong polarity, on porous glass was finally studied at 20, 25 and 35°C. Since the surface of porous glass contains hydroxyl or silanol group (-Si-OH), it is expected that the silanol groups would play an important part in interacting with water molecules in the adsorption process. **Figure 3.44** depicts the possible interaction of water molecules on the silica surface (Christy, 2010). At low pressures, where the adsorption loading is low, the adsorption of water occurs in the vicinity of solid surface by hydrogen bonding with the silanols which can be of two types: one in which water acts as a proton donor in a hydrogen bond to the oxygen of the silanol group, designated as no. **1** in **Figure 3.44**, and

the other in which water acts as a proton acceptor in a hydrogen bond to the hydrogen of the silanol group, shown as no. **2** in **Figure 3.44**. The interaction can also take place by hydrogen bonding between hydrogen and oxygen of the neighboring silanol groups and water molecules can also interact among themselves, shown as no. **3** and no. **4** in **Figure 3.44**, respectively. At higher pressures or at high adsorption loading, the association among water molecules via hydrogen bonding predominates, leading to the forming and growth of water clusters.

Typical adsorption-desorption isotherm of water adsorption by porous glass at 25°C is illustrated in **Figure 3.45**. It displays Type IV isotherm (Type II + hysteresis loop) which is characteristic of a mesoporous adsorbent and associates with the phenomenon of capillary condensation of an adsorbate in various pore sizes. The derived water isotherm is indeed similar to that of ethanol adsorption previously presented except that the water isotherm tends to level off at the relative pressure greater than 0.8. The desorption branch of the isotherm seems to close the loop at the relative pressure around 0.4 but it actually ends at zero pressure.

**Figure 3.46** shows the effect of temperature on the amount of water adsorbed on porous glass. Similar to ethanol adsorption, the adsorption of water vapor is via physical adsorption since the amount adsorbed decreases with increasing in temperature, that is, the adsorption is associated with the liberation of heat (an exothermic process). It is further noted from **Figure 3.46a** that at the relative pressure of 0.1 (point B) at which it represents the completion of monolayer capacity, the amount of water adsorbed is equal to 4 mmol/g which is about twice as much compared to silanol

group loading of 1.82 mmol/g, thus giving the mole ratio of about 2:1 for the amount of water adsorbed to that of adsorption sites. Therefore, if the initial adsorbed layer is formed by the attachment of water molecules with the silanol groups through hydrogen bonds, this means that all the silanol (hydroxyl) surface groups with both the oxygen and hydrogen do participate in the monolayer adsorption of water, that is, each atom of oxygen and hydrogen of the silanol group will interact with water molecules. This proves a strong affinity of water molecules toward the surface hydroxyl groups on the glass surface. It then follows that to promote the uptake of water by an adsorbent, it is necessary to create the surface with oxygen or hydrogen containing groups. **Figure 3.47** shows an example of increased amount of water adsorbed when the hydrophobic graphitic plane of eucalyptus activated carbon is oxidized with strong nitric acid, thus rendering the surface with increased oxygen functional groups (Yuvarat, 2007).



**Figure 3.44** Schematic of water adsorption on silica surface. (Christy, 2010).

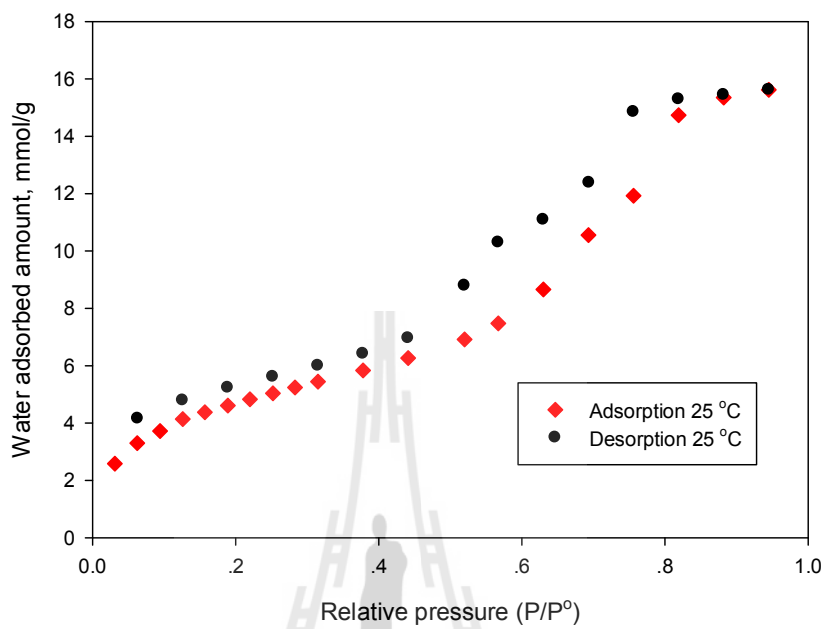


**Figure 3.45** Typical isotherm curves for water vapor adsorption on porous glass at 25 °C.



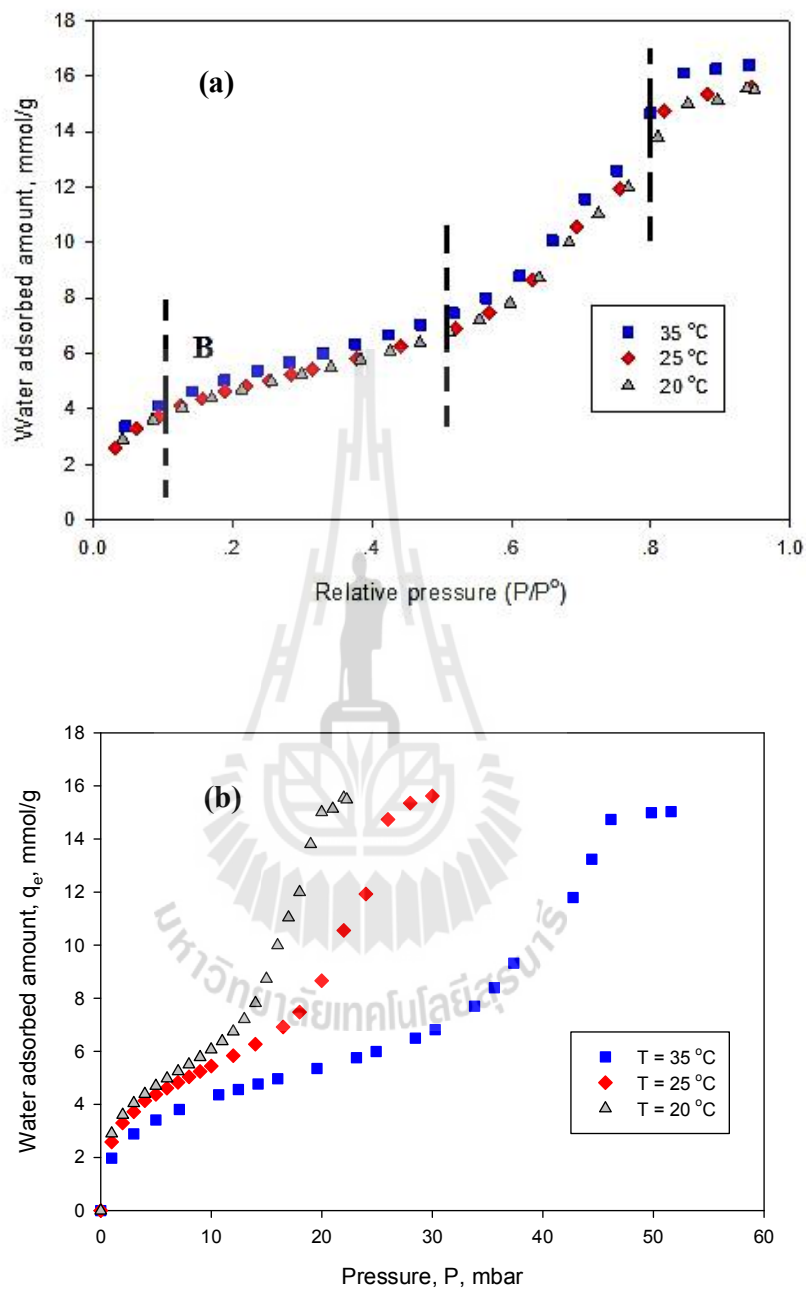


**Figure 3.46** Effect of temperature on water isotherms using porous glass as adsorbent.

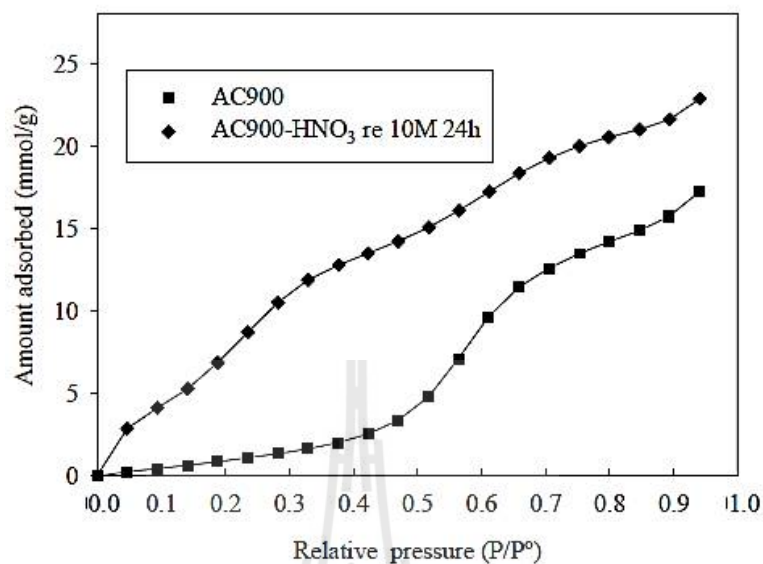


**Figure 3.47** Water isotherms of original and nitric oxidized activated carbon from eucalyptus wood (Yuvarat, 2007).

Both the conventional BET equation and the n-layer BET equation were tested against the water isotherm data and the results are displayed in **Figures 3.48 and 3.49**, respectively. It is seen that the n-layer BET equation can describe the isotherms quite accurately up to the relative pressure of 0.8. **Table 3.37** lists the derived fitted parameters from both isotherm equations along with the regression coefficients of data fitting. The monolayer capacity ( $V_m$ ) of the n-layer BET equation varies from 3.34 to 3.57 mmol/g, giving the average value of 3.44 mmol/g which is much larger than that of ethanol adsorption on the same porous glass sample. The value of constant C systematically decreases from 312 to 195 as the adsorption temperature is increased from

20 to 35°C. The number of adsorbed layer (n) changes over a narrow range from 9.71 to 11.0 with no clear dependence on the adsorption temperature.

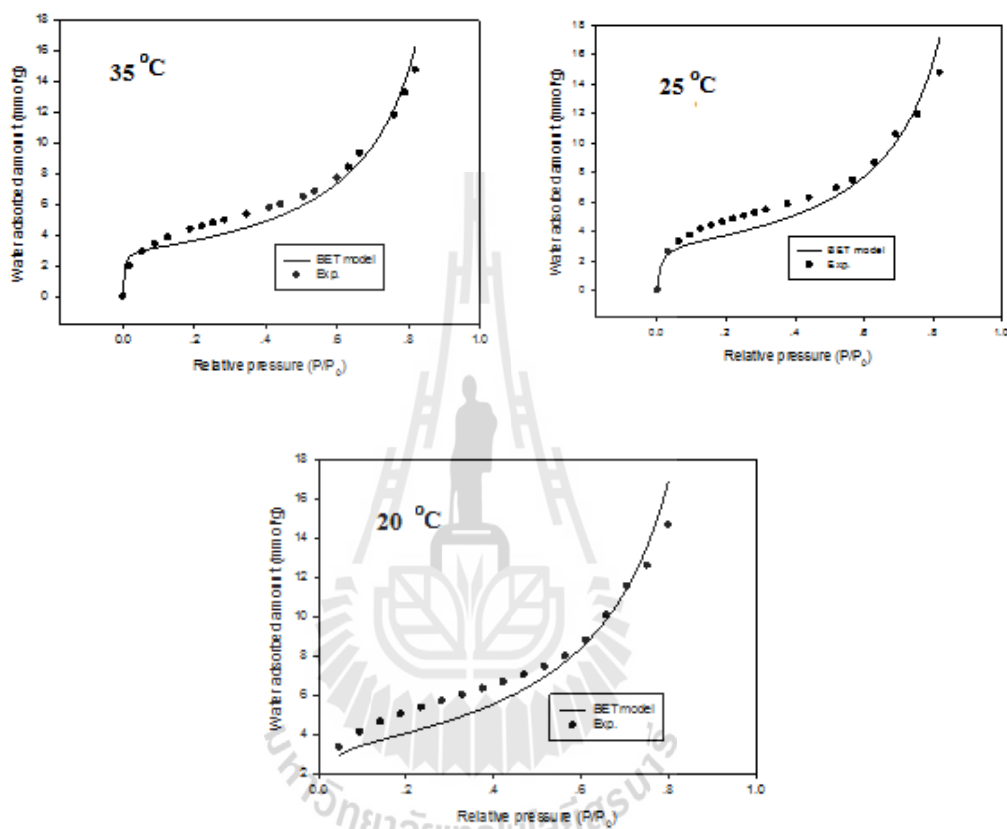


**Figure 3.48** Fitting of water isotherms with conventional BET equation.

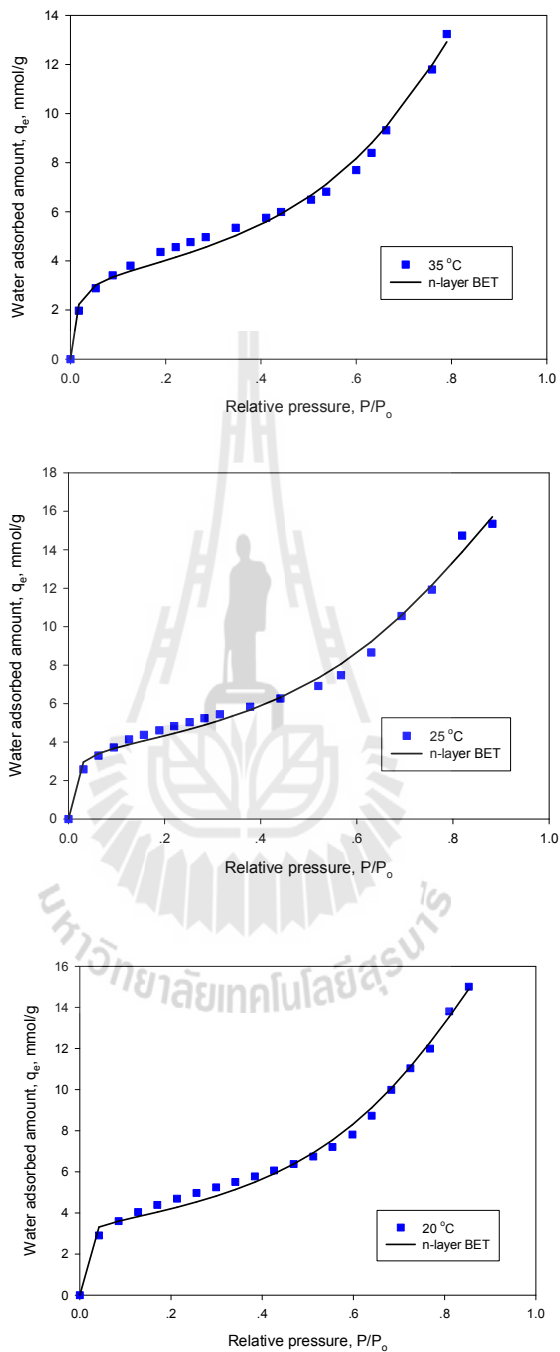


**Figure 3.49** Fitting of water isotherms with n-layer BET equation.

**Table 3.37** Fitted parameters of BET and n-layer BET equations for water vapor adsorption with porous glass from coal fly ash.

Temperature °C	Vapor Pressure (mbar)	BET			n-layer BET			
		$V_m$ (mmol/g)	C	$R^2$	$V_m$ (mmol/g)	C	n	$R^2$
20	30.83	2.7925	3556	0.9542	3.4052	312	10.54	0.9922
25	58.12	3.0718	2483	0.9525	3.5727	127	9.71	0.9910
35	178.68	3.0521	229	0.9716	3.3412	105	11.03	0.9918

**Figure 3.50** shows the variation of isosteric heat for water adsorption on porous glass as a function of adsorption loading. The isosteric heat of adsorption falls continuously down to the loading of 8 mmol/g of water adsorbed and then remains substantially constant at the value of 45 kJ/mol at higher loading which corresponds to the latent heat for bulk condensation of water from gas (Ng et al., 2001). The extrapolated heat of adsorption of water vapor on porous glass at zero loading (limiting heat of adsorption) is estimated to be 68.4 kJ/mol.

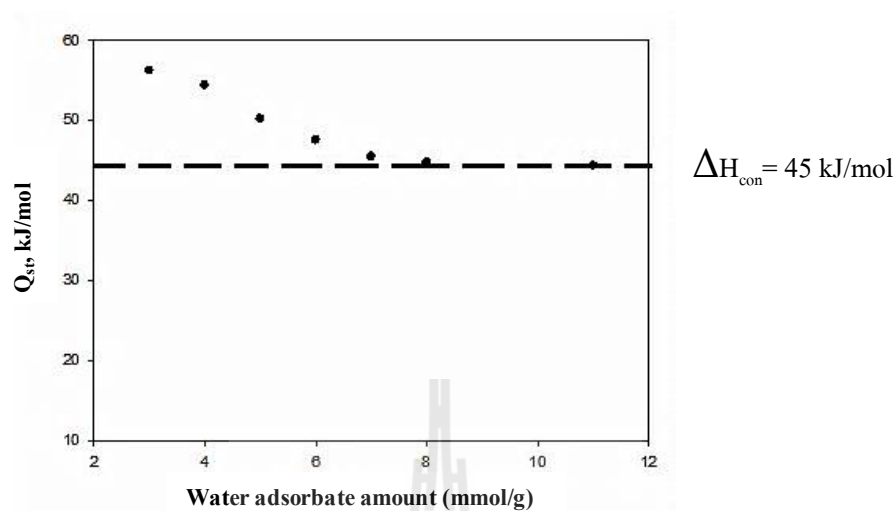


**Figure 3.50** Effect of water loading on isosteric heat of adsorption using porous glass adsorbent.

### 3.5.3.4 Kinetics of water adsorption

Adsorption kinetics of water vapor by porous glass was studied as a function of temperature employing the transient adsorption data at various vapor pressures, as displayed in **Figure 3.51**. Three different kinetic models, including pseudo first-order model, pseudo second-order model and intraparticle-diffusion model(long-time uptake), were tested against the adsorption kinetic data. **Table 3.38** summarizes the fitted model parameters obtained by regression analysis along with the regression coefficients as a measure of model validation, while **Figure 3.52** typically shows the comparison between the kinetics of adsorption uptake from experiments and model prediction at 4 mbar and 20°C.

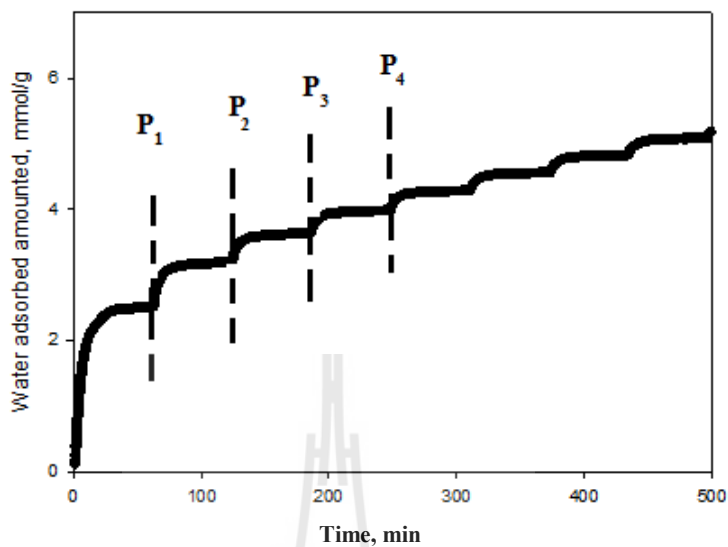


**Figure 3.51** Adsorption kinetic data of water vapor by porous glass at 20 °C and various increasing pressures.

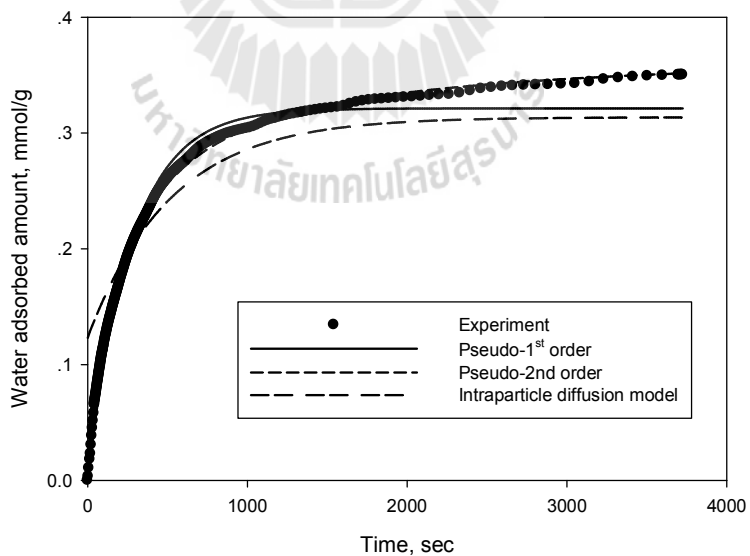


**Figure 3.52** Comparison of adsorption kinetics of water by porous glass from experiments and model prediction ( $P = 4$  mbar and  $T = 20$  °C)

**Table 3.38** Fitted parameters of adsorption kinetic models at various temperatures.

(a) 20°C

P (mbar)	$q_{e,(exp)}$ (mmol/g)	Pseudo-1 <sup>st</sup> order			Pseudo-2 <sup>nd</sup> order			Intraparticle diffusion model		
		$q_{e,1}$ (mmol/g)	$k_1$	$R^2$	$q_{e,2}$ (mmol/g)	$k_2$	$R^2$	$q_{e,p}$ (mmol/g)	$D_e, \times 10^{11}$ (m <sup>2</sup> /s)	$R^2$
4	4.2489	4.2200	0.0037	0.9823	4.2623	0.0010	0.9987	4.2123	0.87	0.844
10	5.9167	5.8998	0.0023	0.9882	6.6309	0.0004	0.9980	5.8831	0.64	0.8128
16	9.8072	9.7814	0.0004	0.9985	9.5547	0.0000	0.9990	9.5630	0.14	0.7285
22	15.3639	15.1462	0.0004	0.9775	15.9575	0.0000	0.9927	15.1285	0.14	0.7914



(b) 25°C

P (mbar)	q <sub>e</sub> (mmol/g)	Pseudo-1 <sup>st</sup> order			Pseudo-2 <sup>nd</sup> order			Intraparticle diffusion model		
		q <sub>e,1</sub> (mmol/g)	k <sub>1</sub>	R <sup>2</sup>	q <sub>e,2</sub> (mmol/g)	k <sub>2</sub>	R <sup>2</sup>	q <sub>e,p</sub> (mmol/g)	D <sub>e</sub> , x 10 <sup>11</sup> (m <sup>2</sup> /s)	R <sup>2</sup>
3	3.7220	3.5471	0.0040	0.9795	3.6000	0.0013	0.9985	3.9945	0.91	0.8528
8	5.0377	4.8722	0.0034	0.9840	4.8977	0.0008	0.9987	4.8669	0.82	0.8372
10	5.4423	5.2775	0.0031	0.9853	5.3140	0.0007	0.9988	5.2700	0.78	0.8267
16.5	6.9147	6.7175	0.0018	0.9845	6.8475	0.0003	0.9946	6.6665	0.55	0.8037
22	10.552	10.3388	0.0004	0.9988	10.7248	0.0000	0.9986	9.9856	0.14	0.7244

(c) 30°C

P (mbar)	$q_{e, \text{exp}}$ (mmol/g)	Pseudo-1 <sup>st</sup> order			Pseudo-2 <sup>nd</sup> order			Intraparticle diffusion model		
		$q_{e,1}$ (mmol/g)	$k_1$	$R^2$	$q_{e,2}$ (mmol/g)	$k_2$	$R^2$	$q_{e,p}$ (mmol/g)	$D_e, \times 10^{11}$ (m <sup>2</sup> /s)	$R^2$
4	4.1293	3.6608	0.0043	0.9926	3.8519	0.0011	0.9991	3.6169	1.28	0.8043
10	5.3795	4.9239	0.0038	0.9854	5.0029	0.0008	0.9961	4.8987	1.14	0.7937
16	6.3364	5.8677	0.0033	0.9770	5.9288	0.0006	0.9905	5.8372	1.05	0.7945
22	7.4628	6.9873	0.0018	0.9788	7.0832	0.0003	0.9886	6.9601	0.59	0.8259
36	16.1191	16.427	0.0002	0.9898	19.153	0.00001	0.9883	15.296	0.18	0.5952

(d) 35°C

P (mbar)	$q_{e,(exp)}$ (mmol/g)	Pseudo-1 <sup>st</sup> order			Pseudo-2 <sup>nd</sup> order			Intraparticle diffusion model		
		$q_{e,1}$ (mmol/g)	$k_1$	$R^2$	$q_{e,2}$ (mmol/g)	$k_2$	$R^2$	$q_{e,p}$ (mmol/g)	$D_e, \times 10^{11}$ (m <sup>2</sup> /s)	$R^2$
12.5	4.4305	4.4135	0.0047	0.9788	4.4446	0.0013	0.9984	4.4104	4.07	0.8548
25.0	5.8556	5.8416	0.0024	0.9835	5.8640	0.0005	0.9974	5.8272	2.83	0.8128
30.0	6.6732	6.6612	0.0015	0.9949	6.7540	0.0002	0.9986	6.6147	2.14	0.7432
37.0	9.1472	9.1381	0.0005	0.9982	9.4936	0.0000	0.9991	8.9845	1.01	0.7311

Based on the consideration of regression coefficient ( $R^2$ ), it is apparent that pseudo second-order model can best describe the adsorption kinetics of water vapor onto porous glass over the ranges of adsorption loading and temperature investigated, followed by pseudo first-order and intraparticle-diffusion models, respectively. The effects of adsorption temperature and loading on the kinetic parameters ( $k_1$ ,  $k_2$  and  $D_e$ ) are shown plotted in **Figure 3.53**. Overall, there is a tendency for the parameters to drop continuously in a liner fashion as the loading is increased and becomes constant when a certain loading is reached. The lowering in the rate constants ( $k_1$  and  $k_2$ ) and the effective diffusivity ( $D_e$ ) indicates a decrease in the transport rate of adsorbate to the adsorption sites as the loading is increased, in agreement with the decreasing slope of the kinetic curve in **Figure 3.52** as time proceeds. This could arise from the result of steric effect or the blockage of the diffusing passage along the internal pores caused by the increased thickness of the adsorbed layer at relatively high loading. The relatively low values of the kinetic parameters, which may be considered as approaching zero, at a threshold loading suggests that the adsorption is approaching equilibrium condition at a given pressure in the bulk fluid phase.

**Figure 3.53** also shows that over the temperature range from 20-35°C and at a given adsorption loading, the kinetic model parameters tend to increase with increasing in the temperature. This implies the increased mobility of adsorbate molecules as the temperature is increased caused by the increase in the thermal energy of the molecules, as would be expected.

The effective diffusivity of water in a porous glass particle ( $D_e$ ) at high loading can be further analyzed to extract the information on pore diffusivity ( $D_p$ ) and surface diffusivity ( $D_s$ ) which characterize the basic transport mechanism of pore diffusion and surface diffusion inside a porous adsorbent, respectively (see **Figure 3.54**). For each uptake curve at a given pressure, the following gives the calculation step to obtain  $D_p$  and  $D_s$ .

(a) First, calculate the effective Knudsen diffusivity in adsorbent pores from the relation: (Toth, 2002)

$$D_{k,eff} = \varepsilon_p D_k / \tau^2 \quad (3.67)$$

where  $D_k = \text{Knudsen diffusivity in cylindrical tube} = \frac{2r}{3} \sqrt{\frac{8R_g T}{\pi M}}$

$\varepsilon_p = \text{particle porosity} = 0.32$  for porous glass

$\tau = \text{tortuosity factor} = 4$  for porous glass (Toth, 2002)

$r = \text{mean pore radius} = 0.21 \text{ nm}$

$M = \text{molecular weight of the diffusing species} = 18 \text{ g/mol}$  for water

(b) Next, calculate the pore diffusivity ( $D_p$ ) from

$$D_p = \frac{1}{\left( \frac{1}{D_{12,eff}} + \frac{1}{D_{k,eff}} \right)} \quad (3.68)$$

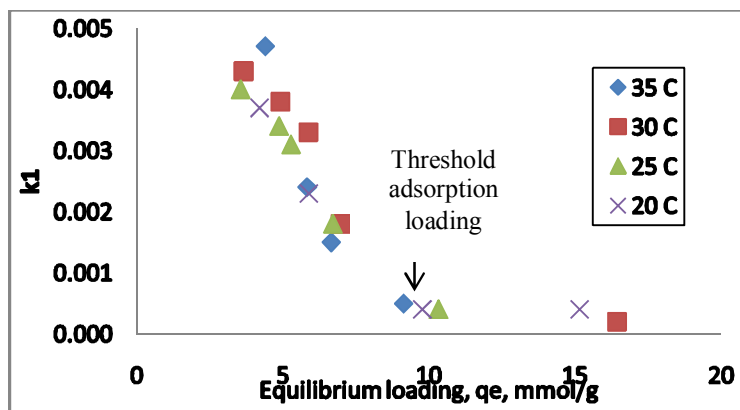
where  $D_{12,eff}$  is the effective molecular diffusivity which is assumed to be zero for single component diffusion. Thus,

$$D_p \approx D_{k,eff}$$

(c) Finally, calculate the surface diffusivity ( $D_s$ ) from the following equation,

$$D_p = \frac{\varepsilon_p D_p + (1 - \varepsilon_p) D_s (\partial q / \partial C)}{\varepsilon_p + (1 - \varepsilon_p) (\partial q / \partial C)} \quad (3.69)$$

where the term  $(\partial q / \partial C)$  is the slope of the isotherm curve at a given adsorption loading ( $q$ ) for a curved isotherm.



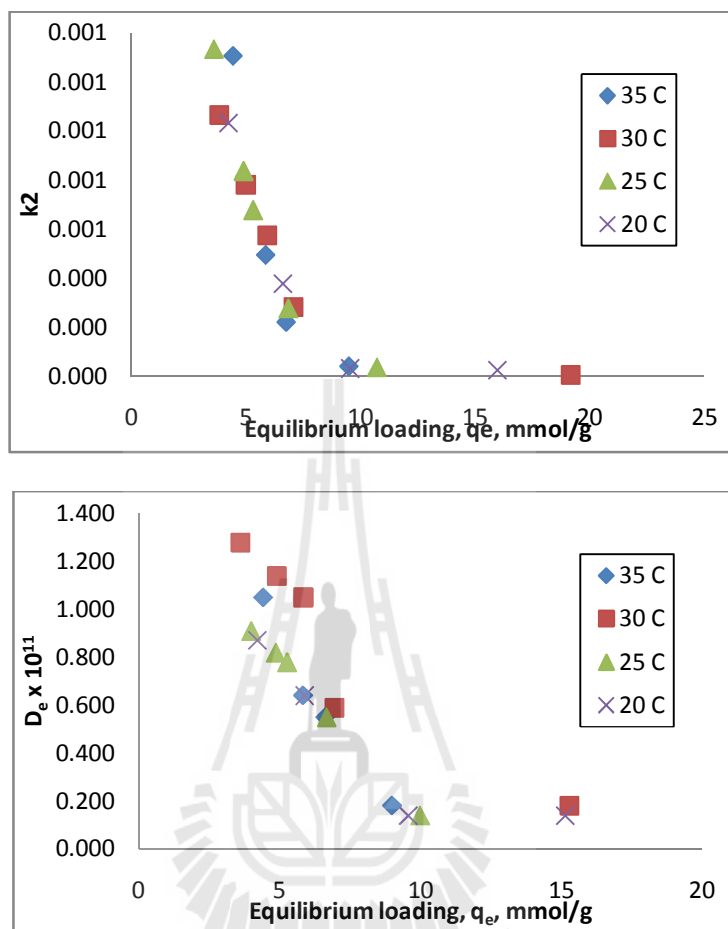


**Figure 3.53** Effect of water loading and temperature on adsorption with model parameters ( $k_1$ ,  $k_2$  and  $D_e$ )

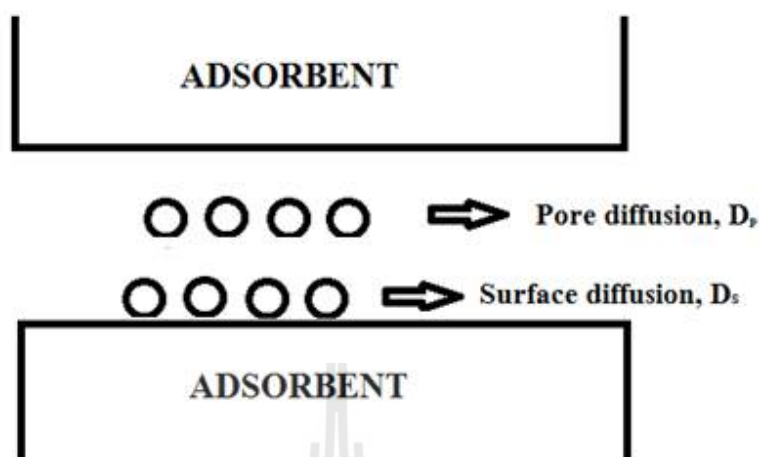


**Figure 3.54** Schematic of adsorbate diffusion in adsorbent pores.

**Table 3.39** shows the effects of temperature from 20°C (293K) to 35°C (308K) and adsorption loading ( $q_e$ ) on pore diffusivity and surface diffusivity of water vapor in porous glass adsorbent. It is observed that the pore diffusivity ( $D_p$ ) is relatively constant over a limited range of both the temperature and the loading. On the other hand, the surface diffusivity ( $D_s$ ) depends on both the temperature and loading, as shown plotted in **Figure 3.55**. Surface diffusivity of water on the pore wall of adsorbent decreases with increased loading and tends to approach a common constant value independent of temperature at high loading. It is observed that the surface diffusivity seems to increase with the increase in temperature and the effect is more pronounced at low adsorption loading. It is quite interesting to note that this result is in contrast with the adsorption of water on activated carbon which shows an increase of surface diffusivity with increasing loading (Qi and LeVan, 2005). With limited available data from this



work, it is fair to infer that the underlying mechanism of water transport in the pores of both adsorbents are fundamentally different.

Surface diffusion is considered to be an activated process since the adsorbed molecule requires a minimum energy to move from one adsorption site to the next adjacent site. The temperature dependence of surface diffusivity ( $D_s$ ) can be described by the usual Eyring expression,

$$D_s = D_{s\infty} \exp(-E_a/R_g T) \quad (3.70)$$

or in linear form,

$$\ln D_s = \ln D_{s\infty} - E_a/R_g T \quad (3.71)$$

where  $D_{s\infty}$  is the surface diffusivity at  $T = \infty$  and  $E_a$  is the activation energy of surface diffusion.

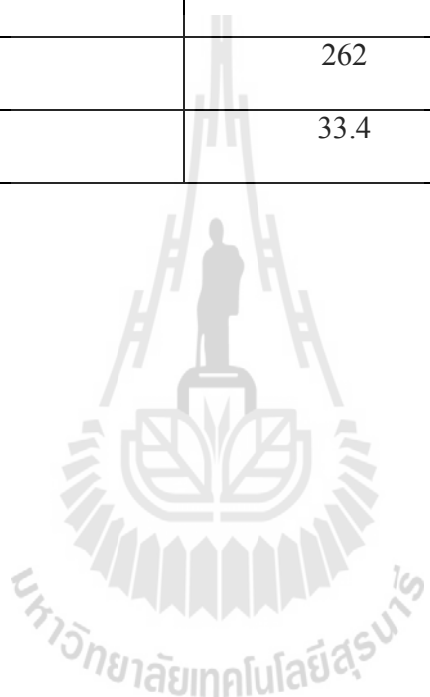
The linear plot of Eyring equation is typically shown in **Figure 3.56** for a narrow variation of adsorption loading from 5-8 mmol/g and the values of  $E_a$  and  $D_{s\infty}$  are estimated from the slope and intercept of the straight line plot and are summarized in **Table 3.40**. The activation energy for surface diffusion of water molecules along the pore wall decreases by 10% for about a twofold increase in adsorption loading from 5 to 8 mmol/g.

**Table 3.39** Effects of temperature and loading for water adsorption by porous glass on the pore and surface diffusivities.

<b>T (°C)</b>	<b>P (mbar)</b>	<b>q<sub>e</sub> (mmol/g)</b>	<b>D<sub>e</sub> (m<sup>2</sup>/s)</b>	<b>D<sub>p</sub> (m<sup>2</sup>/s)</b>	<b>D<sub>s</sub> (m<sup>2</sup>/s)</b>
20	4	4.2489	0.87 x 10 <sup>-11</sup>	1.49 x 10 <sup>-8</sup>	0.83 x 10 <sup>-11</sup>
	10	5.9167	0.64 x 10 <sup>-11</sup>	1.49 x 10 <sup>-8</sup>	0.59 x 10 <sup>-11</sup>
	16	9.8072	0.14 x 10 <sup>-11</sup>	1.49 x 10 <sup>-8</sup>	0.13 x 10 <sup>-11</sup>
	22	15.364	0.14 x 10 <sup>-11</sup>	1.49 x 10 <sup>-8</sup>	0.12 x 10 <sup>-11</sup>
25	3	3.7220	0.91 x 10 <sup>-11</sup>	1.49 x 10 <sup>-8</sup>	0.90 x 10 <sup>-11</sup>
	8	5.0377	0.82 x 10 <sup>-11</sup>	1.49 x 10 <sup>-8</sup>	0.81 x 10 <sup>-11</sup>
	10	5.4423	0.78 x 10 <sup>-11</sup>	1.49 x 10 <sup>-8</sup>	0.77 x 10 <sup>-11</sup>
	16.5	6.9147	0.55 x 10 <sup>-11</sup>	1.49 x 10 <sup>-8</sup>	0.55 x 10 <sup>-11</sup>
	22	10.552	0.14 x 10 <sup>-11</sup>	1.49 x 10 <sup>-8</sup>	0.14 x 10 <sup>-11</sup>
30	4	4.1293	1.28 x 10 <sup>-11</sup>	1.51 x 10 <sup>-8</sup>	1.26 x 10 <sup>-11</sup>
	10	5.3795	1.14 x 10 <sup>-11</sup>	1.51 x 10 <sup>-8</sup>	1.06 x 10 <sup>-11</sup>
	16	6.3364	1.05 x 10 <sup>-11</sup>	1.51 x 10 <sup>-8</sup>	1.02 x 10 <sup>-11</sup>
	22	7.4628	0.59 x 10 <sup>-11</sup>	1.51 x 10 <sup>-8</sup>	0.58 x 10 <sup>-11</sup>
	36	16.119	0.18 x 10 <sup>-11</sup>	1.51 x 10 <sup>-8</sup>	0.18 x 10 <sup>-11</sup>
35	12.5	4.4305	4.07 x 10 <sup>-11</sup>	1.52 x 10 <sup>-8</sup>	3.78 x 10 <sup>-11</sup>
	25.0	5.8556	2.83 x 10 <sup>-11</sup>	1.52 x 10 <sup>-8</sup>	2.78 x 10 <sup>-11</sup>
	30.0	6.6732	2.14 x 10 <sup>-11</sup>	1.52 x 10 <sup>-8</sup>	2.12 x 10 <sup>-11</sup>
	37.0	9.1472	1.01 x 10 <sup>-11</sup>	1.52 x 10 <sup>-8</sup>	0.99 x 10 <sup>-11</sup>

**Table 3.40** Effect of water loading on the pre-exponential factor ( $D_{sc}$ ) and activation energy ( $E_a$ ) of surface diffusion equation.

<b>Equilibrium loading (mmol/g)</b>	<b><math>D_{sc}</math> (<math>m^2/s</math>)</b>	<b><math>E_a</math> (kJ/mol)</b>
5	1,920	81.7
6	262	77.2
8	33.4	73.2



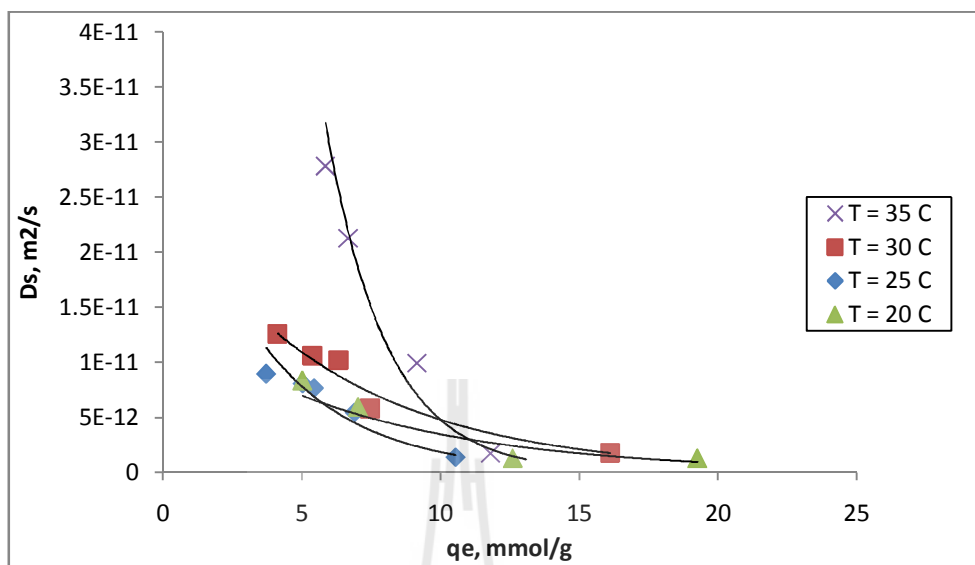


**Figure 3.55** Effects of temperature and adsorption loading on surface diffusivity ( $D_s$ ) for water adsorption onto porous glass

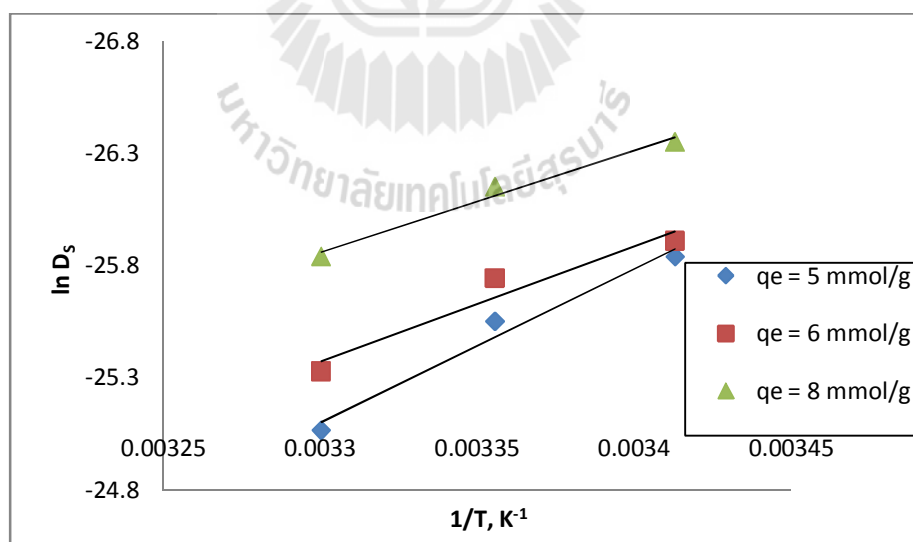


**Figure 3.56** Linear plots of  $\ln D_s$  versus  $1/T$  for determining the pre-exponential factor ( $D_\infty$ ) and activation energy for surface diffusion.

### 3.5.5 Monte Carlo Simulation of CO<sub>2</sub> adsorption on porous glass

Additional attempt was made here to use Monte Carlo Simulation for simulating the equilibrium adsorption of carbon dioxide on porous glass adsorbent. Experimental adsorption data are also presented for comparison. Details of this work are given in the appendix A at the end of this thesis.

## 3.6 Conclusions

Single metal ions of Cu<sup>2+</sup> and Ag<sup>+</sup> cannot be removed by adsorption with the virgin porous glass from coal fly ash. After being chemically grafted, however, porous glass containing amino and thiol groups could enhance and selectively adsorb Cu<sup>2+</sup> and Ag<sup>+</sup>, respectively. The equilibrium isotherms of both ions were best described by the three-parameter Sips model, followed by the Langmuir and Freundlich models, respectively. The adsorption kinetics of both metal ions by the surface-modified porous glass was best described by the pseudo second-order kinetic model. Similarly, the fixation of amino and thiol groups onto the glass surface helped increase the adsorption of gold considerably. Mechanisms were proposed for the adsorption of gold ion by the grafted porous glass adsorbents.

The binary adsorption of Cu<sup>2+</sup> and Ag<sup>+</sup> from solution was also studied using the grafted porous glass containing amino and thiol groups. It was found that the amount adsorbed of both ions in the mixture was the same as that in the pure state, indicating a high selectivity for a specific adsorbate of the grafted adsorbents. The ideal adsorption

solution theory (IAST) was found to predict the isotherms of both metal ions extremely well.

Gas-phase adsorption of adsorbates with increasing surface polarity by porous glass including CO<sub>2</sub>, ethanol and water vapors were studied using virgin porous glass as an adsorbent. It was found that the adsorption of CO<sub>2</sub> on the surface active sites involves the dispersive-force interaction, whereas the adsorption of ethanol and water occurs by hydrogen bonding through the silanol or hydroxyl groups on the glass surface. The adsorption isotherms of CO<sub>2</sub> was well described by the Langmuir and Freundlich isotherm equations, while the n-layer BET equation is appropriate for predicting the isotherms of water and ethanol adsorption.

### 3.7 References

- A. Romero-Perez, G. Aguilar-Armenta, **J. Chem. Eng. Data**, 55, (2010), 3625-3630.
- Badruzzaman, M., Westerhoff, P. and Knappe, D.R.U., (2004). Intraparticle diffusion and adsorption of arsenate onto granular ferric hydroxide (GFH). **Water Research**, 38(18): 4002-4012.
- Bois, L., Bonhommé, A., Ribes, A., Pais, B., Raffin, G. and Tessier, F., (2003). Functionalized silica for heavy metal ions adsorption. **Colloids and Surfaces A: Physicochemical and Engineering Aspects**, 221(1-3): 221-230.
- Brunauer, S., Emmett, P.H. and Teller, E., (1938). Adsorption of Gases in Multimolecular Layers. **Journal of the American Chemical Society**, 60(2): 309-319.

- Burk, S., Gorr, B. and Christ, H.-J., (2010). High temperature oxidation of Mo–Si–B alloys: Effect of low and very low oxygen partial pressures. **Acta Materialia**, 58(18): 6154-6165.
- Christy, A.A., (2010). New insights into the surface functionalities and adsorption evolution of water molecules on silica gel surface: A study by second derivative near infrared spectroscopy. **Vibrational Spectroscopy**, 54(1): 42-49.
- Do Duong, D., (1998). **Adsorption Analysis: Equilibria and Kinetics**. Imperial College Press.
- El-Nahhal, I.M. and El-Ashgar, N.M., (2007). A review on polysiloxane-immobilized ligand systems: Synthesis, characterization and applications. **Journal of Organometallic Chemistry**, 692(14): 2861-2886.
- Enke, D., Janowski, F. and Schwieger, W., (2003). Porous glasses in the 21st century--a short review. **Microporous and Mesoporous Materials**, 60(1-3): 19-30.
- Fu, F. and Wang, Q., (2011). Removal of heavy metal ions from wastewaters: A review. **Journal of Environmental Management**, 92(3): 407-418.
- Hameed, B.H., (2008). Equilibrium and kinetic studies of methyl violet sorption by agricultural waste. **Journal of Hazardous Materials**, 154(1-3): 204-212.
- Hand, D.W., Loper, S., Ari, M. and Crittenden, J.C., (1985). Prediction of multicomponent adsorption equilibria using ideal adsorbed solution theory. **Environmental Science & Technology**, 19(11): 1037-1043.

- Ho, Y.S. and McKay, G., (1998). Kinetic Models for the Sorption of Dye from Aqueous Solution by Wood. **Process Safety and Environmental Protection**, 76(2): 183-191.
- Kikukawa, T., Kuraoka, K., Kawabe, K., Yamashita, M., Fukumi, K., Hirao, K. and Yazawa, T., (2005). Stabilities and pore size effect of proton-conducting organic-inorganic hybrid membranes prepared through surface modification of porous glasses. **Journal of Membrane Science**, 259(1-2): 161-166.
- Lam, K.F., Fong, C.M., Yeung, K.L. and McKay, G., (2008). Selective adsorption of gold from complex mixtures using mesoporous adsorbents. **Chemical Engineering Journal**, 145(2): 185-195.
- Lam, K.F., Yeung, K.L. and McKay, G., (2006). A Rational Approach in the Design of Selective Mesoporous Adsorbents. **Langmuir**, 22(23): 9632-9641.
- Moradi, O., (2011). **Thermodynamics of Interfaces**.
- Murphy, P.J. and LaGrange, M.S., (1998). Raman spectroscopy of gold chloro-hydroxy speciation in fluids at ambient temperature and pressure: A re-evaluation of the effects of pH and chloride concentration. **Geochimica et Cosmochimica Acta**, 62(21-22): 3515-3526.
- Myers, A.L. and Prausnitz, J.M., (1965). Prediction of the adsorption isotherm by the principle of corresponding states. **Chemical Engineering Science**, 20(6): 549-556.



- Ng, K.C., Chua, H.T., Chung, C.Y., Loke, C.H., Kashiwagi, T., Akisawa, A. and Saha, B.B., (2001). Experimental investigation of the silica gel–water adsorption isotherm characteristics. **Applied Thermal Engineering**, 21(16): 1631-1642.
- Parida, S.K., Dash, S., Patel, S. and Mishra, B.K., (2006). Adsorption of organic molecules on silica surface. **Advances in Colloid and Interface Science**, 121(1-3): 77-110.
- Pearson, R.G., (1963). Hard and Soft Acids and Bases. **Journal of the American Chemical Society**, 85(22): 3533-3539.
- Qi, N. and LeVan, M.D., (2005). Adsorption equilibrium modeling for water on activated carbons. **Carbon**, 43(11): 2258-2263.
- Rees, K.L. and van Deventer, J.S.J., (2000). Preg-robbing phenomena in the cyanidation of sulphide gold ores. **Hydrometallurgy**, 58(1): 61-80.
- Toth, J., (2002). **Adsorption**. Taylor & Francis.
- Trokhimchuk, Trokhimchuk, A.K., Andrianova, Andrianova, E.B., Losev and Losev, V.N., (2004). Interaction Peculiarities of Gold(III) with Silica Gels Containing Both Aminopropyl and Mercaptopropyl Surface Groups. **Adsorption Science & Technology**, 22(10): 837-848.
- Wan Ngah, W.S. and Hanafiah, M.A.K.M., (2008). Removal of heavy metal ions from wastewater by chemically modified plant wastes as adsorbents: A review. **Bioresource Technology**, 99(10): 3935-3948.

Wang, S., Yang, Q. and Zhong, C., (2008). Adsorption and separation of binary mixtures in a metal-organic framework Cu-BTC: A computational study. **Separation and Purification Technology**, 60(1): 30-35.





#### **4.1 Abstract**

Porous glass prepared from coal fly ash was used to study the removal of methylene blue from aqueous solution in a fixed-bed adsorber. The effects of such parameters as adsorbent bed height, feed flow rate, feed concentration, and particle size and mean pore size of porous glass on the breakthrough characteristics were investigated. Three breakthrough models based on the difference in isotherm curvature were validated with the measured breakthrough data. It was found that Thomas model based on the pseudo second-order reaction kinetic rate law and a favorable curved isotherm can best describe the breakthrough curves for the fixed-bed adsorption of methylene blue by porous glass adsorbent under the conditions studied.

#### **4.2 Introduction**

Fixed-bed adsorption has been widely used in the separation and purification of gases and liquids. To be able to design such an adsorption process, it is important to understand the dynamic characteristics of the adsorbent-adsorbate system. One way to comprehend these characteristics is by way of examining the concentration and

time curves of the effluent which is called breakthrough curves. The breakthrough curve depends on such parameters as bed geometry, operating conditions, transport properties, heat effects and types of equilibrium isotherms.

In order to predict the breakthrough times, knowledge of both the adsorption equilibrium capacity and the adsorption kinetics is required. A number of adsorption models have been proposed for predicting the break through point in fixed-bed adsorption under varying adsorption criteria (Cruz-Olivares et al., 2013; Sotelo et al., 2013; Won et al., 2012). Generally, in adsorption studies methylene blue is frequently used as one of the model dyes for two reasons. Firstly, methylene blue is one of the most commonly used commercial dyes since its adsorption characteristic is well studied and documented. Secondly, it finds wide applications in many areas including coloring paper, temporary hair colorant, cotton dyeing and coating for paper stock, etc (Auta and Hameed, 2014; Pratoto et al., 1998; Rozada et al., 2007). However, the presence of methylene blue in industrial effluent poses serious threat to the environment because it can cause eye burns which may be responsible for permanent eye injury in human and animals. Moreover, it is reported that the intermediates formed during biodegradation of the dyes are more toxic than the original molecules. Photochemical oxidation can mineralize the components efficiently, but it is energy intensive and therefore not preferable for large-scale applications. Similarly, many other physical and chemical techniques available for color removal are either costly or inefficient. Among them adsorption is proven to be one of the most efficient processes (Askalany et al., 2012; Malamis and Katsou, 2013; Pang et al., 2013). In this work, porous glass prepared from coal fly ash by the phase-separation method is tested as an

adsorbent for the removal of methylene blue from an aqueous solution in fixed-bed system.

The purpose of the present investigation is thus to study and model the adsorption of methylene blue from aqueous solution by sorption in a fixed-bed column packed with porous glass adsorbent. This work deals primarily with studying the effect of process parameters on adsorption performance, including feed flow rate, bed height or amount of adsorbent, feed concentration particle size and mean pore size of porous glass. The validation of various breakthrough models against the experimental breakthrough data is also attempted.

### 4.3 Characteristic of fixed-bed adsorption

Separation by adsorption in a fixed bed of adsorbent particles occurs under a dynamic condition, as shown in **Figure 4.1**, under which the adsorbate concentration varies with time and distance along the adsorption bed. At time  $t_1$  when an adsorbate-containing fluid is first admitted into a bed of adsorbent in an adsorption column, most of the adsorbate is initially adsorbed near the inlet part of the bed and the fluid passes on with little adsorption taking place, showing a continuous drop of concentration with a reverse S-shaped curve. At time  $t_2$ , the adsorption bed over distance  $L_1$  becomes saturated with the adsorption continuing further along the bed. The zone of the bed where the concentration gradient exists, like the ones at  $t_2$  and  $t_3$ , is often called “the Mass Transfer Zone” or MTZ. The unused part of the bed that is free of adsorbate lies between distance  $L_B$  and  $L_2$  at time  $t_2$  and between distance  $L_B$  and  $L_3$  at time  $t_3$ . As time progresses, the concentration front moves forward and the

saturated zone behind the concentration front enlarges along the bed distance. When the leading edge of the concentration front reaches the bed exit ( $L_B$ ), the time at this breakthrough point is called “the breakthrough time ( $t_B$ )” at which the exit concentration of adsorbate begins to rise rapidly toward the inlet concentration of adsorbate in the feed fluid.

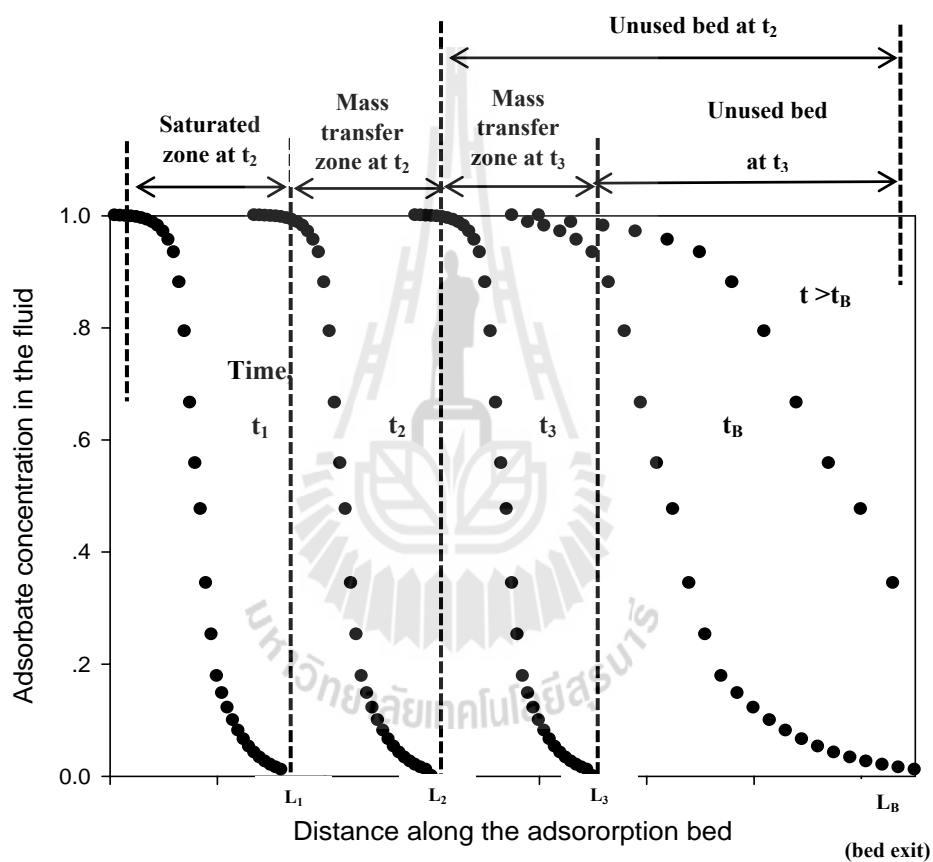


**Figure 4.1** Formation and progression of mass transfer zone (MTZ) within a fixed bed of adsorbent until the breakthrough is reached at the bed exit.

**Figure 4.2** shows the breakthrough curve for a single adsorbate from a fixed bed adsorption column. It is a plot of the adsorbate concentration at the adsorber

outlet versus time. In practice, the breakthrough time is defined as the time at which the exit concentration of adsorbate attains a maximum permissible concentration, for example, at the level of 5% of the feed concentration ( $C_e/C_o = 0.05$ ). As the breakthrough continues, the concentration of adsorbate in the effluent rises continuously to the feed concentration ( $C/C_o = 1$ ). When this occurs no more adsorption can take place which means that the bed is completely exhausted and the regeneration of the adsorption bed is necessarily required. The followings are typical factors that affect the dynamics of a fixed-bed adsorber,

- Type of adsorbent
- Particle size of an adsorbent which also determines the maximum allowable pressure drop
- Depth of the adsorbent bed
- Fluid velocity
- Temperatures of the fluid stream and the adsorbent
- Concentration of adsorbate in the feed stream
- Concentration of the contaminants in the feed
- Pressure of the system for gas-phase adsorption

Information on the breakthrough curves under varying adsorption condition is of prime importance for the rational design and optimization of a fixed-bed adsorption process.

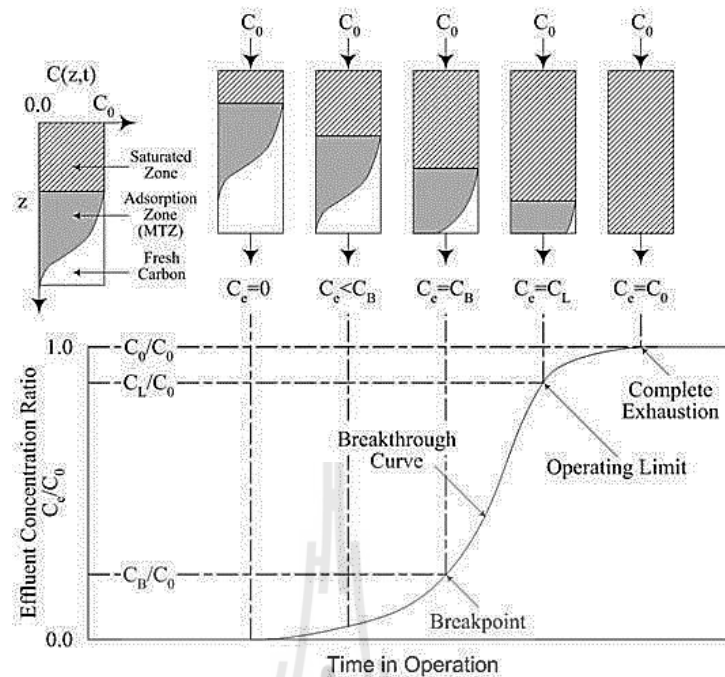


**Figure 4.2** Breakthrough Characteristics of a Fixed-Bed Activated Carbon Adsorber (Pure water website).

#### 4.4 Breakthrough equations

The dynamics of adsorption in a fixed bed can be assessed by following the response of adsorbate concentration at the column exit as a function of time when a step change in the adsorbate concentration is introduced at the column inlet. This information is known as a breakthrough curve. For isothermal and single component adsorption at low concentration, a mathematical model that describes this dynamic behavior of the adsorption system can be achieved through a mass balance of an adsorbate over a differential element of the adsorbent bed. The resulting equation reads



$$-D_z \frac{\partial^2 C}{\partial z^2} + u \frac{\partial C}{\partial z} + \frac{\partial C}{\partial t} + \frac{(1-\varepsilon_b)}{\varepsilon_b} \frac{\partial \bar{q}}{\partial t} = 0 \quad (4.1)$$

where

$$\bar{q} = \frac{3}{R_p^3} \int_0^{R_p} R^2 q dr$$

$D_z$  = axial dispersion coefficient

$C$  = adsorbate concentration in the fluid phase

$u$  = interstitial fluid velocity

$\bar{q}$  = adsorbed-phase concentration

$R_p$  = particle radius

$\varepsilon_b$  = bed porosity

$z$  = distance along the bed

$t$  = time

The initial and boundary conditions for a bed free of adsorbate at time zero with a step change in adsorbate concentration ( $C_0$ ) at the column inlet at time zero are as follows.

$$t \leq 0, q(R, 0, z) = C(0, z) = 0 \quad (4.2)$$

$$t \geq 0, C(t, 0) = C_0$$

The solution for the breakthrough curve can be directly obtained by solving Eq (4.1) subject to the above initial and boundary conditions and the appropriate expression for the adsorption rate ( $d\bar{q}/dt$ ). Overall, the complexity of the breakthrough models depends on the nature of equilibrium isotherm, the choice of rate equation and the flow model.

Since in this work the adsorption of methylene blue by porous glass is well described by the Langmuir isotherm equation, three breakthrough models dealing with three types of isotherm curvature are applied to describe the experimental breakthrough data. They are Klinkenberg model for a linear isotherm, Thomas model for a favorable Langmuir isotherm, and Bohart and Adams model for an irreversible or square isotherm. All these models assume isothermal adsorption and plug flow with no axial dispersion effect ( $D_z = 0$ ).

The **Klinkenberg model** assumes a linear adsorption isotherm and the linearized rate expression known as the linear driving force model (LDF) for the rate of adsorption into the adsorbent pellet. That is,

$$\frac{\partial q}{\partial t} = k_p (q^* - \bar{q}) = kK(C - C^*) \quad (4.3)$$

where  $k_p$  is the particle mass-transfer coefficient,  $q^*$  is the adsorbate-phase concentration that is in equilibrium with the bulk-phase concentration  $C^*$ , and  $K$  is the Henry's constant which can be derived from Langmuir equation to be,  $K = bq_m$ , where  $b$  is the Langmuir or affinity constant and  $q_m$  is the monolayer adsorbed capacity. The breakthrough solution from the Klinkenberg model is approximated by

$$C = \frac{1}{2} \left[ 1 + \operatorname{erf} \left( \sqrt{\tau} - \sqrt{\xi} + \frac{1}{8\sqrt{\tau}} + \frac{1}{8\sqrt{\xi}} \right) \right],$$

(error < 0.6% for  $\zeta > 2.0$ ) (4.4)

where  $\xi = \frac{k_p K_z}{u} \left( \frac{1 - \varepsilon_b}{\varepsilon_b} \right) =$  dimensionless distance coordinate

$\tau = k_p \left( t - \frac{z}{u} \right) =$  dimensionless time coordinate corrected for

displacement,  $z$  is the bed length and  $\varepsilon_b$  is the porosity of adsorbent bed.

**Thomas model** (Thomas, 1944) was developed for an equilibrium Langmuir isotherm and 2<sup>nd</sup>-order reversible reaction kinetics based on anion exchange theory. The basic assumptions of Thomas or reaction model are negligible axial and radial dispersion in the fixed bed column and the adsorption is described by a pseudo second-order reaction rate principle which reduces to a Langmuir isotherm at equilibrium with no intra-particle diffusion and external resistance during the mass transfer processes. The expression for adsorption kinetics is described as,

$$\frac{\partial q}{\partial t} = k_1(q_0 - q)C - k_2q(C_0 - C) \quad (4.5)$$

where  $k_1$  and  $k_2$  are velocity constants,  $C_0$  is the inlet concentration of adsorbate in the fluid stream, and  $q_0$  is the adsorbed-phase concentration which is in equilibrium with the feed concentration. The above expression describes the second-order reversible reaction kinetics which can be applicable to both favorable and unfavorable adsorption conditions.

By assuming plug flow, negligible axial dispersion, the mass balance equation of an adsorbate Eq. (4.1) and Eq (4.5) were solved by Thomas to obtain the solution below

$$\frac{C}{C_o} = \frac{J(\beta\xi, \tau)}{J(\beta\xi, \tau) + [1 - J(\xi, \beta\tau)] \exp[(\beta - 1)(\tau - \xi)]} \quad (4.6)$$

where  $\beta = \frac{1}{1 + bC_o}$  = equilibrium factor (a measure of isotherm curvature),  $\tau = k_t C_o \left( t - \frac{z}{u} \right)$  and  $\xi = \frac{k_t q_o z}{u} \left( \frac{1 - \varepsilon_b}{\varepsilon_b} \right)$ . For the long bed condition the

solution can be approximated by

$$\frac{C}{C_o} = \frac{1}{1 + \exp[k_t (q_o m_c - C_o V_{eff}) / Q]} \quad (4.7)$$

where  $k_t$  is the Thomas rate constant,  $q_o$  is the adsorptive capacity of adsorbent that is in equilibrium with the feed concentration, that is,  $q_o = q_m b C_o / (1 + b C_o)$ ,  $m_c$  is the mass of adsorbent in the column,  $V_{eff}$  is the throughput volume, and  $Q$  is the volumetric flow rate.

**Bohart and Adams model** was proposed (Bohart & Adams, 1920) for one component adsorption that has been widely used to describe adsorption dynamics when chemical reaction takes place. It was found that this model can be used to describe the initial part of the breakthrough curve for many one component adsorption systems with chemical reaction. The model incorporates an irreversible

adsorption isotherm, which indicates that any solute adsorbed onto the carbon surface cannot desorb.

The kinetics of adsorption are described using the quasi-chemical rate law below:

$$\frac{\partial q}{\partial t} = k_b C(q_e - q) \quad (4.8)$$

where  $q_e$  is the constant value of  $q$  that corresponds to the equilibrium condition at the gas/adsorbent interface, and  $k_b$  is a constant.

The rate of adsorption as in Eq (4.8) is proportional to the concentration of the adsorbate in the bulk phase, and to the fraction of the capacity of the adsorbent which still remains at a moment in time. The model uses the rectangular, irreversible isotherm normally used to describe reaction systems.

$$q_e = \begin{cases} 0, & \text{if } C = 0 \\ q_o, & \text{if } C > 0 \end{cases}$$

For negligible axial dispersion, the differential mass balance was solved by Cooney (Cooney, 1999) and the solution below was obtained,

$$\frac{C}{C_o} = \frac{\exp(\tau)}{\exp(\tau) + \exp(\xi) - 1} \quad (4.9)$$

where

$$\tau = k_b C_o \left( t - \frac{z}{u} \right)$$

and

$$\xi = \frac{k_b q_o z}{u} \left( \frac{1 - \varepsilon_b}{\varepsilon_b} \right)$$

where  $q_o$  is the adsorptive capacity of the adsorbent in equilibrium with the feed concentration,  $C_o$ .

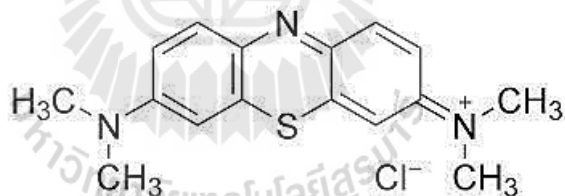
## 4.5 Experimental method

### 4.5.1 Materials and characterization

Two types of porous glass with different porous properties were prepared from coal fly ash by the phase-separation and used for methylene blue adsorption study in a fixed bed column. One was prepared at 650°C for 20 hours and the other at 725°C for 72 hours of heat treatment conditions with the preparation method being reported in Chapter II.

Porous properties of the porous glasses were determined using  $N_2$  adsorption isotherm data at  $-196\text{ }^\circ\text{C}$  acquired by the automated adsorption apparatus (ASAP2010, Micrometrics). From the obtained isotherm data, the specific surface area,  $S_{\text{BET}}$ , was estimated by applying Brunauer-Emmett-Teller (BET), the total pore volume,  $V_T$ , was found from the amount of  $N_2$  gas adsorbed at the relative pressure of 0.99 and converted to volume of nitrogen in liquid state, and the mesopore volume was determined by BJH theory (Barrett, Joyner, and Halenda theory).

The adsorbate used for liquid adsorption tests in the batch and fixed-bed systems was methylene blue (MB). It is a heterocyclic aromatic chemical compound with the chemical formula  $C_{16}H_{18}N_3SCl$  (MW  $320\text{ g mol}^{-1}$ ) and the following chemical structure:



The stock solutions of MB with various concentrations were prepared in distilled water. The solution pH was around 7.0 and no attempt was made to adjust the pH throughout the adsorption experiments.

#### 4.5.2 Batch adsorption experiments

The batch adsorption was studied using 50 ml of MB solution and 0.1 g of porous glass in a 100 ml flask. The experiments were performed at 30°C with different initial dye concentrations varying from 0 – 25 mg/L. The shaking time for each batch was 24 h for adsorption to reach equilibrium. MB concentration in solution was monitored and determined using a UV spectrophotometer (Varian model Cary1E) by measuring the solution absorbance at the wavelength of maximum absorbance (628 nm). The amount of dye adsorbed onto the unit weight of the adsorbent in mg/g was calculated using the following equations:

$$q = \frac{V(C_0 - C)}{m} \quad (4.9)$$

where  $V$  is the solution volume in L,  $C_0$  is the initial MB concentration in mg/L,  $C$  is the MB concentration at any time  $t$  in mg/L and  $m$  is the weight of porous glass in g.

#### 4.5.3 Fixed-bed adsorption experiments

MB adsorption tests in a fixed-bed were conducted in a glass column of 1.6 cm inside diameter (cross-sectional area of  $2.04 \times 10^{-2} \text{ m}^2$ ) and 20 cm in height. A known concentration of MB solution was pumped from the bottom of the column and the solution at the outlet was collected and its concentration analyzed as a function of time to obtain the breakthrough information. The effects of bed height, solution feed rate, feed concentration, particle size and pore size of porous glass on MB adsorption were investigated. All experiments were carried out at room temperature of 30°C. Table 4.1 lists the experimental conditions used for the



parametric study of fixed-bed adsorption of methylene blue by porous glass adsorbents.

**Table 4.1** Experimental conditions for fixed-bed adsorption of methylene blue by porous glass performed at 30°C.

<b>Bed height (cm)</b>	<b>Feed rate (cm<sup>3</sup>/min)</b>	<b>Feed conc. of MB (mg/L)</b>	<b>Particle size (μm)</b>	<b>Pore size (nm)</b>
3-10	10	10	600-850	6.32
5	10-20	10	600-850	6.32
10	10	5-20	600-850	6.32
5	10	10	600-850	6.32
5	10	10	250-600	5.30
5	10	10	600-850	5.30
5	10	10	600-850	6.32

## 4.6 Results and discussion

### 4.6.1 Physical and porous properties of porous glass

Four types of porous glass samples with different pore texture (PG1, PG2, PG3 and PG4) were employed for the adsorption of methylene blue in the batch and fixed-bed systems. **Figure 4.3 and Table 4.2** show the nitrogen adsorption isotherms at 77K and physical and porous properties of the test adsorbents, respectively. The  $N_2$  isotherms indicate that all the porous glass samples exhibit the characteristic of Type IV isotherm (Type II + hysteresis loop) which is indicative of a mesoporous solid.

It appears that porous glasses with smaller pore size (PG2 and PG4) can take up more adsorbate gas due to their higher specific surface area and pore volume. For a given particle size, porous glass with smaller mean pore size gives larger pore volume and surface area but with less particle porosity (PG1 vs. PG2 and PG3 vs. PG4). However, particle size has virtually no effect on the physical and porous properties of the porous glass samples provided that they have the same pore size. Porous glass with smaller pore size gives the particle apparent density about 30% less as compared to the larger pore size particle, while the particle true density differs by almost 100%.

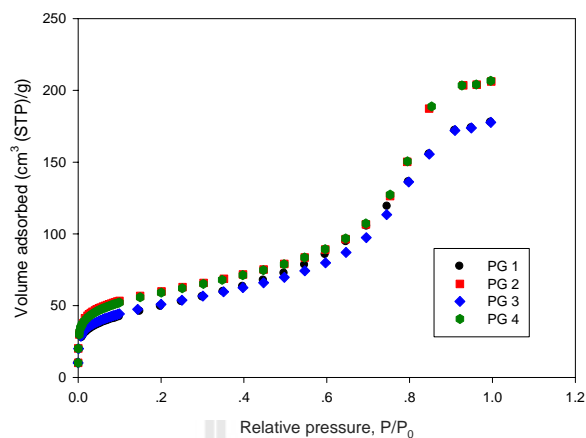


**Figure 4.3** Nitrogen adsorption isotherms of porous glass samples at 77K.

**Table 4.2** Physical and porous properties of porous glass adsorbents used for methylene blue adsorption tests.

	<b>PG1</b>	<b>PG2</b>	<b>PG3</b>	<b>PG4</b>
Particle size, $\mu\text{m}$	600-850	600-850	250-600	250-600
BET surface area, $\text{m}^2/\text{g}$	174	205	174	203
Total pore volume, $\text{cm}^3/\text{g}$	0.275	0.320	0.285	0.320
Micropore volume, $\text{cm}^3/\text{g}$	0.0054	0.0083	0.0140	0.0044
Mesopore volume, $\text{cm}^3/\text{g}$	0.270	0.312	0.271	0.316
Mean pore size, nm	6.32	5.22	6.32	5.30
Particle porosity	0.53	0.32	0.53	0.32
Apparent particle density, $\text{kg}/\text{m}^3$	3541	2638	3541	2638
Particle true density, $\text{kg}/\text{m}^3$	7530	3880	7530	3880
Bed porosity	0.58	0.54	0.57	0.53

**Note:**

- PG1=large particle size/large pore size,
- PG2=large particle size/small pore size
- PG3=small particle size/large pore size,
- PG4=small particle size/small pore size.

**4.6.2 Batch adsorption tests**

**Figure 4.4** shows the equilibrium adsorption isotherms of methylene blue by the four porous glass adsorbents. Langmuir and Freundlich isotherm equations were used to fit the measured isotherm data of methylene blue adsorption. Table 4.3 lists the values of isotherm model parameters derived from data fitting. Overall, both adsorption models can describe the methylene blue isotherm reasonably well with the Langmuir equation giving slightly better fitting when compared with the Freundlich equation.

As to the effect of porous glass type on the monolayer adsorbed capacity ( $q_m$ ) of the Langmuir model, the following decreasing order of the monolayer capacity ( $q_m$ ) is observed: PG1 > PG3 > PG4 > PG2. This result clearly indicates that the increased adsorbed capacity of methylene blue can be better achieved with the porous glass adsorbent with larger pore size (PG1 and PG3). Similarly, the higher  $b$  value of the porous glass with larger pore size indicates a stronger affinity of dye molecules towards the adsorbent surface.

The adsorption of methylene blue on porous glass is the result of electrostatic interaction between the negatively charged silica surface due to the presence of silanol (hydroxyl) groups at pH above 3 and the positively charged dye molecules (Gude et

al., 2008). As noted from the characteristic of the adsorption isotherm in Figure 4.4, the amount of methylene blue adsorbed increases rapidly over the initial low concentration range due to the excess number of silanol active sites, followed then by a slow increase of the adsorbed amount at higher concentrations before finally approaching a final constant value caused by the competition among the dye molecules toward the continued depletion in the number of surface adsorption sites.

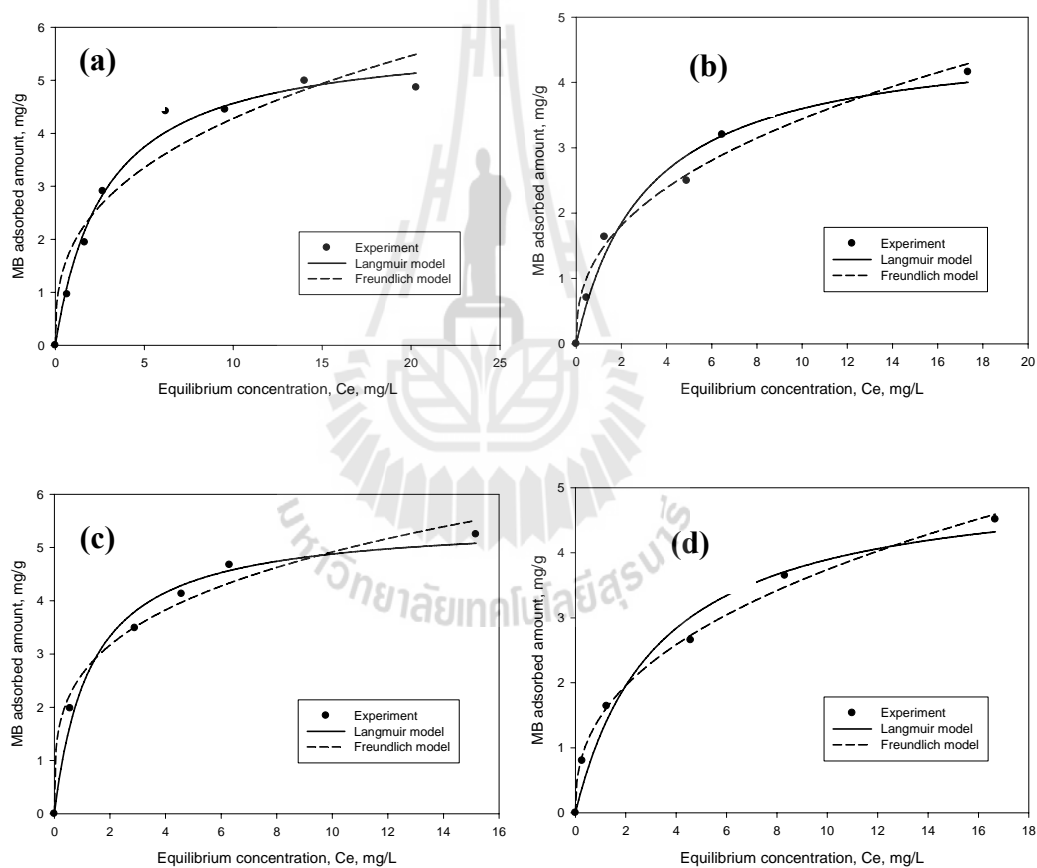


**Figure 4.4.** Equilibrium isotherms of methylene blue adsorption by different types of porous glass at 30°C ; (a) PG1, (b) PG2, (c) PG3, and (d) PG4.

**Table 4.3** Fitted parameters of isotherm models for the adsorption of methylene blue by porous glass at 30°C.

Sample type	Langmuir model			Freundlich model		
	$q_m$ (mg/g)	$b$ (L/mg)	$R^2$	KF	nF	$R^2$
PG 1	5.85	0.3554	0.9875	1.90	2.84	0.9326
PG 2	4.72	0.3203	0.9780	1.37	2.50	0.9711
PG 3	5.52	0.7616	0.9827	2.62	3.66	0.9850
PG 4	5.17	0.3038	0.9841	1.48	2.48	0.9767

#### 4.6.3 Breakthrough curves

Figure 4.5 depicts a typical breakthrough curve showing the various definitions of breakthrough parameters. The breakthrough time ( $t_B$ ) is defined here as the time at which the detected exit solute concentration ( $C$ ) reaches the level of 5% of the feed concentration ( $C_0$ ), that is  $C/C_0 = 0.05$ , while the equilibrium time ( $t_E$ ) is defined as the time at which  $C/C_0$  is equal to 0.95. The amount of solute adsorbed at time  $t$  ( $q_s$ ) can be estimated from the product of solute feed rate ( $Q_s$ ) multiplied by the mean stoichiometric time ( $t_M$ ). The mean stoichiometric time is the time spent by an ideal concentration front travelling in the bed that gives the same adsorbed amount as in the actual adsorption bed. Therefore, we have

$$q_s = Q_s t_M = C_0 Q t_M \quad (4.10)$$

where  $Q$  is the solution feed flow rate,  $C_o$  is the methylene blue concentration in the feed, and  $t_M$  can be calculated from the area above the breakthrough curve at time  $t$  corresponding to the exit solute concentration  $C$ . Thus,

$t_M$  = area above breakthrough curve

$$\int_0^t [1 - C/C_o] dt \quad (4.11)$$

When applying Eq (4.11) to the conditions at breakthrough time and equilibrium time, we obtain respectively

$$t_{MB} = \int_0^{t_B} [1 - C/C_o] dt \quad (4.12)$$

and

$$t_{ME} = \int_0^{t_E} [1 - C/C_o] dt \quad (4.13)$$

The amounts of solute (methylene blue) adsorbed at time  $t_B$  and  $t_E$  can then be computed from the following equations:

$$q_B = C_o Q t_{MB} \quad (4.14)$$

and

$$q_E = C_o Q t_{ME} \quad (4.15)$$

Figure 4.6 shows the influence of bed height, feed concentration, feed flow rate, pore size and particle size, respectively, on the derived breakthrough curves. The effects of these process variables on the breakthrough parameters, including  $t_B$ ,  $t_E$ ,  $q_B$  and  $q_E$ , are summarized in Tables 4.4 and 4.5. The results show that the times at the breakthrough and equilibrium ( $t_B$  and  $t_E$ ) as well as the corresponding adsorbed capacities ( $q_B$  and  $q_E$ ) all increase with either the decrease in feed concentration, decreasing feed flow rate, or increasing in the adsorption bed length. However, Table 4.5 shows that the effects of pore size and particle size on the breakthrough parameters do not follow those on the maximum monolayer adsorbed capacity ( $q_m$ ) of the equilibrium Langmuir isotherm. That is, porous glass with smaller pore size gives larger values of breakthrough time and capacity, for example, comparing PG2 vs. PG1 and PG4 vs. PG3. The effect of particle size is also obscure, that is, for large pore size samples the larger size particle gives smaller  $t_B$  and  $q_B$  (cf. PG1 vs. PG3), while the opposite trend is true for smaller pore size adsorbents (cf. PG4 vs. PG2).



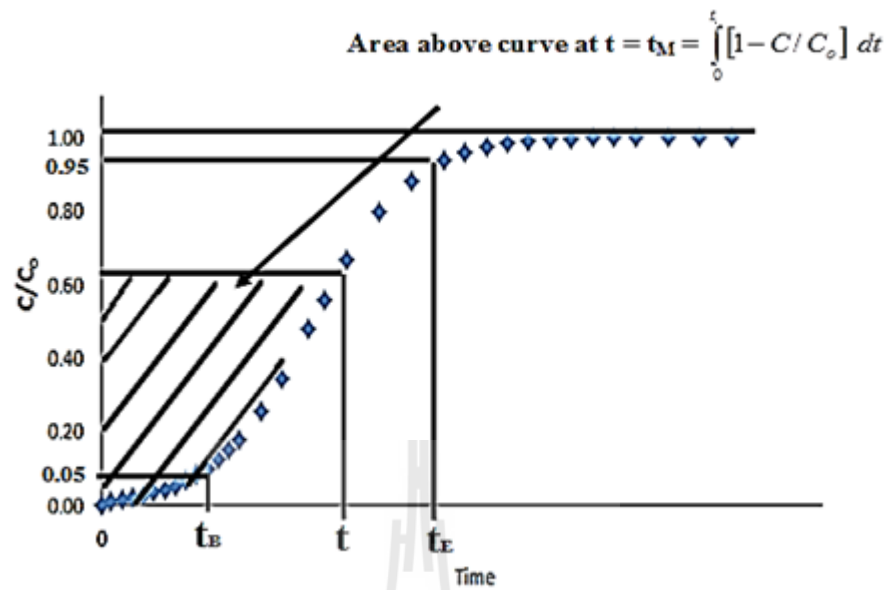


**Figure 4.5** Typical breakthrough curve showing the estimation of breakthrough parameters ( $t_B$  = breakthrough time,  $t_E$  = equilibrium time, and  $t_M$  = mean stoichiometric time)



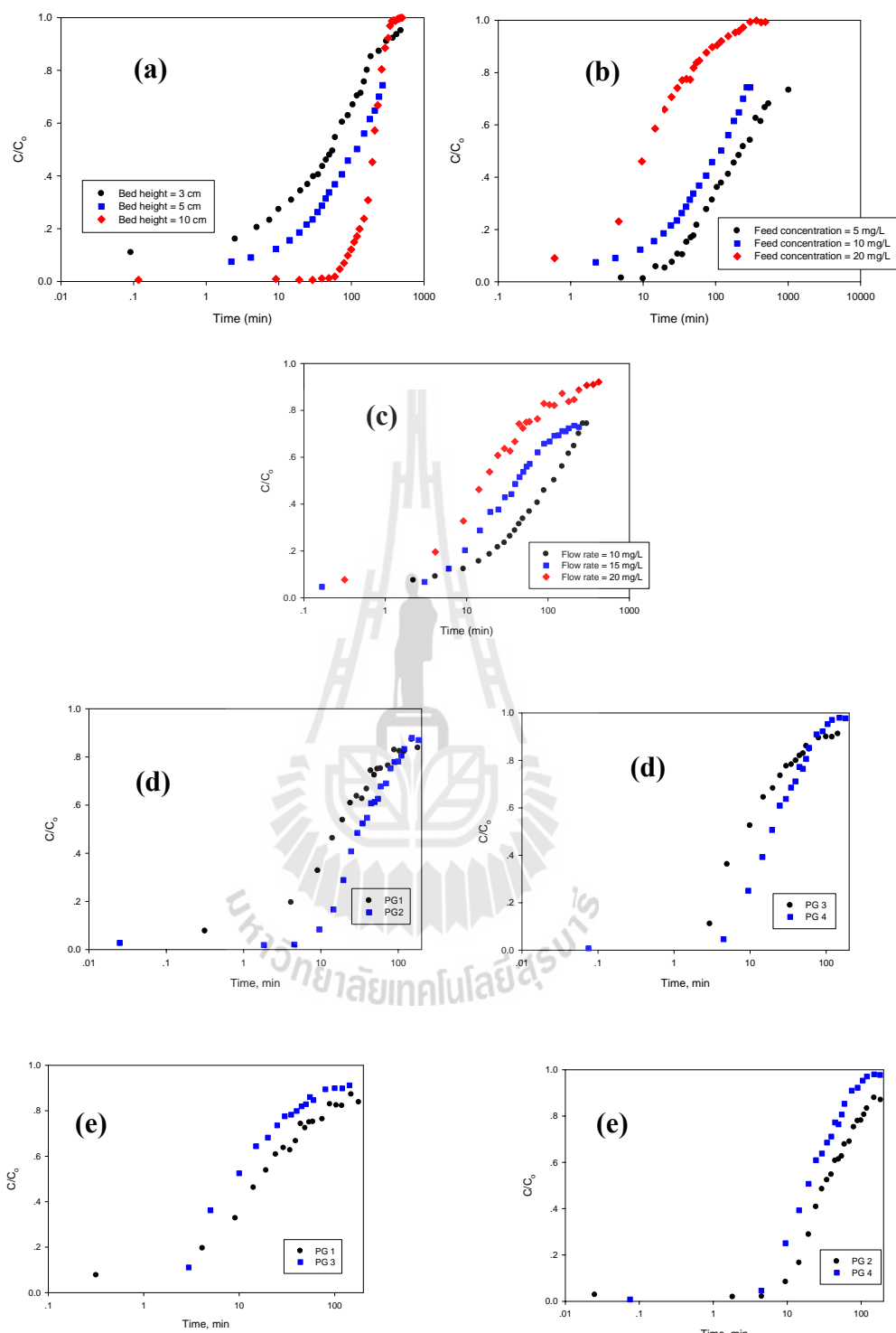


**Figure 4.6** Effects of process variables on the breakthrough curves of methylene blue adsorption by porous glass PG1 at 30°C: (a) bed height, (b) feed concentration, (c) feed flow rate, (d) pore size, and (e) particle size.

**Table 4.4** Effect of bed height, feed concentration and feed flow rate on the breakthrough parameters for the adsorption of methylene blue by porous glass PG1 at 30°C.

Parametric	Bed height (cm)	C <sub>o</sub> (mg/L)	Flow rate (mL/min)	t <sub>B</sub> (min)	t <sub>E</sub> (min)	W (g)	Area above curve at t <sub>B</sub> (min)	Area above curve at t <sub>E</sub> (min)	q <sub>B</sub> (mg/g)	q <sub>E</sub> (mg/g)	% Saturation
Bed height	3	10	10	0.04	113.70	1.2446	0.0010	51.24	0.0001	4.1166	0.002
	5	10	10	1.49	225.75	2.0743	0.0374	102.97	0.0018	4.9642	0.036
	10	10	10	70.52	332.00	4.1486	2.6424	192.66	0.0637	4.6440	1.371
Feed concentration	5	5	10	14.15	1321.00	2.0743	0.6055	1044.67	0.0146	25.1814	0.058
	5	10	10	1.49	225.75	2.0743	0.0374	102.97	0.0018	4.9642	0.036
	5	20	10	0.33	178.00	2.0743	0.0082	48.78	0.0008	4.7034	0.017
Flow rate	5	10	10	1.49	225.75	2.0743	0.0374	102.97	0.0018	4.9642	0.036
	5	10	15	0.20	81.53	2.0743	0.0048	36.78	0.0003	2.6599	0.011
	5	10	20	0.18	30.83	2.0743	0.0045	13.97	0.0004	1.3468	0.030

**Table 4.5** Effects of pore size and particle size of porous glass on the breakthrough parameters for the adsorption of methylene blue at 30°C.

Sample	Bed height (cm)	C <sub>0</sub> (mg/L)	Flow rate (mL/min)	Particle size, d <sub>p</sub> (um)	Mean pore size, d <sub>po</sub> (nm)	t <sub>B</sub> (min)	t <sub>E</sub> (min)	q <sub>B</sub> (mg/g)	q <sub>E</sub> (mg/g)	% Saturation
PG 1	5	10	10	725	6.32	0.2056	432.46	0.0002	3.0799	0.006
PG 2	5	10	10	725	5.22	0.9513	291.08	0.0011	8.7859	0.013
PG 3	5	10	10	425	6.32	4.5985	99.11	0.0055	1.6451	0.334
PG 4	5	10	10	425	5.30	6.5392	593.89	0.0112	3.4091	0.328



#### 4.6.4 Breakthrough models

In fitting the breakthrough models to the experimental data, two calculation schemes were employed, as shown in Table 4.6. The first one (Scheme I) is to fix the calculated isotherm related parameters ( $K$ ,  $q_0$ ,  $\beta$ ) and optimize the rate constants ( $k_p$ ,  $k_b$  and  $k_t$ ), while the second one (Scheme II) involves the optimization of both the isotherm and rate parameters. The minimization of sum of square error (SSE) between the experimental and predicted results was used as a criterion for the best data fitting by regression analysis. Table 4.7 shows the estimated values of model parameters along with the values of SSE and regression coefficients ( $R^2$ ) as an indicator of fitting accuracy.

The accuracy of data fitting by the two schemes is presented in **Figures 4.7 and 4.8** for a selected set of breakthrough data. It is noted that the application of Scheme I fails to predict accurately the breakthrough data, while Scheme II gives a good description of the breakthrough curves. It should be remembered that the good fitting derived by Scheme II, based on the optimization of both the kinetic and isotherm parameters, is the result of increased flexibility of more adjustable parameters from one to two for the Klinkenberg and Bohart and Adams models, and from one to three parameters for Thomas model. Therefore, it is not surprising that Thomas model will give the best fitting compared to the other two models, as can be seen from the values of  $R^2$  in Table 4.7 and Figure 4.8 under various adsorption conditions. Further notice on the optimum rate parameters ( $k_p$ ,  $k_b$ , and  $k_t$ ) of the three models indicate that the values of the three parameters increase with increasing in the bed length, feed concentration and feed flow rate. Overall, it can be inferred that the utilization of the three breakthrough model based on the

difference in the isotherm curvature is able to give a sound prediction of breakthrough results for the adsorption of methylene blue from solution by porous glass under the studied conditions, provided that the rate and isotherm parameters need to be optimized simultaneously.

The best fitted parameters of the Thomas model ( $k_t$ ,  $q_0$  and  $\beta$ ) for a selected set of data ( $L= 10$  cm,  $C_0 = 10$  mg/L,  $Q = 10$  mL/min) are further analyzed for their sensitivities on the predicted breakthrough curves. Table 4.8 and Figure 4.9 show the results for the variation of each model parameter by  $\pm 50\%$  from the reference best fitting values. It is observed from Figure 4.9 that the breakthrough curve is not sensitive to the change in the  $\beta$  value which is a measure of isotherm curvature, while the variation of the rate constant ( $k_t$ ) and adsorbed capacity  $q_0$  has a definite effect on the breakthrough characteristics. Increasing the value of  $k_t$  from -50% to 50% of the reference value tends to increase the slope of the curve. This is understandable since the increased adsorption rate due to the increased  $k_t$  value means a corresponding decrease in the pore resistance and hence the concentration front inside the bed will approach a sharp wave front, hence giving the breakthrough curve with steeper slope. For an ideal wave front where there is no resistance in the adsorbent pores (equilibrium model), the moving front shows a vertical line perpendicular to the column axis. The variation in  $q_0$ , which is the adsorbed capacity of the bed in equilibrium with the feed concentration ( $q_0 = q_0(C_0)$ ), has a direct influence on the position (time scale) of the breakthrough curve but not on the slope (sharpness) of the curve. Increasing in the value of  $q_0$  relative to the base value shifts the breakthrough curve toward a longer time position, thus indicating a better adsorption efficiency by the adsorption bed.

**Table 4.6** Curve fitting schemes for obtaining breakthrough model parameters by regression analysis for the adsorption of methylene blue by porous glass PG1 at 30°C.

Scheme	Breakthrough models						
	Klinkenberg		Bohart&Adams		Thomas		
	$K_p$	$K$	$K_b$	$q_0$	$K_t$	$q_0$	$\beta$
	Fitting approach						
<b>I</b>	✓	✓✓	✓	✓✓	✓	✓✓	✓✓
<b>II</b>	✓	✓	✓	✓	✓	✓	✓

**Note:** ✓ optimally searched, ✓✓ calculated and fixed



**Table 4.7** Fitted parameters of breakthrough models for predicting breakthrough curves of methylene blue adsorption by porous glass PG1 at 30°C.

Parameter	Bed height (cm)	C <sub>0</sub> (mg/L)	Flow rate (mL/min)	Scheme I – Klinkenberg's model			Scheme II - Klinkenberg's model			
				k <sub>p</sub>	K	SSE	k <sub>p</sub>	K	SSE	R <sup>2</sup>
Bed height	3	10	10	0.1772	1.5716	6.327	0.015	329	0.0559	0.9745
	5	10	10	0.2204	1.5716	10.18	0.0148	387	0.4434	0.8840
	10	10	10	9.6757	1.5716	12.73	0.0614	235	0.0173	0.9970
Feed concentration	5	5	10	0.04	1.5716	14.25	0.0046	580	0.821	0.7354
	5	10	10	0.2204	1.5716	10.18	0.0148	387	0.4434	0.8840
	5	20	10	9.6756	1.5716	2.656	0.2193	121	0.622	0.8359
Flow rate	5	10	10	0.2204	1.5716	10.18	0.0148	387	0.4434	0.8840
	5	10	15	0.0399	1.5716	6.383	0.0132	250	0.4706	0.7287
	5	10	20	0.1153	1.5716	2.462	0.0302	88	0.1588	0.8795



Parameter	Bed height (cm)	C <sub>o</sub> (mg/L)	Flow rate (mL/min)	Scheme I Bohart-Adams			Scheme II Bohart-Adams model			
				k <sub>b</sub>	q <sub>0</sub>	SSE	k <sub>b</sub>	q <sub>0</sub>	SSE	R <sup>2</sup>
Bed height	3	10	10	0.0207	3.8938	6.516	0.0016	3270	0.0622	0.9678
	5	10	10	0.0398	3.8938	10.55	0.001	389	0.4167	0.8225
	10	10	10	0.0029	3.8938	12.94	0.0022	2313	0.0073	0.9986
Feed concentration	5	5	10	0.0071	3.8938	15.51	0.0006	3718	0.2623	0.8213
	5	10	10	0.0398	3.8938	10.55	0.001	389	0.4167	0.8225
	5	20	10	0.0398	3.8938	3.140	0.0035	1584	0.2559	0.8579
Flow rate	5	10	10	0.0398	3.8938	10.55	0.001	389	0.4167	0.8225
	5	10	15	0.0137	4.2444	6.487	0.006	3718	0.2623	0.7167
	5	10	20	0.0071	4.4444	2.633	0.012	1784	0.1874	0.8367

Parameter	Bed height (cm)	C <sub>0</sub> (mg/L)	Flow rate (mL/min)	Scheme I Thomas model				Scheme II Thomas model				
				k <sub>t</sub>	q <sub>0</sub>	Beta	SSE	k <sub>t</sub>	q <sub>0</sub>	Beta	SSE	R <sup>2</sup>
Bed height	3	10	10	5368709	3.8938	0.2478	6.565	0.0009	6429	0.2906	0.0153	0.9918
	5	10	10	5368709	3.8938	0.2478	10.97	0.0008	6193	0.1812	0.2839	0.9704
	10	10	10	117977	3.8938	0.2478	13.00	0.0022	2530	0.0177	0.007	0.9987
Feed concentration	5	5	10	48722	3.8938	0.2478	12.62	0.0003	26746	1.2469	0.0057	0.9958
	5	10	10	5368709	3.8938	0.2478	10.97	0.0008	6193	0.1812	0.2839	0.9704
	5	20	10	5368709	3.8938	0.2478	2.656	0.001	4193	0.2078	0.1224	0.9072
Flow rate	5	10	10	5368709	3.8938	0.2478	10.97	0.0008	6193	0.1812	0.2839	0.9704
	5	10	15	5368709	4.2444	6.5935	6.596	0.0002	62882	2.0963	0.0791	0.9444
	5	10	20	40093	4.4444	2.6555	2.6555	0.0007	2295	0.0001	0.1407	0.8976

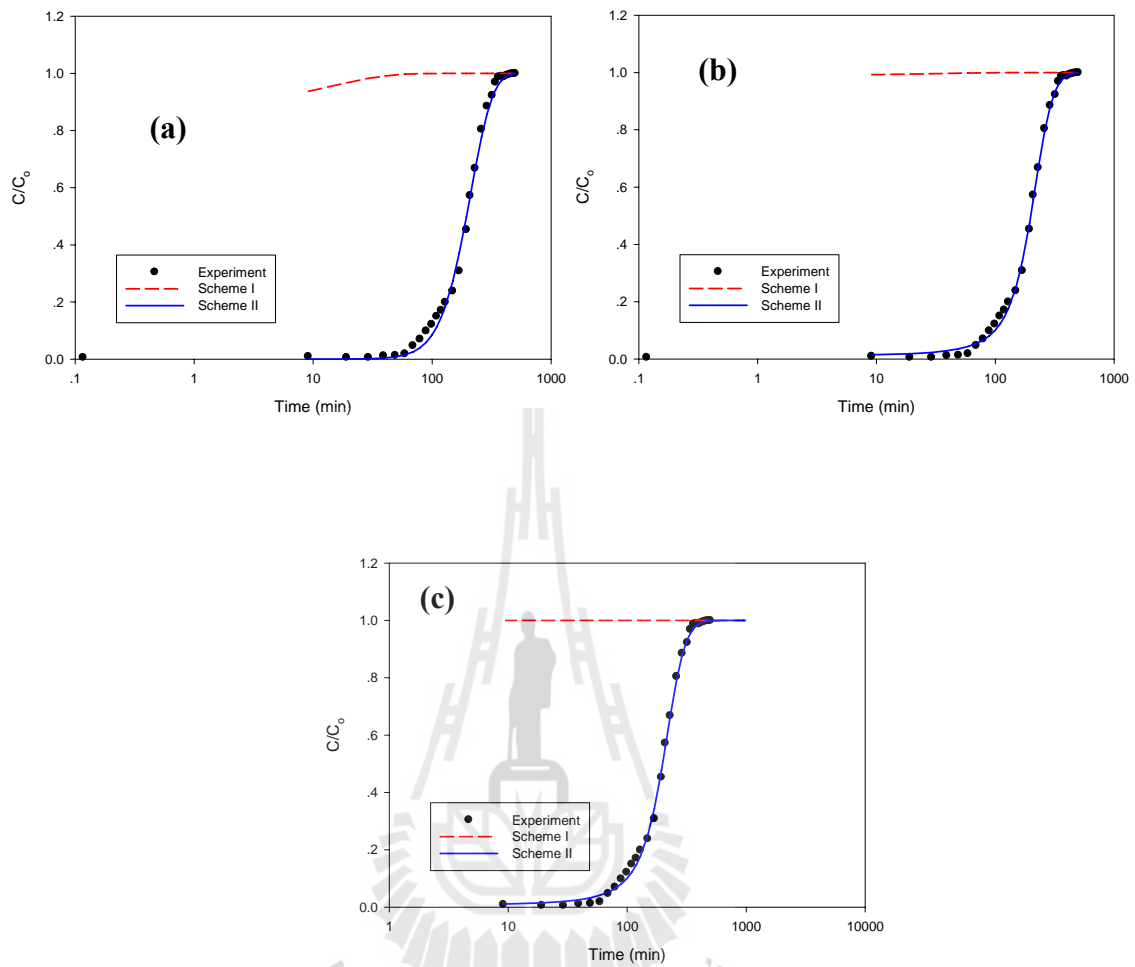


**Figure 4.7.** Testing of fitting schemes (Scheme I) of breakthrough models:(a) Klinkenberg model, (b) Bohart and Adams model, and (c) Thomas model (methylene blue adsorbed on PG1 at bed height 10 cm, feed concentration 10 mg/L and Feed flow rate 10mL/min).

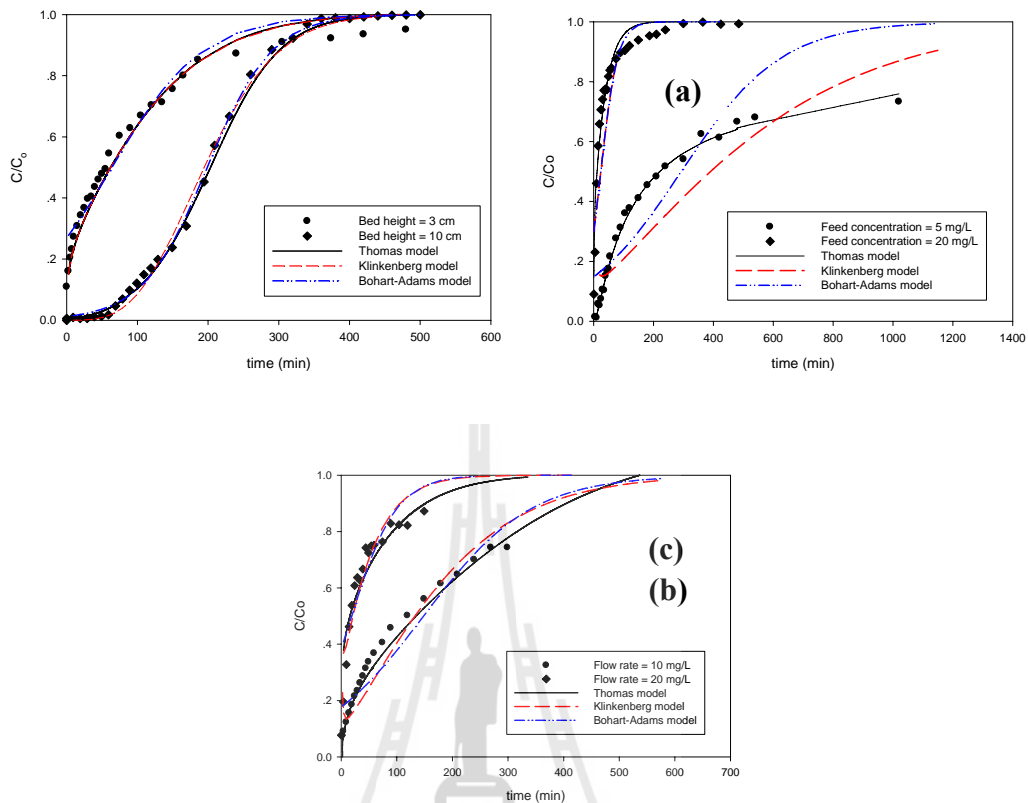
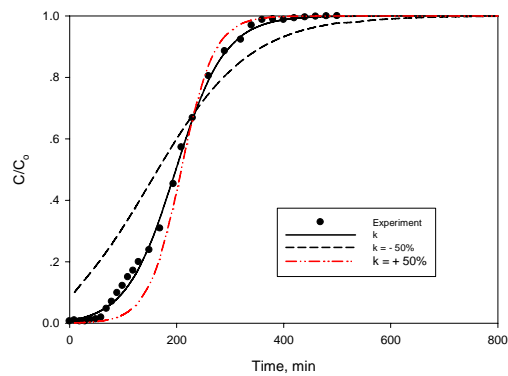


**Figure 4.8** Model prediction of breakthrough curve by Scheme II for methylene blue adsorption by porous glass PG1 at 30°C: Effects of (a) bed height, (b) feed concentration, and (c) feed flow rate.

**Table 4.8** Sensitivity of parameters of Thomas model on the fitting of breakthrough curve for the adsorption of methylene blue by porous glass PG1 at 30°C (bed length = 10cm, feed concentration = 10mg/L, feed flow rate = 10mL/min).

Sensitivity of parameters	SSE	R <sup>2</sup>
---------------------------	-----	----------------

$k_t$		
○ + 50 %	0.5369	0.8201
○ 0%(base)	0.0070	0.9987
○ - 50 %	0.1010	0.9831
$q_0$		
○ + 50 %	3.0173	0.6493
○ 0%(base)	0.0070	0.9987
○ - 50 %	1.8026	0.8003
$\beta$		
○ + 50 %	0.0081	0.9986
○ 0%(base)	0.0070	0.9987
○ - 50 %	0.0076	0.9985



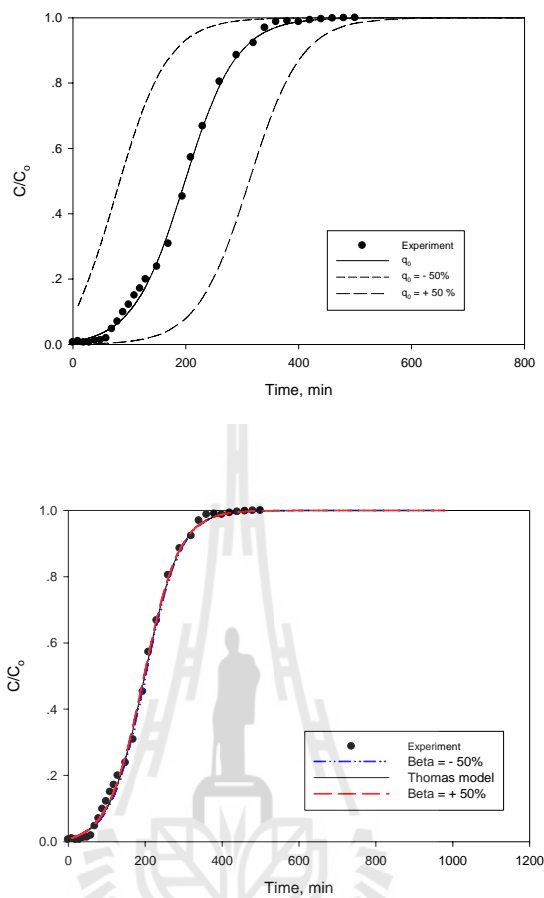


**Figure 4.9** Sensitivity of parameters of Thomas model for breakthrough prediction of methylene blue adsorption by porous glass PG1 at 30°C.

#### 4.7 Conclusion

The removal of methylene blue (MB) from aqueous solution was performed at 30°C in a column (1.6 cm I.D.) packed with porous glass particles prepared from coal fly ash by the phase-separation method. The concentration of MB at the column exit was monitored as a function of time from which the breakthrough curve could be constructed. The effects of system variables on the breakthrough characteristics were

investigated, including the bed height (3-10 cm), the feed flow rate (10-20cm<sup>3</sup>/min), the feed concentration of MB (5-20 mg/L), and the particle size (250-850µm) and mean pore size (5.30-6.32 nm).

The equilibrium isotherms of the porous glass samples, covering the bulk-phase concentration up to 20 mg/L of MB, were reasonably well described by both the Langmuir and Freundlich equations. It appeared that porous glass with larger mean pore size had higher maximum adsorbed capacity as compared to the smaller pore size sample. The breakthrough time and the breakthrough capacity were found to increase with increasing in the adsorbent bed height and a decrease in feed rate and feed concentration. Further, there was no clear effect of pore size and particle size on these breakthrough parameters. Three different types of breakthrough models, based on differing isotherm curvature, were tested against the experimental breakthrough data. It was discovered that the Thomas model for curved isotherm showed the best fitting capability, as compared to the Klinkenberg model for linear isotherm and the Bohart-Adams model for square isotherm, provided that the rate constant and isotherm parameters in the models are simultaneously optimized.

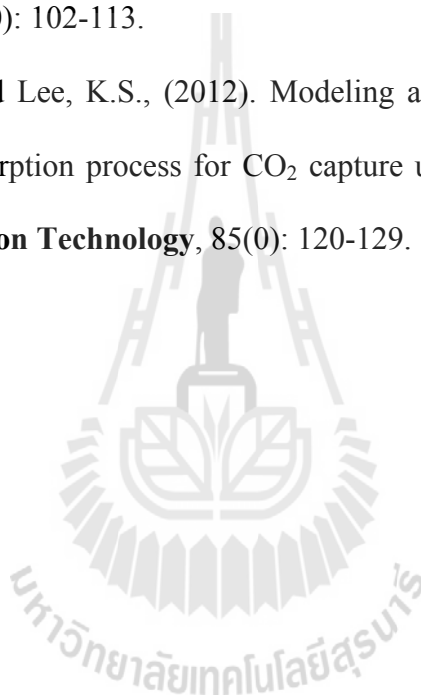
#### 4.8References

Askalany, A.A., Salem, M., Ismail, I.M., Ali, A.H.H. and Morsy, M.G., (2012). A review on adsorption cooling systems with adsorbent carbon. **Renewable and Sustainable Energy Reviews**, 16(1): 493-500.

- Auta, M. and Hameed, B.H., (2014). Chitosan–clay composite as highly effective and low-cost adsorbent for batch and fixed-bed adsorption of methylene blue. **Chemical Engineering Journal**, 237(0): 352-361.
- Cruz-Olivares, J., Pérez-Alonso, C., Barrera-Díaz, C., Ureña-Nuñez, F., Chaparro-Mercado, M.C. and Bilyeu, B., (2013). Modeling of lead (II) biosorption by residue of allspice in a fixed-bed column. **Chemical Engineering Journal**, 228(0): 21-27.
- Gude, K., Gun'ko, V.M. and Blitz, J.P., (2008). Adsorption and photocatalytic decomposition of methylene blue on surface modified silica and silica-titania. **Colloids and Surfaces A: Physicochemical and Engineering Aspects**, 325(1–2): 17-20.
- Malamis, S. and Katsou, E., (2013). A review on zinc and nickel adsorption on natural and modified zeolite, bentonite and vermiculite: Examination of process parameters, kinetics and isotherms. **Journal of Hazardous Materials**, 252–253(0): 428-461.
- Pang, S.C., Masjuki, H.H., Kalam, M.A. and Hazrat, M.A., (2013). Liquid absorption and solid adsorption system for household, industrial and automobile applications: A review. **Renewable and Sustainable Energy Reviews**, 28(0): 836-847.
- Pratoto, A., Daguinet, M. and Zeghmati, B., (1998). A simplified technique for sizing solar-assisted fixed-bed batch dryers: application to granulated natural rubber. **Energy Conversion and Management**, 39(9): 963-971.



- Rozada, F., Otero, M., García, A.I. and Morán, A., (2007). Application in fixed-bed systems of adsorbents obtained from sewage sludge and discarded tyres. **Dyes and Pigments**, 72(1): 47-56.
- Sotelo, J.L., Ovejero, G., Rodríguez, A., Álvarez, S. and García, J., (2013). Analysis and modeling of fixed bed column operations on flumequine removal onto activated carbon: pH influence and desorption studies. **Chemical Engineering Journal**, 228(0): 102-113.
- Won, W., Lee, S. and Lee, K.S., (2012). Modeling and parameter estimation for a fixed-bed adsorption process for CO<sub>2</sub> capture using zeolite 13X. **Separation and Purification Technology**, 85(0): 120-129.



## CHAPTER V

### CONCLUSION AND RECOMENADATIONS

#### 5.1 Conclusions

This research thesis aims to utilize coal fly ash for the preparation of porous glass adsorbent which has many advantageous properties of high thermal and chemical stability, relatively narrow pore size distribution, well controlled pore size distribution, ease of shaping ability, and capability of surface modification for selective adsorption of specific species. The preparation of porous glass by the phase-separation technique in this work basically consists of melting the ash of proper base glass compositions, followed by heating the resulting glass product in the range of 650-780°C and for the heating time up to 150 h to effect the phase separation of borosilicate glass, then removing the borate rich phase with dilute mineral acid to create the porous framework of silica rich phase, and finally leaching out the remaining silica colloids by the alkaline solution. The research tasks consist of the preparation and characterization of porous glass prepared from selected coal fly ash using the phase-separation procedure and the adsorption study of the porous glass both in the batch mode for equilibrium and kinetic aspects in liquid and gas systems, as well as the adsorption study of methylene blue dye in a continuous fixed-bed system. The following conclusions can be drawn from the present study.

### **Porous glass preparation**

1. In preparing porous glass adsorbent from fly ash, it is necessary to adjust its composition by adding appropriate amounts of various oxides to create borosilicate glass upon melting in the region where the separation of silica and boron glass phase can be affected after the subsequent thermal treatment of the glass product.

2. The appearance colors of the derived porous glass adsorbents depend on the heat treatment conditions, for example, it could vary from transparent at low treatment temperature to white opaque or gray opaque color at treatment temperature higher than 700°C.

Typical chemical compositions of the final porous glass product are 64% SiO<sub>2</sub>, 10% Al<sub>2</sub>O<sub>3</sub>, 7% B<sub>2</sub>O<sub>3</sub>, 6% Na<sub>2</sub>O, 4% CaO, and 2% K<sub>2</sub>O, giving the porous glass from fly ash similar in composition to the commercial Shirasu porous glass.

Porous properties determined by mercury porosimetry indicate that the prepared porous glass contains mainly mesopores and macropores with median pore diameter varying from 10 to 2000 nm, with higher temperature and longer time of the heat treatment condition giving porous glass with larger pore size. Specific surface area is relatively low; the maximum surface area around 70 m<sup>2</sup>/g is achieved for the lowest treatment temperature of 650°C that gives mainly small pores of less than 10 nm in diameter.

3. The creation of internal pores of porous glass occurs basically by the mechanism of nucleation and growth. However, there is evidence to support that the

development of interconnected pore structure at high temperatures is by way of spinodal decomposition mechanism.

4. An empirical equation was proposed for predicting the mean pore diameter of porous glass as a function of heat treatment time and temperature, covering the temperature range from 700 to 780°C and treatment time from 10 to 150 hours

### **Batch adsorption study of porous glass**

1. The adsorption of copper ( $\text{Cu}^{2+}$ ) and silver ( $\text{Ag}^+$ ) ions are extremely low when adsorbed with a virgin porous glass. However,  $\text{Cu}^{2+}$  and  $\text{Ag}^+$  could be specifically adsorbed by porous glass grafted with the amino ( $-\text{NH}_2$ ) and thiol ( $-\text{SH}$ ) groups, respectively.

2. The solution pH has a direct effect on the adsorption of copper and silver ions by the grafted porous glass in that the amounts of metal ions adsorbed increases with increasing pH above  $\text{pH} = 2$  which is the pH at point of zero charge of the porous glass. This result could be explained by the competition towards the adsorption sites between the proton ( $\text{H}^+$ ) and the metal ion in the solution.

3. The time to reach equilibrium for the selective adsorption of  $\text{Cu}^{2+}$  and  $\text{Ag}^+$  by the grafted porous glass samples at 25°C is relatively fast, in the order of about 10 min. The kinetic data of metal ion adsorption can be best described by the pseudo second-order kinetic model, followed by the pseudo first-order model and the intraparticle- or pore-diffusion model, respectively. The effective pore diffusivities of the pore-diffusion model have the values of  $5.74 \times 10^{-9}$  and  $2.61 \times 10^{-9}$   $\text{m}^2/\text{s}$  for the

diffusion of copper ion and silver ion in porous glass grafted with amino group and thiol group, respectively.

4. The single adsorption isotherms of  $\text{Cu}^{2+}$  and  $\text{Ag}^+$  at  $25^\circ\text{C}$  by porous glass grafted with amino group and thiol group, respectively, are best predicted by the three-parameter Sips model, followed by Langmuir and Freundlich isotherm models, respectively. The “Hard and Soft (Lewis) Acids and Bases or HSAB theory” is used to explain the selective adsorption of copper and silver ions on the grafted porous glass samples.

5. The adsorption of gold ion by the virgin unmodified porous glass is almost negligible while porous glass grafted with amino and thiol groups can increase the amount of gold adsorbed considerably. Again, the Sips model can describe the equilibrium isotherm of gold adsorption better than the Langmuir and Freundlich equations. The time required for the adsorption of gold to reach equilibrium for both adsorbents is around 200 min and 600 min for porous glass grafted with amino and thiol groups, respectively. This is reflected by the larger effective diffusivity of  $3.0 \times 10^{-10} \text{ m}^2/\text{s}$  for amino-grafted porous glass, as compared to a lower value of  $7.86 \times 10^{-11} \text{ m}^2/\text{s}$  for the thiol-grafted porous glass. Concerning the adsorption mechanism of gold ion on porous glass surface, it is proposed that ion-exchange mechanism is responsible for the adsorption of gold by amino-grafted porous glass where the protonated amino group ( $\text{R-NH}_3^+$ ) interacts with  $\text{AuCl}_4^-$  anion existing at solution pH lower than 4. The adsorption of gold by thiol-grafted porous glass involves the forming of gold complex  $\text{AuCl}_3$  with the sulfur atom of the thiol group on the glass surface.

6. There is no difference for the selective adsorption of copper and silver ions in terms of the amounts adsorbed between the pure state as a single ion and in the binary mixture of both ions. This indicates a strong affinity of a selective ion towards a specific surface functionality on the adsorbent surface irrespective of the presence of the other available ion. Attempt was made to predict the isotherm of copper and silver ions in the mixture by the grafted porous glass using empirical correlations (the extended Langmuir and the extended Langmuir-Freundlich isotherms) and thermodynamic approach model (the Ideal Adsorption Solution Theory, IAST). By solving a set of equations of the IAST, the isotherms calculated from this theory match extremely well with the measured data, while the empirical approach requires the searching of all the best fitted parameters in the equation, thus lacking the theoretical support.

7. The prepared porous glass from coal fly ash was used to study the adsorption in gas phase as a function of temperature using three adsorbates with increasing degree of surface polarity, namely carbon dioxide, ethanol vapor and water vapor, respectively. The adsorption of all adsorbates involves physical adsorption forces with the liberation of heat since the amounts adsorbed decreases with increasing in the temperature over the range of 10-30°C for CO<sub>2</sub>, 10-40°C for ethanol and 20-35°C for water.

8. The isotherm curve of CO<sub>2</sub> up to the pressure of 1,000 mbar is concave towards the pressure axis resembling the initial portion of Type II isotherm which can be best fitted with Langmuir and Freundlich isotherm equations. The isosteric heat of carbon dioxide adsorption on porous glass drops from 21.7 to 17.4

kJ/mol over a decrease of adsorption loading from 0.2 to 1.6 mmol/g and the limiting heat of adsorption at zero loading is estimated to be 22.7 kJ/mol and the binding of CO<sub>2</sub> on solid surface is attributed to dispersive interaction forces.

9. Adsorption of ethanol for pressure up to 100 mbar and water up to 60 mbar yields a similar Type IV isotherm showing a characteristic of multilayer adsorption with hysteresis loop. This is indicative of adsorption in mesoporous solid that is associated with the phenomenon of capillary condensation. The isotherms of both adsorbates are best fitted with the n-layer BET equation that gives, for comparison, the monolayer capacity parameter,  $q_m$ , at 20°C to be 2.8 mmol/g for water adsorption as compared to the value of only 0.44 mmol/g for ethanol. The basic underlying mechanism for the adsorption of these polar adsorbates involves hydrogen bonds between adsorbate molecules and the silanol groups (-OH) on the porous glass surface.

10. The kinetics of water adsorption on porous glass was studied by following the amount adsorbed as a function of time over the temperature range from 20 to 35°C for various adsorption loadings. Overall, the pseudo second-order kinetic model can best predict the adsorption kinetics, followed by the pseudo first-order kinetic model and the pore-diffusion model, respectively. It was found that the kinetic parameters of the first two kinetic models and the effective diffusivity of the pore-diffusion model tend to decrease almost linearly and becomes constant at a certain threshold loading. For a given loading, the kinetic parameters of the three models appear to decrease with the increase in the adsorption temperature.

### **Fixed-bed adsorption of methylene blue**

1. Adsorption of methylene blue from solution by the prepared porous glass at 30°C was also studied in a continuous fixed-bed operation to arrive at the breakthrough data as a function of adsorbent bed height, feed flow rate, feed concentration, and particle size and mean pore size of porous glass.

2. From the batch adsorption study, it was found that the adsorption isotherm of methylene blue can be reasonably well described by the Langmuir and the Freundlich equations. Porous glass with large mean pore size gives a larger adsorbed capacity, independent of the size of adsorbent particles.

3. Breakthrough parameters including the breakthrough time and equilibrium time as well as the corresponding adsorbed capacities appear to increase with the increase in the bed height and the decrease in the feed rate and feed concentration, while the effects of particle size and mean pore size are not clearly observed.

4. Three breakthrough models, based on the difference in the assumption of isotherm curvature, were tested against the measured breakthrough data. In terms of fitting accuracy, Thomas model for a favorable isotherm is superior to Klinkenberg model for linear isotherm and Bohart-Adams model for square isotherm.



## 5.2 Recommendations for further works

The following area of works is noteworthy concerning the preparation, adsorption and utilization of porous glass prepared from coal fly ash.

1. Study should be made on the effect of additional preparation conditions on the close control of pore size distribution of porous glass such as the type of fly ash from different coal rank, the initial composition of raw mix of base glass, and concentration and kind of acid and alkaline solution used for the leaching step following the heat treatment of the phase-separated glass.

2. Kinetic study on the forming of phase-separated glass during the thermal treatment step of the molten glass product to gain a better understanding of the phase separation mechanism.

3. The potential use of porous glass adsorbent in the area of liquid-phase adsorption should be extended to different types of metal ions and dye molecules.

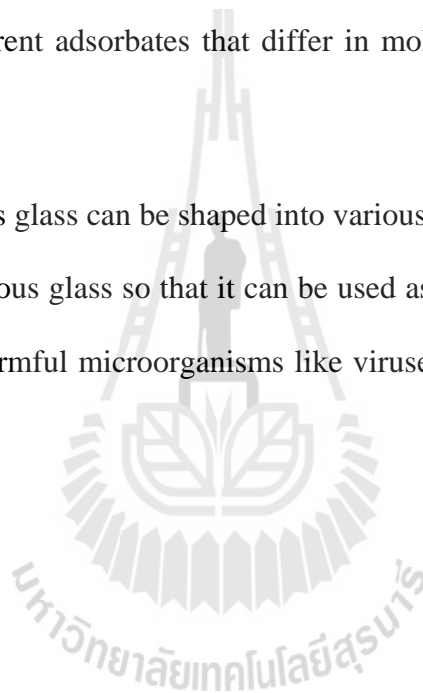
4. Study of binary mixture adsorption of metal ions should be performed with different types of binary components. Other theories of multicomponent adsorption, e.g., the vacancy-solution model should be tested.

5. To gain a deeper insight into the mechanism of gas-phase adsorption by porous glass, particularly the role of surface silanol groups, the application of molecular simulation, for example, the Grand Canonical Monte Carlo (GCMC) simulation should be thoroughly explored.

6. To improve the prediction accuracy of breakthrough curves for the adsorption of methylene blue from aqueous solution by porous glass from coal fly ash, it is worthwhile to employ a more sophisticated breakthrough models that incorporate the effects of axial dispersion, and external and internal mass transfer resistances of the adsorption process.

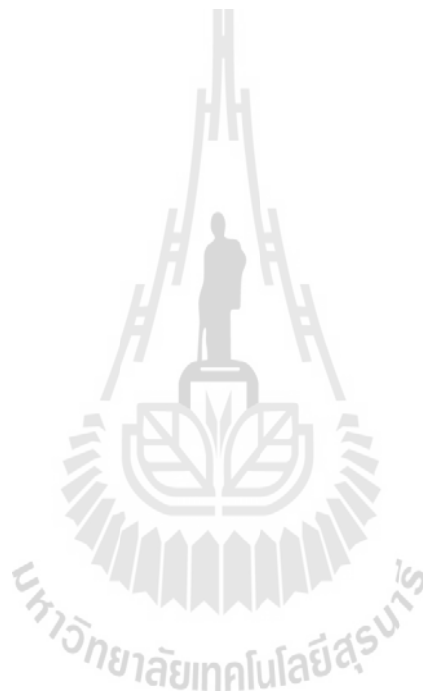
7. The fixed-bed adsorption for liquid systems by porous glass should be carried out with different adsorbates that differ in molecular properties such as size and polarity.

8. Since porous glass can be shaped into various forms, it should be interesting to produce a plate porous glass so that it can be used as a filter medium for removing fine particulates or harmful microorganisms like viruses and bacteria from the liquid phase.



## Publication

Nimjaroen, C.; Morimoto, S.; Tangsathikulchai, C. (2009). Preparation and properties of porous glass using fly ash as a raw material. *Journal of Non-Crystalline Solids*, Vol. 355 (34–36), pp. 1737-1741, (2009 Impact factor = 1.597)



## Monte Carlo Simulation and Experimental Study for Adsorption of CO<sub>2</sub> on Porous Glass

*Chaturaporn Nimjaroen, Atichat Wongkoblaph and Chaiyot Tangsathitkulchai*

School of Chemical Engineering, Suranaree University of Technology, Nakhon Ratchasima, 30000 Thailand

### Abstract

In this study, experimental data and the molecular simulation for the adsorption of carbon dioxide on porous glass are presented. Porous glass represents an important sub-group of adsorbents because of its high thermal stability and chemical resistance. Tests on carbon dioxide adsorption are performed by using a Gravimetric Analyser, while a Grand Canonical Monte Carlo (GCMC) simulation method is used to investigate the adsorption behaviour of carbon dioxide on porous glass. In this study, the molecular model of glass is assumed to be composed of SiO<sub>4</sub> crystal and the atoms in it are laid in different planes while the porous glass prepared from coal fly ash in our laboratory is used as the adsorbent. The adsorption isotherm shows a sharp change of isotherm at low pressures and then gradual increase with increasing pressure. The adsorption capacity depends on temperature, it decreases by increasing temperature. Finally, we investigate the heat of adsorption of carbon dioxide in porous glass. We compare our simulation results and the experimental data and have found that the heat of adsorption agreed quite well; it decreases with surface loading although the magnitude of the value is different. The isosteric heat of adsorption is contributed by fluid-fluid and fluid-solid interactions.

### 1. Introduction

The development of new advanced adsorbents for gas separation in industrial applications by adsorption process has been of significant interest to scientists and engineers. However, these materials need to be characterized for a wide variety of gases. From the environmental point of view, the reduction of carbon dioxide is

becoming more important and adsorption process is one of technologies used to control CO<sub>2</sub> emission to atmospheric environment. In addition, the removal of carbon dioxide from natural gas and the recovery of methane from landfill gas are examples of interesting separations. Among the potential routes explored for gas separations, adsorption processes involving porous glass have shown an increasing importance because these materials have a high thermal, mechanical, and chemical stability.

In this work, the porous glass was prepared by a conventional phase separation method using coal fly ash as a raw material and used to adsorb carbon dioxide at 10, 20 and 30°C. The single component adsorption isotherm was obtained by vapour-phase adsorption using an Intelligent Gravimetric Analyser (IGA) and the isosteric heat of adsorption was calculated by using van't Hoff equation. The simulation adsorption isotherm and isosteric heat of CO<sub>2</sub> in porous glass at 10°C were obtained by using a Grand Canonical Monte Carlo (GCMC) simulation. For comparison, only the adsorption isotherm and isosteric heat of CO<sub>2</sub> adsorption at 10°C will be used to gain a better understanding of adsorption mechanism of CO<sub>2</sub> in porous glass that may be applied solve the the environmental problem.

## **2. Methodology**

### 2.1 Preparation of porous glass

In this study, porous glass was prepared from coal fly ash supplied by “Rayong coal burning thermal power plant” in Thailand. The heat treatment conditions of prepared porous glass were operated at temperature of 650 °C and treatment time of 20 hours, the detail procedure was found in the literature (Nimjaroen et al., 2009). Porous glass sample prepared under heat treatment condition of 650 °C and 20 hours was selected for studying CO<sub>2</sub> adsorption in this work.

### 2.2 Experimental measurement

The measurement of isotherms of CO<sub>2</sub> at 10, 20 and 30°C was performed by using an Intelligent Gravimetric Analyzer (IGA) supplied by Hiden Analytical Ltd., UK. Prior to adsorption experiment, the porous glass sample about 0.2 grams was outgassed at 300 °C for 12 hours. The numbers of pressure points were specified and

the measurement of the adsorbed amount at equilibrium for a given temperature was performed for each scan of adsorption and desorption steps.

### 2.3 Simulation Method

#### 2.3.1 Fluid-fluid potential models

In this study, carbon dioxide is modelled as a 3-center-Lennard-Jones (LJ) molecule having LJ interaction sites on the atoms and point charges to account for the quadrupole moment proposed by (Harris and Yung, 1995). The molecular parameters for carbon dioxide used in this study are listed in Table 1.

**Table 1** Molecular parameters for carbon dioxide.

Parameter	Value	Parameter	Value
$\sigma_{ff}^{C-C}$	2.757 Å	$\varepsilon_{ff}^{C-C} / k$	28.129 K
$\sigma_{ff}^{O-O}$	3.033 Å	$\varepsilon_{ff}^{O-O} / k$	80.507 K
qc	0.6512 e	qo	-0.3256e
$\lambda_{C-O}$	1.149 Å		

where  $\varepsilon_{ff}$  and  $\sigma_{ff}$  are the energy well depth and the collision diameter of fluid, respectively, subscript C-C and O-O are carbon atom and oxygen atom of carbon dioxide, respectively, k is the Boltzmann's constant, q is the point charge on each atom and  $\lambda$  is the distance between carbon and oxygen atoms. A cut-off radius in the calculation of interaction energy of five times the collision diameter of carbon atom ( $5\sigma^{C-C}$ ) is used in this study. The interaction energy between fluids ( $\varphi_{ff}$ ) is calculated using the Lennard-Jones 12-6 equation (Do et al., 2003).

$$\varphi_{ff}(r) = 4\varepsilon_{ff} \left[ \left( \frac{\sigma_{ff}}{r} \right)^{12} - \left( \frac{\sigma_{ff}}{r} \right)^6 \right] \quad (1)$$

where r is the separation distance. Beside the interaction between two LJ sites, the interaction between two charges for carbon dioxide molecule should be taken into account. The interaction between two charges, each of which is on different molecule, takes the form of a Coulomb law of electrostatic interaction.

$$\varphi_{q^a q^b}(r^{ab}) = \frac{1}{4\pi\epsilon_0} \frac{q^a q^b}{r^{ab}} \quad (2)$$

where  $\epsilon_0$  is the permittivity of free space,  $r^{ab}$  is the distance between two charges  $a$  and  $b$ .

### 2.3.2 Solid model

The solid model used in this study is the SiO<sub>4</sub> crystal which formed tetrahedral structure, a silicon atom is at the centre of a tetrahedron and four oxygen atoms are positioned at the vertices of the tetrahedron. These four sites represent the dispersive sites and have negative charge of  $-1.025 \times 10^{-20}$  C while the positive charge of  $2.05 \times 10^{-20}$  C is that of silicon atom. The molecular parameters of SiO<sub>4</sub> used in this study are  $\epsilon_{zz}/k$  of 93.53K,  $\sigma_{zz}$  of 3.0 Å, the distance between oxygen atoms of 3.06 Å and the angle of O-Si-O about 147° (Calero et al., 2004). Two layers of crystal are stacked on each other with the distance of 40 Å.

### 2.3.3 Monte Carlo simulation

A Monte Carlo (MC) simulation involves the use of random numbers to sample phase space. Basically a large number of possible configurations of particles in proportion to the probability of their occurrence are generated. This series of configuration is called the Markov chain. This chain of configurations is then used to compute the various properties using ensemble averages. In this paper we adopt the Metropolis algorithm in the simulations (Frenkel and Smit, 2001). In the MC simulation, all length-scale and energy-scale variables are made non-dimensional by scaling against the collision diameter and the energy well-depth of CO<sub>2</sub>, respectively. There are a number of ensembles that are commonly used in MC simulation for example Canonical ensemble (NVT), Gibbs ensemble (GEMC) and Grand Canonical ensemble (GCMC).

In this study, the GCMC is used to obtain the adsorption isotherms of CO<sub>2</sub> in a finite length porous glass with a linear dimension of 40 Å in the x and y directions. We specify the volume of the box (i.e. pore volume), the chemical potential and the temperature of the system to obtain the adsorption equilibrium. One GCMC cycle consists of one thousand displacement moves and attempts of either insertion or deletion with equal probability. For an adsorption branch of the isotherm 10,000

$$\varphi_{q^a q^b}(r^{ab}) = \frac{1}{4\pi\epsilon_0} \frac{q^a q^b}{r^{ab}} \quad (2)$$

where  $\epsilon_0$  is the permittivity of free space,  $r^{ab}$  is the distance between two charges  $a$  and  $b$ .

### 2.3.2 Solid model

The solid model used in this study is the  $\text{SiO}_4$  crystal which formed tetrahedral structure, a silicon atom is at the centre of a tetrahedron and four oxygen atoms are positioned at the vertices of the tetrahedron. These four sites represent the dispersive sites and have negative charge of  $-1.025 \times 10^{-20}$  C while the positive charge of  $2.05 \times 10^{-20}$  C is that of silicon atom. The molecular parameters of  $\text{SiO}_4$  used in this study are  $\epsilon_{zz}/k$  of 93.53K,  $\sigma_{zz}$  of 3.0 Å, the distance between oxygen atoms of 3.06 Å and the angle of O-Si-O about  $147^\circ$  (Calero et al., 2004). Two layers of crystal are stacked on each other with the distance of 40 Å.

### 2.3.3 Monte Carlo simulation

A Monte Carlo (MC) simulation involves the use of random numbers to sample phase space. Basically a large number of possible configurations of particles in proportion to the probability of their occurrence are generated. This series of configuration is called the Markov chain. This chain of configurations is then used to compute the various properties using ensemble averages. In this paper we adopt the Metropolis algorithm in the simulations (Frenkel and Smit, 2001). In the MC simulation, all length-scale and energy-scale variables are made non-dimensional by scaling against the collision diameter and the energy well-depth of  $\text{CO}_2$ , respectively. There are a number of ensembles that are commonly used in MC simulation for example Canonical ensemble (NVT), Gibbs ensemble (GEMC) and Grand Canonical ensemble (GCMC).

In this study, the GCMC is used to obtain the adsorption isotherms of  $\text{CO}_2$  in a finite length porous glass with a linear dimension of 40 Å in the x and y directions. We specify the volume of the box (i.e. pore volume), the chemical potential and the temperature of the system to obtain the adsorption equilibrium. One GCMC cycle consists of one thousand displacement moves and attempts of either insertion or deletion with equal probability. For an adsorption branch of the isotherm 10,000



cycles are typically needed for the system to reach equilibrium, and additional 10,000 – 20,000 cycles are used to obtain ensemble averages. For each point on the adsorption branch, we use an empty box as the initial configuration, and the simulation is carried out until the number of particles in the box does not change (in statistical sense). A cut-off radius of  $5\sigma^{C-C}$ , and initial displacement step length of  $0.5\sigma^{C-C}$  are used in the simulation. The displacement length is decreased 5% when the acceptance ratio is less than 0.5 and increased 5% when this ratio is greater than 0.5. The pressure of the bulk gas corresponding to a given chemical potential are calculated from the equation of state proposed by Johnson *et al.* (Johnson *et al.*, 1993).

### 3. Results and Discussion

#### 3.1 Porous properties of prepared porous glass

The adsorbed amount versus relative pressure ( $P/P_0$ ) for  $N_2$  adsorption in porous glass derived from coal fly ash at 77K are presented in Figure 1. The adsorption isotherms show type IV isotherm (type II with hysteresis loop) indicating that the adsorbent is dominantly mesoporous. The porous properties of porous glass used in this study are presented in Table 2.

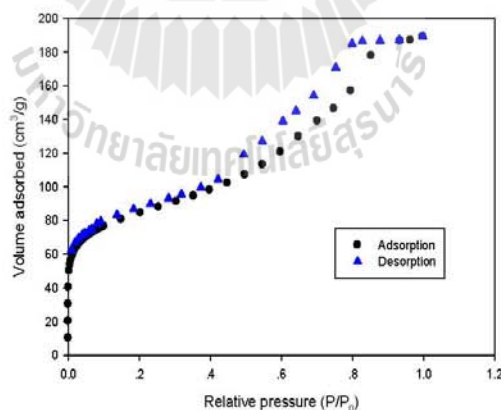


**Figure 1**  $N_2$  adsorption isotherms at 77K on prepared porous glass.

It is seen that the porous glass mostly composed of mesopores (87.6%) and its average pore size is 38 Å. In the chemical analysis, chemical composition of prepared

porous glass in our laboratory consists of silicon oxide of 70% and aluminum oxide of 10%. Therefore, we choose the structure of silicon oxide as the solid model in our simulation.

**Table 2** Porous properties of prepared porous glass.

Adsorbents	BET area $S_{\text{BET}}$ ( $\text{m}^2/\text{g}$ )	Total pore volume, $V_{\text{tot}}$ ( $\text{cm}^3/\text{g}$ )	Micropore volume, $V_{\text{mic}}$		Mesopore volume, $V_{\text{meso}}$	
			$\text{cm}^3/\text{g}$	%	$\text{cm}^3/\text{g}$	%
Prepared porous glass	286	0.293	0.039	13.30	0.254	86.70

### 3.2 Carbon dioxide adsorption

Adsorption isotherms of carbon dioxide on porous glass at three different temperatures of 10, 20 and 30°C are shown in Figure 2(a) and 2(b) for plotting against relative pressure ( $P/P_0$ ) and absolute pressures, respectively. Over the pressure up to 1 atm, the amount of  $\text{CO}_2$  adsorbed at each temperature increases with increasing pressure. The experimental data show a sharp change at low relative pressures and then increase gradually at higher relative pressures. It is seen that the amount adsorbed decreases with an increase of temperature which signifies that  $\text{CO}_2$  adsorption on the porous glass surface is an exothermic process.

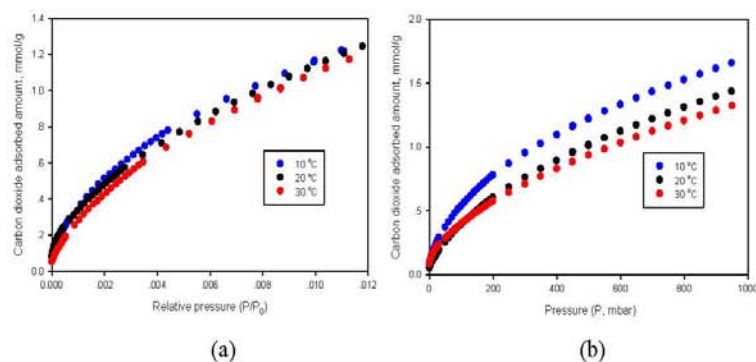


**Figure 2** Adsorption isotherms of carbon dioxide on porous glass derived from coal fly ash at various temperatures.

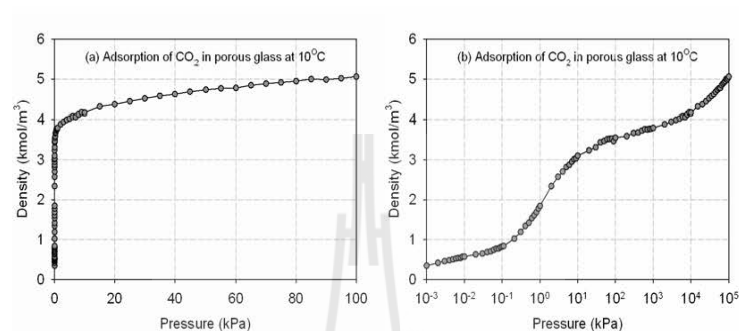


**Figure 3** Simulation adsorption isotherm of carbon dioxide on SiO<sub>4</sub> crystal at 10°C.

The simulated isotherm versus pressure for CO<sub>2</sub> on SiO<sub>4</sub> crystal at 10°C obtained by using the GCMC method is shown in Figure 3(a) and 3(b), presented in linear and semi-log scales, respectively. As one can see, the change in density is continuous filling at low pressures and then dramatically increases to form the layer and the inner core is then filled. At pressure approaching saturated pressure, it may rise rapidly due to the capillary condensation which is a typical isotherm observed for the mesoporous material.

### 3.3 Isosteric heat of adsorption

The effect of CO<sub>2</sub> adsorption loading on the isosteric heat of adsorption is numerically obtained from Van't Hoff equation and its plot is shown in Figure 4. It is observed that the heat of adsorption decreases continuously from 21.7 to 17.4 kJ/mol with increasing carbon dioxide loading from 0.2 to 1.6 mmol/g and there is a tendency to approach a constant value at higher loading. The isosteric heat of adsorption at zero coverage is obtained by extrapolation to be 22.7 kJ/mol. The heat of adsorption is high initially owing to the strong interaction between the adsorbate molecules and the surface adsorption sites. At higher surface coverage, however, weak dispersive forces among adsorbate molecules start to play an important role,

thus releasing less amount of heat of adsorption. The slow decrease of heat of adsorption with increased surface loading could result from the large value of permanent quadrupole moment of  $\text{CO}_2$  ( $-13.71 \times 10^{-40}$  Coulomb-m<sup>2</sup>) that could promote additional interaction with the polar surface of porous glass by electrostatic contribution. It is noted that the gradual decreasing of heat of adsorption with increased loading has also been observed in activated carbon and zeolite adsorbents (Zhao et al., 2010). In comparison with other types of adsorbents, the data on limiting heat of adsorption were reported to be in the range from 15-30 kJ/mol for activated carbons, depending on the types of precursors and the porous structure and chemical modification of carbons (Himeno et al., 2005; Saha et al., 2011), and a higher value of around 40 kJ/mol for zeolite 13X and zeolite 4A (Lee et al., 2002).

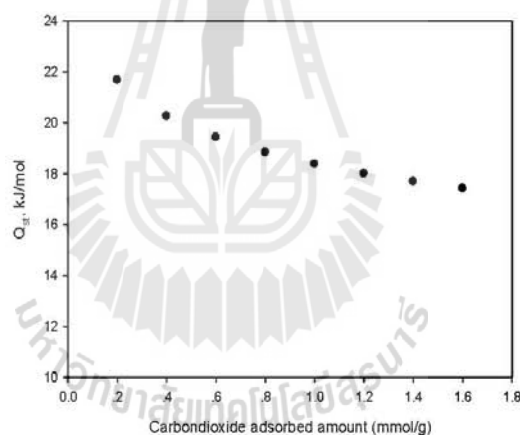


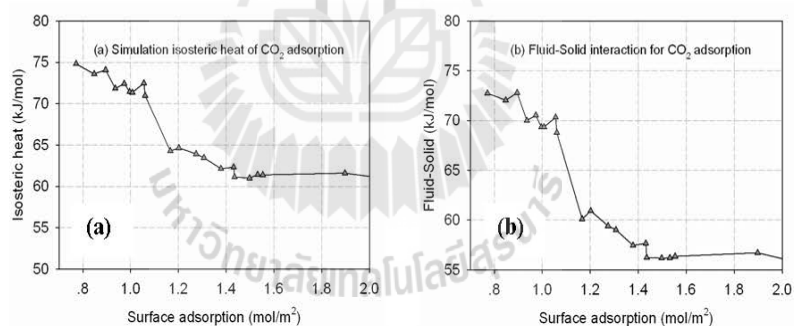
**Figure 4** Isosteric heat of carbon dioxide adsorption onto porous glass.

The simulated isosteric heat of carbon dioxide adsorption on glass is shown in Figure 5 where the isosteric heat versus loading, the solid-fluid contribution and the fluid-fluid contribution to this isosteric heat are shown in Figure 5(a), 5(b) and 5(c), respectively. A number of features that we note from the observation of these plots are mentioned as follows;

- (i) The isosteric heat of adsorption decreases with loading and it approaches a constant value which is similar to the heat of adsorption

derived from the experimental data. This is due to the strong interaction between fluid and solid as one can see from Figure 5(b) presented the heat contributed by the solid-fluid interaction.

- (ii) The heat contributed by the solid-fluid interaction is initially high and then decreases with loading. This is due to the effects of electrostatic force between silicon oxide and carbon dioxide which leads to the initial adsorption of carbon dioxide on the solid surface. This is an indication of newly added carbon dioxide particles staying at distance further away from the surface, which is a direct consequence of favoring the fluid-fluid interaction.
- (iii) The heat contribution by the fluid-fluid interaction, which is much less than the fluid-solid interaction, steadily increases with surface loading. The isosteric heat is thus the sum of the heats contributed by the fluid-fluid and solid-fluid interactions.



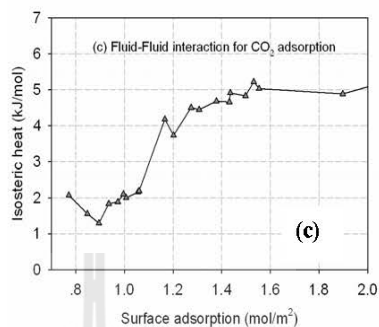


**Figure 5** Simulated isosteric heat of adsorption for carbon dioxide at 10°C on glass crystal (a). The solid-fluid contribution is shown in the middle plot (b) while the fluid-fluid contribution is in the bottom plot (c).

#### 4. Conclusion

This study is concerned with the adsorption of CO<sub>2</sub> on porous glass derived from coal fly ash, the experimental and simulation studies were performed to investigate the adsorption behaviour. It was found that the behavior of CO<sub>2</sub> adsorption on the porous glass corresponded to that of the mesopore. The isosteric heat of adsorption obtained from experiment is initially high and then decreases with loading which agrees well with the simulation results.

#### 5. Reference

- Calero, S., Dubbeldam, D., Krishna, R., Smit, B., Vlugt, T.J.H., Denayer, J.F.M., Martens, J.A. and Maesen, T.L.M., (2004). Understanding the Role of Sodium during Adsorption: A Force Field for Alkanes in Sodium-Exchanged Faujasites. *Journal of the American Chemical Society*, 126(36): 11377-11386.

- Do, D.D., Do and Do, H.D., (2003). Pore Characterization of Carbonaceous Materials by DFT and GCMC Simulations: A Review. **Adsorption Science & Technology**, 21(5): 389-423.
- Frenkel, D. and Smit, B., (2001). Understanding Molecular Simulation: From Algorithms to Applications. **Elsevier Science**.
- Harris, J.G. and Yung, K.H., (1995). Carbon Dioxide's Liquid-Vapor Coexistence Curve And Critical Properties as Predicted by a Simple Molecular Model. The **Journal of Physical Chemistry**, 99(31): 12021-12024.
- Himeno, S., Komatsu, T. and Fujita, S., (2005). High-Pressure Adsorption Equilibria of Methane and Carbon Dioxide on Several Activated Carbons. **Journal of Chemical & Engineering Data**, 50(2): 369-376.
- Johnson, J.K., Zollweg, J.A. and Gubbins, K.E., (1993). The Lennard-Jones equation of state revisited. **Molecular Physics**, 78(3): 591-618.
- Lee, J.-S., Kim, J.-H., Kim, J.-T., Suh, J.-K., Lee, J.-M. and Lee, C.-H., (2002). Adsorption Equilibria of CO<sub>2</sub> on Zeolite 13X and Zeolite X/Activated Carbon Composite. **Journal of Chemical & Engineering Data**, 47(5): 1237-1242.
- Nimjaroen, C., Morimoto, S. and Tangsathitkulchai, C., (2009). Preparation and properties of porous glass using fly ash as a raw material. **Journal of Non-Crystalline Solids**, 355(34-36): 1737-1741.
- Saha, B.B., Jribi, S., Koyama, S. and El-Sharkawy, I.I., (2011). Carbon Dioxide Adsorption Isotherms on Activated Carbons. **Journal of Chemical & Engineering Data**, 56(5): 1974-1981.

Zhao, G., Aziz, B. and Hedin, N., (2010). Carbon dioxide adsorption on mesoporous silica surfaces containing amine-like motifs. **Applied Energy**, 87(9): 2907-2913.







Contents lists available at ScienceDirect

## Journal of Non-Crystalline Solids

journal homepage: [www.elsevier.com/locate/jnoncrysol](http://www.elsevier.com/locate/jnoncrysol)

## Preparation and properties of porous glass using fly ash as a raw material

Chaturaporn Nimjaroen<sup>a</sup>, Shigeki Morimoto<sup>b,\*</sup>, Chaiyot Tangsathitkulchai<sup>a</sup><sup>a</sup>School of Chemical Engineering, Institute of Engineering, Suranaree University of Technology, 111 University Avenue, Muang District, Nakhon Ratchasima 30000, Thailand<sup>b</sup>School of Ceramic Engineering, Institute of Engineering, Suranaree University of Technology, 111 University Avenue, Muang District, Nakhon Ratchasima 30000, Thailand

## ARTICLE INFO

## Article history:

Received 28 May 2008

Received in revised form 4 June 2009

Available online 6 July 2009

## PACS:

61.43.G

64.75

81.05.R

## Keywords:

Composition

Microstructure

Porosity

Oxide glasses

Borosilicates

## ABSTRACT

The porous glasses were prepared by a conventional phase separation method using coal fly ash as a raw material, and the properties of these porous glasses were investigated. The composition of coal fly ash is basically composed of  $\text{SiO}_2\text{-Al}_2\text{O}_3\text{-Fe}_2\text{O}_3\text{-CaO}$  system and the  $\text{SiO}_2\text{-B}_2\text{O}_3\text{-Al}_2\text{O}_3\text{-CaO-Na}_2\text{O}$  system of glass was chosen as base glass composition. The pore diameter increases proportional to cube root of heating time ( $t^{1/3}$ ), however, the early stage of phase separation is not clear. It is estimated that the rate determining step may be the diffusion process of structural units involving oxygen ions and the phase separation may take place by the nucleation and growth mechanism, and the relatively larger pores of above  $1\ \mu\text{m}$  can be obtained easily. The chemical composition of porous glasses is  $\text{SiO}_2\text{-B}_2\text{O}_3\text{-Al}_2\text{O}_3\text{-CaO-Na}_2\text{O}$ . A relatively large amount of fly ash (>40%) can be used successfully for the preparation of porous glass.

© 2009 Elsevier B.V. All rights reserved.

## 1. Introduction

The amount of coal ash discharged from coal burning power plants has increased steadily due to the consequent increase in the electricity demand in the country. In Thailand, the amount of coal ash discharged is roughly 4 million tons/year and about 1 million ton is utilized directly in cement industry [1]. The rest is mainly disposed through land filling, and this coal ash waste has caused both the environmental and the ecological problems [2].

Although many applications or utilizations and researches on the effective utilization of coal fly ash have been made [3–10], the most coal fly ash is used in construction-related applications [1], which include cement and concrete manufacturing and the production of bricks and lightweight aggregates, and as additives for ceramics. Under these circumstances, the effective utilization of coal ashes is strongly desired from environmental, ecological and economical point of view.

The fly ash is basically composed of  $\text{SiO}_2\text{-Al}_2\text{O}_3\text{-CaO}$  system with a considerable amount of  $\text{Fe}_2\text{O}_3$ , and consists of glassy phase with a small amount of crystals [11]. Recently, many researches and development investigations have been conducted in the utilization of fly ash as a raw material for glass-ceramics in floor tile or side wall production industries [8–10]. However, there are some

inherent problems associated with the use of coal fly ashes due to their various qualities being dependent on the coal compositions, combustion conditions, etc. This may be the reason that prevents the wide application and effective utilization of coal fly ash.

Porous glass is one of inorganic porous materials. The important features of this material are as follows [12]: thermal stability, high mechanical strength, resistance for bacteria, high chemical stability, very narrow pore size distribution, excellent shaping ability, wide controlled pore size range and transparency. Porous glass is manufactured mainly by three processes including, phase separation process, sol-gel process and crystallized process. The phase separation method is the most important method. Applications of porous glasses are of very wide range. It is used as a separation membrane, catalyst and its support, enzyme support, packing material for chromatography, support for DNA synthesis and chemical durable resistor. However, the substantial application is not yet fully developed.

In this research, porous glasses were prepared using fly ash as a raw material by a conventional phase separation method, and the properties of porous glasses were investigated.

## 2. Experimental

## 2.1. Coal fly ash

The coal fly ash used in this study was supplied by "Rayong coal burning thermal power plant" in Rayong, Thailand. The fly ash

\* Corresponding author. Tel.: +66 44 22 4475; fax: +66 44 22 4612.  
E-mail address: shigeki@sut.ac.th (S. Morimoto).

**Table 1**  
Chemical composition (wt%) of fly ash from Rayong thermal power plant, Thailand.

SiO <sub>2</sub>	Al <sub>2</sub> O <sub>3</sub>	Fe <sub>2</sub> O <sub>3</sub>	MgO	CaO	Na <sub>2</sub> O	K <sub>2</sub> O	S	lg. loss
41.62	23.11	6.03	1.59	14.92	1.15	1.92	0.77	2.60

appeared to be dark grey in color. The fly ash sometimes contains a small amount of organic materials or reducing materials which attack a Pt/Rh alloy severely, hence it was calcined at 900 °C for 10 h in an electric furnace in air to remove these reducing materials, and stored in a desiccator.

The chemical composition of fly ash was analyzed by XRF method and shown in Table 1. It is clear that this fly ash is basically composed of SiO<sub>2</sub>-Al<sub>2</sub>O<sub>3</sub>-CaO system with a considerable amount of Fe<sub>2</sub>O<sub>3</sub> and SO<sub>3</sub> (or S). The fly ash consists mainly of glassy phase (~75%) with crystalline phases (~25%) of  $\alpha$ -quartz, anorthite (CaAl<sub>2</sub>Si<sub>2</sub>O<sub>8</sub>) and gehlenite (Ca<sub>2</sub>Al<sub>2</sub>SiO<sub>7</sub>), and the average particle size was 33  $\mu$ m with a small amount of fine powder (smaller than 1  $\mu$ m) [11].

In order to use this fly ash as a raw material for the preparation of porous glass, the chemical composition of this material should be considered, and also a larger quantity must be used. This fly ash is basically composed of SiO<sub>2</sub>-Al<sub>2</sub>O<sub>3</sub>-CaO system, and hence a well-known glass of SiO<sub>2</sub>-B<sub>2</sub>O<sub>3</sub>-Na<sub>2</sub>O system is not suitable for base glass. Although, the three component system

**Table 2**  
Properties of porous glasses after acid leaching (powder specimens).

Heat treatment		Surface area (m <sup>2</sup> /g)	Pore volume (cc/g)	Pore diameter (nm)
Temperature (°C)	Time (h)			
650	90	51.0	0.16	9.1
	120	65.9	0.18	9.5
	150	29.3	0.13	11.4
700	50	13.2	0.15	52.1
	90	16.3	0.16	71.1
	120	13.3	0.24	95.9
725	72	9.0	0.29	296
	90	9.6	0.18	544
	120	8.1	0.3	581
750	10	17.9	0.26	159
	20	11.5	0.32	467
	40	6.7	0.32	1123
780	5	14.0	0.32	565
	10	15.4	0.16	1615
	20	3.5	0.34	2097
800	5	12.5	0.13	752
	8	24.4	0.23	2011
	16	15.2	0.32	6663

of SiO<sub>2</sub>-B<sub>2</sub>O<sub>3</sub>-CaO exhibits a very wide apparent phase separation region [13], it is difficult to control phase separation, and

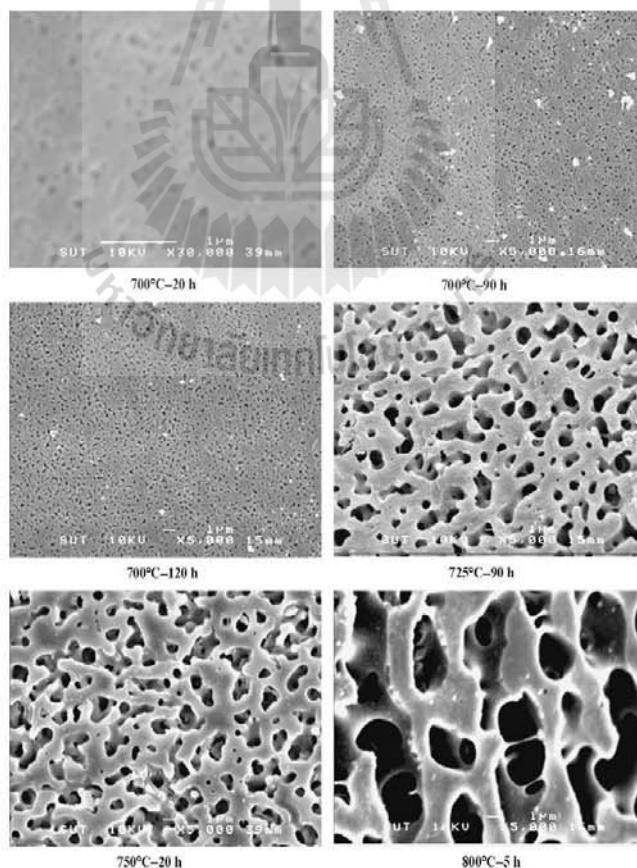


Fig. 1. SEM photos of porous glasses obtained under various heat treatment conditions.

therefore  $\text{Al}_2\text{O}_3$  should be added to suppress and control the phase separation. Thus, the  $\text{SiO}_2\text{-B}_2\text{O}_3\text{-Al}_2\text{O}_3\text{-CaO}$  system must be suitable for the preparation of porous glass using fly ash as a raw material, and finally, the  $\text{SiO}_2\text{-B}_2\text{O}_3\text{-Al}_2\text{O}_3\text{-CaO}$  system was chosen as the base glass.

## 2.2. Sample preparation

The composition of parent glass was  $51.7\text{SiO}_2\text{-}9.2\text{Al}_2\text{O}_3\text{-}17.6\text{B}_2\text{O}_3\text{-}2.4\text{Fe}_2\text{O}_3\text{-}0.6\text{MgO}\text{-}13.2\text{CaO}\text{-}4.5\text{Na}_2\text{O}\text{-}0.8\text{K}_2\text{O}$  (wt%). Silica sand, fly ash, and reagent grade chemicals of  $\text{CaCO}_3$ ,  $\text{H}_3\text{BO}_3$  and  $\text{Na}_2\text{B}_4\text{O}_7\cdot 10\text{H}_2\text{O}$  were used as raw materials. A batch corresponding to 150 g of glass was mixed thoroughly and melted in 100 cc Pt/Rh crucible at  $1450\text{ }^\circ\text{C}$  for 2 h in an electric furnace in air. The amount of fly ash introduced into the batch was about 60 g for 150 g of glass. The molten glass was poured onto iron plate and pressed by another one and then heat treated under various conditions ( $650\text{--}800\text{ }^\circ\text{C}$ ,  $5\text{--}150\text{ h}$ ) for phase separation. After heat treatment, they were cut and polished into a plate of about 1.5 mm in thickness, and also powder samples of  $0.425\text{--}1\text{ mm}$  in size were prepared.

## 2.3. Acid leaching

Usually sulfuric acid and hydrochloric acid are used for acid leaching process of porous glass production. However, the solubility of sulfates and chlorides in acid and water is much smaller than those of nitrates, especially calcium sulfate. Therefore, the nitric acid was used as a leaching solution in this study. The phase separated glasses were acid leached by 1 N of  $\text{HNO}_3$  solution at  $95\text{ }^\circ\text{C}$  for 24 h, and the acid to glass ratio was about 10 (ml/g). Then they were washed and rinsed by running water for 24 h and dried at  $120\text{ }^\circ\text{C}$  for 24 h.

In some cases, porous glasses were treated by a dilute alkali solution (1N-NaOH) at room temperature for 5 h to remove  $\text{SiO}_2$  colloids remained inside the pores after acid leaching.

## 2.4. Characterization of porous glass

The chemical composition of porous glasses was examined by XRF method, and the wet chemical analysis was applied for the determination of  $\text{B}_2\text{O}_3$  (MTEC, Thailand). The structures of porous glasses were observed by scanning electron microscopy (SEM, JEOL JSM 6400).

The pore characteristics of porous glasses were examined by mercury intrusion porosimetry (Autopore III, Micromeritics).

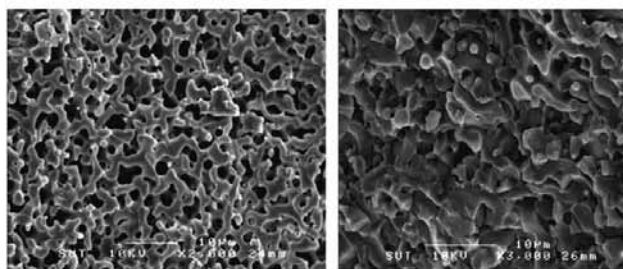
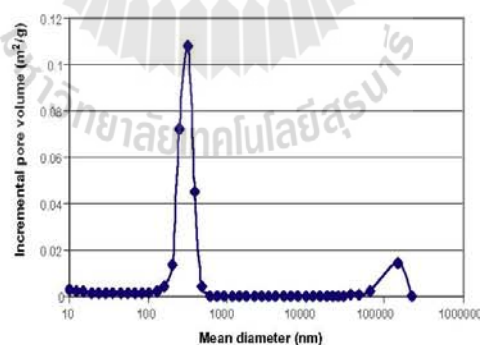
## 3. Results

### 3.1. Phase separation

The glass appeared to be deep grey-green in color, and turned to colorless transparent to white after acid leaching. This suggests that the  $\text{Fe}_2\text{O}_3$  moved to soluble phase and was leached out.

The surface area, pore volume and mean pore diameter of porous glasses are summarized in Table 2. The pore diameter increases abruptly with an increase in heat treatment temperature and time. However, the pore volume increases slightly with increase in heat treatment temperature and time.

Fig. 1 shows SEM photos of porous glasses. The pore structure of porous glass looks like droplet type in the early stage of phase separation ( $700\text{ }^\circ\text{C}$ , 20 h), however, the typical three-dimensional interconnected structures can be seen clearly ( $700\text{ }^\circ\text{C}$ , 120 h;  $725\text{ }^\circ\text{C}$ , 90 h;  $750\text{ }^\circ\text{C}$ , 90 h;  $750\text{ }^\circ\text{C}$ , 90 h and  $800\text{ }^\circ\text{C}$ , 5 h) and pore diameter increases with an increase in heat treatment temperature and time.



(a). Near surface

(b). Center part

Fig. 2. Pore distribution and SEM photos of porous glass plate (~1.5 mm thick). Heat treatment:  $725\text{ }^\circ\text{C}$ , 72 h.

Fig. 2 shows the pore distribution and SEM photos of plate porous glass (725 °C, 72 h). Though the small particles of silica colloids were observed, the three-dimensional interconnected structure can be clearly seen even in center portion of plate porous glass.

Fig. 3(a) shows the relationship between mean pore diameter and cube root of heating time ( $t^{1/3}$ ). Although the process is not clear in early stage of phase separation, a good linearity between pore diameter and root cube of heating time can be obtained in later stage of phase separation. The Arrhenius type plot has been carried out as shown in Fig. 3(b) and a good linearity can be obtained. The Arrhenius equation is also shown in Fig. 3(b). The activation energy for phase separation was calculated to be 104.3 kcal/mol (24.9 kJ/mol).

### 3.2. Effect of alkali treatment

Fig. 4 shows the SEM photos and the pore distribution of porous glass before and after alkali treatment (700 °C, 120 h). The interconnected structure can be seen clearly after alkali treatment. It is clear that the pore diameter increases slightly and the pore volume increases markedly by alkali treatment. This indicates that a relatively large amount of silica colloids remained inside pores.

Table 3 shows the chemical composition of porous glasses before and after alkali treatment. The chemical composition of porous glasses is basically composed of  $\text{SiO}_2\text{-Al}_2\text{O}_3\text{-B}_2\text{O}_3\text{-RO-R}_2\text{O}$  system, and is very similar to Shirasu porous glass [14]. The amounts of  $\text{Al}_2\text{O}_3$  and  $\text{B}_2\text{O}_3$  increase slightly by alkali treatment because of the removal of silica colloids remained inside pores. It should be noted that the amount of  $\text{Fe}_2\text{O}_3$  in porous glass also decreased. This indicates that a large amount of  $\text{Fe}_2\text{O}_3$  moved to soluble phase through phase separation.

## 4. Discussion

### 4.1. Mechanism of phase separation

The two mechanisms for the formation of three-dimensional interconnected structures of phase separation have been proposed, one is the spinodal decomposition [15] and the other is the nucleation and growth [16]. In the latter process, the pore diameter increases proportional to square root of heat treatment time ( $t^{1/2}$ ) until the volume fraction of two phases reaches the constant [17]. After reaching the constant volume fraction, the pore diameter increases proportional to cube root of heat treatment time ( $t^{1/3}$ ) [18]. From results of Fig. 3, although the initial stage of phase separation is not clear, the pore diameter increases proportional to cube root of heating time ( $t^{1/3}$ ) in the later stage. This implies that the small particle melts again and grows to large particles. Then, the large particles contact together and form the three-dimensional interconnected structure. The activation energy for phase separation was calculated to be 104.3 kcal/mol (24.9 kJ/mol). This value is similar to that of viscous flow of glasses, and hence the rate determining step for phase separation seems to be the diffusion process of structural units involving oxygen ions [19].

As shown in Fig. 1, the structure of porous glass is seen like droplet type structure (700 °C, 20 h) in the early stage, and after that this structure grows to interconnected structure with an increase in heating time (700 °C, 120 h). This result indicates that the interconnected structure observed in this study might be formed by the nucleation and growth mechanism.

### 4.2. Pore structure and chemical composition of porous glass

Generally acid soluble phase ( $\text{B}_2\text{O}_3\text{-RO-R}_2\text{O}$  rich phase) contains a considerable amount of  $\text{SiO}_2$  [19] and the solubility of this

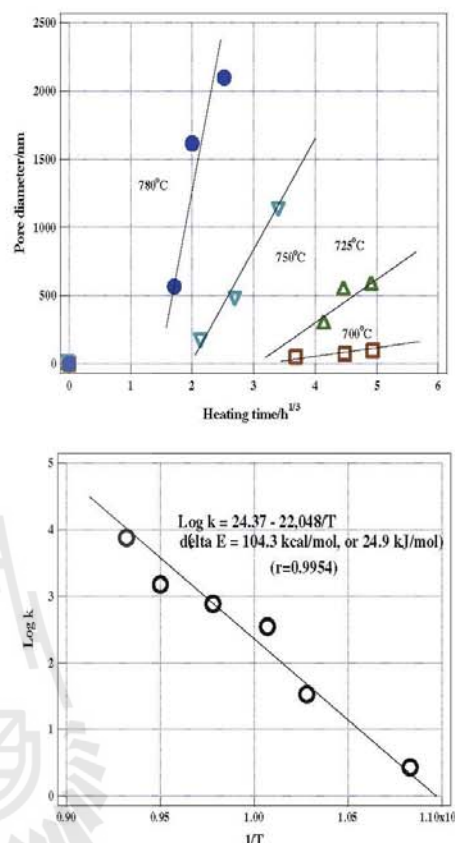


Fig. 3. Relation between pore diameter and cube root of heating time at various temperatures. After acid leaching.

$\text{SiO}_2$  component in acid solution is very low, and therefore  $\text{SiO}_2$  colloids tends to remain inside pores during acid leaching. And therefore it is difficult to observe the clear microstructure of porous glass in  $\text{SiO}_2\text{-B}_2\text{O}_3\text{-Na}_2\text{O}(-\text{Al}_2\text{O}_3)$  system of glass [19]. On the contrary, the three-dimensional interconnected structure can be observed clearly even in center portion of plate porous glass after acid leaching as shown in Fig. 2. This reveals that the acid soluble phase was leached out sufficiently by hot  $\text{HNO}_3$  acid solution. The pore volume increases markedly, but the pore diameter increases slightly by further alkali treatment (Fig. 4). These silica colloids remained inside pores play important role in some application [20], however usually it should be removed out.

The composition of two phases, acid soluble and acid insoluble phases, after phase separation in the system of  $\text{SiO}_2\text{-B}_2\text{O}_3\text{-Al}_2\text{O}_3\text{-CaO-Na}_2\text{O}$  is much different from those of porous glass obtained by  $\text{SiO}_2\text{-B}_2\text{O}_3\text{-Na}_2\text{O}(-\text{Al}_2\text{O}_3)$  system of glass. This system of glass contains a large amount of  $\text{Al}_2\text{O}_3$  to suppress and control the phase separation unlike  $\text{SiO}_2\text{-B}_2\text{O}_3\text{-}(\text{Al}_2\text{O}_3)\text{-Na}_2\text{O}$  glass. When a large amount of  $\text{Al}_2\text{O}_3$  is introduced into strongly phase separable glass system, such as  $\text{SiO}_2\text{-B}_2\text{O}_3\text{-CaO}$  system, the porous glass containing a relatively large amount of  $\text{Al}_2\text{O}_3$  can be obtained [18]. By the simple calculation from original glass composition and porous glass composition, the composition of acid soluble phase is estimated to be rich in  $\text{B}_2\text{O}_3\text{-CaO}(\text{SiO}_2\text{-Al}_2\text{O}_3\text{-R}_2\text{O-Fe}_2\text{O}_3)$  and that of insoluble phase is  $\text{SiO}_2\text{-B}_2\text{O}_3\text{-Al}_2\text{O}_3\text{-CaO}(-\text{R}_2\text{O})$ .

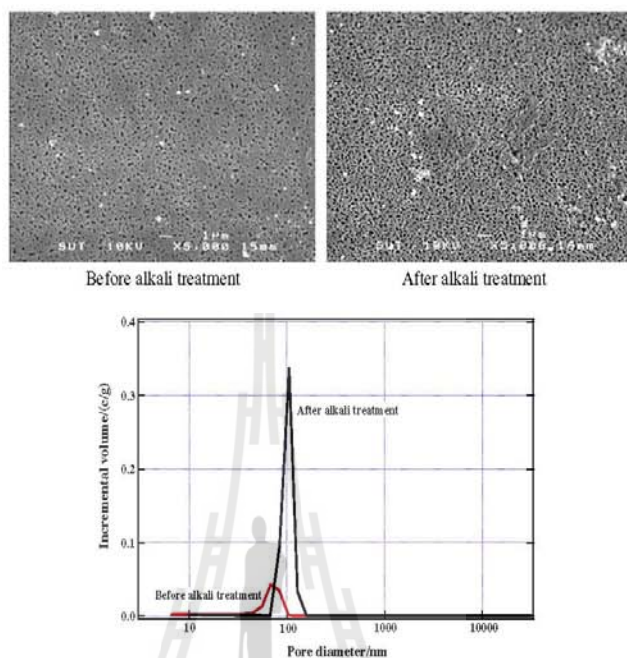


Fig. 4. SEM photos and pore distribution of porous glass before and after alkali treatment. Heat treatment: 700 °C, 120 h.

Table 3  
Chemical compositions (wt%) of porous glass (750 °C, 20 h) before and after alkali treatment.

Porous glass	SiO <sub>2</sub>	Al <sub>2</sub> O <sub>3</sub>	B <sub>2</sub> O <sub>3</sub>	Fe <sub>2</sub> O <sub>3</sub>	MgO	CaO	Na <sub>2</sub> O	K <sub>2</sub> O	Others
Before alkali treatment	69.6	9.16	11.36	0.82	0.2	2.84	4.57	1.08	0.37
After alkali treatment	63.5	11.6	12.28	1.06	0.24	3.66	6.17	1.38	0.11

## 5. Conclusion

The porous glasses were prepared by a conventional phase separation method using coal fly ash as a raw material, and the properties of these porous glasses were investigated.

The composition of coal fly ash is basically composed of SiO<sub>2</sub>–Al<sub>2</sub>O<sub>3</sub>–Fe<sub>2</sub>O<sub>3</sub>–CaO system of glass and the SiO<sub>2</sub>–B<sub>2</sub>O<sub>3</sub>–Al<sub>2</sub>O<sub>3</sub>–CaO–Na<sub>2</sub>O system was chosen as a base glass composition.

The microstructure of porous was observed clearly after acid leaching using HNO<sub>3</sub>. The pore diameter increases proportional to cube root of heating time ( $t^{1/3}$ ) in the later stage, however, the early stage of phase separation is not clear. It is considered that the phase separation takes place by nucleation and growth mechanism. The rate determining step seems to be the diffusion process of structural units involving oxygen ions. The relatively larger pores of above 1 μm can be obtained easily. The pore volume increases markedly by further alkali treatment, but the pore diameter increases slight. The chemical composition of porous glasses is basically SiO<sub>2</sub>–B<sub>2</sub>O<sub>3</sub>–Al<sub>2</sub>O<sub>3</sub>–CaO–Na<sub>2</sub>O.

A relatively large amount of fly ash (>40%) can be used successfully for the preparation of porous glass.

## Acknowledgement

This research was supported by the Royal Golden Jubilee (RGJ) Ph.D. Program of Thailand Research Fund (TRF), to which we are indebted.

## References

- [1] Electricity Generating Authority of Thailand, EGAT Power Plant, 2007. <http://www.egat.co.th/> (online).
- [2] M. Miyake, J. Ceram. Soc. Jpn. 115 (2007) 1.
- [3] J.M. Goumans, H.A. Van der Sloot, Th.G. Albers (Eds.), Environmental Aspects of Constructions with Waste Materials, Elsevier, Amsterdam, 1994.
- [4] G. Dirk, Waste Manage. 16 (1996) 51.
- [5] I. Andres, J.R. Ortiz, J.R. Viguri, A. Irabien, J. Hazard. Mater. 40 (1995) 31.
- [6] A. Garea, J.R. Viguri, A. Irabien, Chem. Eng. Sci. 52 (1997) 715.
- [7] J.R. Kastner, K.C. Das, N.D. Melear, J. Hazard. Mater. B95 (2002) 81.
- [8] T.W. Cheng, Y.S. Cheng, Chemosphere 51 (2003) 817.
- [9] M. Erol, U. Demirler, S. Kucubayrak, A. Ersoy, M.L. Ovecoglu, J. Eur. Ceram. Soc. 23 (2003) 757.
- [10] C. Ferricia, A. Ribeiro, L. Ottosen, J. Hazard. Mater. B96 (2003) 201.
- [11] W. Emem, Effective Utilization of Coal Fly Ash for High Thermal Shock Resistance Glass-Ceramic Ware, Master Thesis, Suranaree University of Technology, 2005.
- [12] T. Yazawa, in: D.-M. Liu (Ed.), Porous Ceramic Materials, Trans Tech Publications, Switzerland, 1995, p. 125.
- [13] E.M. Levin, Phase Diagram for Ceramists, vol. I, J. Am. Ceram. Soc., Ohio, 1964, Fig. 646.
- [14] T. Nakashima, Y. Kuroki, J. Chem. Soc. Jpn. 8 (1981) 1231.
- [15] J.W. Cahn, R.J. Charles, J. Chem. Phys. 42 (1965) 181.
- [16] W. Haller, J. Chem. Phys. 42 (1965) 686.
- [17] S.M. Ohlberg, H.R. Golob, J.J. Hammel, R.R. Lewchuck, J. Am. Ceram. Soc. 48 (1965) 331.
- [18] Y. Moriya, D.H. Warrington, R.W. Douglas, Phys. Chem. Glasses 8 (1981) 19.
- [19] S. Morimoto, in: D.-M. Liu (Ed.), Porous Ceramic Materials, Trans Tech Publications, Switzerland, 1995, p. 147.
- [20] S.V. Phillips, D.S. Crozier, P.W. McMillan, J.M. Taylor, Desalination 14 (1974) 209.

## **BIOGRAPHY**

Mr Chaturaporn Nimjaroen was born on 15<sup>th</sup> of August 1982 in Chonburi, Thailand. He earned his Bachelor's degree in Chemical Engineering in 2005 from Suranaree University of Technology (Thailand). He continued with his Doctoral study in Chemical Engineering at School of Chemical Engineering, Suranaree University of Technology (Thailand), 2013. His expertise is in the area of adsorption and separation processes.

